MLF ANNUAL REPORT 2012

J-PARC/MLF

CROSS

J-PARC 13-03
KEK Progress Report 2013-4

J-PARC/MLF

Materials and Life Science Division
J-PARC Center
Tokai, Naka-gun, Ibaraki 319-1195, Japan
http://j-parc.jp/MatLife/en/index.html

J-PARC was jointly constructed and is now operated by the High Energy Accelerator Research Organization (KEK) and the Japan Atomic Energy Agency (JAEA).

CROSS

Comprehensive Research Organization for Science and Society
http://www.cross-tokai.jp/

Preface to the MLF Annual Report 2012

After recovering from the damage of the devastating disaster occurred in 2011, J-PARC resumed its operation in January 2012. The accelerator operation started at 100 kW and the power was increased to 200 kW in February, when we restarted the user program. Very stable operation continued until the summer shutdown. In October, the operation resumed and then we tested maximum possible power of the accelerator with the equipment then, just before ramping up to 350 kW. And we achieved 534 kW as the maximum power although it was just for a short time due to the license regulation. This result encouraged people to foresee a possible new goal of 1.5 MW instead 1 MW in the future. The 350 kW operation was successfully operated after the maximum power test through the end of March to the end of May, when we encountered another difficulty, the accident at the Hadron Facility.

Delivery of the Bubbling system to mitigate pitting of target container was delayed for half a year, but we were able to install it in the Hg loop and started operation in November, which enabled us to ramp up the accelerator power to 350 KW. The mitigation effect was clearly observed by a laser Doppler vibrometry, although we had another trouble due to the unexpected intrusion of Hg to the branching He pipes. This problem will be solved by improving the piping this year.

Four new beam lines joined the user program club. Those are BL02 (DNA, back scattering inst.), BL15 (TAIKAN, wide angle diffractometer), BL17 (SHARAKU, vertical reflection), BL18 (SENJU, single crystal diffractometer). All of them are constructed and operated under the legislation for the user promotion program. A new beam port of muon, U-line, was also funded by a grant and started construction.

I am happy to announce that JFY 2012 was the most successful year so far for J-PARC and MLF. We received 500 general proposals and the number of the unique users reached 900 and is still growing. Prominent scientific results were created in various scientific fields, such as protein science, superconductor, magnetism and industrial use. A new national project, Element Strategic Program has started and J-PARC/MLF is expected to be a key facility and a large contribution to the program.

Masatoshi Arai
Division Director of Materials and Life Science Division (MLF)

This is the second MLF Annual Report to be compiled jointly between J-PARC Center and CROSS-Tokai. It describes the scientific, technical and operational activities of the MLF during JFY2012 (April 2012 – March 2013).

Two years have now passed since CROSS-Tokai commenced operations in support of the Public Neutron Beam Facility at J-PARC. Though the start of direct user support activities on the Public Beamlines was delayed by about 10 months due to the Great East Japan Earthquake of March 2011, CROSS-Tokai is now fully engaged in its core business of managing the proposal selection process for the Public Beamlines, delivering high-quality user support and promoting facility utilization.

During JFY2012, the suite of Public Beamlines consisted of five fully-operational instruments: BL01 *4SEASONS*, BL02 *DNA*, BL15 *TAIKAN*, BL17 *SHARAKU* and BL18 *SENJU*. From JFY2013, the sixth Public Beamline at J-PARC•MLF – BL11 *PLANET* – will become available to users. With the addition of *PLANET*, the range of science enabled on the Public Beamlines will be extended to the study of liquids and solids under extreme temperature and pressure conditions with particular application in the Earth•Planetary and Materials Sciences.

In keeping with our mandate to promote facility utilization and actively support national research priorities, from the latter half of JFY2012, CROSS-Tokai initiated two new user programs on the Public Beamlines:

- **Trial Use** – a program that promotes the use of neutrons by first-time or novice users from both the industrial and academic sectors; and,
- **Elements Strategy Initiative** – a Japanese Government program that aims to promote the development of alternative materials and technologies in the target areas of permanent magnets, catalysis and batteries, electronic and structural materials.

In the area of facility utilization promotion, we have in the last year joined with JASRI – our sister organization at SPring-8 – to develop a system of Complementary Use proposals. This system aims to encourage and facilitate complementary and collaborative use of multiple large-scale facilities – initially neutron and synchrotron radiation sources – in a single research project. We hope that, ultimately, the system will develop to a stage where users can make a single research proposal to multiple facilities.

Also starting this year, CROSS-Tokai is undertaking the task of reviewing the operation and performance of contract beamlines at the MLF. Specifically, during JFY2012, we established and set terms of reference for the Contract Beamline Evaluation Committee that will carry out the interim review of two Ibaraki Prefecture beamlines (BL03 *iBIX* and BL20 *iMATERIA*) during JFY2013.

As you can see, CROSS-Tokai is now fully up and running and continues to expand the scope and scale of its activities at the MLF. Though by no means exhaustive, I hope that this report will be a useful resource to anyone wishing to know more about CROSS-Tokai and what we do.

As always, and on behalf of the team at CROSS-Tokai, I extend a warm welcome to researchers from around the world who wish to make use of the Public Beamlines at J-PARC•MLF.

Yasuhiko Fujii
Director, CROSS-Tokai

* Research Center for Neutron Science and Technology, Comprehensive Research Organization for Science and Society
www.cross-tokai.jp

Contents

Preface to the MLF Annual Report 2012

Research and Development Highlights

Realization of Pressure Wave Mitigation in a Mercury Target by Microbubble Injection ····· 2
Switching of Intra-Orbital Spin Excitations in Electron-Doped Iron Pnictide Superconductors ····· 4
Dynamics of a Model Protein of the Amyloid Fibril Formation Observed by Neutron Scattering ····· 6
Crystal and Magnetic Structure Investigation on Solid Solution of $BiFeO_3$-$BaTiO_3$ ····· 8
Novel Dielectric Oxides for High-Temperature-Operating Devices ····· 10
Structural and Electrical Properties of Pb-substituted $La_2Mo_2O_9$ Oxide Ion Conductors ····· 12
Determination of the Microstructural Properties of Four Ancient Japanese Steel Arrow Tips through Wavelength Resolved Neutron Transmission Analysis ····· 14
Study of Neutron Radiation Hardness of Hybrid Avalanche Photo Detector for the Belle-II Experiment ····· 16
Evaluation of Manufacturing Process with Energy Selective Neutron Radiography ····· 18
Time-resolved Neutron Imaging with Resonance Absorption Reactions and Its Application in Computed Tomography ····· 20
Two-Dimensional Focusing of Pulsed Neutron Beam with Elliptic Supermirrors ····· 22
Confirmation of Spin Gap Excitations in the Spin-3/2 Substances $RCrGeO_5$ (R = Y or ^{114}Sm) ····· 24
Neutron Brillouin Scattering Experiments on HRC ····· 26
Reentrant-Type Metal–Nonmetal Transition in $Pr_{1-x}Ce_xRu_4P_{12}$ ····· 28
Spin Waves in the Ferromagnetic Phase of MnP ····· 30
Dynamical Properties of Low-Dimensional Quantum Spin Systems ····· 32
Temperature and Element Substitution Effects on Magnetic Excitations in the Triangular-Lattice Antiferromagnet $CuCrO_2$ ····· 35
Chiral Magnetic Soliton Lattice in MnSi ····· 37
Adsorption of Water into DN-gels with Hierarchical Structure ····· 39
Dewetting Process of Deuterated Polystyrene and Poly (vinyl methyl ether) Blend Thin Films via Phase Separation ····· 41
Development of Piezo-Based Low Temperature 2-Axes Goniometer System ····· 43
Investigation of the Degradation Mechanism of ITER CS Conductor Sample using TAKUMI ····· 45
Neutron Diffraction Study on the Structure of Aqueous $LiNO_3$ Solutions ····· 48
Local Lattice Distortion Caused by Short Range Charge Ordering in $LiMn_2O_4$ ····· 50
2D Neutron Diffraction Imaging on an Ammonite ····· 52
New Electronics Board for GEM Detector System (nGEM) ····· 54
Diffusive Behavior of Garnet-type Compounds ····· 56
Development of Non-destructive an Multi-elemental Analysis System by Muonic X-ray ····· 59
μSR Study of Different Magnetic States in Electron-Doped $Pr_{1.3-x}La_{0.7}Ce_xCuO_{4+\delta}$ ($x = 0.10$) Single Crystals Depending on the δ Value ····· 61

Neutron Source

Beam Commissioning in MLF for High Power Operation for JSNS and MUSE ····· 64

New Mercury Target Vessel with Advanced Design ····· 66
Cryogenic Hydrogen System ····· 68
Neutron Target Station ····· 70
Radiation Safety ····· 72
Cooling System for Neutron Source ····· 73
General Control System of MLF ····· 75
Scenes from the Neutron Target Station ····· 77

Neutron Science

BL01: Fermi Chopper Spectrometer 4SEASONS —Improvement in the Background Suppression— ···· 80
BL02: Si Crystal Analyzer near Backscattering TOF Spectrometer DNA
—Specification and Commissioning Results — ····· 82
Upgrading of the IBARAKI Biological Crystal Diffractometer iBIX at BL03 ····· 84
Cross-section Measurement of Neutron Capture for Np-237 at ANNRI (BL04) ····· 86
Studies of Neutron Optics for Physics Researches ····· 88
Development of SuperHRPD and Structural Study of Functional Materials ····· 90
Development of an Advanced Special Neutron Powder Diffractometer
under Extreme Environment for Materials ····· 93
BL10: NOBORU ····· 95
BL11: Performance of High Pressure Neutron Diffractometer PLANET ····· 96
High Resolution Chopper Spectrometer at BL12 ····· 98
BL14 AMATERAS ····· 100
Development and Commissioning of TAIKAN ····· 102
Free Liquid Interface Measurement Using Horizontal Type Neutron Reflectometer SOFIA ····· 104
BL17: Polarized Neutron Reflectometer SHARAKU ····· 106
BL18: Status of SENJU ····· 108
BL19-TAKUMI Engineering Materials Diffractometer ····· 110
The Current Status of the Versatile Neutron Diffractometer, iMATERIA ····· 112
Status of the High Intensity Total Diffractometer (BL21, NOVA) ····· 114
Development and Application of an in-situ SEOP ^{3}He Neutron Spin Filter at J-PARC/MLF ····· 116
Progress of Manyo-Library ····· 118
Activity Report of the Sample Environment at J-PARC/MLF ····· 120
Activity Reports of Chemical Safety Group in MLF ····· 122
ZnS/$^{10}B_2O_3$ Ceramic Scintillator Contributing to Nuclear Security ····· 124
High Pressure MWPC Neutron Detector for Pulsed Neutrons ····· 125
Focusing Supermirrors on Precisely Figured Elliptical Surfaces ····· 126
Development of a Multi-Channel Spheroidal Focusing Mirror ····· 128
Scenes from the Neutron Experimental Hall ····· 130

Muon Science

Status of J-PARC MUSE ····· 132
Commissioning Test for the Remote-Controlled Replacement of the Muon Rotating Target ····· 135
H Line Installation Work ····· 138
Installation of Front-end Magnets for the S-Line ····· 141

Installation of Superconducting Curved Solenoid for the U-line ····· 143
Installation of Superconducting Axial Focusing Magnet for U-line ····· 145
Performance of the DC-separator at the U-line ····· 147
Kicker System – Noise Reduction at D-line – ····· 150
U-line Interlock System ····· 152
Magnetic Shields for W-target Chamber in U-line ····· 154
Development of a Manufacturing Method of Highly Pure Tungsten Foil
for Thermal Muonium Generation ····· 157
Construction of the J-PARC/MUSE Ultra-Slow Muon Beamline ····· 160
Installation and Simulation of Ultra-Slow Muon Beam Line ····· 162
Transport System of Laser Pulses ····· 164
Coherent Lyman-α Resonance Radiation Source for Ultra-Slow Muon Microscope ····· 167
Installation of Kalliope additional positron detectors to DΩ-1 spectrometer ····· 169
Installation of Dilution Refrigerator at J-PARC MUSE ····· 171
Scenes from the Muon Experimental Hall ····· 173

What's new at the MLF in 2012?

Advance Neutron Beam Line for VIllage of Neutron ResOnance Spin Echo Spectrometers
(VIN ROSE) at BL06 ····· 176
Construction of The Pulsed Neutron Imaging Beam Line at J-PARC ····· 178
Polarized Inelastic Neutron Spectrometer POLANO ····· 180
Beam Commissioning of the U-line and Update of the World Record
of the Strongest Pulsed Muon Source ····· 182
Strategic Use ····· 185
JASRI – CROSS-Tokai Complementary Use Proposal Program ····· 186

MLF Operations in 2012

CROSS-Tokai - 2012 Update ····· 188
Status of Beam Operations at the MLF ····· 193
Users at the MLF ····· 195
Proposal Review System ····· 196
MLF Proposals Summary – FY2012 ····· 197
MLF Division Staff 2012 ····· 199
CROSS-Tokai Staff 2012 ····· 201
Committee and Meetings ····· 202
The Government Review of J-PARC ····· 209
MLF Workshops in 2012 ····· 210
Workshops in 2012 ····· 212
Seminars and Courses in 2012 ····· 216
Schools in 2012 ····· 217
Award List ····· 218
MLF Publication 2012 ····· 219

Editorial Board - MLF Annual Report 2012 ····· 227

Organization Chart

Organization Chart of J-PARC Center

- Director, J-PARC Center
  - Deputy Director, J-PARC Center
  - Deputy Director, J-PARC Center
  - Accelerator Division
  - MLF Division
    - Materials and Life Science Division
      - Neutron Source Section
      - Neutron Science Section
      - Neutron Instrumentation Section
      - Muon Science Section
  - Particle and Nuclear Physics Division
  - Transmutation Section
  - Cryogenics Section
  - Safety Division
  - Management Supporting Section
  - Information System Section
  - Public Relations Section
  - Administration Division
    - User Office Team

Organization Chart of CROSS

CROSS is "Registered Institution for Facility Use Promotion" for the public-access neutron beam facilities at J-PARC.

- President
  - CROSS Head Office
  - Director, CROSS-Tokai
    - Science Coordinators
    - Safety Division
    - Administration Division
    - Utilization Promotion Division
    - Neutron R&D Division

The Role of CROSS-Tokai

Under the terms of the legislation that supports the Public Neutron Beam Facility, CROSS-Tokai is entrusted with specific responsibilities. In practical terms, the core functions of CROSS-Tokai can be summarized as follows:

- *Proposal Selection and Beamtime Allocation on the Public Beamlines*
- *User Support on the Public Beamlines*
- *Establishment of an Information Resource for Facility Users*
- *Outreach and Facility Utilization Promotion*
- *Contract Beamline Assessment and Selection*

J-PARC MAP

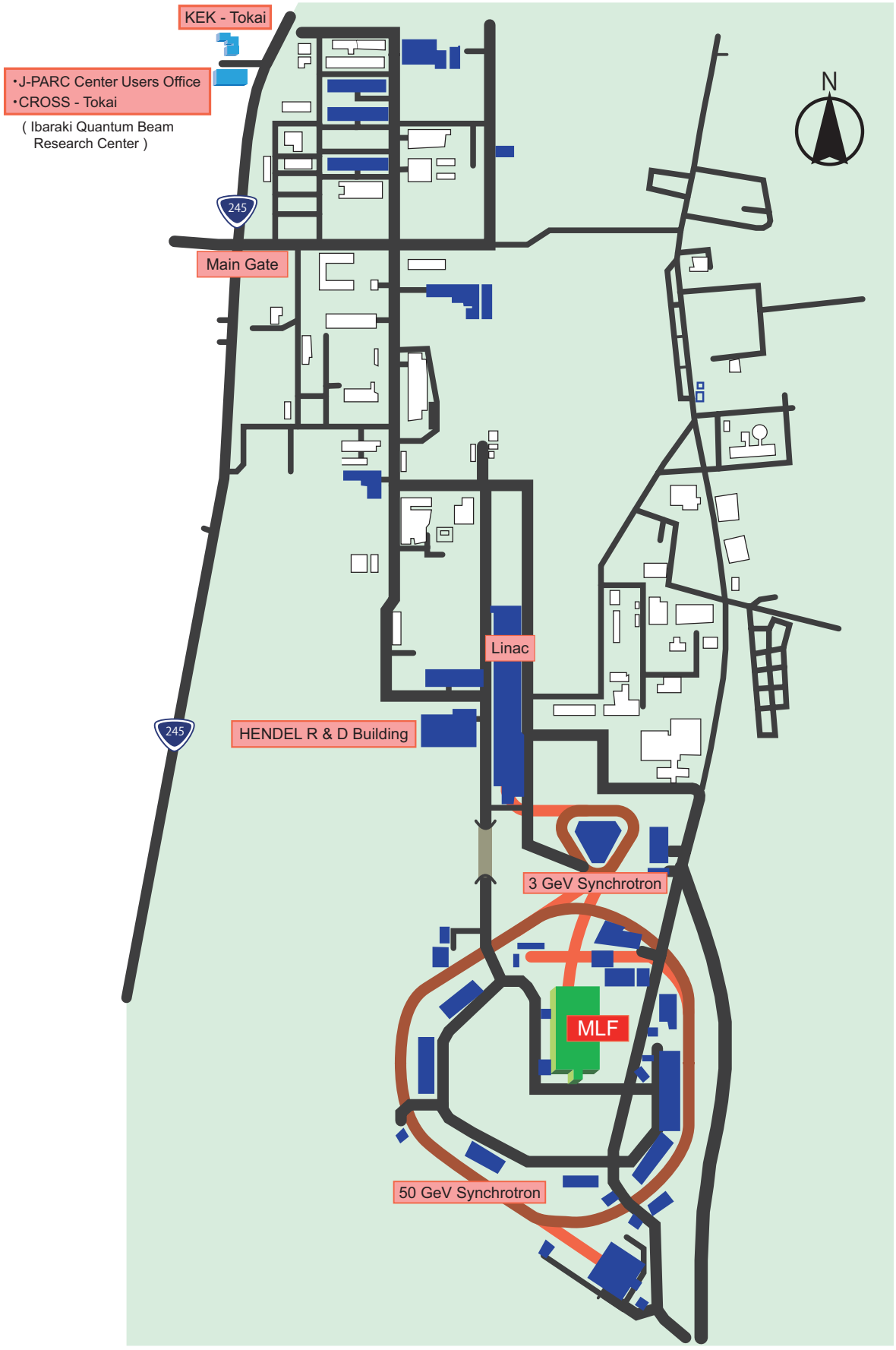
KEK - Tokai
・J-PARC Center Users Office
・CROSS - Tokai
(Ibaraki Quantum Beam
Research Center)
N
245
Main Gate
Linac
245
HENDEL R & D Building
3 GeV Synchrotron
MLF
50 GeV Synchrotron

Muon and Neutron Instruments

Muon Source

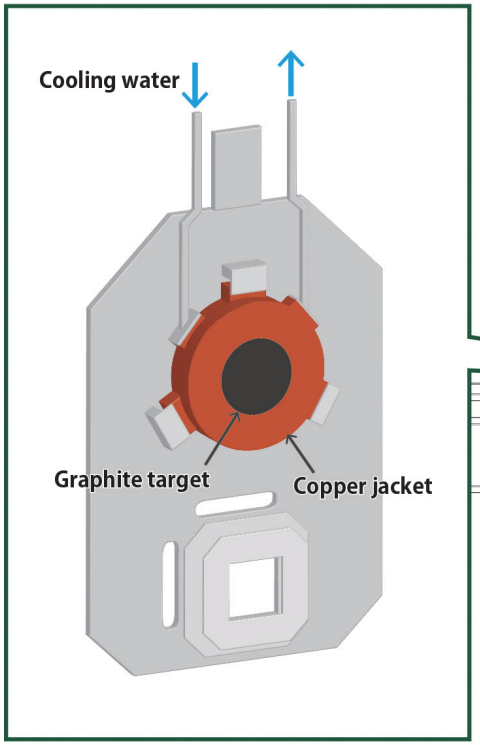

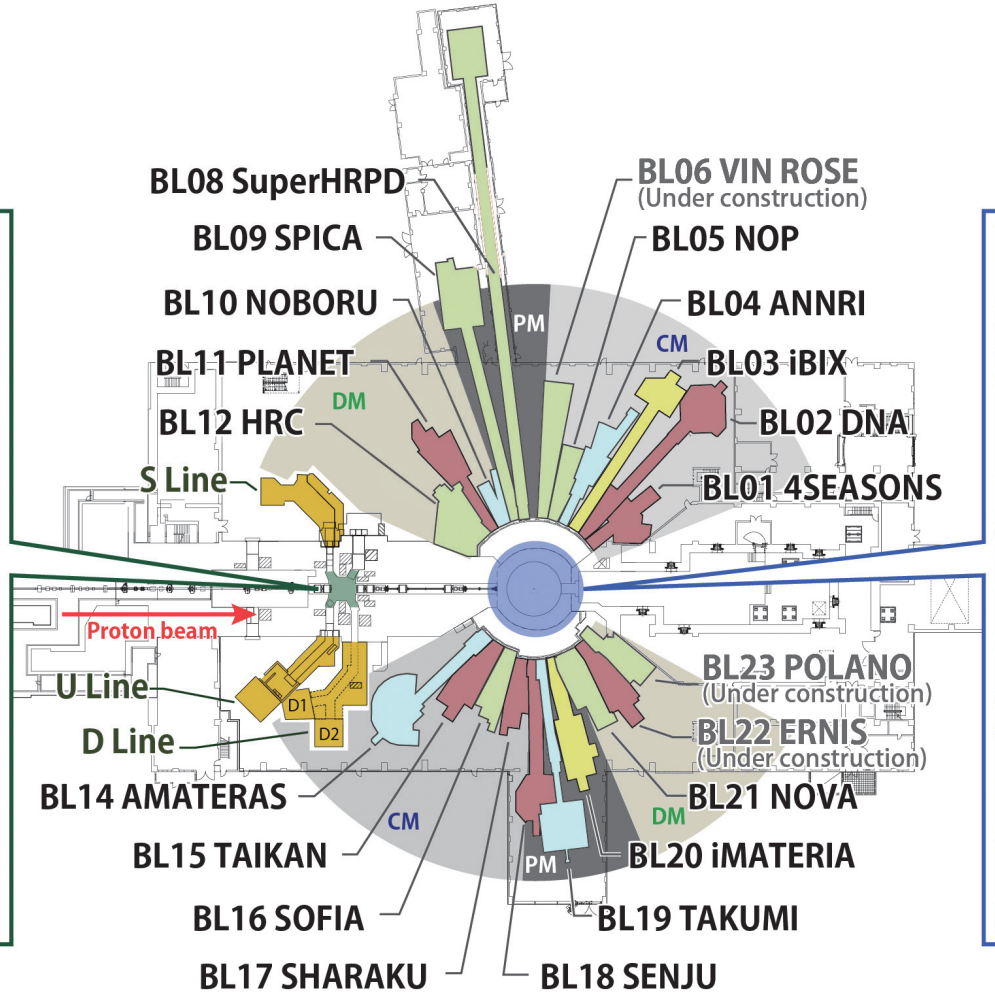

Neutron Source

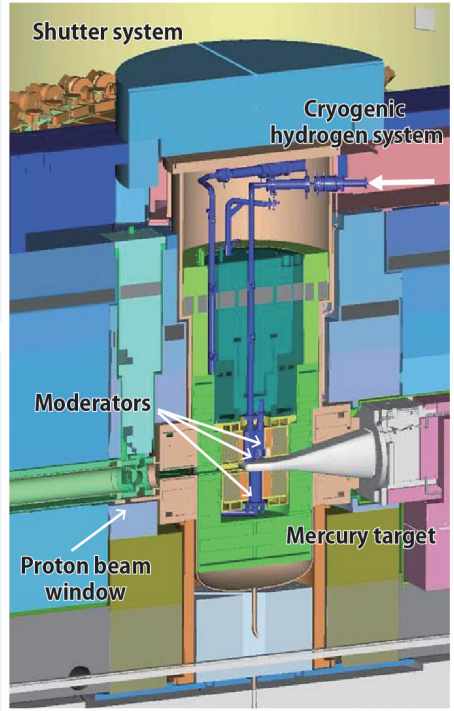

Muon Instruments

Neutron Instruments

JAEA

KEK

Public beam lines

Ibaraki Pref.

Type of moderators

CM Coupled moderator

DM Decoupled moderator

PM Poisoned moderator

Research and Development Highlights

Realization of Pressure Wave Mitigation in a Mercury Target by Microbubble Injection

1. Introduction

A mercury target vessel, which contains liquid mercury for a pulsed neutron target, suffers from cavitation damage induced by the pressure waves propagation in mercury. This damage determines the lifetime of the target vessel. Our approach to reduce the damage, that is, to mitigate the pressure waves, involves injecting microbubbles into the mercury. The microbubbles play the role of a cushion in the mercury; in short, the microbubbles absorb mercury's thermal expansion due to a rapid temperature rise caused by pulsed proton beam bombardment.

A bubble generator, which injects microbubbles into mercury, has been developed [1] and the mercury target operation with bubble injection has been started since October 2012.

2. Operation status

Helium gas is provided to the bubble generator from cover gas in a surge tank of a mercury circulation loop. Figure 1 shows a schematic drawing of the mercury circulation loop with a gas supplying system which has been newly set during the summer shutdown in 2012. Some of the generated microbubbles coalesce into gas layer. The helium gas layer is supposed to accumulate in the target vessel at the outlet. A vent line, which connects the outlet of the target vessel with the surge tank, was set to vent the accumulated helium gas to the surge tank. However, the mercury penetrated the gas supplying line which connects the surge tank with the gas supplying system. The increase of the amount of mercury going into the gas supplying line blocks the helium gas flow to the bubble generator. Then we decided to operate the system closing the vent valve. Figure 2 shows the time histories of the mercury flow rate, Q_{Hg}, the helium gas flow rate, Q_{He}, and the pressure in the cover gas, P_{CG}, when the vent valve is closed. Because of gas accumulation at the target outlet, P_{CG} was decreased, which caused decrease of Q_{He}. Since the accumulated gas creates resistance against the mercury flow, Q_{Hg} was decreased. However these values became constant after 180 hours of operation. Although Q_{Hg} and Q_{He} were decreased at the beginning of the operation, we could operate the target system with microbubbles for 3 weeks keeping the gas flow rate at over 0.06 m^3/h; this value is half of the required value. When the vent valve was opened, a decrease in these values was not observed. Then a gas-liquid separator will be installed in the vent line, which will prevent the mercury from penetrating the gas supplying line.

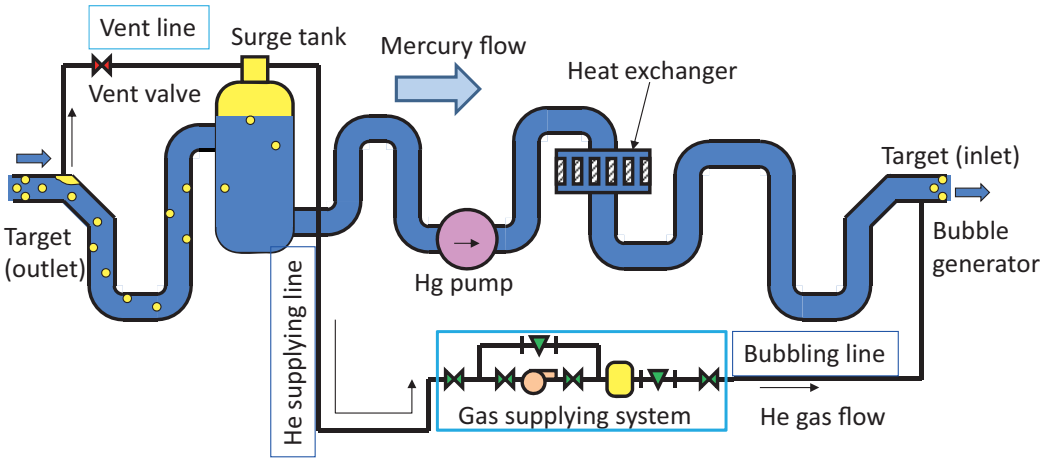

Figure 1. Schematic drawing of a mercury circulation loop with a gas supplying system.

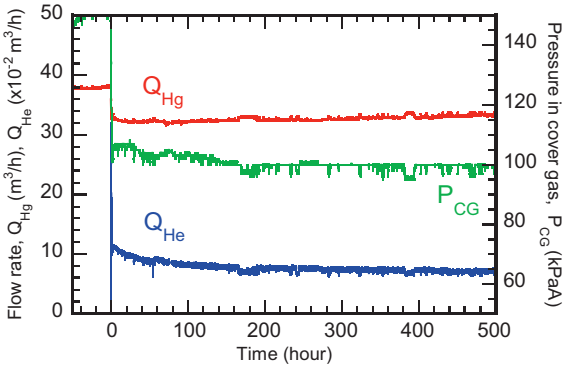

Figure 2 Time histories of the mercury flow rate, Q_{Hg}, the helium gas flow rate, Q_{He}, and the pressure in the cover gas, P_{CG}, when the vent valve is closed.

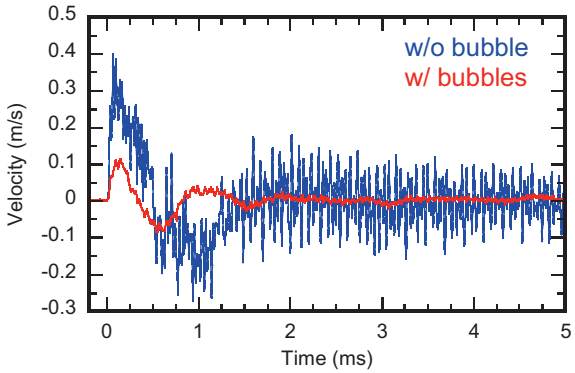

Figure 3 Time history of the vibrational velocities obtained by the laser Doppler diagnostic system.

3. Change in the dynamic response

The vibrational velocity of the target vessel induced by the pressure waves was measured using the laser Doppler diagnostic system [2]. In order to demonstrate the effect of distributed microbubbles on pressure waves in mercury, the vibrational velocities were measured both with and without microbubbles injecting. Figure 3 shows the typical examples of the time histories of vibrational velocities of both without and with microbubbles [3]. The beam power and peak energy in the mercury are approximately equivalent to 300 kW and 3.0 J/cc/pulse, respectively. In the case of without bubbles, high-frequency components resulting from the ringing of the target vessel were superimposed after a beam injection. In the case of with bubbles, on the other hand, it can be seen that the amplitude of the velocity immediately after a beam injection was clearly reduced and so were the high-frequency components. Furthermore, damping of the vibration was relatively shorter than that in the without bubbles case.

Figure 4 shows the relationship between the maximum velocity reduction due to the bubble injection and the injected gas fraction to the mercury flow. The maximum vibrational velocity decreases with the increase of the injected gas. This result encourages us to improve the gas flow rate by the installation of a gas-liquid separator to reduce much more the pressure wave. Furthermore, we have confirmed that the cavitation damage is correlated

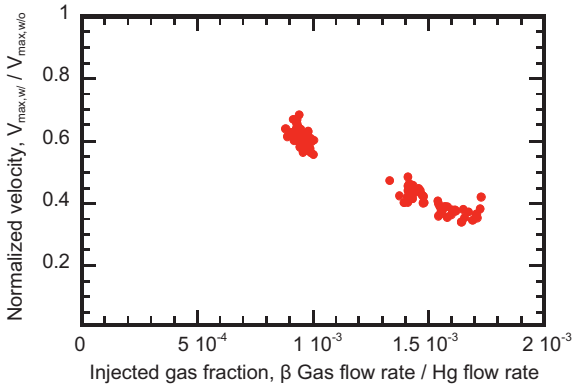

Figure 4 Relationship between the maximum velocity reduction due to the bubble injection and injected gas ratio to the mercury flow.

with the maximum vibrational velocity through the on-beam experiments. Therefore, we expect that the cavitation damage induced by the pressure waves would be dramatically reduced by the microbubbles injection. In the future, we will observe the beam window portion of the target vessel that has been continuously operated under the microbubbles injecting condition to verify the effect of the microbubbles on the cavitation damage.

References

[1] MLF ANNUAL REPORT 2010 **4**.

[2] M. Teshigawara, *et al.*, J. Nucl. Mater. **398** (2010) 238.

[3] http://j-parc.jp/en/topics/2013/MLFMicroBubbles130130.html

H. Kogawa, T. Naoe, T. Wakui, K. Haga, and H. Takada

Neutron Source Section, Materials and Life Science Division, J-PARC Center

Switching of Intra-Orbital Spin Excitations in Electron-Doped Iron Pnictide Superconductors

1. Introduction

The iron pnictide superconductor $LaFeAsO_{1-x}H_x$ shows a unique phase diagram [1]. In addition to the first superconducting dome with the optimal critical temperature (T_c) of 29 K adjacent to the AFM phase, the second dome with an optimal T_c of 36 K is broadly spread around $x \sim 0.35$; a T-linear resistivity, often referred to as non-Fermi-liquid state, is observed above the T_c. According to previous theoretical calculations, the development of the spin density wave (SDW)-type spin fluctuations is unlikely in such heavy electron-doping conditions $x > 0.3$ due to the change of the Fermi surface (FS) [2], whereas the observed T-linear resistivity implies the crucial relation between the spin fluctuations and the second dome.

Thus, we performed inelastic-neutron-scattering (INS) measurements to investigate the dynamic spin states of $LaFeAsO_{1-x}D_x$ with $x = 0.1$, 0.2, and 0.4 corresponding to the top of the first dome, the T_c valley, and the top of the second dome, respectively. For the sample compositions $x = 0.1$, 0.2, and 0.4, the T_c's were 27, 14, and 34 K, respectively. Several INS measurements were performed using the Fermi chopper spectrometer 4SEASONS in J-PARC. All data presented here were obtained at an incident energy of 45.1 meV [3].

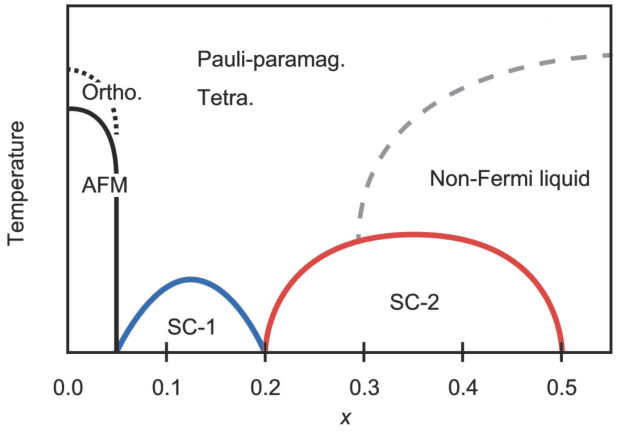

Figure 1. Schematic phase diagram of $LaFeAsO_{1-x}H_x$.

2. Results and Discussion

Figures 2 show the doping dependency of the INS intensity from $LaFeAsO_{1-x}D_x$ with $x = 0.1$, 0.2, and 0.4 at 7 K as a function of momentum transfer (Q) at several fixed energy transfers (E). For composition $x = 0.1$ [Fig. 2(a)], a peak is observed at $Q = 1.14$ Å^{-1} and in $10 < E < 17$ meV. The Q value is very close to the wave vector for the two-dimensional stripe-type AFM order in the parent phase $Q^{2D}_{AFM} = (1\ 0\ 0) \sim 1.1$ Å^{-1} in orthorhombic notation, indicating fluctuations of the SDW. For $x = 0.2$, the magnetic peak completely disappears [Fig. 2(b)]. As x increased to 0.4 [Fig. 2(c)], a peak appears again at $Q = 1.25$–1.38 Å^{-1} in $16 < E < 22$ meV.

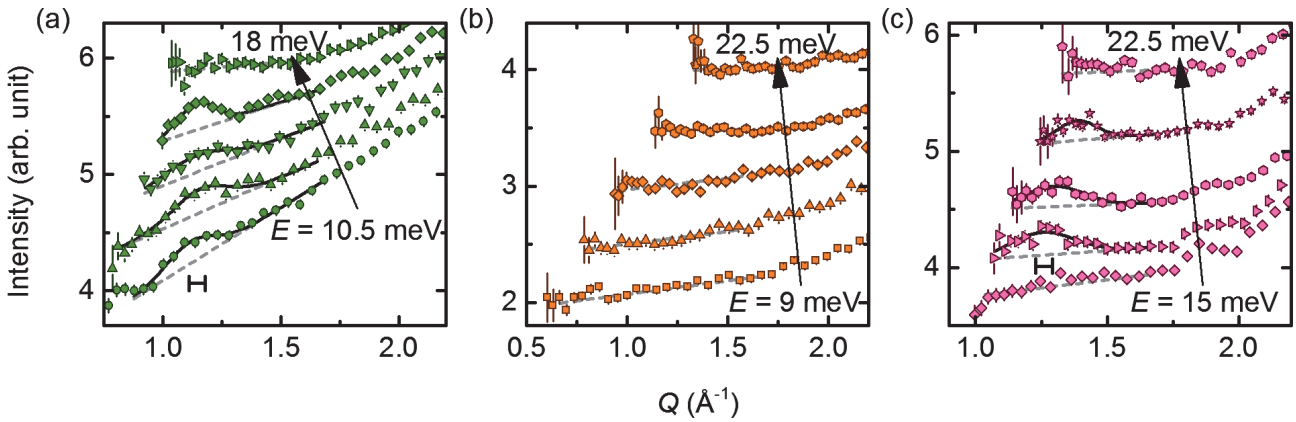

Figure 2. Constant E-scans of $LaFeAsO_{1-x}D_x$ with (a) x = 0.1, (b) 0.2, and (c) 0.4 at $T = 7$ K.

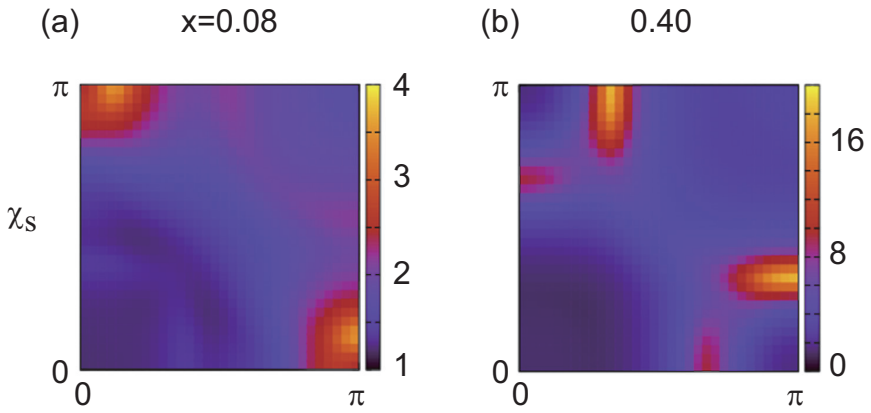

Figure 3. Contour plot of the spin susceptibility for (a) $x = 0.08$ and (b) 0.40.

Figures 3 show the calculated spin susceptibility based on the RPA applied to a five-orbital model of $LaFeAsO_{1-x}H_x$ that was derived from the band calculation using VCA for the doping effect. The calculated χ_s at $x = 0.08$ and 0.40 have a peak at $Q = (\pi, 0) \sim 1.1$ Å^{-1} and $(\pi, 0.35\pi) \sim 1.2$ Å^{-1}, respectively, which agree well with the experimental values. From the FS analysis, the origins of the two χ_s peaks are different; the former is derived from the nesting within Fe-3$d_{YZ, ZX}$, whereas the latter is due to the nesting within Fe-3d_{X2-Y2}, indicating the switching of the two intra-orbital nestings within the 3$d_{YZ, ZX}$ and 3d_{X2-Y2} by electron doping. These experimental findings and calculations imply that the orbital multiplicity plays an important role in the doping and/or material dependence of the T_c of the iron pnictides.

References

[1] S. Iimura *et al.*, Nat. Commun. **3**, (2012) 943.
[2] K. Kuroki, H. Usui, S. Onari, R. Arita, and H. Aoki, Phys. Rev. B **79**, (2009) 224511.
[3] S. Iimura *et al.*, Phys. Rev. B **88**, (2013) 060501(R).

S. Iimura[1], S. Matsuishi[2], M. Miyakawa[3], T. Taniguchi[4], K. Suzuki[5], H. Usui[5], K. Kuroki[6], R. Kajimoto[7], M. Nakamura[8], Y. Inamura[8], K. Ikeuchi[7], S. Ji[7], and H. Hosono[1,9]

[1]Materials and Structures Laboratory, Tokyo Institute of Technology; [2]Materials Research Center for Element Strategy, Tokyo Institute of Technology; [3]Superconducting Properties Unit, National Institute for Materials Science; [4]Materials Processing Unit, National Institute for Materials Science; [5]Department of Engineering Science, The University of Electro-Communications; [6]Department of Physics, Osaka University; [7]Neutron R&D Division, CROSS-Tokai; [8]Neutron Science Section, Materials and Life Science Division, J-PARC Center; [9]Frontier Research Center, Tokyo Institute of Technology

Dynamics of a Model Protein of the Amyloid Fibril Formation Observed by Neutron Scattering

1. Introduction

Amyloid fibrils are filamentous protein aggregates found as deposits in patients of various diseases such as Alzheimer's disease, Parkinson's disease, and senile systemic amyloidosis. These abnormal protein aggregates and/or intermediate structures towards the mature fibrils are related to the pathogenesis of these diseases. The elucidation of the amyloid fibril formation mechanism is thus important for elucidation of the mechanism of pathogenesis.

Although the proteins known to form the amyloid fibrils are not related to each other at all, the fibrils formed have similar structures [1], suggesting a common mechanism of the amyloid fibril formation. The investigation of the amyloid fibrils of some "model" protein should therefore provide insights into this common mechanism. We selected hen egg-white lysozyme (HEWL) as a model protein. HEWL assumes various structural states from monomers to the amyloid fibrils as a function of HEWL and ethanol concentrations [2]. It is thus easy to control the structural states of HEWL by changing the amount of ethanol and HEWL in the samples. This HEWL-water-ethanol system is therefore suitable to investigate the mechanism of the amyloid fibril formation.

Since partial unfolding of a protein is likely to trigger the formation of the intermediate(s) towards the amyloid fibrils, investigation of the dynamics of the protein should be important. Here we investigated the dynamics of HEWL in the monomer and the amyloid fibril state by neutron scattering. Neutron scattering provides unique tools to directly measure the dynamics of the proteins. In particular, elastic incoherent neutron scattering (EINS) provides a measure of flexibility of the protein. We performed the EINS measurements of HEWL in the monomer and the amyloid states.

2. Experiments

50 mg/ml HEWL in D_2O and 10 mg/ml HEWL in 90% (v/v) of deuterated ethanol were prepared as samples for the monomer state and the amyloid fibril state, respectively. The EINS measurements of these samples were carried out using the near-backscattering spectrometer *DNA* at MLF/J-PARC. The measurements were done at several temperature points between 280 K and 300 K, at an energy resolution of 12 μeV.

3. Results

Figure 1 shows the EINS curves of HEWL in the monomer and the amyloid fibril states at various temperatures plotted against Q^2 ($Q = 4\pi\sin\theta/\lambda$,

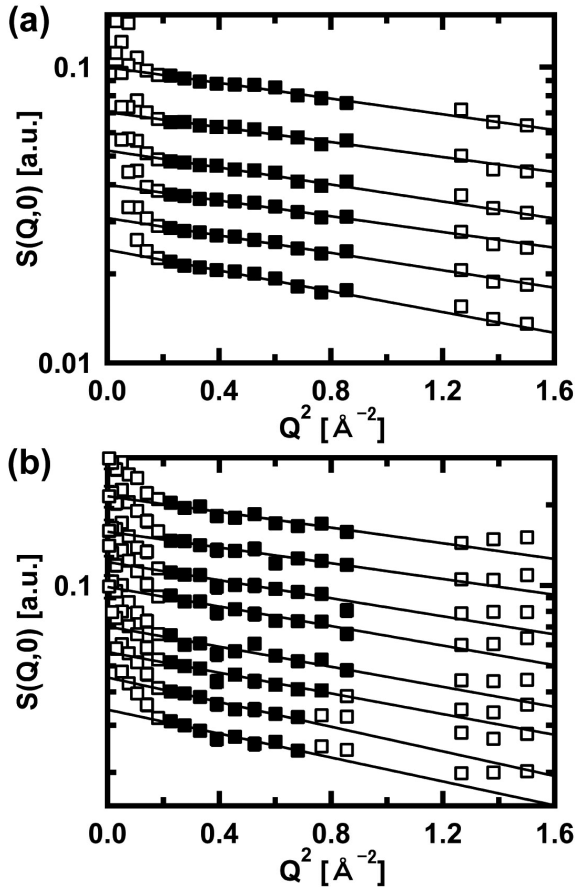

Figure 1. The EINS curves of HEWL (a) in the monomer state and (b) in the amyloid fibril state. In (a), the curves at 280 K, 282.5 K, 285 K, 290 K, 295 K, and 300 K, from top to bottom, are shown. In (b), the curves at 280 K, 282.5 K, 285 K, 287.5 K, 290 K, 292.5 K, 295 K, and 300 K, from top to bottom, are shown.

where 2θ denotes the scattering angle and λ the wavelength of the incident neutrons, is the momentum transfer).

Linear fits to these curves provide the atomic mean square displacements $\langle u^2 \rangle$, shown as data points represented by the filled squares and the fits represented by the solid lines in Fig .1.

Temperature dependence of $\langle u^2 \rangle$ obtained is shown in Fig. 2.

Differences are observed between the monomer and the amyloid fibril states. Linear fits to the data in Fig. 2 provide the values of the effective force constant, which is a measure of flexibility of the protein. From this force constant analysis, the effective force constants were estimated to be 0.10 ± 0.02 N/m for HEWL in the monomer state and 0.058 ± 0.025 N/m for HEWL in the amyloid fibril state, respectively. This indicates that the protein in the amyloid fibril states is more flexible than in the monomer state. This difference in the dynamics of the protein implies the correlation between the aberration in dynamics and the aberration in structures.

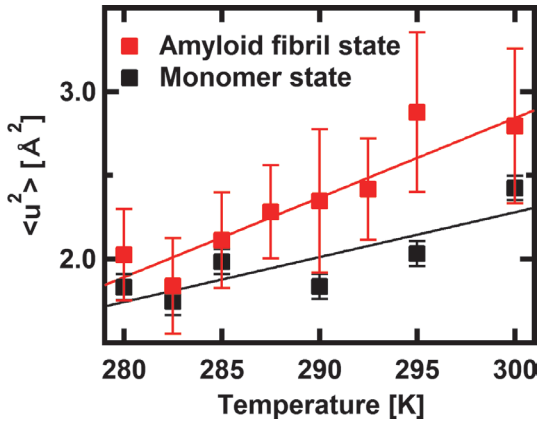

Figure 2. Temperature dependence of $\langle u^2 \rangle$ of HEWL in the monomer state and the amyloid fibril state. Straight lines are the results of the force constant analysis.

References

[1] J. Greenwald and R. Riek: Structure **18** (2010) 1244.

[2] Y. Yonezawa, S. Tanaka, T. Kubota, K. Wakabayashi, K. Yutani and S. Fujiwara: J. Mol. Biol. **323** (2002) 237.

S. Fujiwara[1,2], T. Yamada[3], T. Matsuo[1], N. Takahashi[2], K. Kamazawa[3], Y. Kawakita[2], and K. Shibata[3]

[1]Quantum Beam Science Directorate, JAEA; [2]Neutron Science Section, Materials and Life Science Division, J-PARC Center; [3]Neutron R&D Division, CROSS-Tokai

Crystal and Magnetic Structure Investigation on Solid Solution of $BiFeO_3$-$BaTiO_3$

Multiferroic materials are a group of materials that exhibit several ferroic characteristics simultaneously. Because of their potential to be utilized as actual applications, extensive studies have been conducted for decades. In most of the multiferroic materials multiferroicity manifests itself only under low temperatures, however $BiFeO_3$ (BFO) exhibits multiferroicity, ferroelectricity and antiferromagnetism at room temperature [1-3]. The ferroelectricity appears below T_C ~ 1100 K and the antiferromagnetism below T_N ~ 640 K. The crystal structure below T_C is of a rhombohedrally distorted perovskite type (*R*3c), and the magnetic structure below T_N is of a modulated G-type with an incommensurate period of 620 Å [4].

Recently, the solid solution of BFO with $BaTiO_3$ (BTO), which is a well-known and widely used ferroelectric material, was reported to exhibit improved ferroelectricity and spontaneous magnetization [5,6]. Meanwhile, a structural study by X-ray powder diffraction suggested that the structure of the solid solution is cubic in the ferroelectric region though a cubic symmetry is non-polar. In this study, X-ray and neutron powder structure analyses were performed to clarify the crystal and magnetic structures of the (1-*x*)BFO-*x*BTO solid solutions.

The samples synthesized by the solid state reaction were measured by a laboratory X-ray powder diffractometer (RINT2000@IMRAM, Tohoku University) and the neutron powder diffractometer (HERMES@JRR-3M, JAEA). In addition, the pulsed neutron high-resolution powder diffractometer (SHRPD@J-PARC/MLF) was also used to measure magnetic superlattice reflections in order to examine the variation of the modulated magnetic structure.

The reflection at *R*-point, which characterizes the rhombohedral structure, and the magnetic reflections were observed in the samples of $0 < x < 0.8$. The Rietveld analyses of the X-ray and neutron powder data revealed a complex phase diagram of the BFO-BTO system. For example, at room temperature, there is only a hexagonal phase in $x < 0.15$, coexisting hexagonal and cubic phases in $0.15 < x < 0.8$ and coexisting hexagonal and tetragonal phases in $x > 0.6$. The analyses also revealed that the compositions of the coexisting phases differ from each other. Ba and Ti atoms mostly go into the cubic or the tetragonal phase, and the change of the composition in the hexagonal phase is little. At the same time, the rhombohedral distortion was found to be released as *x* increases.

The observed magnetic superlattice reflections are shown in the figure (left). The overlapping of the peaks is due to the quality of the sample since the resolution of the instrument, $\delta d/d \sim 0.1\%$, should be high enough to resolve the peaks well. The shifts

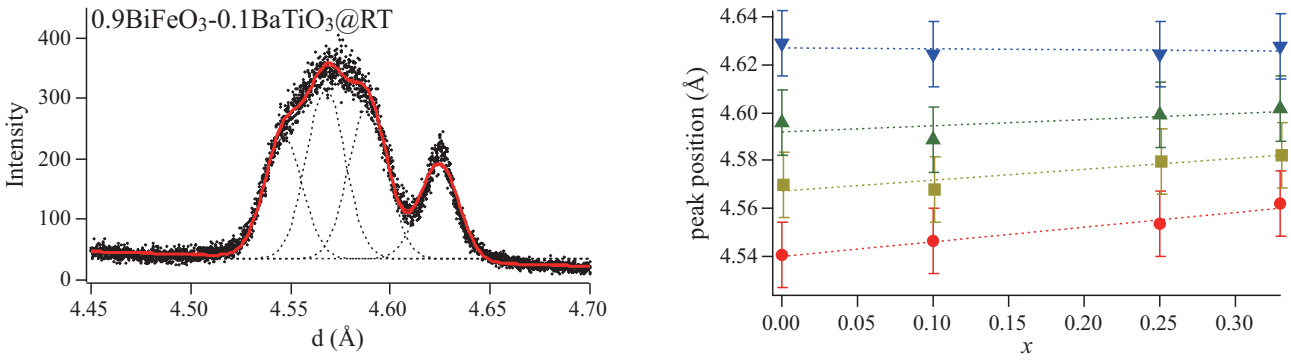

Figure 1. Observed magnetic superlattice reflections (left) and the variation of their position with respect to the nominal composition *x* (right).

of the peak positions are also shown in the figure (right). The positions of the peaks barely varied against the change of *x*. This is a good contrast to the case of BFO doped with manganese, where the peaks shift towards Γ point as the manganese concentration increases [7]. The difference may be attributed to the actual compositions of the hexagonal phase. Hence it can be conjectured that the modulated magnetic structure is affected mainly by its composition rather than its structure. More detailed results can be found in the reference of [8].

References

[1] J. R. Teague, R. Gerson and W. J. James, Solid State Commun. **8** (1970) 1073.

[2] D. Lebeugle, D. Colson, A. Forget, M. Viret, P. Bonville, J. F. Marucco and S. Fusil, Phys. Rev. B **76** (2007) 024116.

[3] S. V. Kiselev, R. P. Ozerov, and G. S. Zhdanov, Sov. Phys. Dokl. **7** (1963) 742.

[4] I. Sosnowska, T. Peterlin-Neumaier, and E. Steichele, J. Phys. C **15** (1982) 4835.

[5] M. M. Kumar, S. Srinath, G. S. Kumar and S. V. Suryanarayana, J. Magn. Magn. Mater. **188** (1998) 203.

[6] T. Ozaki, S. Kitagawa, S. Nishihara, Y. Hosokoshi, M. Suzuki, Y. Noguchi, M. Miyayama and S. Mori, Ferroelectrics **385** (2009) 6155.

[7] I. Sosnowska, W. Schafer, W. Kockelmann, K. H. Andersen, and I. O. Troyanchuk, Appl. Phys. A **74** (2002) S1040.

[8] R. Kiyanagi, T. Yamazaki, Y Sakamoto, H. Kimura, Y. Noda, K. Ohoyama, S. Torii, M. Yonemura, J. Z. Zhang, and T. Kamiyama, J. Phys. Soc. Jpn **81** (2012) 024603.

R. Kiyanagi[1], T. Yamazaki[2], Y. Sakamoto[2], H. Kimura[2], Y. Noda[2], S. Torii[1,3], Y. Yonemura[1,3], J. Zhang[1,3], and T. Kamiyama[1,3]

[1]Neutron Science Section, Materials and Life Science Division, J-PARC Center; [2]IMRAM, Tohoku University; [3]Institute of Materials Structure Science, KEK

Novel Dielectric Oxides for High-Temperature-Operating Devices

1. Introduction

The next-generation power electronics has attracted a great deal of attention because these power electronic devices can markedly reduce an electric power consumed by mortars used for various applications such as electric/hybrid vehicles, trains, and air conditioners. The 50-90% reduction of the electric power loss is expected to be achieved by replacing the currently-used Si-based semiconductors with silicon carbide (SiC)-based ones in the inductors for the mortars. Dielectric capacitors that can be used at high temperatures of up to 200°C are required to realize the SiC-based power devices. However, the currently available capacitors are guaranteed only at a maximum temperature of 175°C.

In this study, $Bi_{0.5}Na_{0.5}TiO_3$ is selected to be a base ferroelectric material for high-temperature dielectric capacitors. Solid solutions of ferroelectric $Bi_{0.5}Na_{0.5}TiO_3$ and paraelectric $Ba(Mg_{1/3}Nb_{2/3})O_3$, $(1-x)Bi_{0.5}Na_{0.5}TiO_3$–$xBa(Mg_{1/3}Nb_{2/3})O_3$ [(1−*x*)BNT–*x*BMN] are chosen. It is shown that (1−*x*)BNT–*x*BMN ceramics with $x = 0.3$ had a high ε_r value of approximately 1000 in the wide temperature range of 25–400°C.

3. Results and Discussion

(1−*x*)$Bi_{0.5}Na_{0.5}TiO_3$–*x*$Ba(Mg_{1/3}Nb_{2/3})O_3$: (1−*x*)BNT–*x*BMN powders were prepared by a solid-state reaction. Time-of-flight neutron powder diffraction data were collected at 25°C using the SuperHRPD at J-PARC. The structure parameters were refined by the Rietveld method using the program Z-Rietveld.

Figure 1 indicates the integrated-intensity ratio of the 113_{hexa} to 111_c peaks, $I(113_{hexa}) / I(113_c)$, calculated from the neutron diffraction data, where "hexa" and "cubic" indicate the hexagonal and cubic notations, respectively. The value of $I(113_{hexa}) / I(113_c)$ is a character showing the volume fraction of the *R*3*c* phase. The intensities of the 113_{hexa} peak originating from the *R*3*c* phase were relatively high for $x = 0.01$ and 0.03, and their values of $I(113_{hexa}) / I(113_c)$ were over 0.1. However, $I(113_{hexa}) / I(113_c)$ decreased markedly around $x = 0.04$ and its value became 0.03 for $x = 0.04$. Although the 113_{hexa} peak was likely to disappear for $x = 0.05$, $I(113_{hexa}) / I(113_c)$ was calculated to be 0.01 for $x = 0.05$. This result shows that powders for $x = 0.05$ contain a small amount of the rhombohedral *R*3*c* phase. The 113_{hexa} peak completely disappeared for $x = 0.10$.

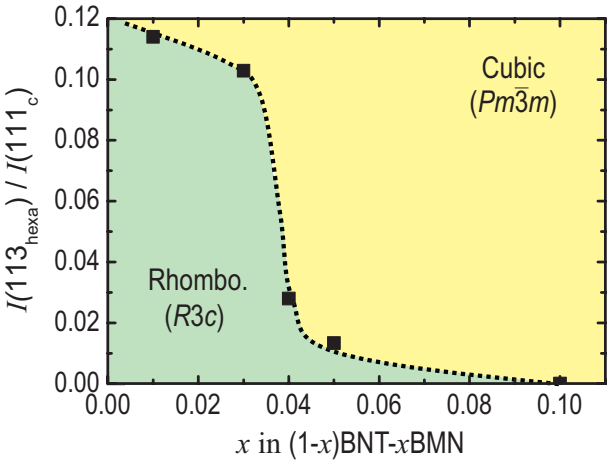

Figure 1. Phase diagram in (1−*x*)BNT–*x*BMN.

Figure 2 shows the temperature dependences of dielectric permittivity (ε_r) and dielectric loss (tanδ). In the temperature (T) range below 200°C, ε_r was strongly dependent on the frequency (f) and ε_r was suppressed when f increased. In this temperature region, tanδ had a relatively high value and increased with increasing f. Above 200°C, ε_r gradually increased with T and showed a maximum at T_m at around 300°C, and then decreases with T.

The strong ε_r and tanδ dependences on T below 200°C are quite similar to the "relaxor" dielectric behavior observed for $Pb(Mg,Nb)O_3$, $Pb(Zn,Nb)O_3$. The "relaxor" dielectric behavior disappeared at high temperatures of $T > 200$°C, which is likely due to the phase transition from the rhombohedral *R*3*c* to the tetragonal *P*4*bm*.

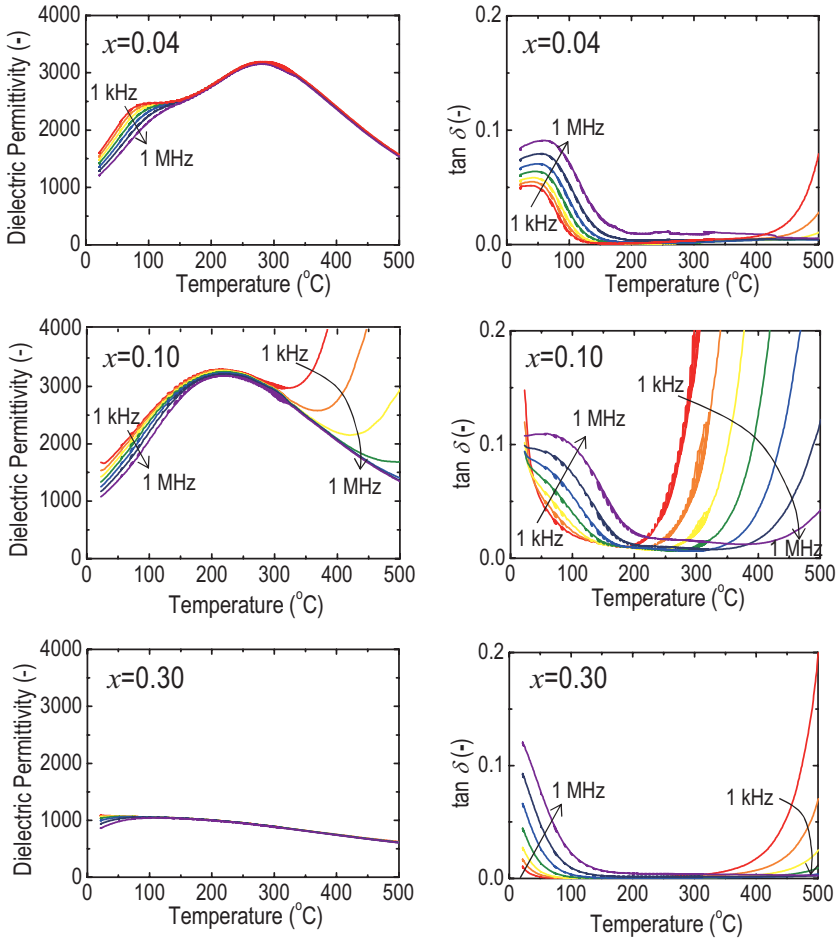

Figure 2. Temperature dependence of dielectric permittivity (ε_r) and dielectric loss (tanδ) of (1−*x*)BNT–*x*BMN ceramics measured at different frequencies.

It is interesting to note that $x = 0.04$ showed an extremely high ε_r over 2,000 at high temperatures in the range of 200°C < *T* < 400°C. This value of ε_r observed for $x = 0.04$ was much higher than that of $BaTiO_3$-based ceramics that have been utilized for ceramics capacitors. In addition, $x = 0.30$ exhibited a dielectric property in which ε_r showed an almost constant value in the wide temperature range from 25°C to 400°C. These stable dielectric properties with respect to *T* are suitable for application in high-temperature capacitors. Further investigations of crystal structures and properties are required to elucidate the origin of this dielectric behavior observed in (1−*x*)BNT–*x*BMN ceramics.

References

[1] Y. Ohshima, Y. Noguchi, T. Oguchi, Y. Kitanaka, M. Miyayama, S. Torii, and T. Kamiyama, ECS Transactions, **45**[3], (2012) 195-207.

Y. Ohshima[1], Y. Noguchi[1], T. Oguchi[1], Y. Kitanaka[1], M. Miyayama[1], S. Torii[2,3], and T. Kamiyama[2,3]

[1]Research Center for Advanced Science and Technology, The University of Tokyo; [2]Neutron Science Section, Materials and Life Science Division, J-PARC Center; [3]Institute of Materials Structure Science, KEK

Structural and Electrical Properties of Pb-substituted $La_2Mo_2O_9$ Oxide Ion Conductors

1. Introduction

The $La_2Mo_2O_9$ oxide ion conductor has been intensively studied for use in the electrolyte of solid oxide fuel cells (SOFC), since the first report by Laccore et al. While pure $La_2Mo_2O_9$ undergoes the phase transition at 580°C accompanied by a drop in conductivity when the temperature decreases, the high-temperature cubic phase (Fig. 1) can be preserved down to room temperature by substituting some cations. Although the bismuth substituted system $La_{2-x}Bi_xMoO_9$ has been widely studied to stabilize the high temperature phase, a Pb-substituted system $La_{2-x}Pb_xMoO_{9-x/2}$ has not been reported yet. Assuming that the chemical properties of bismuth and lead are relatively close and the major difference is the charge valence with the resultant oxide ion vacancy concentration, the contribution of oxide ion vacancy to the ionic conduction property and crystal structure can be discussed by comparing $La_{2-x}Pb_xMoO_{9-x/2}$ and $La_{2-x}Bi_xMoO_9$. In the present study, we synthesize $La_{2-x}Pb_xMoO_{9-x/2}$ samples to clarify the stability, electrochemical properties and crystal structure.

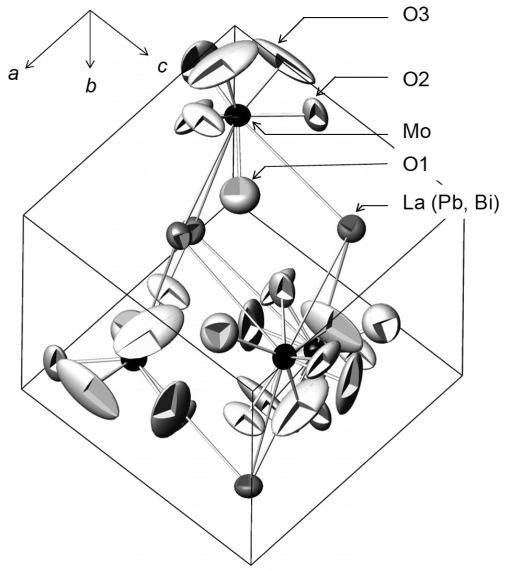

Figure 1. Crystal structure of the high-temperature phase of $La_2Mo_2O_9$.

2. Experimental

$La_2Mo_2O_9$-based solid solutions are prepared by the conventional solid state reaction method. The calcining and sintering temperatures are selected at 500°C and 1000°C, respectively. To confirm the stability of the high temperature phase, samples have been annealed at 450–500°C for more than 10 hours before XRD and thermal analyses.

Electric conductivities are measured by AC two-probe method, and EMF of oxygen gas concentration cells using the sample discs are also measured to determine the dominant charge carrier.

Neutron diffraction experiments are carried out at TOF-type diffractometer Super HRPD installed at MLF of J-PARC. The diffraction data are analyzed by Rietveld method using Z-Rietveld assuming cubic symmetry ($P2_13$).

3. Results and Discussion

From the phase stability experiments by XRD and DSC, it was found that $La_{2-x}Pb_xMoO_{9-x/2}$ exhibits a single phase of high temperature form in the range $0.06 \leq x \leq 0.6$, which is essentially similar to the Bi-substituted system.

Figure 2 shows the Arrhenius plots of electric conductivity. EMF measurements indicate that the transport number of oxide ion is 1.0 for all the solid solutions. Ionic conductivity decreases with the amount of substitution, the trend of which is similar to $La_{2-x}Bi_xMoO_9$ despite the larger number of oxide ion vacancy in the Pb-substituted system. Nevertheless, $La_{2-x}Pb_xMo_2O_{9-x/2}$ exhibits slightly higher conductivity under conditions of lower temperature, while they almost coincide at high temperatures.

In order to find a structural variation with Pb-substitution, neutron diffraction experiments have been carried out on $La_{2-x}Pb_xMo_2O_{9-x/2}$, the results of which are then compared with $La_{2-x}Bi_xMo_2O_9$. Some of the refined structural parameters are represented in Fig. 3. The lattice parameters of both systems

develop with composition showing Vegard's rule. However, the occupation factor of oxide ion at O2 site decreases with the Pb-substitution, while it almost remains the same for Bi-substituted samples. Assuming that the major diffusion path at low temperature is oxide ion hopping between O2 and O3 sites, it is favorable for higher conductivity that defects are likely to form at O2 site with a higher occupancy. Therefore, the slight enhancement in ionic conduction of $La_{2-x}Pb_xMo_2O_{9-x/2}$ at low temperature can be explained in the terms of defect formation. On the other hand, the oxide ion occupancy is thought not to be effective for ionic conductivity at elevated temperatures, because oxide ion motion would be highly activated.

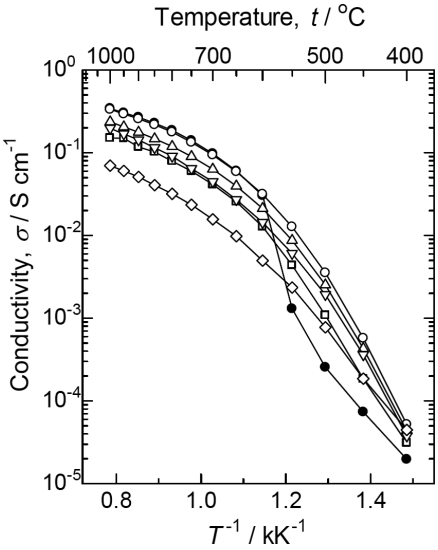

Figure 2. Arrhenius plot of electric conductivity for $La_{2-x}Pb_xMo_2O_{9-x/2}$. ●: x = 0, ○: 0.06, △: 0.10, □: 0.20, ▽: 0.30 and ◇ : 0.60.

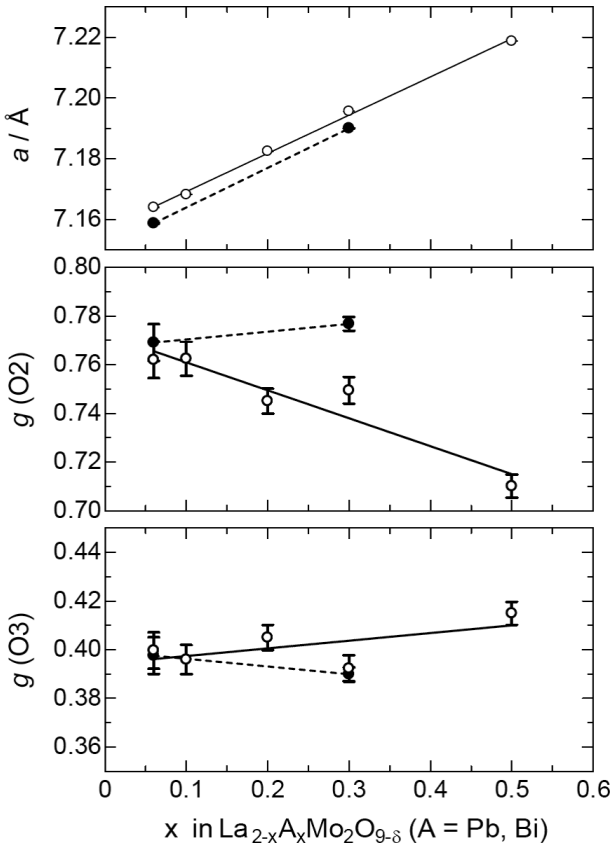

Figure 3. (a) Lattice parameter and occupation factors of (b) O2 and (c) O3 sites for $La_{2-x}Pb_xMo_2O_{9-x/2}$ (○) and $La_{2-x}Bi_xMo_2O_9$ (●).

S. Takai[1,*], Y. Doi[1], S. Torii[2,3], J. Zhang[2,3], T. Y. S. P. Putra[3], P. Miao[3], T. Kamiyama[2,3], and T. Esaka[1]

[1]Graduate of School of Engineering, Tottori University; [2]Neutron Science Section, Materials and Life Science Division, J-PARC Center; [3]Institute of Materials Structure Science, KEK; [*]present address, Graduate School of Energy Science, Kyoto University

Determination of the Microstructural Properties of Four Ancient Japanese Steel Arrow Tips through Wavelength Resolved Neutron Transmission Analysis

1. Introduction

Japanese arms and armors represent one of the most important topics in the field of historical metallurgy. Since ancient times, the Japanese swords are recognized as outstanding in terms of hardness, resilience and, last but not least, aesthetics. The importance of the Japanese arms and armors has increased as a result of several studies conducted since the late 19th century, both from stylistic point of view [1-2] and from the analytical scientific approach [3-6]. Until now, the scientific analysis was based mostly on the traditional metallurgy techniques: metallography and scanning electron microscopy (SEM), both of them invasive [3-4]. More recently, Japanese swords have been analyzed through non-invasive quantitative methods as time of flight neutron diffraction (ToF-ND) [5-8] and neutron imaging (NI) [9] allowed obtaining important information about composition as well as about the thermal and mechanical treatments. The two neutron techniques have their limitations that, however, can be overcome by applying a third neutron-based method, namely position sensitive wavelength resolved neutron transmission analysis (PS-WRNTA).

We have analyzed 4 Japanese arrow tips attributed to the Edo period (17th-19th century) with different shape, composition and conservation status (see fig. 1). The sample composition was determined through ToF-ND [10].

The PS-WRNTA measurements were performed exploiting the time of flight feature to determine the microstructural properties of the samples as microstrain, phase distribution and degree of crystallinity. An innovative high spatial, high time resolution detector, developed by A. Tremsin [11], was used to obtain, at the same time, a whole set of radiographies, each for a specific neutron wavelength.

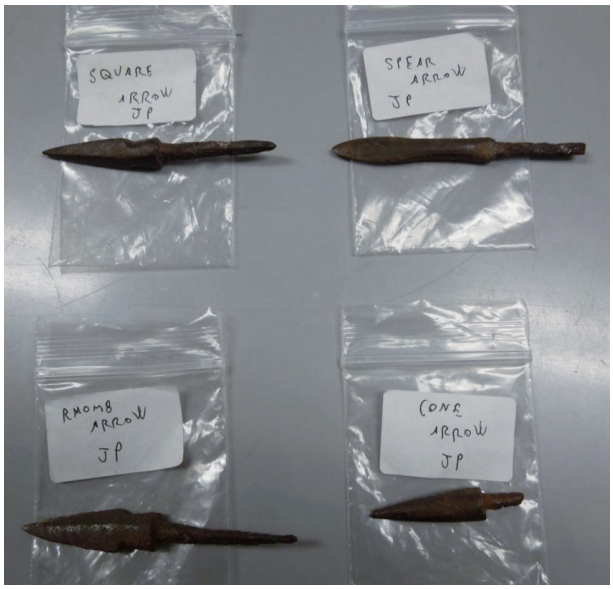

Figure 1. Picture of the four analyzed samples. Square (Sq) and rhomb (Rh) are low carbon steel, spear (Sp) is high carbon steel, and cone (Co) is iron.

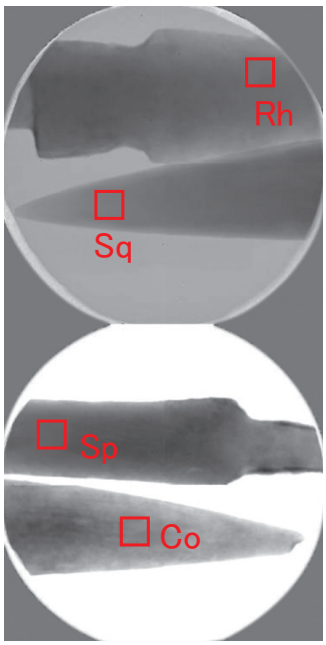

Figure 2. Energy integrated radiography of the samples. The microstructural features are revealed by the different levels of gray. The red squares define the areas of the wavelength distribution intensity (fig. 3).

2. Results

The detector was set to scan regions corresponding to the main Bragg edges in the transmis-

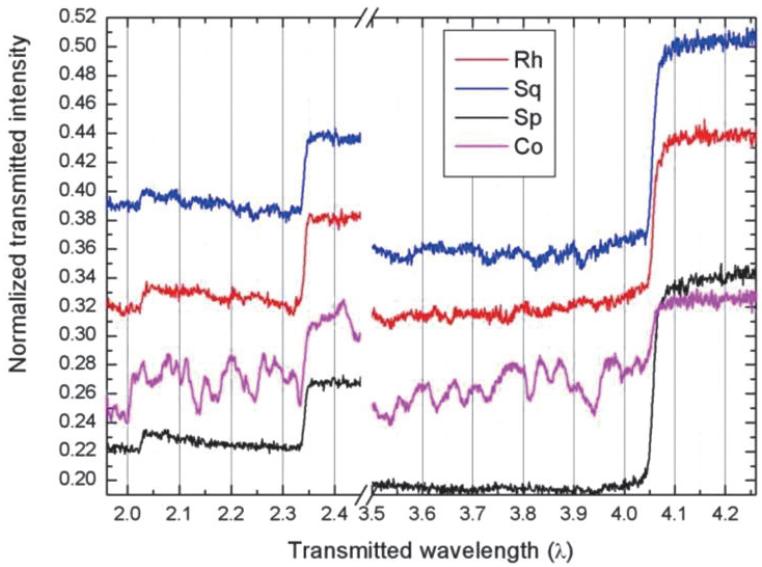

Figure 3. Wavelength distribution intensity of the highlighted areas of fig. 2 corresponding to the 211 and 110 Bragg edges. The cone sample (pink) presents several ferrite single crystal oriented grains, identified by the presence of dips on the left side with respect to the edge. Minor presence of oriented single crystals is present in rhomb (red) and square (blue) samples while the spear one (black) appears to be isotropic.

sion spectrum of ferrite (the main phase of each sample), namely the 110 (4.05 Å), 200 (2.68 Å), and 211 (2.34 Å) reflections. The data were normalized using the open beam images.

In this way it was possible to map the Bragg edge features through the whole volume of the samples (see figs. 2 and 3). Identification and mapping the presence and orientation of single crystals in iron, represents an outstanding result in the study of ancient and modern metallurgy.

References

[1] L. Kapp, *et al.*, *The Craft of the Japanese Sword*, Kodansha International (1998).

[2] K. Nagayama, *The Connoisseurs Book of Japanese Swords*, Kodansha International (1997).

[3] M. Chkashige, *Oriental Alchemy*, Samuel Weiser press (1974).

[4] J. Piaskowski, J. Hist. Met. Soc. **27** (1993) 110.

[5] F. Grazzi, *et al.*, Anal. Bioanal. Chem. **395** (2009) 1961.

[6] F. Grazzi, *et al.*, Mater. Sci. Forum **652** (2010) 157.

[7] F. Grazzi, *et al.*, Anal. Bioanal. Chem. **400** (2011) 1493.

[8] F. Grazzi, *et al.*, J. Anal. At. Spectrom. **26** (2011) 1030.

[9] F. Salvemini, J. Anal. At. Spectrom. **27** (2012) 1494.

[10] E. Barzagli, *et al.*, Proceedings IUCR2011 meeting, Madrid (2011).

[11] A. S. Tremsin, *et al.*, Nucl. Instrum. Meth. Phys. Res. A **628** (2011) 415.

F. Grazzi[1], E. Barzagli[1], F. Salvemini[1], F. Civita[2], H. Sato[3], T. Shinohara[4], T. Kamiyama[3], Y. Kiyanagi[3], A. Tremsin[5], and M. Zoppi[1]

[1]CNR-ISC, Firenze, Italy; [2]Stibbert Museum, Firenze, Italy; [3]Hokkaido University; [4]Neutron Science Section, Materials and Life Science Division, J-PARC Center; [5]Space Sciences Laboratory, University of California, Berkeley, USA.

Study of Neutron Radiation Hardness of Hybrid Avalanche Photo Detector for the Belle-II Experiment

1. Introduction

The search for New Physics (NP) beyond the Standard Model is one of the main subjects in the experimental particle physics today. The LHC experiment at CERN performs direct search for NP through high energy proton-proton collisions. Another way of NP search is to find any signature of the interference between the Standard Model process and NP process. The Belle II experiment is aimed to find such interference in the B-meson and tau lepton decays. To find small signature of new physics process, a SuperKEKB accelerator that will be used for the Belle II experiment, has been designed to produce 40 times higher luminosity compared to the KEKB accelerator that was used for the previous B-factory experiment (Belle experiment). On the other hand, high luminosity causes high background at the Belle II detector. A GEANT based Monte Carlo simulation shows that electrons coming from the Bhabha scattering will hit heavy components around the Belle II detector and will produce fast neutrons. All detector components of Belle II are required to have sufficient neutron radiation hardness. We adopt Aerogel Ring Image Cherenkov counter (A-RICH) as the particle identification device for the end-cap part of the Belle II detector. A-RICH consists of Aerogel radiators, Hybrid Avalanche Photo Detectors (HAPDs) and their readout electronics. The fast neutrons could cause displacement damage on the bulk part of Avalanche Photo Diodes contained in a HAPD. At the Belle II end-cap region where HAPDs are to be located, the flux of fast neutrons (1 MeV equivalent neutrons) is estimated to be 1×10^{12} neutrons / cm^2 or slightly higher, assuming that SuperKEKB and Belle II run for 10 years. The specification of the HAPD is mostly finalized and the remaining issue is the neutron radiation hardness. We study the radiation hardness of the HAPD using BL10.

2. Experimental setup

We made four types of HAPDs that had slightly different specifications. At this experiment, those four HAPDs are ordered in a row that would allow the neutron beam to penetrate them. In addition to those HAPDs, two aerogel Cherenkov radiator tiles are also placed in front of them. The total neutron flux is measured using small diodes that have a known relation between neutron dose and leakage current increase. Figure 1 shows the measured total neutron flux at this experiment. This neutron flux is the integrated flux of two irradiation periods:

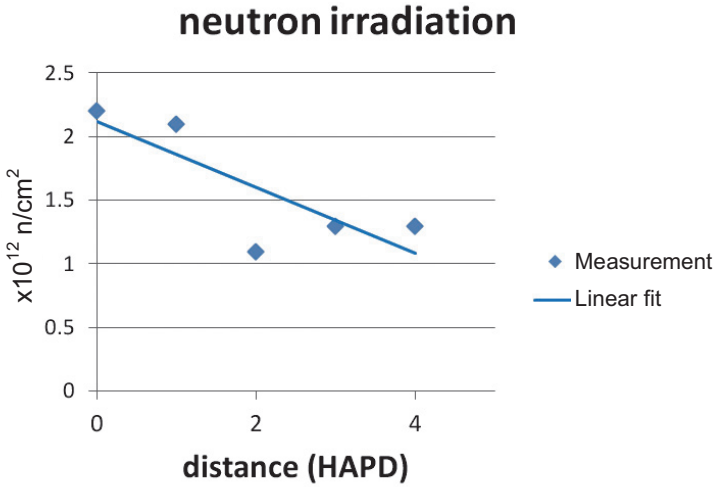

Figure 1. Neutron flux VS ID of diodes (upstream: ID = 0, downstream: ID = 4).

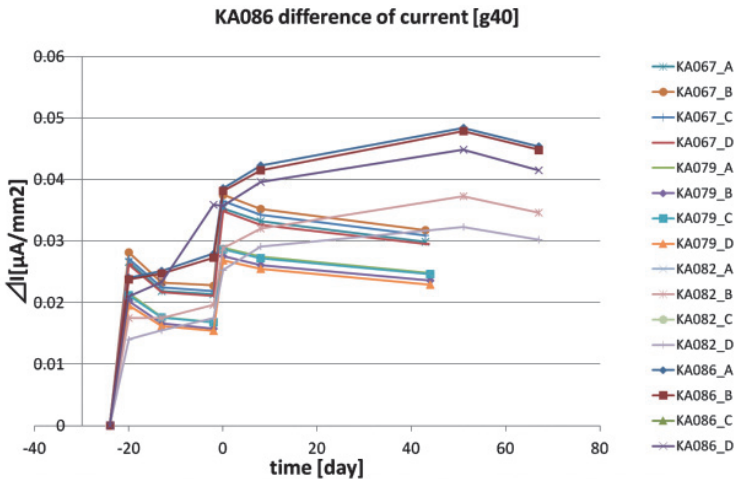

Figure 2. Leakage current VS time (-20 and 0 correspond to the first and second irradiation, respectively).

Feb. 16-19, 2013 andMarch 9-11, 2013. The total neutron flux (1 MeV equivalent neutrons per cm^2) is measured to be 2×10^{12} neutrons / cm^2 and 1×10^{12} neutrons / cm^2 for the HAPD at the extreme upstream and downstream position, respectively. These numbers correspond to the total neutron dose estimated for the 10 years operation at the Belle II experiment.

The performance of the HAPDs is checked seven times: before the neutron irradiation, right after the first irradiation period, one week after the first irradiation period, before the second irradiation, right after the second irradiation period, one week after the irradiation period, and one or two month after the second irradiation period. The performance check consists of the measurement of the leakage current, measurement of the noise, and measurement of the gain for a single or a few photons. Figure 2 shows a result of the leakage current measurement as a function of time. We found that the increase of the leakage current right after the irradiation was similar for all four types of HAPDs. We also found that the leakage current of 1×10^{12} neutrons / cm^2 gradually decreased after stopping the irradiation for two types of HAPDs and increases for the other two types of HAPDs. This result indicates that not only the bulk part but also the surface part of APD is affected by neutron irradiation, since differences among these HAPDs are only in the surface part of the APD.

From the noise and gain measurement, the signal-to-noise ratio (S/N) is measured to be S/N = 4.3 for the HAPD that is irradiated to 2.0×10^{12} neutrons / cm^2. This S/N is acceptable for K/π separation at the Belle II experiment. We conclude that the HAPD have sufficient neutron radiation hardness for the Belle II experiment.

H. Kakuno[1], I. Adachi[2], N. Hamada[3], S. Iwata[1], and S. Nishida[2]

[1]Grduate School of Science and Engineering, Tokyo Metropolitan University; [2]Instritute of Particle and Nuclear Studies, KEK; [3]Graduate School of Science, Toho University

Evaluation of Manufacturing Process with Energy Selective Neutron Radiography

1. Introduction

In manufacturing industries some products need to be manufactured to have special features of crystalline, such as strain, crystalline size or orientation, especially for products that need high quality assurance such as aero engine parts. In such products, the manufacturing process should be controlled and also evaluated strictly. Usually X-ray diffraction, microscopy or electron backscatter diffraction is used to evaluate the crystal features. However it takes too much time to conduct an evaluation in a macro scale because only features on the surface or in a micro scale are obtained.

In this study we applied energy selective neutron imaging and analysis with RITS code [1] in order to evaluate spatial distribution of crystalline structure in macro scale. We evaluated forged Ni-based alloy and found that we could distinguish a different process condition from the differences in crystalline features with neutron imaging and analysis with RITS code. The results indicated that this method has the possibility to be a powerful tool for evaluation of the production process.

2. Experimental Methods and Results

The experiments were executed at BL10, NOBORU. We used Li-glass scintillation detector [2] (Fig. 1), which has cross section of 48 × 48 mm, channel number of 256 and spatial resolution of 3 mm. The pulsed neutron beam was divided in time and measured for every 5us in each pixel, which enables spectroscopic imaging with neutrons.

Test pieces of Ni-based alloy, one of the typical materials used in aero engine parts, are shown in Fig. 2. Both of them were forged by 80% with different forging speed, and have diameter of 50 mm and thickness of 7 mm. Also, α-iron was measured to estimate the flight length of the neutron beam as a standard with a known lattice constant. The time for irradiation was about 13 hours for test pieces, and 10 hours for an open beam.

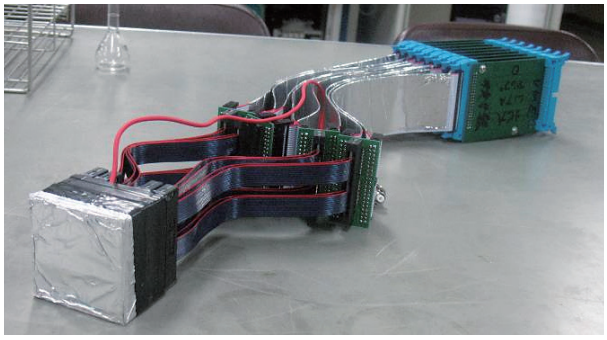

Figure 1. Picture of 256-channel Li-glass scintillation detector.

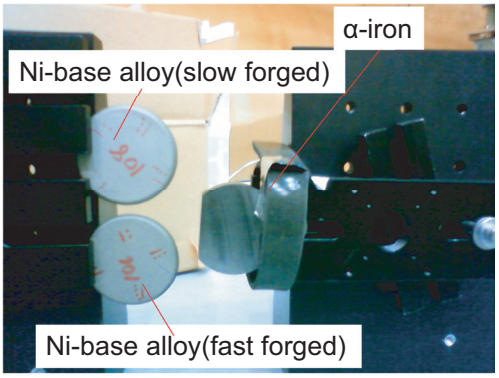

Figure 2. Picture of the test pieces.

Figure 3 shows the dependency of neutron transmittance on neutron wavelength in some pixels of the detector. Clear Bragg edges are shown and different edge shapes indicate different crystal structure. Then we applied RITS analysis to the spectra in every pixel, and evaluated the spatial distribution of crystal strain and anisotropy.

Figure 4 shows the spatial distributions of strain and crystal anisotropy. There is no clear difference in the strain distribution, which is considered, because both samples have the same forge rate. On the other hand, in the distribution of crystal anisotropy a slowly forged sample shows much more anisotropy. It is assumed that in a slowly forged sample the crystallite is more likely to be oriented to its preferable direction, which causes crystal anisotropy.

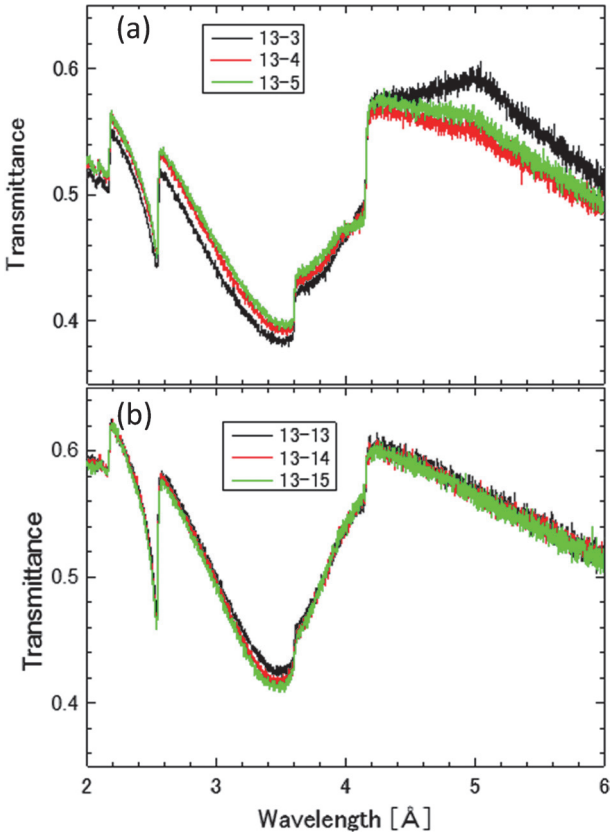

Figure 3. Neutron transmittance spectra of forged Ni-based alloy on neutron wavelength ((a):fast forged, (b):slowly forged).

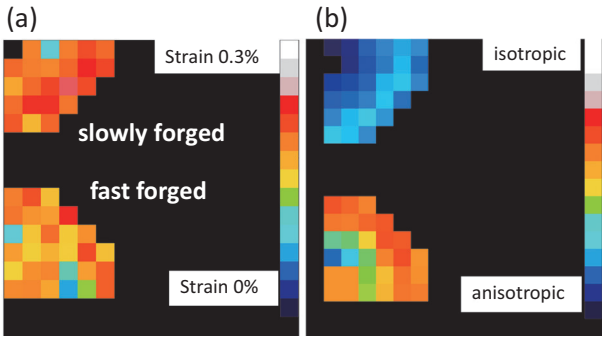

Figure 4. Spatial distribution of strains (a) and crystal anisotropy (b) in Ni-based alloy evaluated with RITS analysis.

In this study we discovered the potential of energy selective neutron radiography and RITS analysis for process assessment or non-destructive inspection of Ni-based alloy. In the future we would like to verify these results by comparing them to the outcome of other experiments, which involve a different method, detector or beam line.

References

[1] H. Sato, T. Kamiyama, K. Iwase and Y. Kiyanagi, Nucl. Instrum. Meth. **A651** (2011) 216.

[2] K. Iwase, K. Sakuma, T. Kamiyama and Y. Kiyanagi, Nucl. Instrum. Meth. **A605** (2009) 1.

H. Nose[1], T. Kamiyama[2], H. Sato[2], N. Kawaguchi[3], and Y. Kiyanagi[2]

[1]IHI Europe Ltd.; [2]Division of Quantum Science and Engineering, Hokkaido University; [3]Advanced Applied Science Department, IHI Corporation

Time-resolved Neutron Imaging with Resonance Absorption Reactions and Its Application in Computed Tomography

1. Introduction

Neutron resonance absorption techniques take advantage of the tendency of some nuclides to preferentially absorb neutrons at specific energies, unique to each nuclide, for the non-destructive study of isotopic density and temperature [1]. At a pulsed neutron source, resonance absorption can be directly observed in the sample transmission, determined from the ratio of neutron intensities with and without the sample measured as a function of time-of-flight (TOF). Employing a detector with good spatial and time resolutions allows the direct imaging of isotopic density and temperature over an entire sample in a single measurement and is suitable for computed tomography (CT).

To demonstrate such a resonance CT measurement, we have used our Micro PIxel Chamber (μPIC)-based neutron imaging detector [2,3], developed under the Quantum Beam Technology Program, MEXT (Fig. 1). The detector consists of a micro-pattern gaseous detector with 400 μm pitch coupled with an all-digital, FPGA-based data acquisition system. Featuring 3D tracking and energy measurement via time-over-threshold, it achieves 100 μm spatial resolution and ultra-low gamma sensitivity of $<10^{-12}$, along with 0.6 μs time resolution, 18% efficiency for thermal neutrons (using ^{3}He), and ~Mcps rate capability.

The experiment was performed at NOBORU (BL10) [4] in December 2012. The detector was positioned at 14.5 m from the moderator, and the sample, consisting of Cu, Mo, W, Ag, and In rods with diameters of 2 to 6 mm, was placed on a goniometer located at ~50 cm upstream of the detector (Fig. 2). A rotary collimator was set to 10 × 10 mm^2, and 50 mm Pb and 1 mm boron-silicate filters were used to reduce the intensity of the T0 gamma flash and the overlap neutrons, respectively. Measurements were taken at 16 angles (11~17 × 10^6 neutrons per angle), with an additional 'no-sample' run.

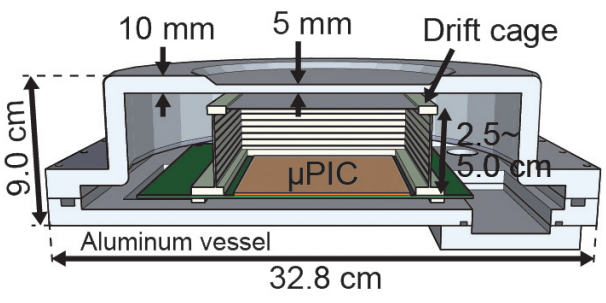

Figure 1. Schematic of the μPIC detector.

2. Preliminary Results

Figure 3 shows the neutron transmission of the sample with resonance peaks for each element indicated. Figure 4 shows the preliminary CT images

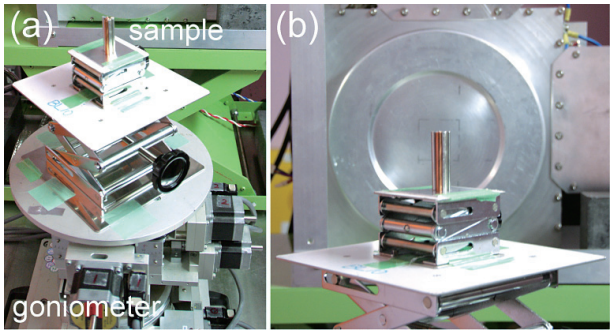

Figure 2. Experimental setup. (a) Sample on goniometer and (b) detector and sample from upstream beam position are shown.

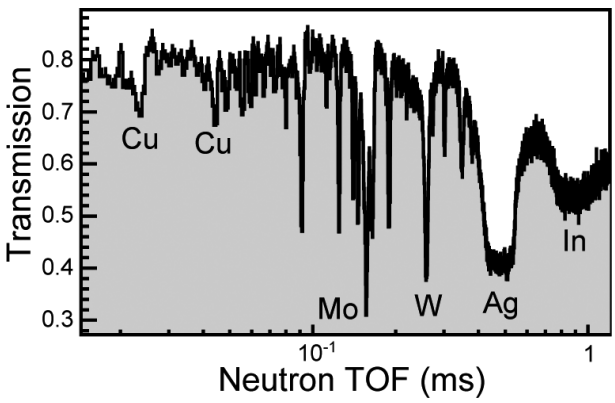

Figure 3. Neutron transmission versus TOF. Several peaks are labeled by element.

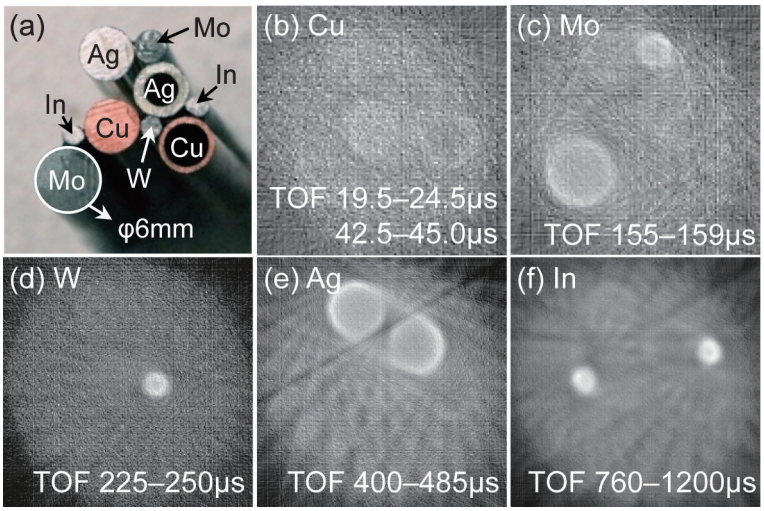

Figure 4. Resonance CT. (a) Photo of sample from above, and (b—f) computed tomography images of the specific elements indicated in each figure.

reconstructed using a simple filtered back-projection method. The indicated neutron TOF cuts, chosen to select resonances at 2039 and 579 eV (Cu), 45 eV (Mo), 19 eV (W), 5.2 eV (Ag), and 1.5 eV (In), clearly enhance the individual elements in each image. A more accurate analysis method using fits to the known cross-sections is under development.

References

[1] H. Sato, T. Kamiyama and Y. Kiyanagi, Nucl. Instr. and Meth. A **605** (2009) 36.

[2] J.D. Parker *et al.*, Nucl. Instr. and Meth. A **697** (2013) 23.

[3] J.D. Parker *et al.*, Nucl. Instr. and Meth. A **726** (2013) 155.

[4] F. Maekawa *et al.*, Nucl. Instr. and Meth. A **600** (2009) 335.

J. D. Parker[1], M. Harada[2], K. Hattori[1], S. Iwaki[1], S. Kabuki[1], Y. Kishimoto[1], H. Kubo[1], S. Kurosawa[1], Y. Matsuoka[1], K. Miuchi[3], T. Mizumoto[1], H. Nishimura[1], T. Oku[4], T. Sawano[1], T. Shinohara[4], J. Suzuki[5], A. Takada[1], T. Tanimori[1], and K. Ueno[1]

[1]Department of Physics, Kyoto University; [2]Neutron Source Section, Materials and Life Science Division, J-PARC Center; [3]Department of Physics, Kobe University; [4]Neutron Science Section, Materials and Life Science Division, J-PARC Center; [5]Neutron R&D Division, CROSS-Tokai

Two-Dimensional Focusing of Pulsed Neutron Beam with Elliptic Supermirrors

1. Introduction

At spallation neutron sources, a focusing device is required to accept and reflect wideband beam with large divergence into small area with high efficiency and high signal-to-noise ratio. In order to meet these demands, we developed focusing supermirrors with a large critical angle, high reflectivity, and low diffuse scattering[1], by using ion-beam sputtering (IBS) technique, and with precise surface figure of the focusing mirror by using the numerically controlled local wet etching (NC-LWE) process [2][3].

In this report, we have developed a two dimensional focusing device which is called Kirkpatrick-Baez mirror based on these cutting–edge technologies in order to enhance the q-resolution of neutron experiments such as small angle neutron scattering (SANS), and space resolution such as prompt gamma activation analysis (PGAA) and so on.

Even though this system was established in the field of x-ray focusing experiments, it is very difficult to apply it to neutron experiments because the neutron intensity is several orders weaker than the advanced synchrotron X-ray sources; to solve the problem, large scale focusing mirrors with sub-micrometer figure shape and high performance supermirror are required to focus on a small target.

We have been developing ultra-precise focusing mirrors combining a high-performance neutron supermirror and very precise surface figuring technique.

2. Mirror Fabrication

The elliptical KB mirror system is an aberration free system, which consists of two total reflection elliptical mirrors. One is used for vertical focusing and the other for horizontal focusing at separate positions.

Mirror substrates were prepared by figuring a surface of synthesized quartz glass into a planoelliptical shape using the NC-LWE process. The peak-to-valley flatness was 1.33 μm over 400 $\times$ 50 mm. The surface roughness was 0.202 nm rms.

NiC/Ti supermirrors were deposited using the IBS method on the elliptic quartz surface. The neutron reflectivity was measured using the CHOP beam port of JRR-3. The reflectivity of m = 4 supermirror reseaches $\simeq$ 0.6 at the critical wavelength is also a typical value.

3. Experimental setup and result

The focusing performance of the fabricated KB supermirror system was evaluated at BL10 NOBORU. Figure 1 shows a photograph of perfor-

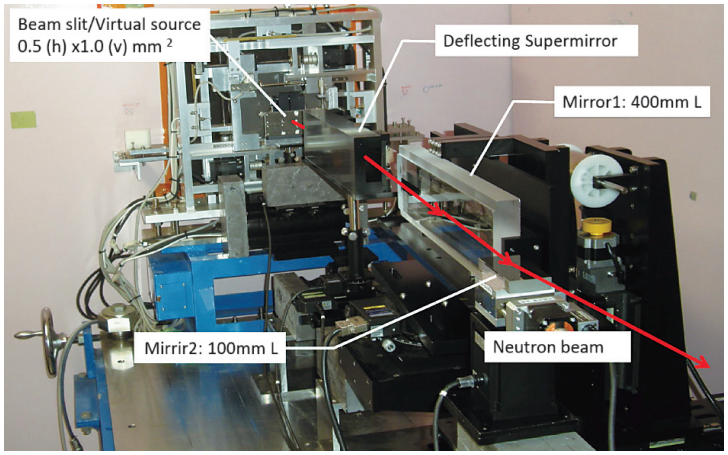

Figure 1. A photograph of performance test of the KB system.

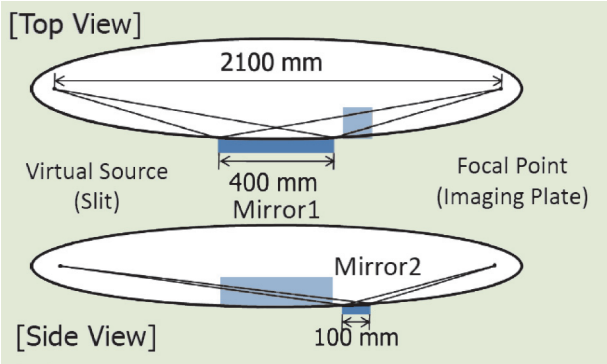

Figure 2. A KB system configuration.

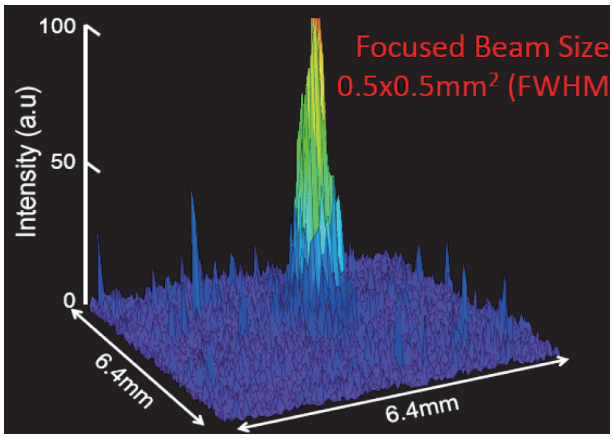

Figure 3. 2-d profile of focused beam.

mance test of the KB system at BL10 NOBORU. NOBORU provides a neutron beam of ≥ 3 Å. Figure 2 shows a conceptual diagram of the KB system. The focal length of the ellipsoid is 2100 mm. The horizontal focusing mirror with m = 4 has a length of 400 mm. The vertical focusing mirror with m = 3 has a length of 100 mm. The two mirrors are set at separate positions. Reduction ratios of this system are x1 for horizontal axis and x0.4 for vertical axis.

The virtual source was set using the pinhole slit with 0.5 mm (H) and 1 mm (V) at the focal point position. Focused beam shape was observed with an imaging plate placed at 2100 mm after the virtual focusing point. Figure 3 shows a result of the focusing test of the KB system. The focused beam area is 0.5 mm × 0.5 mm in full width at half maximum, almost reproducing the beam size determined by the KB system.

References

[1] R. Maruyama, D. Yamazaki, T. Ebisawa, K. Soyama, J. Appl. Phys. **105** (2009) 083527.
[2] K. Yamamura, Ann. the CIRP **56/1** (2007) 541-4.
[3] D. Yamazaki, *et al.*, J. Phys.: Conf. Ser. **251** (2010) 012076.

D. Yamazaki[1], R. Maruyama[1], H. Hayashida[1], K. Soyama[1], M. Nagano[2], F. Yamaga[2], and K. Yamamura[2]
[1]*Neutron Instrumentation Section, Materials and Life Science Division, J-PARC Center;* [2]*Graduate School of Engineering, Osaka University*

Confirmation of Spin Gap Excitations in the Spin-3/2 Substances $RCrGeO_5$ (R = Y or ^{114}Sm)

1. Introduction

One important phenomenon in quantum spin systems is the appearance of a spin-singlet ground state with spin gap (singlet-triplet excitation). To understand this phenomenon properly, experimental as well as theoretical investigations are necessary. We know model substances when S = 1/2, 1 or 2. Although a spin-singlet ground state with a spin gap is possible in spin-3/2 systems such as antiferromagnetic (AF) alternating chains [1], there is no model substance with S = 3/2.

Spin-3/2 AF alternating chains of Cr^{3+} can be expected in $RCrGeO_5$ (R = Y or rare earth) [2]. We would like to prove that these substances have a spin-singlet ground state with spin gap. However, we cannot prove it in magnetization results because of the rare earth or other magnetic phase included in samples. Consequently, we performed inelastic neutron scattering (INS) measurements on $RCrGeO_5$ (R = Y or ^{154}Sm) powders to confirm the spin gap excitations. We used the High Resolution Chopper (HRC) spectrometer at BL 12 in J-PARC.

2. Results and Discussion

Excitations are apparent at 4.0 K in small Q regions in $YCrGeO_5$ as shown in Fig. 1(a). The intensity decreases with increasing T. Most of the excitations are magnetic and indicate spin gap excitations. We obtained the intensity map in the q_{1D}-ω plane [Fig. 1(b)] from the data at 4.0 K using the conversion method [3]. $Q_{1D}$is the scattering vector parallel to the spin chain and $q_{1D} = Q_{1D}\frac{d}{2\pi}$ where d is the average distance of nearest-neighbor Cr-Cr (d = 2.84 Å). The intensity is the strongest at around q_{1D} = 0.5 as expected in the AF spin chains. The white line shows $\omega = \sqrt{v^2 \sin^2(2\pi q_{1D}) + \Delta^2}$ where v = 20 meV and Δ = 10 meV (spin gap value). As shown in Fig. 1(c), the width of $I(\omega)$ at q_{1D} = 0.5 is broader than the resolution.

We also observed spin gap excitations in $^{154}SmCrGeO_5$. We obtained the intensity map

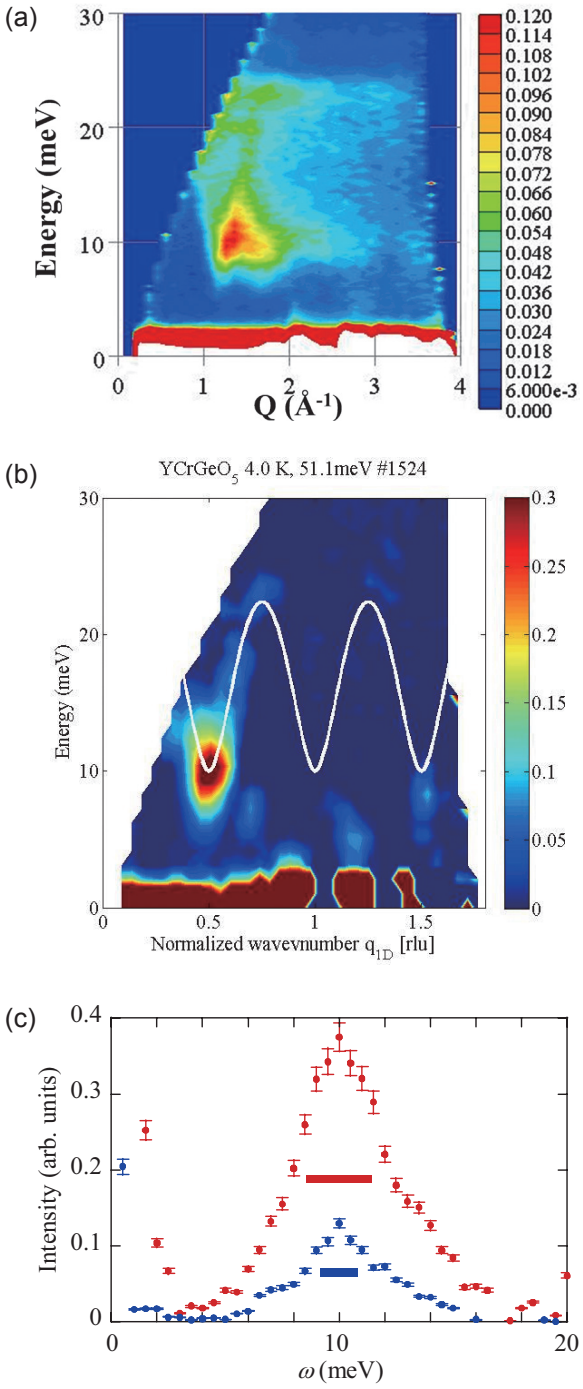

Figure 1. (a) The intensity map in the Q-ω plane in $YCrGeO_5$ at 4.0 K. The incident neutron energy is 51.1 meV. (b) The intensity map in the q_{1D}-ω plane obtained using the conversion method. (c) $I(\omega)$ at q_{1D} = 0.5 obtained using E_i = 51.1 meV (red) and 46.1 meV (blue). The horizontal bars indicate the energy resolution at ω = 0.

in the q_{1D}-ω plane from the data at 7.8 K. The intensity is the strongest around q_{1D} = 0.5 as expected in AF spin chains. The white line shows $\omega = \sqrt{v^2 \sin^2(2\pi q_{1D}) + \Delta^2}$ where v = 15 meV and Δ = 18 meV (spin gap value). $I(\omega)$ at q_{1D} = 0.5 seems resolution limited (not shown).

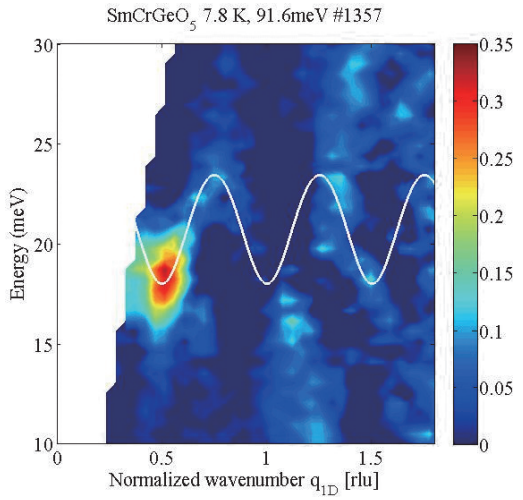

Figure 2. The intensity map in the q_{1D}-ω plane in $^{154}SmCrGeO_5$ at 7.8 K (d = 2.86 Å). The incident neutron energy is 91.6 meV.

The dispersion relation of the lowest magnetic excitations of $YCrGeO_5$ ($SmCrGeO_5$) is similar to the theoretical dispersion relation δ = 0.75 (0.85) (not shown). We estimated J = 9 meV (10 meV) for $YCrGeO_5$ $(SmCrGeO_5)_2$ where the two exchange interaction parameters are defined as $J_{1,2} = J(1\pm\delta)$. To our knowledge, RCrGeO$_5$ is the first spin-3/2 substance showing a spin-singlet ground state with a spin gap.

References

[1] M. Yajima and M. Takahashi, J. Phys. Soc. Jpn. **65** (1996) 39.

[2] R. V. Shpanchenko *et al.*, J. Solid State Chem. **181** (2008) 2433.

[3] K. Tomiyasu *et al.*, Appl. Phys. Lett. **94** (2009) 092502.

M. Hase[1], M. Soda[2], T. Masuda[2], D. Kawana[2,4], T. Yokoo[3,4], S. Itoh[3,4], and M. Kohno[1]

[1]National Institute for Materials Science (NIMS); [2]The Institute for Solid State Physics (ISSP), The Univ. Tokyo; [3]Neutron Science Section, Materials and Life Science Division, J-PARC Center; [4]Institute of Materials Structure Science, KEK

Neutron Brillouin Scattering Experiments on HRC

On the High Resolution Chopper Spectrometer (HRC at BL12), the neutron Brillouin scattering (NBS) experiments became feasible by reducing the background noise at low angles down to ϕ = 0.5° [1]. NBS is the most promising way to observe excitations in the forward direction from powders, polycrystals, or liquids. Owing to the kinematical constraints of neutron spectroscopy, incident neutron energy (E_i) in sub-eV region with high resolution ($\Delta E/E_i$) at low scattering angles (ϕ) is necessary to measure scattering in the meV transferred energy (E) range near (000).

First, an NBS experiment was performed to observe spin waves in a polycrystalline sample of a nearly-cubic perovskite, $La_{0.8}Sr_{0.2}MnO_3$, (Curie temperature: T_C = 316 K), whose magnetic properties are well elucidated [2,3]. Figure 1 shows the dispersion relation of spin waves in $La_{0.8}Sr_{0.2}MnO_3$ measured with E_i = 102 meV and ΔE = 2 meV. The observed dispersion relations at 6 and 245 K were well fitted to $E = DQ^2$, where Q is the scattering vector. The D values obtained were 130 ± 13 and 88 ± 2 meVÅ^2 at 6 and 245 K, respectively. These values are in good agreement with the results (D = 131 and 89 meVÅ^2 at 14 and 250 K, respectively) obtained by the previous experiments using a single crystal [2,3]. Therefore, the feasibility of NBS experiments on the HRC was demonstrated [1].

Next, spin waves in a polycrystalline ferromagnet, $SrRuO_3$ (T_C = 165 K), were similarly measured. This material also has a nearly-cubic perovskite structure showing an anomalous Hall effect [4], but a large single crystal suitable for inelastic neutron scattering experiments has not yet been synthesized. The measurement was performed at 7 K with E_i = 102 meV, and well-defined spin wave peaks were observed. As shown in Fig. 1, the dispersion relation of spin waves in $SrRuO_3$ was well fitted to $E = E_0 + DQ^2$ with an apparent energy gap E_0 [1].

$Nd_2Fe_{14}B$ is a well-known stong permanent magnet with T_C = 580 K. At room temperature, all spins are aligned along the c*-axis. We measured the spin waves in a $Nd_2Fe_{14}{}^{11}B$ polycrystalline sample at 300 K with E_i = 257 meV and ΔE = 5.7 meV. The spin wave peak positions were determined in Fig. 2. The observed peak positions were on the dispersion curve along the c*-axis reported in the previous experiment [5].

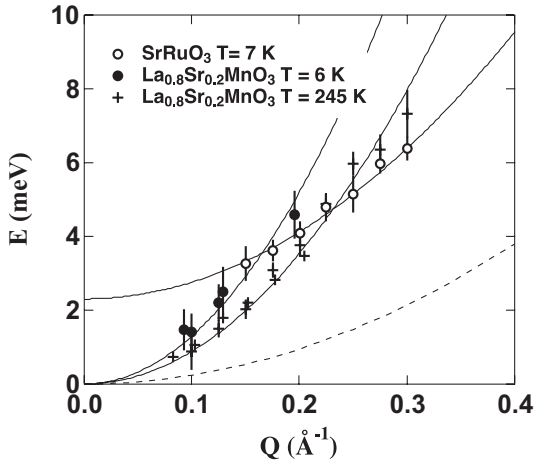

Figure 1. Spin-wave dispersion curves for $La_{0.8}Sr_{0.2}MnO_3$ and $SrRuO_3$ determined on the HRC. The solid lines are fitted curves. The dashed line is the upper boundary accessible with a conventional spectrometer.

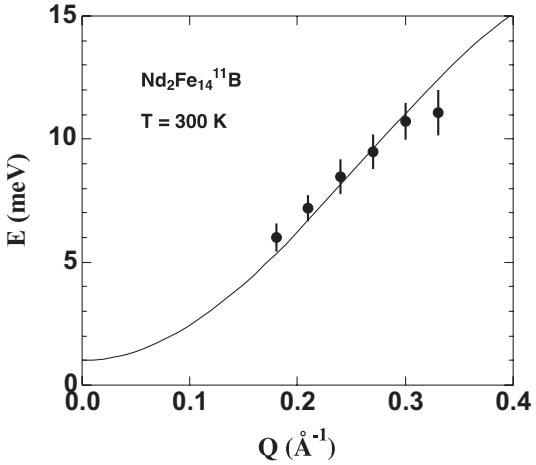

Figure 2. Spin wave dispersion relation of $Nd_2Fe_{14}{}^{11}B$. The solid line is the dispersion curve along the c-axis determined using a single crystal sample [5].

Phononic excitations in a liquid D_2O were measured at 300 K with E_i = 102 meV and ΔE = 2.0 meV. The observed spectra were well fitted with a damped harmonic oscillator scattering function and the peak positions were determined, as shown in Fig. 3. The observed peak positions down to Q = 0.02 Å^{-1} were well fitted to $E = cQ$ with $c = 21.4 \pm 0.2$ meVÅ, which is equivalent to $c = 3250 \pm 30$ m/s. The observed sound velocity c was in good agreement with that for the fast sound observed in the previous experiment with $E_i = 80$ meV and $\Delta E = 4.8$ meV down to $Q = 0.035$ Å^{-1} [6].

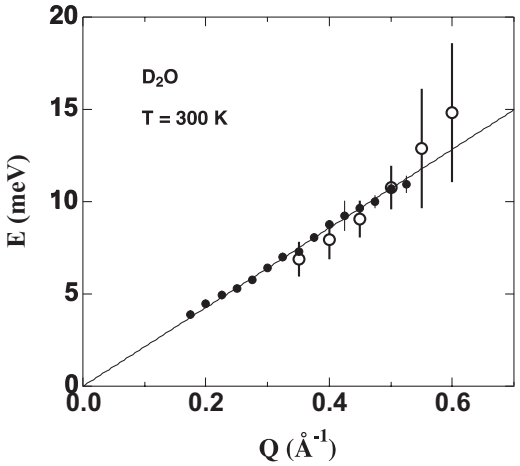

Figure 3. Dispersion relation for phononic excitations, the fast sound, in D_2O (closed circles). The open circles are previous results [6]. The solid line is a fitted line.

References

[1] S. Itoh *et al.*, J. Phys. Soc. Jpn. **82** (2013) 043001.

[2] Y. Endoh and K. Hirota, J. Phys. Soc. Jpn. **66** (1997) 2264.

[3] F. Moussa *et al.*, Phys. Rev. B **76** (2007) 064403.

[4] Z. Fang *et al.*, Science **302** (2003) 92.

[5] H. M. Mayer *et al.*, J. Magn. Magn. Matter. **97** (1991) 210.

[6] J. Teixeira *et al.*, Phys. Rev. Lett. **54** (1985) 2681.

S. Itoh[1,2], T. Yokoo[1,2], D. Kawana[3], Y. Kaneko[4], Y. Tokura[4,5], M. Fujita[6], K. Yoshida[7], K. Saito[2], N. Inami[2], Y. Takeichi[2], K. Ono[2], and Y. Endoh[2,4,6]

[1]*Neutron Science Section, Materials and Life Science Division, J-PARC Center;* [2]*Institute of Materials Structure Science, KEK;* [3]*The Institute for Solid State Physics, The University of Tokyo;* [4]*RIKEN Center for Emergent Matter of Science;* [5]*Department of Applied Physics, The University of Tokyo;* [6]*Institute for Materials Research, Tohoku University;* [7]*Department of Chemistry, Fukuoka University*

Reentrant-Type Metal–Nonmetal Transition in $Pr_{1-x}Ce_xRu_4P_{12}$

1. Introduction

Rare-earth filled skutterudite compounds, which crystallize in *bcc* symmetry, exhibit various properties associated with hybridization between *f* and conduction electrons [1]. The metal–nonmetal transition at $T_{M\text{-}I}$ = 63 K of $PrRu_4P_{12}$ was extensively studied [2]. The nonmetallic phase below $T_{M\text{-}I}$ is characterized by the structural transition to *sc* symmetry with the wave vector $\mathbf{q}_0$ = (1, 0, 0) [3]. Neutron scattering studies revealed the $\mathbf{q}_0$ alignment of two inequivalent crystal-field (CF) level schemes of the Pr-ion $4f^2$ state: a singlet at Pr1 and a triplet at Pr2 at the lowest temperature [4, 5]. This phase transition was interpreted as CDW accompanied by the antiferro-type ordering of an *f*-electron totally symmetric multipole [6, 7]. It is notable that a reentrant-type phase transition is induced by substituting Rh to Ru or Ce to Pr [8, 9]. The electrical resistivity increases once at $T_{M\text{-}I}$ ~ 45 K, and decreases below approximately 10 K. The structural superlattice and the antiferro-type alignment of the CF schemes are expected to disappear.

In order to identify the electronic state, we measured the evolution of the CF scheme and the superlattice on the reentrant-type metal–nonmetal transition of $Pr_{1-x}Ce_xRu_4P_{12}$, based on multi-probe use of neutron and synchrotron X-ray.

2. Experimental Procedure

Samples were synthesized by the Sn-flux method. We measured the CF level schemes by using a high-resolution chopper neutron spectrometer HRC at BL12 in MLF J-PARC. High-resolution X-ray diffraction was performed on a four-circle diffractometer at BL-3A in the Photon Factory of KEK, Tsukuba.

3. Results

Figure 1 shows inelastic neutron scattering (INS) spectra at 44 K for x = 0.05 and at 10 K for x = 0.15. The x = 0.05 system does not undergo the reentrant transition, and exhibits the similar CF schemes as $PrRu_4P_{12}$ at 44 K shown at the top of Fig. 1. It is notable that the spectra at 10 K for x = 0.15 is similar to those at 44 K for the less-Ce concentration. Thus, the ground state for Pr2 site is quasi four-fold degeneracy of the singlet (Γ_1) and the triplet ($\Gamma_4^{(2)}$).

Figure 2 shows the X-ray superlattice diffraction profile at **Q** = (1, 1, 1) for x = 0.15 at 9.1 K (red circles). This is considerably broader than the resolution (broken black line). The superlattice structure in the Ce-substituted system is characterized by short correlation length.

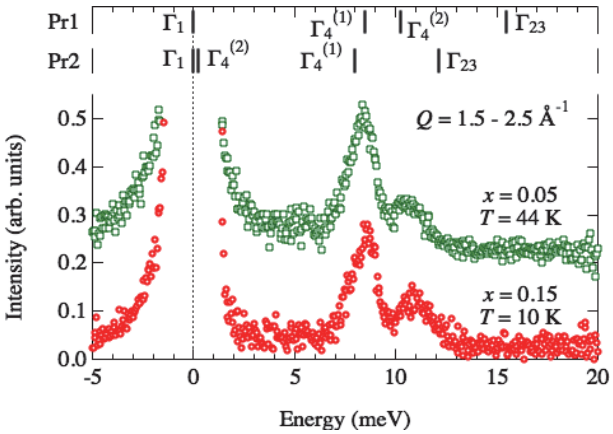

Figure 1. INS spectra for x = 0.05 at 44 K and x = 0.15 for 10 K, together with the CF scheme in the pure material (top).

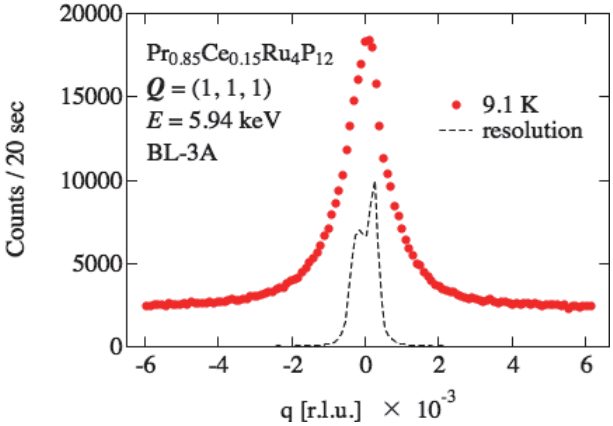

Figure 2. X-ray superlattice reflection for x = 0.15 at 9.1 K (red circles). Broken line shows resolution. Abscissa is the reduced wave vector along the [1 -1 0] direction.

4. Discussion

The degeneracy of the CF ground state in the Ce-substituted system is enhanced with a decrease in temperature, and gives rise to the strong fluctuation of 4*f* electrons in the antiferro-type ordered phase. The fluctuation produces a short-range superlattice structure, which indicates that the nonmetallic ordered phase becomes unstable with decreasing temperature. The reentrant-type behavior may also be associated with carrier doping to the CDW state due to the atomic substitution.

References

[1] H. Sato, H. Sugawara, Y. Aoki, and H. Harima, *Handbook of Magnetic Materials*, ed. K. H. J. Buschow (North-Holland, Amsterdam, 2009) Vol. 18, p. 1.

[2] C. Sekine, T. Uchiumi, I. Shirotani, and T. Yagi, Phys. Rev. Lett. **79** (1997) 3218.

[3] C. H. Lee, H. Matsuhata, H. Yamaguchi, C. Sekine, K. Kihou, T. Suzuki, T. Noro, and I. Shirotani, Phys. Rev. B **70** (2004) 153105.

[4] K. Iwasa, L. Hao, K. Kuwahara, M. Kohgi, S. R. Saha, H. Sugawara, Y. Aoki, H. Sato, T. Tayama, and T. Sakakibara, Phys. Rev. B **72** (2005) 024414.

[5] K. Iwasa, L. Hao, T. Hasegawa, T. Takagi, K. Horiuchi, Y. Mori, Y. Murakami, K. Kuwahara, M. Kohgi, H. Sugawara, S. R. Saha, Y. Aoki, and H. Sato, J. Phys. Soc. Jpn. **74** (2005) 1930.

[6] Y. Kuramoto, J. Otsuki, A. Kiss, and H. Kusunose, Proc. Theo. Phys. Suppl. **160** (2005) 134.

[7] T. Takimoto, J. Phys. Soc. Jpn. **75** (2006) 034714.

[8] C. Sekine, N. Hoshi, I. Shirotani, K. Matsuhira, M. Wakeshima, and Y. Hinatsu, Physica B **378–380** (2006) 211.

[9] C. Sekine, M. Takusari, and T. Yagi, J. Phys. Soc. Jpn. **80** (2011) SA024.

K. Iwasa[1], T. Sato[1], K. Saito[1], H. Nakao[2], Y. Murakami[2], S. Itoh[2,3], T. Yokoo[2,3], and D. Kawana[2]

[1]Department of Physics, Tohoku University; [2]Institute of Materials Structure Science, KEK; [3]Neutron Science Section, Materials and Life Science Division, J-PARC Center

Spin Waves in the Ferromagnetic Phase of MnP

An intermetallic compound, MnP, is ferromagnetic below 292.6 K, and transforms into a proper screw spiral phase at 46.2 K. In the ferromagnetic phase, the easy axis of the magnetization is the c^* axis and the hardest one is the a^* axis. In the proper screw spiral phase, the spin rotates in the b^*-c^* plane with a propagation vector of $0.117a^*$. Early inelastic neutron scattering studies suggested that the proper screw spiral phase is caused by a delicate balance between exchange interactions [1], and also reported that the spin wave dispersion relation in the ferromagnetic phase exhibits an unusual q^3 law along the a^* axis, while the conventional q^2 law was observed along the b^* and c^* axes [2].

It is essential to determine the spin dynamics in the entire Brillouin zone, in order to elucidate the microscopic origin of magnetism of MnP. As a first step in this study, we determined the spin wave dispersion relations in the ferromagnetic phase, by using HRC at J-PARC as well as LTAS, TOPAN, TAS-1 at JRR-3M [3]. Figure 1 shows the observed peak positions of spin waves at 60 K.

The Mn lattice in MnP deviates from a primitive orthorhombic lattice with displacement parameters u and v along the a and b axes, respectively, and therefore the unit cell includes four Mn sites. Since v is negligibly small, the Mn lattice can be approximately divided into two sub-lattices. We consider an isotropic Heisenberg interaction adding a single ion anisotropy for two sub-lattices. We took into account the exchange interactions between Mn pairs up to the 6th neighbors [3,4]. The observed peak positions of spin waves were well described by this model, as shown in Fig.1.

By using the HRC, spin waves were observed in a wide energy momentum space near the zone boundary. In the calculation, the acoustic and optical modes are separated from each other along the a^* axis. Along the b^* axis, these two modes resonate with each other at around $k = 0.2$ rlu (reciprocal lattice unit) and switch roles, but the two modes are not crossed. Observed spin wave peak positions are well explained by the two modes. In fact, two spin wave peaks were clearly observed at $h = 0.5$ rlu on the TAS-1. As shown in Fig. 1 (c), the low energy part in the a^* axis for the presently-improved dispersion relation obtained by the LTAS was also well fitted to the present model, where the calcu-

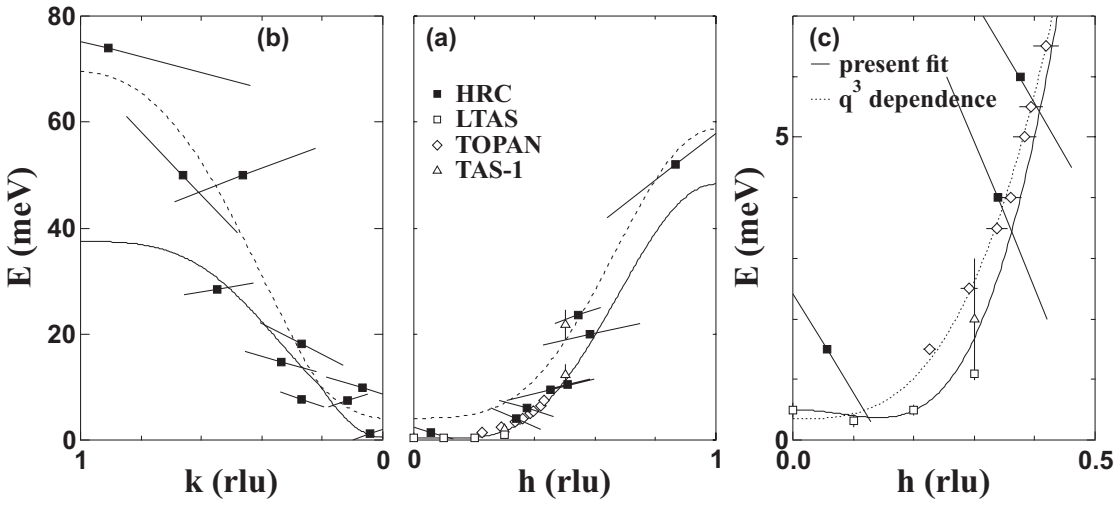

Figure 1. Dispersion relation of spin waves in the ferromagnetic phase of MnP along the a^* (a) and b^* axes (b), with calculated curves, acoustic (solid line) and optical (dashed line) modes. The bars on the marks represent statistical errors along the scan directions. Low energy part along the a^* axis (c), where the dotted line is a result of the previous study [2].

lated dispersion curve along the a^* axis shows a minimum at around $h = 0.14$ rlu. This complicated q dependence is caused by the displacement parameter u, in fact, the minimum disappeared for $u = 0$. The peak positions observed on the TOPAN, in which condition was almost identical to that for the previous study [2], showed the q^3 dependence. The q^3 dependence might be a resolution effect.

In summary, we successfully observed spin waves in the ferromagnetic phase of MnP along the a^* and b^* axes in the entire Brillouin zone. The dispersion relations were well described by a simple model which consists of an isotropic Heisenberg interaction adding a single ion anisotropy with two sub-lattices. The low energy part for the a* axis was improved by high resolution experiments, and the anomalous dispersion relation was found to be caused by an atomic displacement from the primitive lattice. The recent structural study suggested the existence of the Dzyaloshinsky-Moria interaction [5]. Further investigations with inelastic neutron scattering experiments are required to solve such a problem.

References

[1] K. Tajima, Y. Ishikawa, and H. Obara, J. Magn. Magn. Mater. **15-18** (1980) 373.

[2] Y. Todate, K. Yamada, Y. Endoh, and Y. Ishikawa, J. Phys. Soc. Jpn. **56** (1987) 36.

[3] S. Yano, S. Itoh, T. Yokoo, S. Satoh, D. Kawana, Y. Kousaka, J. Akimitsu, Y. Endoh, J. Magn. Magn. Matter. **347** (2013) 33.

[4] S. Takeuchi and K. Motizuki, J. Phys. Soc. Jpn. **24** (1967) 742.

[5] T. Yamazaki, Y. Tabata, T. Waki, T. J. Sato, M. Matsuura, K. Ohoyama, M. Yokoyama, and H. Nakamura, arXiv:1106.4599v2 (2011).

S. Yano[1], S. Itoh[2,3], T. Yokoo[2,3], S. Satoh[3], D. Kawana[3], Y. Kousaka[1], J. Akimitsu[1], and Y. Endoh[3,4]

[1]Department of Physics and Mathematics, Aoyama Gakuin University; [2]Neutron Science Section, Materials and Life Science Division, J-PARC Center; [3]Institute of Materials Structure Science, KEK; [4]Institute for Materials Research, Tohoku University

Dynamical Properties of Low-Dimensional Quantum Spin Systems

1. Introduction

Quantum spin systems exhibit many interesting phenomena due to the quantum fluctuations of spins. In particular, the interplay between the physical degrees of freedom in strongly correlated electron systems, particularly in quantum systems such as high-T_c superconductivity has attracted the condensed matter physics.

2. TiOBr

In a recent discovery of a new type of spin-Peierls system TiO*X* (*X*: Cl, Br), the cooperation between lattice, spin and orbital plays a significant role to realize the one-dimensional (1D) quantum spin correlations [1]. It has been revealed in TiO*X*, showing exotic structural and magnetic properties such as successive phase transitions, 1D nature associated with orbital ordering of Ti atoms and super-lattice reflections being related to the Peierls instability [2]. In the 2D layered material, it is pointed out that as a result only from an arrangement of Ti d_{xy} orbital, 1D spin chains and the spin-Peierls transition will be formed. The orbital of d_{xy} possibly orders along *b* direction through Ti-Ti direct coupling. It has been demonstrated that TiOBr also exhibits two successive phase transitions similar to TiOCl at $T_{c1} = 27$ K and $T_{c2} = 47$ K [3]. An ESR study has shown a possibility of the formation of 1D chains along the *b*-axis, and a strong one-dimensionality with $J = 660$ K by direct-exchange and super-exchange interactions between Ti atoms due to an ordering of d_{xy} orbital [2]. However, the direct evidence of spin-Peierls transition, namely, the observation of the spin gap excitations has not been reported yet.

In the previous report [4], the spin gap energy was expected to be in the energy range of 10-40 meV. Since in this range energy is very contaminated by phonons, the data interpretation requires much more attention. Our typical inelastic result is shown in Fig. 1. Almost no signals are observed except for Al phonons and background. We also surveyed low energy range for low-lying branches with much better energy resolution. At the magnetic zone center $Q = 0.9$ Å, no magnetic signals were found. It is currentely unclear where the spin signals are.

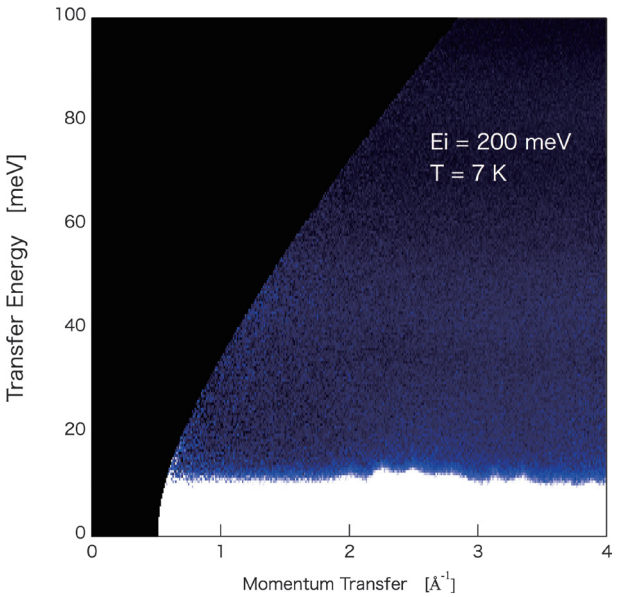

Figure 1. Powder avaraged $S(Q,\omega)$.

3. Nd_2BaNiO_5

Despite the three decades that have passed since Haldane's prediction on a 1D Heisenberg chain with integer spin, much attention is still paid on its research [5]. The spin gap has originated from an energy separation between the singlet ground state and the triplet first excited state. Inorganic nickelate Y_2BaNiO_5 was found to be a good candidate for a Haldane system with a spin gap of 10 meV [6]. In contrast, R_2BaNiO_5 (R: magnetic rare earths) has been known as a classical antiferromagnet (AF) showing 3D long range magnetic ordering at low temperature [7]. However, the inelastic neutron scattering experiments revealed the existence of spin gap [8].

Another item of interest in the transition metal chain oxides is the doping of carriers, which yields

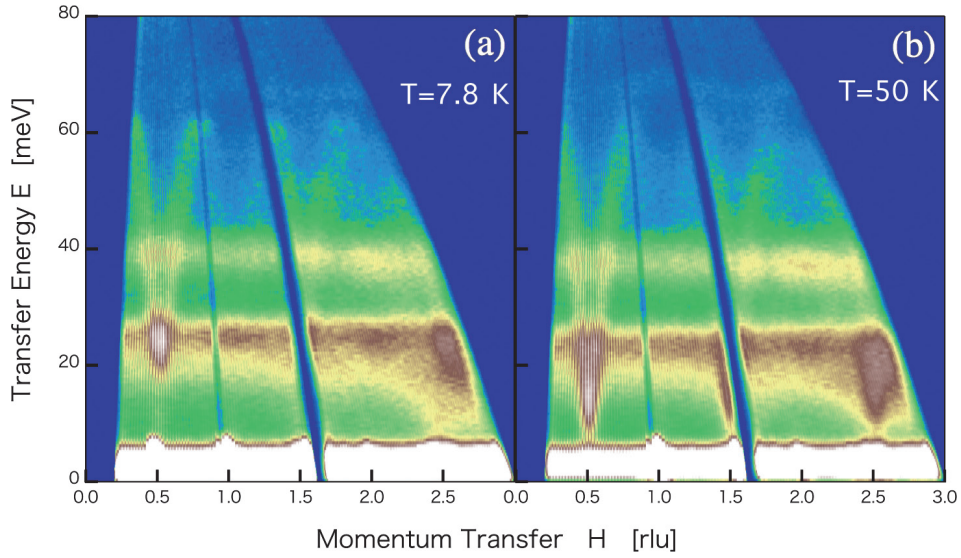

Figure 2. Observed dynamical structures in $(Nd,Ca)_2BaNiO_5$. Both below Neel temperature (a) and above Neel temperature (b).

phenomena ranging from strongly renormalized Fermi liquid behavior to high-temperature superconductivity. In view of the enhanced quantum fluctuations in 1D systems, doping of transition metal chains could well lead to equally surprising discoveries. R_2BaNiO_5 is a charge transfer insulator and some amount of hole carriers are successfully introduced primarily on oxygen sites by replacing a part of the off-chain Y^{3+} by Ca^{2+} [9]. Figure 2 shows the obtained dynamical structures $S(Q,\omega)$ at $T = 7.8$ K (well below $T_N = 38$ K) and $T = 50$ K (above T_N) are shown. Intense crystal field excitations of Nd^{3+} ions lie at $E = 24$ meV and 38 meV. The site symmetry of Nd^{3+} in Nd_2BaNiO_5 is sufficiently low to split the tenfold degenerate $J = 9/2$ multiplet into five Kramers doublets. Excellent dispersion relations for the Ni 1D chain are observed at both temperatures. The minima of the dispersion observed at the magnetic zone center (MZC), $H = 0.5$, 1.5 and even 2.5, occur where magnetic scattering intensity gets weak because of the magnetic form factor and phonon scattering is dominant in this high-Q region. At low temperature, the magnon band width reaches 60 meV with a somewhat large gap energy of $\Delta = 20$ meV. Also, a flat band lying at E = 65 meV corresponding to a phonon or magnon optical branch was observed. At $T = 50$ K, the gap is closed and the spectral weight at the zone boundary is slightly shifted with respect to the MZC. The boundary energy is almost similar under both temperatures. The low incident energy experiments revealed that a weak excitation at the MZC ($H = 0.5$) has appeared as a result of a hole doping (not shown here). The marked changes are taking place at $T = 5$ K. The 1D chain dispersion with the Haldane gap almost completely disappears around the MZC. Still, weak signals remain at around 10 meV and below 10 meV. Also, a flat localized excitation newly appears at 4 meV. In this mixed-spin system, the Haldane gap is known to rapidly increase in energy under the effective staggered magnetic field. The 3D magnetic correlation of Ni^{2+} ions via rare earth (Nd^{3+}) ions is well developed at a low temperature. Therefore, the gap is effectively diminishing. Completely flat dispersion is found in this experiment. This appears only below the 3D magnetic ordering temperature, and developed as a magnetization order parameter possibly related to the Nd spins.

References

[1] R. J. Beynon and J. A. Wilson, J. Phys. Condens Matt. **5** (1993) 1983.; A. Seidel, C. A. Marianetti, F. C. Chou, G. Ceder and P. A. Lee, Phys. Rev. B **67** (2003) 020405(R).; V. Kataev, J. Baier, A. Moller, L. Jongen, G. Meyer and A. Freimuth, Phys. Rev. B **68** (2003) 140405(R).

[2] M. Shaz, S. van Smaalen, L. Palatinus, M. Hoinkis, M. Klemm, S. Horn and R. Claessen, Phys. Rev. B **71** (2005) 100405(R).; C. Kato, Y. Kobayashi and M. Sato, J. Phys. Soc. Jpn.

74 (2005) 473.; S. van Smaalen, L. Palatinus and A. Schonleber, Phys. Rev. B **72** (2005) 020105(R).; T. Sasaki, M. Mizumaki, K. Kato, Y. Watabe, Y. Nishihata, M. Takata and J. Akimitsu, J. Phys. Soc. Jpn. **74** (2005) 2185.

[3] T. Sasaki, M. Mizumaki, T. Nagai, T. Asaoka, K. Kato, M. Takata, Y. Matsui and J. Akimitsu, unpublished.

[4] J. P. Clancy, B. D. Gaulin, C. P. Adams, G. E. Granroth, A. I. Kolesnikov, T. E. Sherline and F. C. Chou, Phys. Rev. Lett. **106** (2011) 117401.; T. Yokoo, S. Itoh, F. Trouw, A. Llobet-Megias and J. Akimitsu, J. Phys. Conf. Series to be published.

[5] F.D.M. Haldane, Phys. Lett. **93** (1983) 464.

[6] T. Yokoo, T. Sakaguchi, K. Kakurai and J. Akimitsu, J. Phys. Soc. Jpn. **64** (1995) 3651.

[7] V. Sachan, D.J. Buttrey, J.M. Tranquada and G. Shirane, Phys. Rev. B **49** (1994) 9658.

[8] A. Zheludev, J.M. Tranquada, T. Vogt and D.J. Buttrey, Phys. Rev. B **54** (1996) 7210.

[9] J.F. DiTusa, S.W. Cheong, J.H. Park, G. Aeppli, C. Broholm and C.T. Chen, Phys. Rev. Lett. **73** (1994) 1857.

T. Yokoo[1,2], S. Itoh[1,2], D. Kawana[3], H. Yoshizawa[3], and J. Akimitsu[4]

[1]Neutron Science Section, Materials and Life Science Division, J-PARC Center; [2]Institute of Materials Structure Science, KEK; [3]The Institue for Solid State Physics, The University of Tokyo; [4]Department of Physics and Mathematics, Aoyama Gakuin University

Temperature and Element Substitution Effects on Magnetic Excitations in the Triangular-Lattice Antiferromagnet $CuCrO_2$

A two-dimensional (2D) triangular-lattice antiferromagnet (TLA) is a typical example of the geometrically frustrated antiferromagnets, in which a novel spin state is expected to originate from competing magnetic interactions and low dimensionality. However, real materials have finite magnetic interactions between triangular-lattice planes, which usually cause three-dimensional (3D) spin ordering at a low temperature. A reduction in the level of interplanar interaction is a key to realizing a novel spin state.

The delafossite oxide $CuCrO_2$ is one of the 2D TLAs. In this compound, $S = 3/2$ spins of Cr^{3+} ($3d^3$) ions form a 2D triangular lattice. Cr layers are separated from each other by Cu layers. Due to finite inter-layer couplings, the compound shows a 3D magnetic ordering below the magnetic ordering temperature T_N. Recently, however, a study of magnetic specific heat (C_{mag}) in $Cu_{1-x}Ag_xCrO_2$ revealed that the low-energy magnetic excitations become more 2D as the substitution of a Cu^+ ion ($3d^{10}$) by a Ag^+ ion ($4d^{10}$) increases, and suggested the appearance of some unconventional spin fluctuations [1].

To elucidate the low-energy magnetic excitations, we have performed inelastic neutron scattering measurements on powder samples of $CuCrO_2$ ($T_N = 24$ K) and $Cu_{0.85}Ag_{0.15}CrO_2$ ($T_N = 14$ K). By close investigation of the temperature (T) dependence of the magnetic excitation spectra in $CuCrO_2$ and the comparison of the two compounds, we found that both T and Ag doping change the characteristics of magnetic excitations and induce unconventional low-energy magnetic excitations [2].

Figure 1 shows the Q-E (momentum transfer-energy transfer) maps of the excitation spectra for $CuCrO_2$ at 6 K and 25 K, and for $Cu_{0.85}Ag_{0.15}CrO_2$ at 5 K. $CuCrO_2$ shows well defined magnetic excitations at 6 K [Fig. 1(a)]. They consist of two kinds of

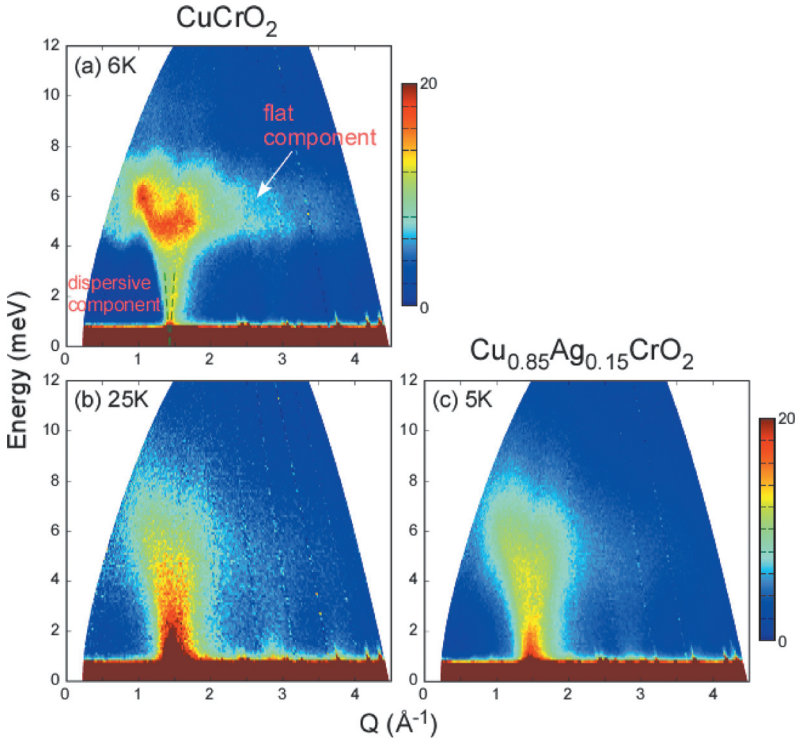

Figure 1. Excitation spectra for $CuCrO_2$ at (a) 6 and (b) 25 K, and for $Cu_{0.85}Ag_{0.15}CrO_2$ at (c) 5 K. The utilized incident energy (E_i) is 15 meV.

components: one is a steep dispersive component at Q ~ 1.4 Å^{-1} ~ Q_m, where $\boldsymbol{Q}_m$ ~ (1/3,1/3,0) is the wave vector of the magnetic ordering. The other is a less dispersive component (flat component) at E ~ 5 meV spreading over a wide Q range. They are consistent with the spin wave excitations observed in a single crystal [3]. With increasing T to 25 K (~T_N), the dispersive component becomes broad and intense, while the flat component is more suppressed [Fig. 1(b)]. In contrast, $Cu_{0.85}Ag_{0.15}CrO_2$ has almost no flat component at 5 K [Fig. 1(c)]. The dispersive component is clearly observed as $CuCrO_2$, but it is diffusive compared with $CuCrO_2$. Interestingly, the excitation spectrum of $Cu_{0.85}Ag_{0.15}CrO_2$ at 5 K with these features resembles that of $CuCrO_2$ at ~T_N.

Then, to characterize the similarity in the excitation spectrum between the two compounds in detail, we investigated the Q profiles of the low-energy excitation spectra. Figure 2 shows the Q profiles of the spectra at E = 1 meV for $CuCrO_2$ at 6 K and 25 K, and for $Cu_{0.85}Ag_{0.15}CrO_2$ at 5 K. The spectrum of $CuCrO_2$ at 6 K consists of a single skewed peak at Q_m. However, that at 25 K has a diffuse component (the shaded area in Fig. 2) spreading over a wide range of Q in addition to the sharper peak at Q_m. On the other hand, the spectrum of $Cu_{0.85}Ag_{0.15}CrO_2$ also shows the diffuse component even at 5 K (the open circles in Fig. 2), which again proves the similarity in the magnetic excitation to $CuCrO_2$ at ~T_N. We analyzed the T dependence of the Q profile of $CuCrO_2$ (not shown), and found that the diffuse component is almost zero at the lowest T, but monotonically increases as a function of T without any change at T_N. The T dependence suggests that the origin of the diffuse component is different from the spin wave excitations.

After comparing the results shown in Figs. 1 and 2, we concluded that the ground state of

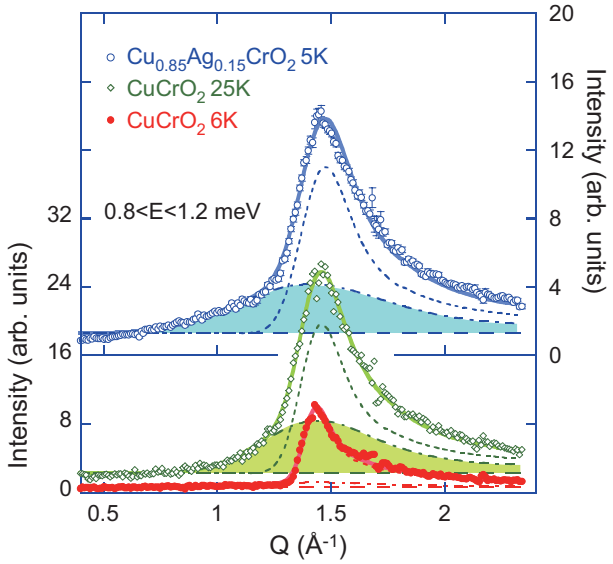

Figure 2. Constant-E cuts of the spectra of $CuCrO_2$ (6 K and 25 K) and $Cu_{0.85}Ag_{0.15}CrO_2$ (5 K) at E = 1±0.2 meV. The utilized E_i is 4.7 meV. The solid lines indicate fits to two Warren functions (dotted and dot-dashed lines) and a constant background (dashed lines).

$Cu_{0.85}Ag_{0.15}CrO_2$ is very similar to that of $CuCrO_2$ at T ~ T_N. The most distinct finding is the appearance of the diffuse component in the low-energy magnetic excitations when the two-dimensionality of the system is enhanced either by element substitution or elevating temperature. It must be the origin of the 2D unconventional low-energy magnetic excitations suggested by C_{mag}. The investigation of the microscopic origin is under way.

References

[1] T. Okuda *et al.*, J. Phys. Soc. Jpn. **78** (2009) 013604.

[2] R. Kajimoto *et al.*, J. Phys. Soc. Jpn. **79** (2010) 123705; J. Phys. Soc. Jpn. **82** (2013) 054702.

[3] M. Frontzek *et al.*, Phys. Rev. B **84** (2011) 094448.

R. Kajimoto[1], K. Nakajima[2], S. Ohira-Kawamura[2], Y. Inamura[2], K. Kakurai[3], M. Arai[2], T. Hokazono[4], S. Oozono[4], and T. Okuda[4]

[1]Neutron R&D Division, CROSS-Tokai; [2]Neutron Science Section, Materials and Life Science Division, J-PARC Center; [3]Quantum Beam Science Directorate, JAEA; [4]Department of Nano-Structures and Advanced Materials, Kagoshima University

Chiral Magnetic Soliton Lattice in MnSi

Chirality is one of the most fundamental building blocks of nature, ranging from nano and biosciences to cosmic sciences. Therefore, it is very important to investigate the chirality in molecules, crystals and magnetic structures. Recently, the interplay between crystallographic and magnetic chiralities has been a focus of attention because the nature of a helimagnetic structure depends on the chiral crystalline structure that allows Dzyaloshinskii-Moriya (DM) interaction [1, 2]. Kishine *et al*. theoretically proposed that the chiral helimagnetic compounds can exhibit a new giant magnetoresistance effect due to the formation of a chiral magnetic soliton lattice [3, 4]. Under an applied field perpendicular to the helical axis in $Cr_{1/3}NbS_2$, the chiral magnetic soliton lattice was observed by means of Lorentz microscopy [5].

An intermetallic compound MnSi has B20 type chiral crystal structure with a cubic space group of $P2_13$, and is known as one of the unique examples of left-handed crystal structure formation, and the helimagnetic chirality follows the crystalline chirality [6, 7]. This compound forms helimangetic ordering with the magnetic propagation vector $k_{mag} = (\delta,\delta,\delta)$. Due to its cubic symmetry, it has several helimagnetic domains along the [1,1,1] direction and its equivalent directions like the [1,1,-1]. With increasing amplitude of an applied magnetic field parallel to one of the helical axis, the population of the helimagnetic domain parallel to the field increases, and that of the other helimagnetic domain declines. It finally forms only one helimagnetic domain [8]. A topological magnetic texture as skyrmion lattice appears in the single-domain helimagnetic phases just below T_C [9]. We report here that MnSi forms the chiral magnetic soliton lattice in the multi-domain phase.

Polarized small angle neutron diffraction experiments were performed at BL15 (TAIKAN) in MLF of J-PARC. The experimental condition was 3 K under an applied magnetic field along the [1,1,1] direction, which was parallel to one of the helical axes. The data was collected in the multi-domain helimagnetic phase. A spin flipper reversed the incident up-spin neutrons along the [1,1,1] to the down-spin neutrons along the [-1,-1,-1]. As the neutron wave vector $\boldsymbol{k}_0$ was parallel to the [-1,1,0] direction, magnetic reflections along the [1,1,1] and [1,1,-1] can

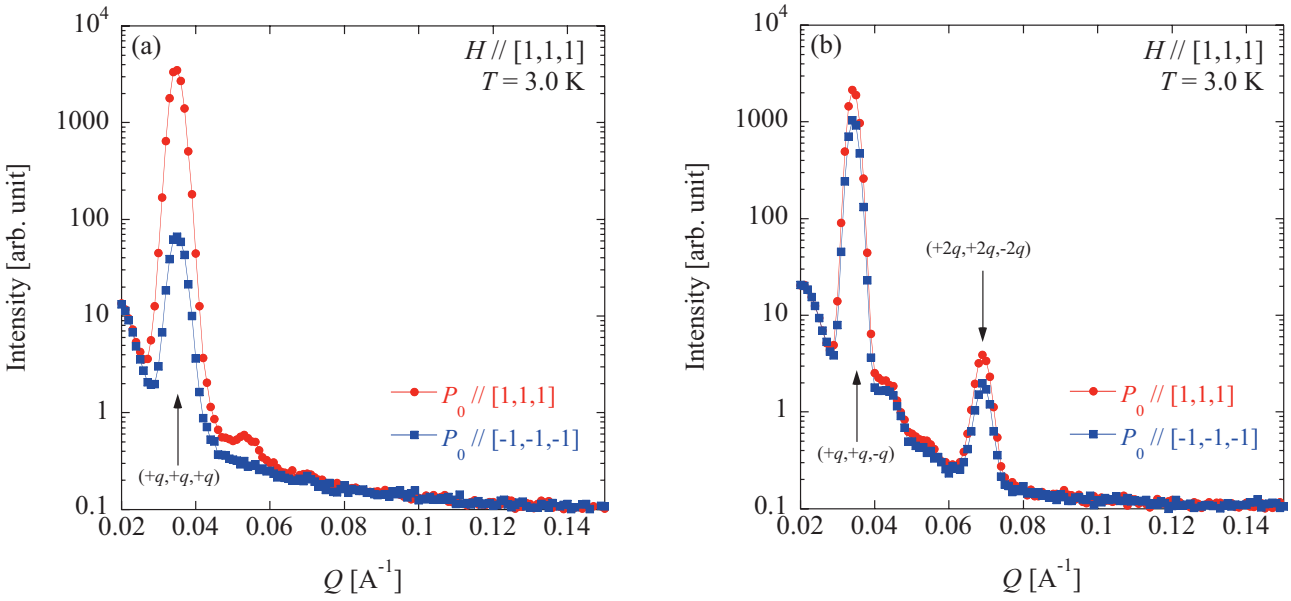

Figure 1. Reciprocal line profiles along (a) the [1,1,1] and (b) the [1,1,-1] directions.

be observed at the detector. Figure 1 shows reciprocal line profiles described in Q-space along the [1,1,1] and [1,1,-1] direction. Both profiles observed helimagnetic satellite peaks indexed as (δ,δ,δ) and $(\delta,\delta,-\delta)$. The result indicates the coexistence of the helimagnetic domains with the helical axes along the [1,1,1] and [1,1,-1]. While there was no higher harmonics along the [1,1,1], a magnetic peak indexed as $(2\delta,2\delta,-2\delta)$ was observed along the [1,1,-1]. By evaluating the difference in these magnetic peak intensities between the up- and down-spin incident neutrons, it was well described by the left-handed incommensurate magnetic structures. Therefore, the higher-order satellite peak at $(2\delta,2\delta,-2\delta)$ was due to the formation of the chiral soliton lattice.

References

[1] I. E. Dzyaloshinskii: J. Phys. Chem. Solids **4** (1958) 241.

[2] T. Moriya: Phys. Rev. **120** (1960) 91.

[3] J. Kishine, K. Inoue, and Y. Yoshida: Prog. Theor. Phys. Suppl. **159** (2005) 82.

[4] J. Kishine, I. Proskurin, and A. Ovchinnikov: Phys. Rev. Lett. **107** (2011) 017205.

[5] Y. Togawa, T. Koyama, K. Takayanagi, S. Mori, Y. Kousaka, J. Akimitsu, S. Nishihara, K. Inoue, A. Ovchinnikov, and J. Kishine: Phys. Rev. Lett. **108** (2012) 107202.

[6] M. Tanaka, H. Takayoshi, M. Ishida, and Y. Endoh: J. Phys. Soc. Jpn. **54** (1985) 2970.

[7] M. Ishida, Y. Endoh, S. Mitsuda, Y. Ishikawa, and M. Tanaka: J. Phys. Soc. Jpn. **54** (1985) 2975.

[8] Y. Ishikawa, K. Tajima, D. Bloch, and M. Roth: Solid State Commun. **19** (1976) 525.

[9] S. Muhlbauer, B. Binz, F. Jonietz, C. Pfleiderer, A. Rosch, A. Neubauer, R. Georgii, and P. Böni: Science **323** (2009) 915.

Y. Kousaka[1], N. Ikeda[1], J. Akimitsu[1], K. Ohishi[2], and J. Suzuki[2]

[1]*Department of Physics and Mathematics, Aoyama-Gakuin University;* [2]*Neutron R&D Division, CROSS-Tokai*

Adsorption of Water into DN-gels with Hierarchical Structure

1. Introduction

Soft matter has a hierarchical structure on the scale of angstroms up to macroscale. Additionally it is known that physical properties of soft matter are greatly influenced by water. Hydrogels are good materials to study the effect of water adsorption because they contain an abundance of water. In fact, most hydrogels, which have a 3-D polymer network, can adsorb more than 90 wt% of water. Nevertheless, most hydrogels are composed of 90 wt% water, which means only 10 wt% of the polymer network governs its mechanical properties. Although there are a number of studies on water in hydrogels, there is little experimental study on water near the polymer network.

Double-network hydrogels (DN-gels) [1,2] are hydrophilic synthetic polymer gels that have high mechanical strength equivalent to cartilage. Several studies on polymer networks of DN-gels have been conducted using small-angle neutron scattering (SANS) [3,4,5] so far, however, it was not determined how water molecules are adsorbed into the polymer network.

In this study, we performed SANS measurements to investigate the humidity dependence of the nanoscale structure of the freeze-dried DN-gels (DN-polymers) in order to clarify the mutual relationship between a polymer network and water.

2. Experiments

The DN-gels made by 2-acrylamide-2-methylpropanesulfonic acid sodium salt and acrylamide were freeze-dried (DN-polymers) [6]. The DN-polymers were placed in a dry state to remove light water. After the drying process, heavy water vapors were introduced into the system for more than an hour to generate certain relative humidity (RH). The SANS measurements were performed on TAIKAN (BL15).

3. Results

The SANS profiles of the DN-polymers under various RH conditions are shown in Fig. 1.

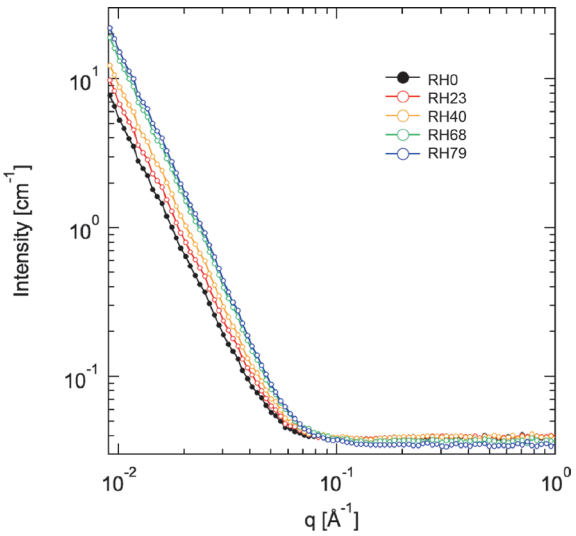

Figure 1. SANS profiles obtained from the DN-polymers under different humidity conditions. The RH is 0% (Black), 23% (Red), 40% (Orange), 68% (Green), and 79% (Blue).

The intensity below $q = 2 \times 10^{-2}$ Å^{-1} increases with increasing RH. The power law behavior is observed in this q-range with an exponent of approximately –3.1 for all RH conditions. SANS intensities would originate from the nanoscale interfaces of polymer networks.

In order to clarify the effect of water adsorption on the SANS profiles, those measured between 23% RH and 79% RH were divided by the profile measured at 0% RH as shown in Fig. 2. The scaled intensity increases with increasing RH below $q \approx 8 \times 10^{-2}$ Å^{-1}. When the RH is less than 68%, the scaled intensity does not change above $q = 8 \times 10^{-2}$ Å^{-1}, but when it is more than 68%, the scaled intensity decreases with increasing RH.

The adsorption behavior of water molecules in the polymer network of the DN-polymers could be interpreted as follows: There is no change in the polymer network structure larger than d ($= 2\pi/q$) = 200 Å. Below 79% RH, water molecules adsorb onto a larger polymer structure than a mesh size scale, which is greater than 80 Å, in the dry state of the DN-polymers. When the RH is 68%–79%,

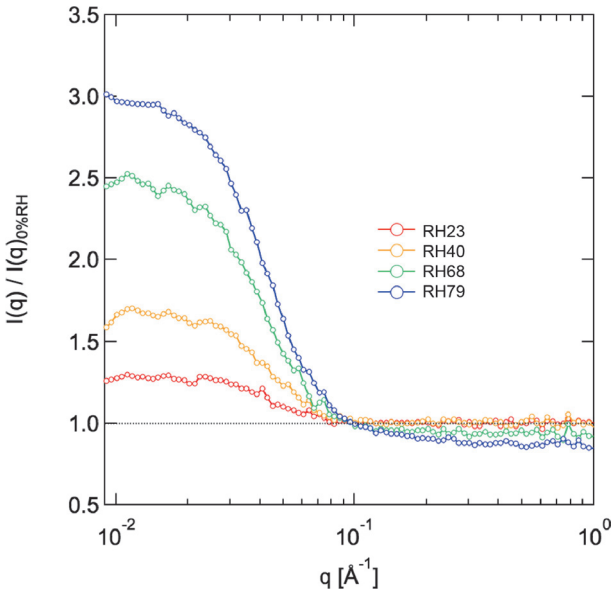

Figure 2. The relative SANS profile divided by the SANS profile measured at 0% RH. The relative humidity is 23%. The RH is 0% (Black), 23% (Red), 40% (Orange), 68% (Green), and 79% (Blue).

water molecules adsorb not only on the large polymer structure but also on internal structures such as polymer segments that are smaller than the mesh size. We are currently analyzing the SANS results.

Acknowledgments

This study was performed under the following project in the MLF: *Structure and dynamics of water molecules in soft matters* (2012P0401, 2013P0401). This work was supported by JSPS KAKENHI (No. 25810131).

References

[1] J.P. Gong *et al.*, Adv. Mater. **15** (2003) 1155.
[2] J.P. Gong Soft Matter **6** (2012) 2583.
[3] T. Tominaga *et al.*, Polymer **48** (2007) 7449.
[4] Taiki Tominaga *et al.*, J. Phys. Chem. B **112** (2007) 3903.
[5] V. R Tirumala *et al.*, J. Phys.Chem. B **112** (2008) 8024.
[6] T. Tominaga *et al.*, ACS Macro Lett. **1** (2012) 432.

T. Tominaga[1], S. Takata[1], J. Suzuki[2], K. Aizawa[1], H. Seto[1,3], and M. Arai[1]

[1]Neutron Science Section, Materials and Life Science Division, J-PARC Center; [2]Neutron R&D Division, CROSS-Tokai; [3]Institute of Materials Structure Science, KEK

Dewetting Process of Deuterated Polystyrene and Poly (vinyl methyl ether) Blend Thin Films via Phase Separation

Dewetting of polymer thin film is a key issue in many industrial fields such as coatings, adhesives, lubrications, and so on. For understanding the dewetting mechanism of such polymer films, the capillary wave and density fluctuations have received considerable attention because they play an important role in the dewetting process of the polymer thin films. In the case of two component films such as polymer blend, much attention is also paid to the phase separation between the polymers because of its important role that affects dewetting. In this study, we investigated the structural development in the dewetting process of deuterated polystyrene (dPS) and poly (vinyl methyl ether) (PVME) thin films by complementary use of time-resolved specular and off-specular neutron reflectivity (NR), specular X-ray reflectivity (XR), light scattering (LS) and optical microscopy (OM) measurements [1].

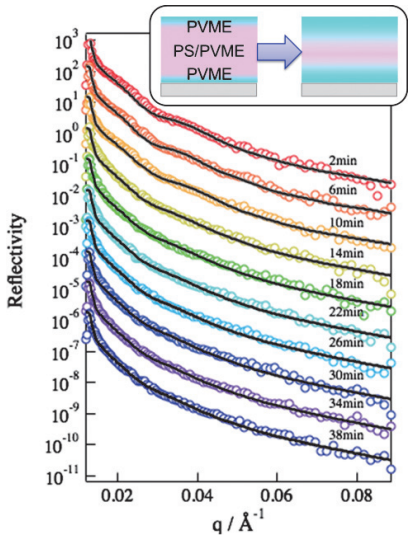

Figure 1. Time evolution of specular NR profiles during the dewetting process.

Figure 1 shows the time evolution of specular NR profiles during the dewetting process using SOFIA reflectometer in J-PARC/MLF [2-4]. In the early stage, the profiles can be explained with a 3-layers model, in which PVME-rich layers exist on top and bottom. According to XR measurement (data not shown), the roughness of the top surface, that is air/polymer interface, keeps constant before the dewetting. On the other hand, NR results indicate that the interfacial roughness between each polymer layer gradually increases with time even before the dewetting. This implies that the phase separation between the polymers proceeds during the incubation period and makes the interfaces rough.

Next, we observed the time evolution of in-plane structure by OM, LS, and off-specular NR measurements. Figure 2 shows the obtained OM images and

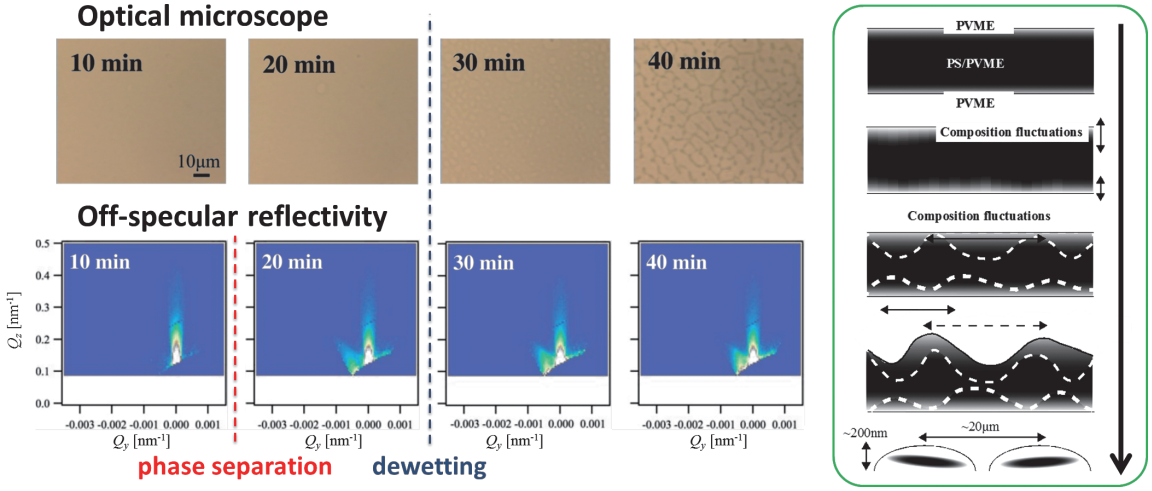

Figure 2. Time evolution of optical microscope images and off-specular NR profiles during the dewetting process.

off-specular NR profiles. No structural change was observed before the dewetting by OM as XR measurements; however, off-specular NR profiles show a characteristic peak not only after but also before the dewetting. This peak was observed by the LS measurements in the same Qy-position (data not shown) only after the dewetting. Therefore, we can conclude that composition fluctuations with micrometer scale in the in-plane direction occurred before the dewetting. This indicates that the phase separation of the polymer blend grew up with the annealing time, and the composition fluctuation caused by the phase separation induces the dewetting.

References

[1] T. Xia *et al.*, Macromolecules **46** (2013) 4540.

[2] K. Mitamura *et al.*, J. Phys.: Conf. Ser. **272** (2011) 012017.

[3] N. L. Yamada *et al.*, Euro. Phys. J. Plus **126** (2011) 108.

[4] K. Mitamura *et al.*, Polymer J. **45** (2013) 117.

T. Xia[1,2], H. Ogawa[3], R. Inoue[2], K. Nishida[2], N. L. Yamada[4,5], G. Li[1], and T. Kanaya[2]

[1]*College of Polymer Science and Engineering, Sichuan University;* [2]*Institute for Chemical Research, Kyoto University;* [3]*Japan Synchrotron Radiation Research Institute;* [4]*Neutron Science Section, Materials and Life Science Division, J-PARC Center;* [5]*Institute of Materials Structure Science, KEK*

Development of Piezo-Based Low Temperature 2-Axes Goniometer System

1. Introduction

Single crystal diffraction experiments require rotation of a crystal in order to have access to arbitrary points in the reciprocal lattice space. A typical instrument to fulfill this demand is a four-circle goniometer equipped with χ, φ and ω stages. In the usual low temperature setup, a whole cryostat is mounted onto the goniometer since a standard stepper motor does not work inside vacuum and at low temperature. This setup causes two difficulties. First, in order to rotate the sample, including the cryostat, a relatively large goniometer with high load capacity is required. The other one is that it is not possible to avoid the intense direct beam hitting radiation shields of the cryostat, which results in higher background. In order to overcome these difficulties, we developed a goniometer that works inside the cryostat. This is achieved with the help of the recent technical development in piezo devices which enables us to make movements even at dilution temperature with small stages. We used the developed goniometer in the new single crystal time-of-flight neutron Laue diffractometer SENJU at BL18 of J-PARC[1].

2. Design of the goniometer

The goniometer consists of two rotatable axes to cover the entire reciprocal space on SENJU. A photo of the goniometer is shown in Fig. 1. The piezo-based rotators used in this system were made by Attocube Systems AG (Germany). The ω stage is directly attached to the cold finger of the standard closed-circle refrigerator. The φ stage is mounted on the fixed-χ (45°) arm. In order to adjust the sample position with respect to the beam center, the XY stage with the sample holder is installed on the top of the φ stage. Because of the poor thermal conductivity of the piezo devices, additional heat paths are attached between the cold finger and the χ arm, and the χ arm and the sample holder. In order to obtain accurate sample temperature, a thermometer is placed at the sample holder.

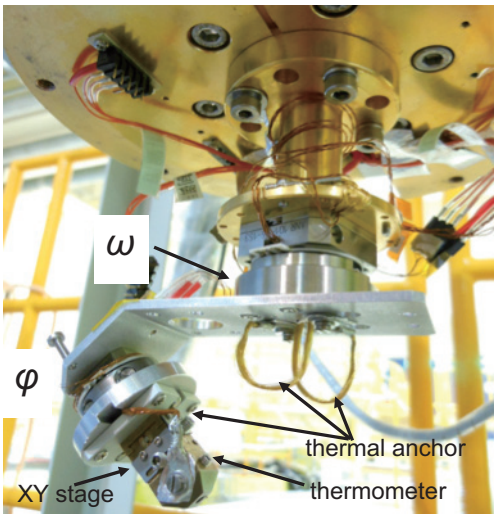

Figure 1. Photograph of piezo motor based goniometer system for SENJU.

3. Results

First, we checked the movement of the two rotators at the base temperature of around 4 K. By optimizing wiring of thermal anchors, we confirmed that both the ω and φ axes work fine at low temperature.

In order to minimize the scattering from two radiation shields made by aluminum with the thickness of 1.5 mm each, we made halls at the direct beam path (50 × 50 mm) in both shields. These halls are then covered by thin Al foils (6 μm in thickness) that is sufficient to reach base temperature of 2.5 K at the cold finger. This modification clearly helps to suppress the background from the radiation shield even without any collimator between the sample and the detector. As shown in Fig. 2, the scattering from the radiation shield is almost negligible as compared with the magnetic Bragg peaks of (3/2 1 1/2) and (2 3/2 1/2) in $TbCoGa_5$.

The cooling performance of the 4 K cryostat was checked subsequently. Due to small torque of the piezo motor, stiff thermal anchors prevent the smooth rotation of the sample. By optimizing the size and wiring of the thermal anchors, we could improve the characteristics of cooling in both the

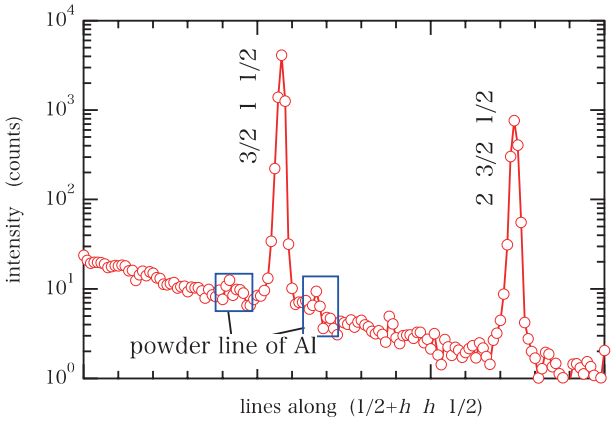

Figure 2. The intensity data of $TbCoGa_5$ measured at 10 K.

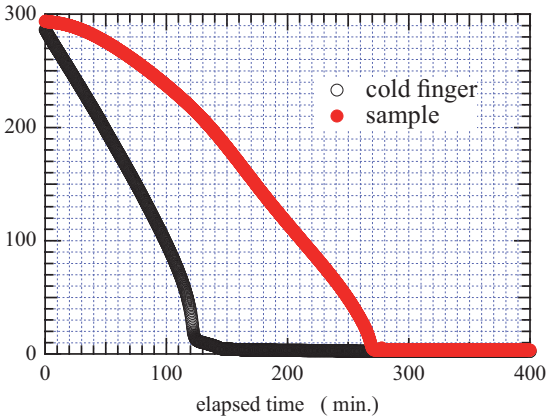

Figure 3. Cooling curves of the 4 K cryostat of SENJU.

lowest temperature and the cooling time. In the present setup, the lowest temperature at the sample position reaches below 4 K within the 4.5 hours of cooling from room temperature. The accuracy of the sample temperature was confirmed by the transition temperature of several compounds including an antiferromagnetic order in $EuGa_4$ at $T_N = 16$ K[2]. Further improvements are still in progress.

References

[1] K. Oikawa *et al.*, J. Phys. Soc. Jpn. Suppl. in press.

[2] T. Kawasaki *et al.*, J. Phys. Soc. Jpn. Suppl. in press.

K. Kaneko[1,2], K. Munakata[3], Y. Dohi[4], Y. Noda[4], T. Hanashima[3], K. Sato[3], T. Kawasaki[1], R. Kiyanagi[1], A. Nakao[3], T. Ohhara[3], K. Oikawa[5], and I. Tamura[1,6]

[1]Neutron Science Section, Materials and Life Science Division, J-PARC Center; [2]Quantum Beam Science Directorate, JAEA; [3]Neutron R&D Division, CROSS-Tokai; [4]Institute of Multidisciplinary Research for Advanced Materials, Tohoku University; [5]Neutron Source Section, Materials and Life Science Division, J-PARC Center; [6]Department of Research Reactor and Tandem Accelerator, JAEA

Investigation of the Degradation Mechanism of ITER CS Conductor Sample using TAKUMI

1. Introduction

ITER is constructed in France under an international collaboration with India, China, EU, Korea, Russia, USA and Japan to prove the viability of nuclear fusion as a power source. To confine and control the plasma, the ITER magnet system consists of a Central Solenoid (CS), 18 Toroidal Field (TF) coils and 6 Poroidal Field (PF) coils as shown in Figure 1. The CS, which is 13.5 m in height and 4.1 m in diameter, generates and controls the plasma current by varying the magnetic field as a maximum of 13 T. JAEA has to responsibly procure all ITER CS conductors. The CS conductor is a cable-in-conduit conductor (CICC) composed of a superconducting cable consisting of 576 Nb_3Sn strands and 288 copper strands, a SS316L central spiral and a JK2LB stainless steel square jacket as shown in Figure 2. After the operation of 60,000 cycles, a current sharing temperature (T_{cs}) of 5.2 K is required at the currents of 40 kA under the magnetic fields of 13 T. Several conductor samples were fabricated to evaluate the performance of the CS conductor and validate its design concept. Two CS conductor samples named CSJA01 and CSJA02, consisting of a pair of conductor samples, were tested in the SULTAN test facility in Switzerland. As reported in [1, 2], gradual degradation was observed in the results for both CSJA01 and CSJA02, which was the same as that of many TF conductors as shown in Figure 3.

Until now, the transverse electromagnetic loading has been considered a major cause of the T_{cs} degradations of Nb_3Sn CICCs due to the local bending at the high loading side (HLS) in the high field zone (HFZ). From the destructive investigation in the HFZ after SULTAN testing, the deflection of strands on the low transverse loading side (LLS) is larger than that for the HLS as shown in Figure 4. Since the bending pith is around 5 mm due to contacting of strands compacted by the electromagnetic transverse loading in the HLS, there is a possibility of a large bending strain with small deflection of strands in the HLS.

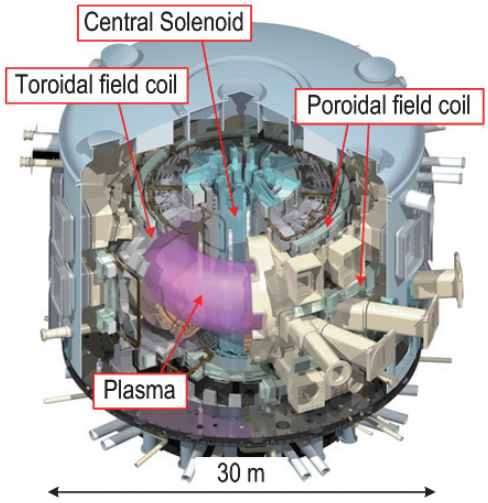

Figure 1. Schematics of ITER.

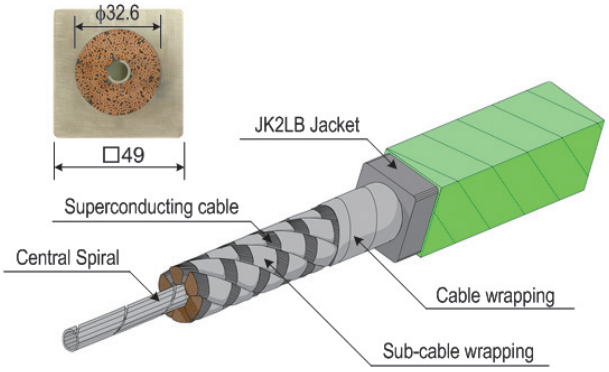

Figure 2. Schematics of ITER CS conductor.

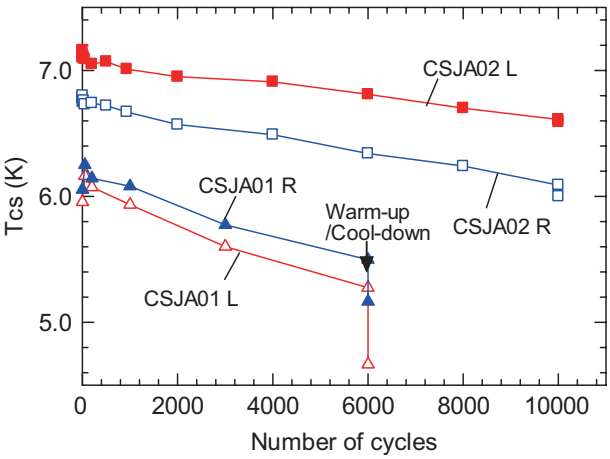

Figure 3. T_{cs} result of CSJA01 and CSJA02.

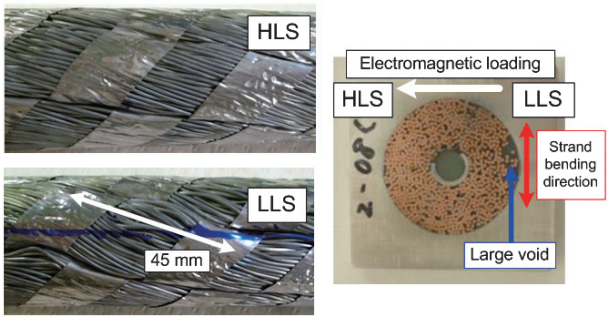

Figure 4. Visually inspected cable in the HFZ of CSJA01 right leg.

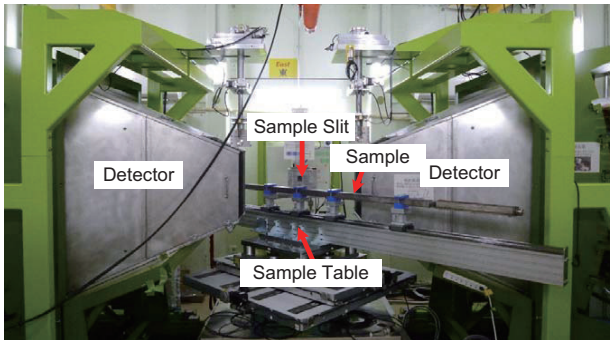

Figure 5. CS conductor sample arranged at TAKUMI.

Neutrons, which have a large penetration depth, are a powerful tool to evaluate the internal strain of Nb_3Sn in the CICC [3]. In order to evaluate the internal strain in ITER CS conductor samples non-destructively and quantitatively, a neutron diffraction measurement using the engineering materials diffractometer 'TAKUMI' (BL19) was carried out on the CSJA01 left leg at room temperature.

2. Neutron diffraction measurement [4]

For neutron diffraction measurement using TAKUMI, the conductor sample of 3.6 m was arranged as shown in Figure 5. The neutron beam was focused using a pair of radial collimator to the gauge volume of $7 \times 2 \times 16$ mm^3 in the measured position of the conductor sample as shown in Figure 6. The sample conductor was turned over to measure whether the LLS and the HLS have the same path as the neutron beam. Figure 7 shows the diffraction profiles for the axial direction of Nb_3Sn (211) at the LLS and the HLS of the field center and 1150 mm from the field center. The Nb_3Sn filaments were taken from the same strand using a chemical process to compare the diffraction profile of the conductor sample. The diffraction peak shapes and positions at the HLS in the HFZ and the low field zone (LFZ) were similar, and the peaks were located at a lower level than that of Nb_3Sn filaments. This peak shift is due to the difference in the thermal contraction between copper/Nb_3Sn filament and cable/jacket from the reaction temperature of Nb_3Sn. However, the peak of the LLS in the HFZ shifted to a tensile direction and became broader, compared to the other peak. The bending strain with the relaxation of the compression strain in the Nb_3Sn strand was irreversibly remained by the SULTAN testing.

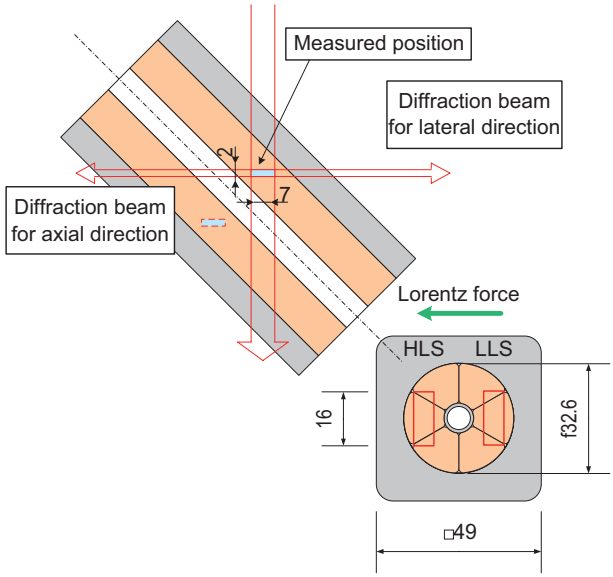

Figure 6. Schematic diagram of the neutron diffraction measurement.

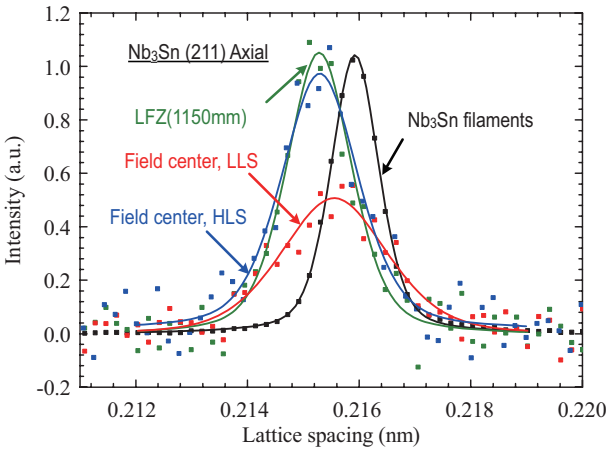

Figure 7. Differences in the diffraction profile.

3. Discussion on the degradation mechanism and improvement

From neutron diffraction measurement, the larger bending strain was found at the LLS of the HFZ in the conductor sample. As a degradation mechanism, strand buckling is considered as follow;

1) The void at the LLS of the HFZ is generated by the transverse movement of the strands in the conductor sample,
2) There is an axial compressive force induced by the difference in the thermal contraction from the reaction temperature of Nb_3Sn,
3) The buckling of the Nb_3Sn strand is occurring via the axial compressive force because the support and the friction of the jacket and the cable on the strand are varied by the large void.

As an improvement method of the conductor performance on the strand buckling, the shorter twisting pitch (STP) can be considered. The cable with the STP has withstood the strand buckling since the bending stiffness and rigidity are quite larger. Figure 8 shows photographs of the cables with original twisting pitch and STP [5]. The result of the SULTAN testing of the conductor sample with STP was found to be very effective, and the performance degradation along the cyclic testing was almost negligible as shown in Figure 9.

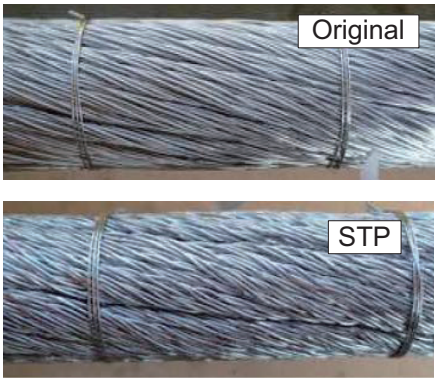

Figure 8. Photograph of the cable with original twisting pitch and STP.

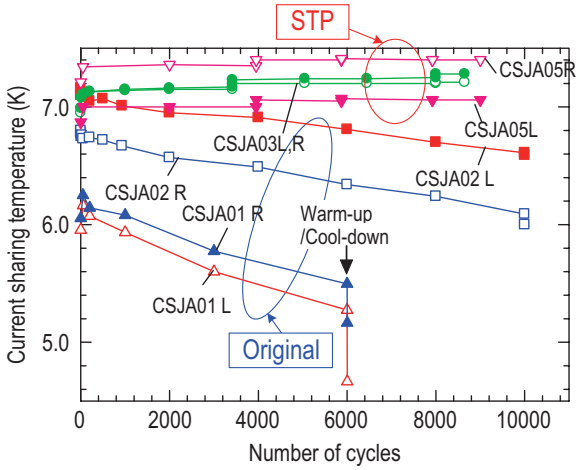

Figure 9. T_{cs} results of SULTAN testing.

4. Conclusion

Neutron diffraction measurement on the ITER CS conductor sample was performed to investigate the degradation mechanism of the conductor sample. As a result of the neutron diffraction measurement, a large bending at the LLS of the HFZ was found. Therefore, it was concluded that the T_{cs} degraded position of the conductor sample due to the cyclic loading was the LLS of the HFZ. The large bending was considered to be a cause of the strand buckling due to the large void generated by the transverse electromagnetic loading and the thermally induced residual compressive strain. By applying the STP on the cable to control the strand buckling, the problem of the performance degradation along cyclic testing was solved.

References

[1] G. Brumfiel, Nature **471** (2011) 150.
[2] T. Hemmi *et al.*, IEEE Trans. Appl. Supercond. **22** (2012) 4803305.
[3] S. Awaji, Supercond. Sci. Technol. **26** (2013) 073001.
[4] T. Hemmi *et al.*, Supercond. Sci. Technol. **26** (2013) 084002.
[5] Y. Takahashi *et al.*, presented in MT-23 conference (2013) 4OrAB-05.

T. Hemmi[1], S. Harjo[2], H. Kajitani[1], Y. Nabara[1], Y. Takahashi[1], Y. Nunoya[1], N. Koizumi[1], J. Abe[2], W. Gong[2], K. Aizawa[2], H. Suzuki[3], S. Machiya[4], and K. Osamura[5]

[1]Fusion Research and Development Directorate, JAEA; [2]Neutron Science Section, Materials and Life Science Division, J-PARC Center; [3]Quantum Beam Science Directorate, JAEA; [4]Daido University; [5]Research Institute for Applied Sciences

Neutron Diffraction Study on the Structure of Aqueous $LiNO_3$ Solutions

1. Introduction

Despite the long-time efforts to resolve it, there are still some serious problems in determining the hydration structure of Li^+. The concentration dependence of the hydration number of Li^+ and the nearest neighbor $Li^+\cdots O$ distance still seems uncertain [1,2]. Neutron diffraction with $^6Li/^7Li$ isotopic substitution method is considered the most reliable experimental technique to determine the values of r_{LiO} and n_{LiO} because the observed difference function involves partial structure factors relating Li-j atom pairs.

In the present report, we describe the results of neutron diffraction measurements on aqueous 1, 5 and 10 mol% $LiNO_3$ solutions in D_2O. The solute concentration range was extended to 1 mol% $LiNO_3$ in order to investigate the hydration structure of Li^+ in a more dilute aqueous solution.

2. Neutron Diffraction Measurements

Neutron diffraction measurements were carried out at 25ºC using the NOVA spectrometer installed at BL21 of the MLF pulsed neutron source in the J-PARC. The incident proton beam power of the proton accelerator was 160 kW in measurements for 5 and 10 mol% $*LiNO_3$ solutions, and 220 kW for 1 mol% $*LiNO_3$ solutions, respectively.

3. Data Reduction

The observed scattering intensities for the sample were corrected for instrumental background, absorption of sample and cell, multiple and incoherent scatterings.

The first-order difference function, $\Delta_{Li}(Q)$ [3], is derived from the difference between the scattering cross sections observed for two solutions that are identical except for the scattering length of Li. The $\Delta_{Li}(Q)_2$, normalized for a stoichiometric unit, $(*LiNO_3)_x(D_2O)_{1-x}$, can be written as a linear combination of partial structure factors, $a_{Lij}(Q)$, involving contributions from the Li-j pair:

$$\Delta_{Li}(Q) = A[a_{LiO}(Q)-1] + B[a_{LiD}(Q)-1] + C[a_{LiN}(Q)-1] + D[a_{LiLi}(Q)-1]. \quad (1)$$

where, $A = 2x(1+2x)(b_{6Li}-b_{7Li})b_O$, $B = 4x(1-x)(b_{6Li}-b_{7Li})b_D$, $C = 2x^2(b_{6Li}-b_{7Li})b_N$, and $D = x^2(b_{6Li}{}^2-b_{7Li}{}^2)$.

4. Results and Discussion

The first order difference function, $\Delta_{Li}(Q)$, observed for 1, 5 and 10 mol% $LiNO_3$ solutions is represented in Fig. 1. Structural parameters concerning the hydration shell of Li^+ were obtained through the least squares fitting procedure applying the following model function [4,5]:

$$\Delta_{Li}{}^{model}(Q) = \Sigma 2c_{Li}n_{Li\alpha}b_\alpha(b_{6Li}-b_{7Li}) \times \exp(-l_{Li\alpha}{}^2Q^2/2)\sin(Qr_{Li\alpha})/(Qr_{Li\alpha}) + 4\pi\rho(A+B+C+D)\exp(-l_0{}^2Q^2/2) \times [Qr_0\cos(Qr_0) - \sin(Qr_0)]Q^{-3} + \gamma \quad (3)$$

where, c_{Li} and $n_{Li\alpha}$ are the number of Li^+ in the stoichiometric unit and the coordination number of α atom around Li^+, respectively. Parameters $l_{Li\alpha}$ and $r_{Li\alpha}$ denote the root-mean-square amplitude and internuclear distance of the $Li^+\cdots\alpha$ pair, respectively. The long-range parameter, r_0, means the distance beyond which the continuous distribution of atoms around Li^+ can be assumed. The parameter, l_0, describes the sharpness of the boundary at r_0. A constant, γ, was introduced to adjust the center of the interference oscillation. Structural parameters $n_{Li\alpha}$, $l_{Li\alpha}$, $r_{Li\alpha}$, l_0, r_0 and γ are determined from the least squares fit to the observed $\Delta_{Li}(Q)$. The fitting procedure was performed in the range of $0.1 \le Q \le 20.0$ Å^{-1}. The nearest neighbor $Li^+\cdots O_W$ distance and coordination number determined for 10, 5 and 1 mol% $LiNO_3$ solutions are 1.97(1) Å and 4.1(1), 1.96(1) Å and 5.2(1), and 2.00(2) Å and 6.0(2), respectively. These results clearly indicate that the concentration dependence of the hydration number of Li^+ is actually present.

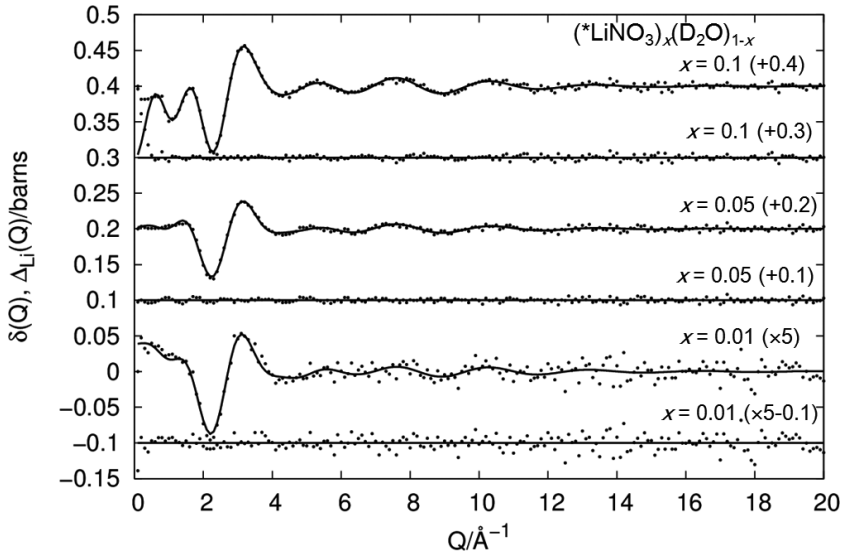

Figure 1. The first-order difference function, $\Delta_{Li}(Q)$, observed for $(*LiNO_3)_x(D_2O)_{1-x}$ solutions, x = 0.1, 0.05 and 0.01.

Acknowledgements

The authors would like to thank the instrumental staff members of the NOVA spectrometer for their help during the course of neutron diffraction measurement and transformation of the scattering data. The neutron scattering experiment was approved by the Neutron Scattering Program Advisory Committee of IMSS, KEK (Proposal No. 2009S06).

References

[1] H. Ohtaki and T. Radnai, Chem. Rev. **93** (1993) 1157.

[2] P. R. Smirnov and V. N. Trosin, Russ. J. Gen. Chem. **76** (2006) 175.

[3] J. E. Enderby and G. W. Neilson, Water, A Comprehensive Treatise, Vol. 6, pp. 1-46, Plenum press, N. Y. (1979)

[4] A. H. Narten, M. D. Danford and H. A. Levy, Discuss. Faraday Soc. **43** (1967) 97.

[5] H. Ohtaki and N. Fukushima, J. Solution Chem. **21** (1992) 23.

Y. Kameda[1], T. Miyazaki[1], Y. Amo[1], T. Usuki[1], and T. Otomo[2,3]

[1]Department of Material and Biological Chemistry, Faculty of Science, Yamagata University; [2]Neutron Science Section, Materials and Life Science Division, J-PARC Center; [3]Institute of Material Structure Science, KEK

Local Lattice Distortion Caused by Short Range Charge Ordering in $LiMn_2O_4$

1. Introduction

$LiMn_2O_4$ has a cubic spinel structure with space group of Fd3-m at room temperature. The Mn atom is surrounded by six O atoms and they form a MnO_6 octahedron. All Li, Mn and O atoms are crystallographically equivalent. At about 260 K, the compound exhibits a structural phase transition to an orthorhombic structure with space group of Fddd accompanied with the charge ordering transition [1]. However, even in the cubic phase, the temperature dependence of the electrical resistivity is not metallic although the metallic conductivity can be expected from the simple band picture since the Mn ion has a valence of +3.5 [2]. It suggests that in the cubic phase, the valence electrons are localized at the Mn site like a glass due to their Coulomb repulsion and the arrangement of localized electrons does not have a long range ordering, resulting in non-metallic electrical conductivity.

We have performed the powder neutron diffraction measurement on ^7Li-enriched $LiMn_2O_4$ at the neutron total scattering spectrometer NOVA (BL-21) installed at the Materials and Life Science Facility (MLF) in J-PARC. In order to observe the local lattice distortion induced by the short range charge ordering in the cubic phase, we performed local structural analysis by using the atomic pair distribution function (PDF) derived from the powder neutron diffraction data.

2. Results and Discussion

The PDF obtained at room temperature where the averaged structure is the cubic structure with space group of Fd3-m, is shown in Fig. 1 by open circles. The fitting result by using the cubic structure model is shown by a blue line. The fitting line does not reproduce the shapes of the first negative peak at about 1.9 Å and the positive peaks around 2.8 Å. The first negative peak and the second positive peaks mainly consist of Mn-O and O-O atomic correlations, respectively. Although the cubic phase contains single Mn-O bond and three kinds of O-O bonds, the calculated PDF cannot reproduce the observed PDF, suggesting the existence of local lattice distortion with lower symmetry than the cubic structure. Furthermore, the weighted R factor, R_{wp}, obtained by fitting the data in

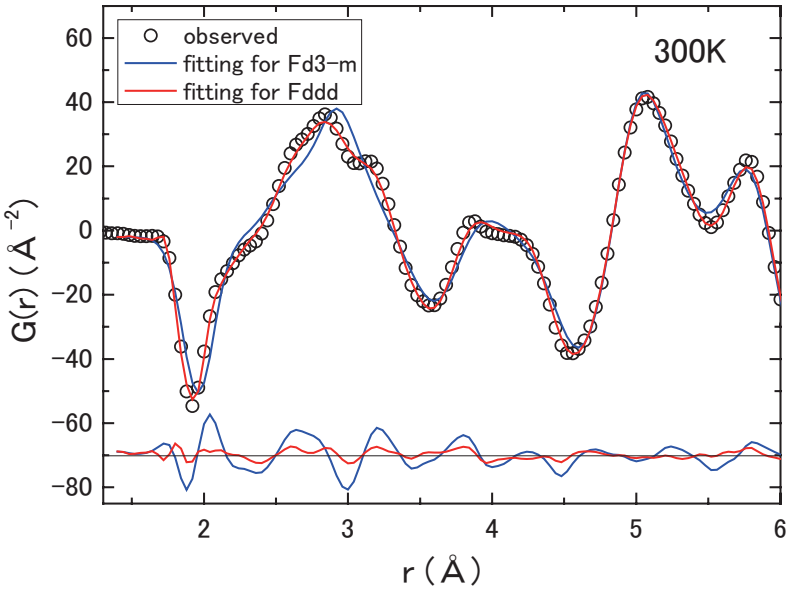

Figure 1. Atomic pair distribution function (PDF) of $^7LiMn_2O_4$ obtained at room temperature (open circle). The blue and red lines show the fittings for cubic and orthorhombic structures with space groups of Fd3-m and Fddd, respectively. The lines at the lower position show the differences between observed data and fitting results.

the region of 1.4 < r <10 Å is 15.4%, indicates that the fitting is not satisfactory.

Then we used the orthorhombic structure with space group of Fddd corresponding with the crystal structure in the charge ordered phase. The fitting result by using the orthorhombic structure model is shown in the figure by a red line. In this structure, five and nine inequivalent Mn and O atoms are contained in the unit cell, respectively. Because the atomic distances of 27 kinds of Mn-O bonds distribute from about 1.82 to 2.23 Å, the shape of the first negative peak can be reproduced. At the same time, the calculated O-O correlation peak can also reproduce the complicated peak structure around 2.8 Å. As a result, the fitting is improved and the R_{wp} value is 6.94%, much smaller than the R_{wp} obtained from the cubic structure. The Mn-O distances averaged in the MnO_6 octahedra, which are determined by the present fitting, correspond with the distances determined by the Rietveld analysis of the orthorhombic phase (charge ordered phase). These results indicate that in the cubic phase, although the valence electrons are localized at a Mn site similar to the charge ordered state, the arrangement of the localized electrons has only a short range periodicity.

References

[1] Rodriguez-Caravajal, G. Rousse, C. Masquelier, and M. Hervieu, Phys. Rev. Lett. **81** (1998) 4660.

[2] J. Sugiyama, T. Atsumi, A. Koiwai, T. Sasaki, T. Hioki, S. Noda, and N. Kamegashira, J. Phys. : Condens. Matter **9** (1997) 1729.

K. Kodama[1], N. Igawa[1], S. Shamoto[1], K. Ikeda[2], H. Oshita[2,3], N. Kaneko[2,3], T. Otomo[2,3], and K. Suzuya[3]

[1]Quantum Beam Science Directorate, JAEA; [2]Institute of Materials Structure Science, KEK; [3]Neutron Science Section, Materials and Life Science Division, J-PARC Center

2D Neutron Diffraction Imaging on an Ammonite

1. Introduction

Neutron radiography is a popular method to observe a material structure by neutron transmission contrast [1]. Neutron phase imaging can be a very sensitive method due to the refractive index contrast of a material [2,3]. Polarized neutron imaging enables us to observe the distribution of magnetic flux or magnetization of a material [4]. Neutron diffraction measurement is also a very powerful tool to observe crystal structure, lattice strain, phase ratio in a mixed sample, and so on. Its imaging can be a powerful tool to observe crystal structure distribution in a material. Energy-dispersive Bragg-edge imaging is one of the neutron diffraction imaging methods [1]. Another one is the simple neutron diffraction imaging. As for x-ray diffraction imaging, heterogeneous materials were studied in a voxel size of $2.3 \times 2.3 \times 1.6\ \mu m^3$ [5]. This small volume is achieved due to high intensity x-ray beam at synchrotron radiation facility (ESRF). Compared to the synchrotron x-ray beam, the neutron beam is still much weaker, but it has high transmission capability. In addition, the diffraction intensity of the highest intensity total diffractometer NOVA (BL-21) at the Materials and Life Science Facility (MLF) in J-PARC increases year by year [6]. We checked the feasibility of the 2-dimensional (2D) diffraction imaging at NOVA by measuring an ammonite.

2. Results and Discussion

A measured ammonite, which originated from China, is shown in Fig. 1(a). Figure 1(b) shows a calcite (1 0 4) peak image of the ammonite, which shows small air chambers divided by several yellow septa in the spiral shell. The white suture lines in Fig. 1(a) seem to correspond to the septa, which are weakly convex toward the inner shell side. This type of convex feature is observed as a relatively rare case for the ammonites [7]. The light blue diagonal line in the left upper part of the shell can be attributed to an adhesive mark, suggesting that broken pieces from one fossil were bonded by adhesive glue.

Figure 1(c) shows a siderite (1 1 3) peak image of the ammonite. The bright greenish region is limited to the last outer whorls. In addition, it has a uniform distribution without any septa. This part corresponds to a grayish part in Fig. 1(a). No air chamber in this part suggests that it is a body chamber, where the molluscous part of ammonite may remain. Therefore, the original molluscous part may consist of Mg and Fe rich chemical composition.

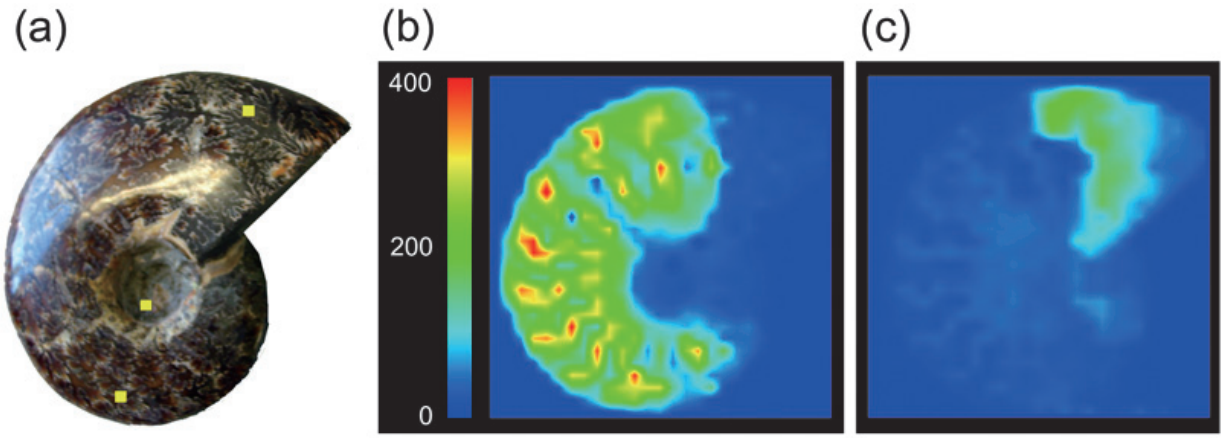

Figure 1. (a) Measured ammonite. (b) Calcite image in the *d*-range from 3.00 to 3.10 **Å**. (c) Siderite image in the *d*-range from 2.10 to 2.20 **Å**. Intensity color bar is a common for both (b) and (c).

3. Conclusion

In our study, the 2D neutron diffraction imaging of an ammonite revealed rich structural information about the fossil. This neutron diffraction imaging method extends the research possibilities on various materials such as fossils from structural point of view.

References

[1] "Neutron Imaging and Applications: A Reference for the Imaging Community" (Springer, 2009): Ian S. Anderson, Robert L. McGreevy and Hassina Z. Bilheux.

[2] W. Treimer, M. Strobl, A. Hilger, C. Seifert and U. Feye-Treimer, Appl. Phys. Lett. **83** (2003) 398.

[3] M. Strobl, W. Treimer and A. Hilger, Appl. Phys. Lett. **85** (2004) 488.

[4] N. Kardjilov, I. Manke, M. Strobl, A. Hilger, W. Treimer, M. Meissner, T. Krist and J. Banhart, Nature Phys. **4** (2008) 399.

[5] P. Bleuet, E. Welcomme, E. Dooryhee, J. Susini, J.-L. Hodeau and P. Walter, Nature Mat. **7** (2008) 468.

[6] H. Ohshita, T. Otomo, S. Uno, K. Ikeda, T. Uchida, N. Kaneko, T. Koike, M. Shoji, K. Suzuya, T. Seya and M. Tsubota, Nucl. Instrum. Methods Phys. Res. Sect. A **672** (2012) 75.

[7] A. E. Igolnikov, Paleontol. J., **41**(2) (2007) 128.

S. Shamoto[1], K. Kodama[1], T. Imaki[2], T. Nakatani[3], H. Oshita[3,4], N. Kaneko[3,4], K. Masuko[2], K. Sakamoto[2], K. Yamaguchi[1], K. Suzuya[3], and T. Otomo[3,4]

[1]Materials Science Research Division, Quantum Beam Science Directorate, JAEA; [2]Information Technology System's Management and Operating Office, Center for Computational Science & e-Systems; [3]Neutron Science Section, Materials and Life Science Division, J-PARC Center; [4]Institute of Materials Structure Science, KEK

New Electronics Board for GEM Detector System (nGEM)

In preparation for the increment of the J-PARC beam power, we have developed a new electronics board for a Gas Electron Multiplier (GEM) [1] detector system (nGEM). The outline view of nGEM is shown in figure 1.

nGEM is a two-dimensional neutron detector, based on a GEM, which has a high counting capability, and is also an upgraded system of an existing neutron beam monitor [2] at NOVA. nGEM's thermal neutron efficiency varies from 0.1% to 1% and is realized by exchanging an enriched-boron deposited aluminum cathode. nGEM has a compact body, including the electronics, and is able to transfer data directly to a PC via a network. Time-slice measurement is possible by using the T0 information from GATENET [3]. Compared to the existing neutron beam monitor's detector performance, the data transfer capability of nGEM is 10 times larger than that of the existing system. Since the repetition of the electronics was changed from 100 MHz to 200 MHz, the recorded minimum time step was reduced from 10 ns to 5 ns. Since we have refined the algorithm of the event selection in the onboard electronics, we expect to improve the high counting capability and the position resolution. The hit information, such as Time Of Flight (TOF), hit position and pulse width, is included in the data format of nGEM. The system information, such as the amount of data loss, is also included in the data format. A detailed analysis and monitoring of the system are possible by using those data. The basic characteristics of nGEM are summarized in table 1.

The neutron irradiation test was performed in May 2013 at the NOVA beam line. The nGEM was set up at the back of the NOVA vacuum chamber. The distance from the surface of the moderator to the detector was approximately 19 m. The proton beam power of J-PARC was typically 300 kW. In this test, TOF distributions and two-dimensional images were measured, and the plateau characteristics were evaluated. The TOF distribution has a shape similar to that of the existing neutron beam monitor. Two-

Table 1. The basic characteristics of nGEM.

Neutron efficiency	0.1%~1% for 1.8 Å
Data taking rate	Over 1 MHz
Position resolution	~0.85 mm(FWHM)
Operation voltage	2600 V
Sensitive area	100 mm × 100 mm
Detector size	524 mm × 254 mm × 50 mm

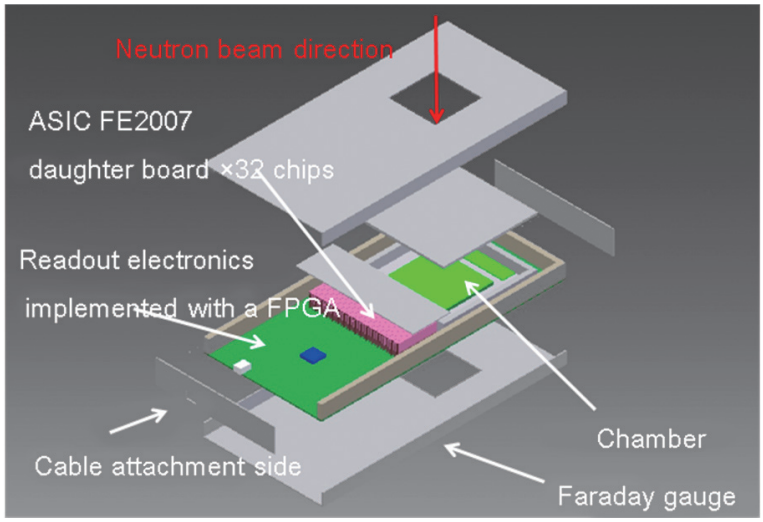

Figure 1. The outline view of nGEM.

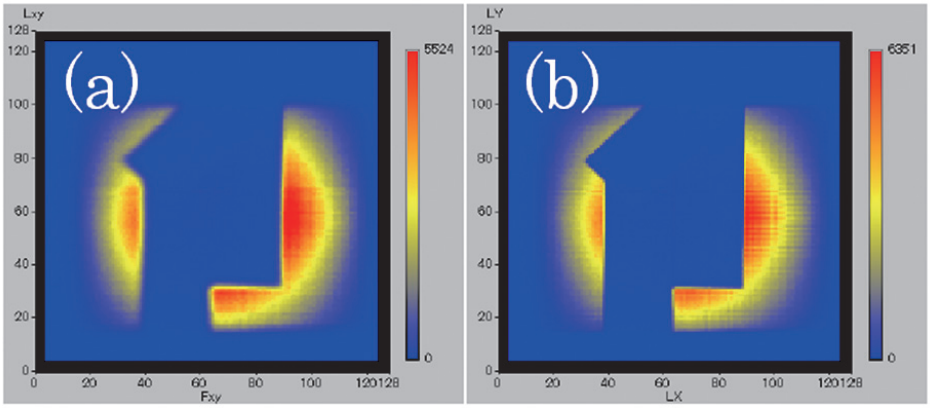

Figure 2. Two-dimensional images with sintered boron carbide blocks.

dimensional images in the case when sintered boron carbide blocks were set in front of the nGEM are shown in figure 2. The image obtained with the past event selection algorithm is shown in figure 2 (a), and the image obtained with the new event selection algorithm is shown in figure 2 (b). Since the new event selection algorithm is able to pick up a channel close to a neutron reaction position, the sharply-defined image is obtainable. The position resolution is evaluated by the edge analysis, and the full width at half maximum (FWHM) is estimated at approximately 0.85 mm. Therefore, nGEM has approximately 30% smaller position resolution than that of the existing neutron beam monitor. The plateau has appeared at input voltage from 2600 V to 2750 V, and the counting rate on the plateau was 1057.1±6.9 evnets/collision; where the counting rate was defined as a number of events per one collision of a proton beam with neutron target. The stable operation of nGEM is realized by setting the operation condition onto the plateau. Even though we confirmed that the data taking rate reached over 1 MHz in an offline test, we will verify the possibility of counting loss under the intense neutron environment of J-PARC. At this stage, four nGEMs have been prepared as an incident neutron beam monitor and a transmitted neutron beam monitor. We will install the nGEMs into NOVA and SPICA in the next spring.

References

[1] F. Sauli, Nucl. Instr. and Meth. A **386** (1997) 531.

[2] H. Ohshita, *et al.*, Nucl. Instr. and Meth. A **623** (2010) 126.

[3] S. Satoh, *et al.*, Development of a Trigger-Gate (GATENET) Module for Pulse Neutron Experiments, Presented at the TIPP 09.

H. Ohshita[1,2], M. Ishiwata[3], and K. Iwase[3]

[1]Neutron Science Section, Materials and Life Science Division, J-PARC Center; [2]Institute of Materials Structure Science, KEK; [3]Bee Beans Technologies Co. Ltd.

Diffusive Behavior of Garnet-type Compounds

A garnet-type oxide, $Li_{5+x}La_3Zr_xNb_{2-x}O_{12}$ with x = 0-2 (LLZONb) (Fig. 1), has been investigated as a solid electrolyte for an all solid-state Li-ion battery due to its high Li ion conductivity (σ_{Li}) [1, 2]. Interestingly, σ_{Li} was found to depend on x and reach a maximum at $x = 1.75$ at ambient temperature (T), for reasons currently unknown [3, 4]. However, considering the parameters to determine σ_{Li}, we could line up the following two candidates; namely, a diffusion coefficient of Li^+ (D_{Li}) and the number density of mobile Li^+ (n_{Li}). Unfortunately, it is difficult to measure n_{Li} directly, while there are three microscopic techniques to measure intrinsic D_{Li} in solids [5, 6, 7], that is, a Li-NMR, quasielastic neutron scattering (QENS), and μ^+SR technique. Here, we report the result obtained by μ^+SR and compare it with that obtained by QENS [8, 9].

The μSR spectra obtained in zero field (ZF) were well fitted by a combination of a dynamic Gaussian Kubo-Toyabe (KT) function due to a fluctuating nuclear magnetic field and time-independent offset. Figure 2 shows the T dependencies of Δ and ν for the samples with $x = 0$, 1, 1.75, and 2. The $\Delta(T)$ curve for each sample exhibits a steplike decrease around 300 K with a wide transition width ($\Delta T \sim 150$ K). At the same T range, ν increases with T and reaches a maximum around 350 K. These behaviors are reasonably explained by motional narrowing due to Li diffusion, as in the case for $Li_{5+x}La_3Hf_xTa_{2-x}O_{12}$ observed by Li-NMR above 260 K [10]. However, at T above 350 K, the μ^+SR spectra showed a simple exponential relaxation, because $\nu >> \Delta$, indicating that Li^+ ions diffuse too fast to be visible by μ^+SR.

If we assume a thermal activation process for Li diffusion, we could estimate the activation energy (E_a) in LLZONb from the $\nu(T)$ curve. Figure 3 shows the x dependence of E_a estimated by μ^+SR ($E_a^{\mu SR}$) and QENS [9] together with that determined by AC impedance measurements (E_a^{AC}) [3]. It has been found that $E_a^{\mu SR}$ is comparable to E_a^{QENS}, as expected, but both values are almost a half of E_a^{AC}. A very similar discrepancy between E_a obtained by

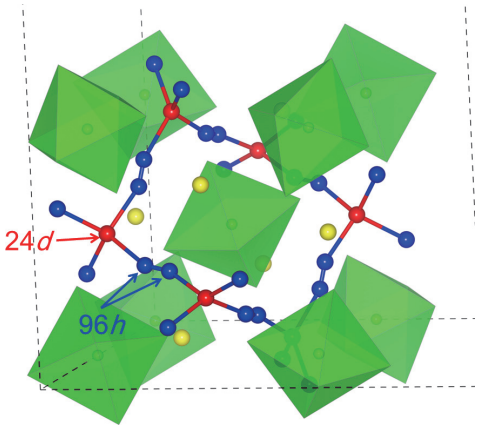

Figure 1. The crystal structure of garnet-type $Li_{5+x}La_3Zr_xNb_{2-x}O_{12}$. There are two Li-sites, namely, 24*d* and 96*h*, in the lattice.

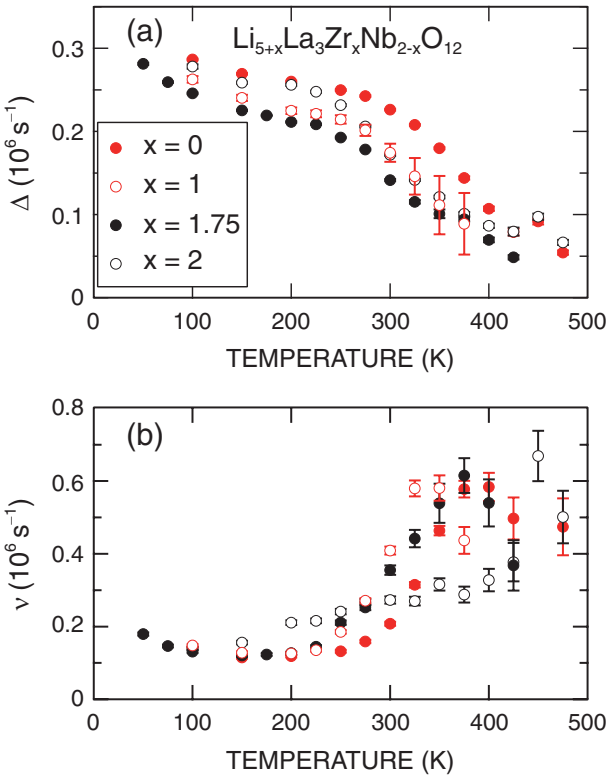

Figure 2. Temperature dependencies of (a) the Δ and (b) the ν obtained by fitting the μ^+SR spectra using a combination between a dynamic Kubo-Toyabe signal and a time-independent offset signal.

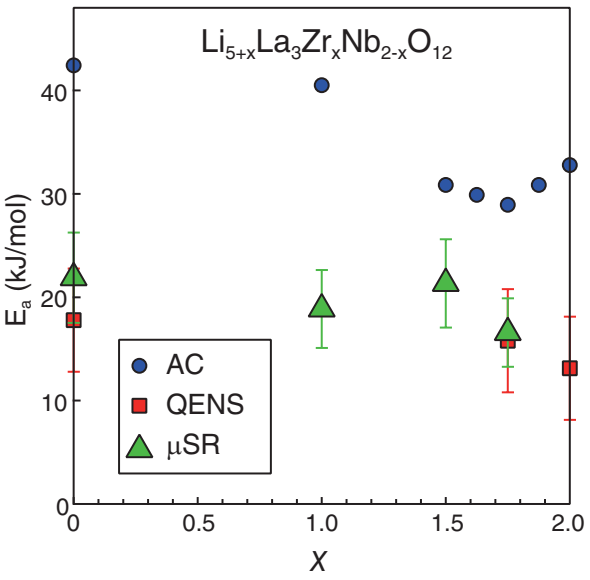

Figure 3. The relationship between the thermal activation energy (E_a) and x for LLZONb. Triangles and squares represent E_a estimated by μ^+SR and QENS [9]. Circles represent E_a determined by AC impedance measurements [3].

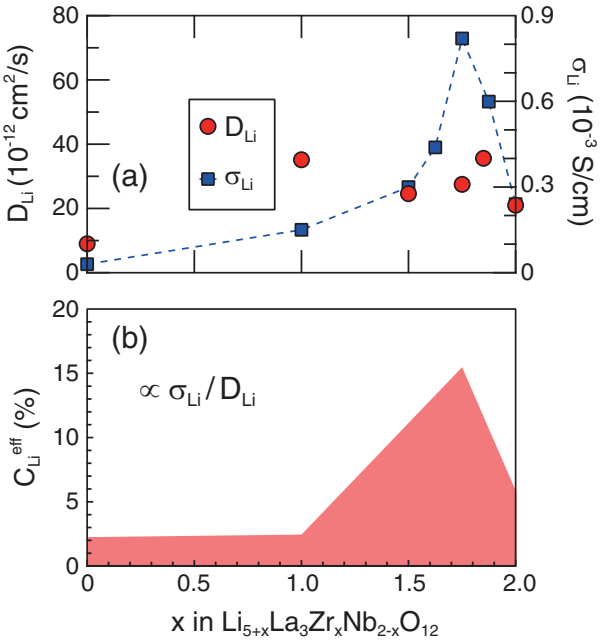

Figure 4. x dependences of (a) D_{Li} obtained by μSR and σ_{Li} by ac impedance measurements and (b) the number of mobile Li^+ per unit cell [9].

NMR and AC impedance is also reported for several materials [5]. This suggests that the overall diffusion of Li^+ is not determined by an intrinsic nature of LLZONb but by other factors, such as, grain boundaries, impurities, and defects. In other words, E_a^{AC} would be reduced by improving the sample preparation process.

The field fluctuation rate (ν) is thought to correspond to the jump rate of Li^+ ions between the neighboring sites, as in the case for Li_xCoO_2 [6]. A self-diffusion coefficient of Li^+ (D_{Li}) is, therefore, given by

$$D_{Li} = \sum_{i=1}^{n} \frac{1}{N_i} Z_{v,i} s_i^2 \nu, \qquad (1)$$

where N_i is the number of Li sites in the i-th path, $Z_{v,i}$ is the vacancy fraction, s_i is jump distance, and ν is the field fluctuation rate obtained by μ^+SR measurements. Structural analyses using a neutron diffraction technique suggest that $n = 3$, namely, from the 24*d* site to the neighboring four 96*h* sites, from the 96*h* site to the neighboring four 24*d* sites, and from the 96*h* site to the neighboring four 96*h* sites (see Fig. 1) [9]. Using these structural data, we can clarify the relationship between D_{Li} and x [see Fig. 4(a)]. Interestingly, D_{Li} is found to be almost independent of x, particularly $x \geq 1$.

Back to a Nernst-Einstein equation, σ_{Li} is connected with D_{Li} as;

$$D_{Li} = \frac{\sigma_{Li} RT}{n_{Li} F^2 Z^2}, \qquad (2)$$

where R is the gas constant, F is the Faraday's constant, z is ionic valence, and n_{Li} is the density of mobile Li^+ ions. Since LLZONb is an insulator in the whole x range prepared, we naturally assumed that only Li^+ is responsible for charge transport. Moreover, we introduced a number of mobile Li^+ per unit cell, $C_{Li}^{eff}[\equiv \frac{n_{Li}}{a^3(5+x)}]$, where a is the lattice constant of LLZONb. Figure 4(b) shows C_{Li}^{eff} as a function of x. The $C_{Li}^{eff}(x)$ curve is the same to the σ_{Li} curve, since D_{Li} is almost constant in this x range. Therefore, it has been clarified that σ_{Li} is mainly governed by the number of mobile Li^+ rather than D_{Li}. Also, it has been found that, even for LLZONb with $x = 1.75$ that exhibits the highest σ_{Li}, the percentage of the mobile Li^+ is only 15% among the whole Li in the lattice. This leads to the question about the origin of the mobile Li^+ ions. In order to respond to that question, we need to further clarify the relationship between C_{Li}^{eff} and x for other garnet systems.

References

[1] V. Thangadurai and W. Weppner, J. Am. Ceram. Soc. **88** (2005) 411.

[2] L. Truong, S. Narayanan, and V. Thangadurai, ECS Trans. **45** (2013) 21, and references cited therein.

[3] S. Ohta, T. Kobayashi, and T. Asaoka, J. Power Sources **196** (2011) 3342.

[4] S. Ohta *et al.*, J. Power Sources **202** (2012) 332.

[5] P. Heitjans and S. Indris, J. Phys.: Condens. Matter **15** (2003) R1257.

[6] J. Sugiyama *et al.*, Phy. Rev. Lett. **103** (2009) 147601.

[7] J. Sugiyama *et al.*, J. Phys. Soc. Jpn. **82** (2013) SA023.

[8] H. Nozaki *et al.*, J. Phys. Soc. Jpn. **82** (2013) SA004.

[9] H. Nozaki *et al.*, Solid State Ionics (2013), http://dx.doi.org/10.1016/j.ssi.2013.10.014

[10] A. Gupta *et al.*, J. Power Sources **209** (2012) 184.

H. Nozaki[1], M. Harada[1], S. Ohta[1], J. Sugiyama[1], and Y. Miyake[2,3]

[1]Toyota Central Research & Development Laboratories, Inc. (TCRDL); [2]Muon Science Section, Materials and Life Science Division, J-PARC Center; [3]Institute of Materials Structure Science, KEK

Development of a Non-destructive and Multi-elemental Analysis System by Muonic X-ray

An elemental composition analysis method utilizing muonic X-ray has several unique advantages compared with other analytical techniques. One of its most remarkable features is the ability to conduct non-destructive elemental analysis of the interior of a sample. The high energy of the muonic X-rays enables quantification of the amount of the elements embedded deeply in a sample where the ordinary X-ray fluorescence analysis and electron microprobe analysis are not applicable due to the attenuation by self-absorption of the electronic X-rays in the sample. Tuning the incident negative muon energy, the muon-stopping depth is controllable as far as a few centimeters from the sample surface to give the information at the stopping site. This fiscal year, while developing the muonic X-ray analysis method [1-3], we carried out an analysis of a Japanese gold coin. The coin is known to have been made of an alloy of 57% gold and 43% silver in weight. As a result of the special chemical technique called 'Iroage', within the thin layer within a few μm from the surface, we concluded that its gold content is significantly higher than that in the inside, reaching as high as 95% at the surface. Our previous studies, which showed that the Au contents were 74% and 56% at 1.6 μm and 14 μm from the surface, agreed quite well with the result obtained by the Auger spectroscopy combined with ion sputtering. One of the objectives of the project this year was to obtain and refine the depth profile of gold-to-silver ratio (Au/Ag) between 2 to 5 μm from the surface.

At the D2 area of the MUSE facility, two HP Ge detectors were employed to measure the muonic X-rays from the gold coin. The gold coin was placed in an aluminum vacuum chamber when the incident muon energy as low as being significantly scattered by the air and inducing unnecessary muonic X-ray signals arising from oxygen and nitrogen. The coin faced the muon beam and the detectors at an angle of 45°. The detectors were shielded with lead blocks in order to prevent the background radiations from the beam duct. The detector heads and the surface of the lead blocks facing the detectors were also covered with 1-mm thick Sn metal sheet to absorb the Pb electronic X-rays emitted from the lead blocks entering the detectors to cause significant background noise overlapping the muonic X-ray peaks in the energy region of interest. The signal processing system was coordinated with the pulsed muon beam at the MUSE to minimize the continuum background in the energy spectrum. By varying the incident muon energy from 7.5, 8.0 and 10.2 MeV/c muonic X-rays from the coin were measured. Three Au-Ag alloy samples of 30 mmϕ containing 50%, 60% and 80% Au in weight were also measured as reference standards.

Muonic X-ray signals detected within 1.5 μs from the muon pulse arrival were analyzed. The detection efficiency of the HP detectors was estimated from an EGS5 calculation. Figure 1 shows the muonic X-ray intensity ratio changes with the muon stopping depth in the coin. Au(5-4) denotes the muonic X-ray emitted during the negative muon transition from the orbital of principal quantum number 5 to the one of 4. At this stage the depth is assumed to be equal to the stopping range in pure Au estimated by the PHITS code. The middle three points at 2.1, 2.5 and 4.6 μm are the result of the present experiment. The Au/Ag profile resembles closely the one obtained by the Auger spectroscopy. The coin has a high Au content only within a few μm from the surface. The surface shows the highest Au content and the bulk body of the coin deeper

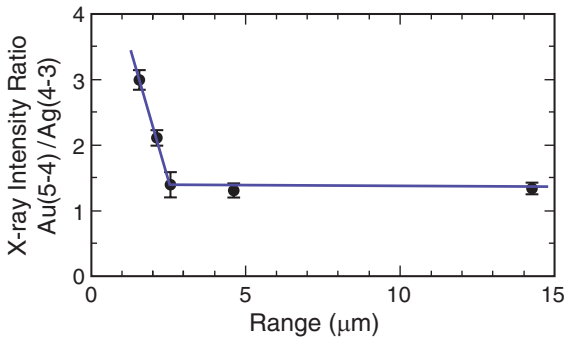

Figure 1. Muonic Au and Ag X-ray intensity ratio change with the muon stopping depth from the coin surface.

than 3 μm has a uniform chemical composition.

Our previous coin spectra have had peaks not assigned by muonic X-rays. A detailed analysis has revealed that these peaks originate from excited nuclei produced by muonic capture reactions. After transitions from the muonic atom orbitals of initial high principal quantum number to muonic 1s state, the negative muon stays in the 1s state. The proximity of the nucleus to the 1s orbital induces a negative muon capture by the nucleus similar to the electron capture decay process in neutron deficient unstable isotopes. The process competes with the muon natural decay. The average radius of the muonic 1s orbital shrinks with the change of the number of protons in the nucleus and the muon capture by nucleus is more likely to occur in the muonic atoms with more protons (high Z nuclei). The negative muon capture reaction leads to a highly excited nuclear state while emitting a muon neutrino. The highly energetic nucleus de-excites by emitting one or a few neutrons and γ-rays. One neutron emission reaction is the most probable de-excitation path [4]. The γ-rays emitted from the nucleus are available for nucleus-specific analysis.

Figure 2 exhibits the comparison of the two muonic X-ray and γ-ray spectra in the energy range from 290 keV to 450 keV of the coin for two initial muonic momenta, 6.4 MeV/c and 15.2 MeV/c. The two momenta correspond to the analysis depth of 2.2 μm and 14.6 μm from the coin surface, respectively. The two spectra are normalized and the μAg(4-3) X-ray peaks at 306 keV from muonic Ag have the same peak height. Other peaks are considered to originate from muonic Au and ^{196}Pt and ^{108}Pd. ^{196}Pt is a stable isotope produced via the ^{197}Au(μ$^-$,n)^{196}Pt reaction. Five γ-rays from the excited ^{196}Pt nucleus (denoted as ^{196}Pt*) are observed in the spectrum. Since Au has only one stable isotope ^{197}Au, the formation of ^{196}Pt by one neutron emission from the muonic Au is the most probable process as the fate of muonic Au. Natural Ag consists of ^{107}Ag (51.8%) and ^{109}Ag (48.2%). The 434 keV peak is assigned to a γ-ray

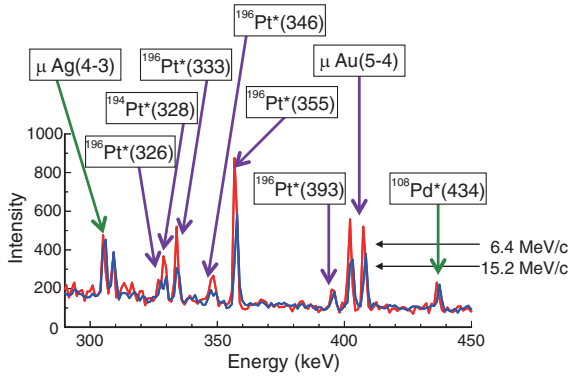

Figure 2. Comparison of energy spectra obtained with different initial negative muonic momenta.

from ^{108}Pd formed via the ^{109}Ag(μ$^-$,n)^{108}Pd reaction. The peak intensities of the 434 keV γ-ray are the same for both spectra because the peak originates from Ag and we normalized the spectra for the other muonic Ag X-ray peak at 306 keV. The other five γ-ray peaks and one muonic Au X-ray peak μAu(5-4), seen in Fig. 2, have higher intensities for the 6.4 keV spectrum results from the higher Au content near the coin surface. The intensity ratio of the 355 keV γ-ray from ^{196}Pt to the 434 keV γ-ray from ^{108}Pd showed similar change with the muon stopping depth as the muonic X-ray ratio. The measurements of γ-rays from excited nucleus after negative muon capture were studied extensively in the nuclear physics area, but the applicability to elemental analysis has not been examined thoroughly. Utilizing γ-ray would be promising not only for chemical composition analysis but also for isotope specific abundance determination of bulk materials without destruction.

References

[1] M. K. Kubo *et al.*, J. Radioanal. Nucl. Chem. **278** (2008) 777.

[2] K. Ninomiya *et al.*, J. Phys. Conf. Ser. **255** (2010) 012040.

[3] K. Ninomiya *et al.*, J. Chem. Soc. Jpn. **85** (2012) 228.

[4] D. F. Measday, Phys. Rep. **354** (2002) 243.

M. K. Kubo[1], K. Ninomiya[2], M. Inagaki[2], G. Yoshida[2], A. Shinohara[2], T. Nagatomo[3,4], N. Kawamura[3,4], P. Strasser[3,4], K. Shimomura[3,4], Y. Miyake[3,4], W. Higemoto[3,5], S. Sakamoto[5], and T. Saito[6]

[1]College of Liberal Arts, International Christian University; [2]Graduate School of Science, Osaka University; [3]Muon Science Section, Materials and Life Science Division, J-PARC Center; [4]Institute of Materials Structure Science, KEK; [5]Advanced Science Research Center, JAEA; [6]National Museum of Japanese History

μSR Study of Different Magnetic States in Electron-Doped $Pr_{1.3-x}La_{0.7}Ce_xCuO_{4+\delta}$ (x = 0.10) Single Crystals Depending on the δ Value

In the history of the research of high-T_c superconductivity, enormous efforts have been paid to the establishment of the phase diagram both of hole-doped and electron-doped cuprates. Formerly, Matsumoto *et al*. have reported that, through the appropriate reduction of excess oxygen from as-grown thin films of the electron-doped cuprate of $Nd_{2-x}Ce_xCuO_4$, superconductivity appears even in a parent compound of x = 0 and in a wide range of x, resulting in a completely different phase diagram from that formerly suggested [1]. If this is the case, the superconductivity in the electron-doped cuprates cannot be understood in terms of doping of carriers into Mott insulators as in the case of the hole-doped cuprates.

Very recently, we have grown high-quality single crystals of electron-doped $Pr_{1.3-x}La_{0.7}Ce_xCuO_{4+\delta}$ (PLCCO) in the underdoped regime of x = 0.10 [2]. Through the improved reduction annealing, we have succeeded in obtaining superconducting (SC) crystals of x = 0.10 which was believed to be non-SC [3]. From measurements of the *ab*-plane electrical resistivity in magnetic fields and *c*-axis resistivity in zero field, it has been found that, through the reduction annealing, the strongly localized state of carriers accompanied by the pseudogap due to the antiferromagnetic (AF) fluctuations in an as-grown non-SC crystal changes to a Kondo state without pseudogap in a SC crystal. These results can be understood in terms of a simple band model including the strong correlation of electrons [2].

In the magnetic point of view, on the other hand, it has not yet been clarified whether or not the AF spin fluctuations survive even in a SC crystal. From zero-field (ZF) μSR, we have formerly found possible slowing down of the Cu-spin fluctuations at low temperatures in SC polycrystals of $Pr_{1-x}LaCe_xCuO_4$ with x = 0.14 [4], although this is not so clear due to the presence of Pr^{3+} moments [5]. Therefore, we have performed ZF-μSR measurements using high-quality underdoped single crystals of PLCCO with x = 0.10 at J-PARC MUSE in February, 2013, in order to investigate the magnetic states depending on the amount of excess oxygen δ.

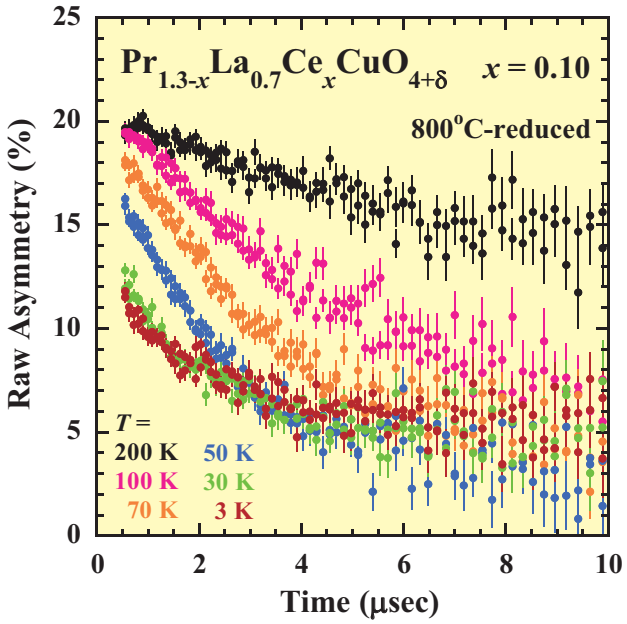

Figure 1. Zero-field μSR spectra of the 800°C-reduced SC single crystals of $Pr_{1.3-x}La_{0.7}Ce_xCuO_{4+\delta}$ with x = 0.10.

For as-grown crystals, the muon-spin precession was observed around 3 K due to the formation of a long-range AF order. Figure 1 shows ZF-μSR spectra of the 800°C-reduced SC crystals with T_c ~ 27 K. It is found that, while the spectrum shows Gaussian-like depolarization due to randomly oriented nuclear spins at 200 K, the depolarization of muon spins becomes fast gradually with decreasing temperature below 200 K. At 3 K, the spectrum consists of fast depolarization below ~ 1 μs, slow depolarization between ~ 1 μs and ~ 4 μs and almost flat spectrum above ~ 4 μs. This peculiar behavior of the spectrum at 3 K suggests the coexistence of a slowly fluctuating region of Cu spins and a region of a short-range magnetic order in a crystal. Therefore, it is concluded that there exist the AF spin fluctuations even in the SC crystals of $x = 0.10$, which is consistent with our simple band model including the strong correlation of electrons [2].

References

[1] O. Matsumoto *et al*., Physica C **469** (2009) 924.

[2] T. Adachi *et al*., J. Phys. Soc. Jpn. **82** (2013) 063713.

[3] X. F. Sun *et al*., Phys. Rev. Lett. **92** (2004) 047001.

[4] Risdiana *et al*., Phys. Rev. B **82** (2010) 014506.

[5] R. Kadono *et al*., J. Phys. Soc. Jpn. **72** (2003) 2955.

T. Adachi[1], A. Takahashi[2], K. M. Suzuki[2], M. A. Baqiya[2], I. Watanabe[3], A. Koda[4,5], M. Miyazaki[4,5], R. Kadono[4,5], and Y. Koike[2]

[1]Department of Engineering and Applied Sciences, Sophia University; [2]Department of Applied Physics, Tohoku University; [3]Advanced Meson Science Laboratory, RIKEN Nishina Center; [4]Muon Science Section, Materials and Life Science Division, J-PARC Center; [5]Institute of Materials Structure Science, KEK

Neutron Source

Beam Commissioning in MLF for High Power Operation for JSNS and MUSE

Last year, the beam power increased to 200 kW by watching precious beam status after the earthquake. After installation of the helium bubbler in the mercury target, a high power beam operation matching a target replacing schedule is available. With the increase of the beam power, the proton beam should be carefully tuned because the high power beam can cause serious damage to the beam components such as the magnet and the vacuum chamber.

In the MLF, the cascade target scheme is chosen for the muon and neutron production in a way that requires a careful tuning between the targets. During the summer of 2011, relatively high radioactivity was observed in the beam monitor located at the downstream of the muon production target. The radiation dose at the beam profile monitor of M23 was at a level of 15 mSv/h as shown in Fig. 1, which was ~10 times larger than the calculated design value. Around the M23, quadrupole and stirring magnets are located, whose coils are made of a low radiation hardening materials such as polyimide insulator. It is important to control the beam loss around the M23 monitor.

In order to understand the reason for the activation, an additional beam loss monitor of the plastic scintillator was placed above the M23 monitor. The result from the beam loss monitor showed that the high activation at the M23 was produced by the beam loss due to interaction at the muon production target. By changing the beam size at the muon target, we observed that the beam loss quantity increased as decreasing of the beam size at the muon target.

Because of the muon target maintenance scenario, the muon production target was required to be used till the summer of 2013. In order to reduce the damage to the target, the beam size was normally expanded at the target. However, when the beam size expands at the muon target, the quantity of the beam loss increases between the muon and neutron targets. We developed a new technique to satisfy both requirements for the reduction of the damage and the beam loss. At the muon target, the beam orbit was bumped as shown in Fig. 2. The beam was conserved at a narrow width so that the beam loss could be kept smaller. Because of the bump, the quantity of the beam loss did not increase drastically. By the periodical rotation of the beam bump position at the muon target shown in Fig. 3, the damage on the muon target can be decreased. The present technique is called EXILE, which is a

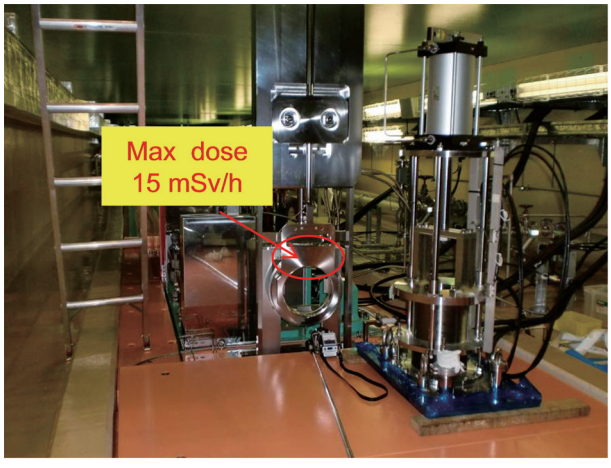

Figure 1. High radiation dose observed at the beam profile monitor of M23.

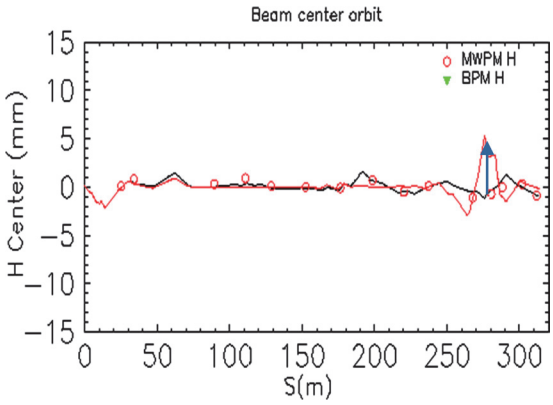

Figure 2. Beam position observed monitors along the beam transport line. Beam bump orbit was made at the muon production target.

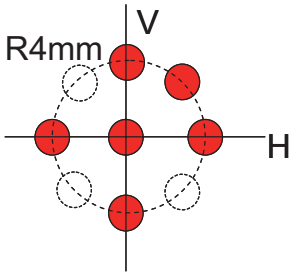

Figure 3. Schematic of the beam rotation scheme at the muon target (called EXILE).

famous dance group, because the scheme is similar to their famous spiral sequence dance. Because of the EXILE, the muon target can stand up for the 0.3 MW beam operation till the summer of 2013 as scheduled.

For the demonstration of the accelerator performance, we succeeded to deliver a high power beam such as 0.5 MW to the spallation neutron source. The intensity of the proton beam was 20 kJ/pulse, which exceeds the intensity in SNS at ORNL.

For a steady beam operation, an automatic beam collection system was developed in the beam transport system. Due to the leakage of the magnetic field of the solenoid magnet at a new muon beam line of the H line, whose current is often changed for muon

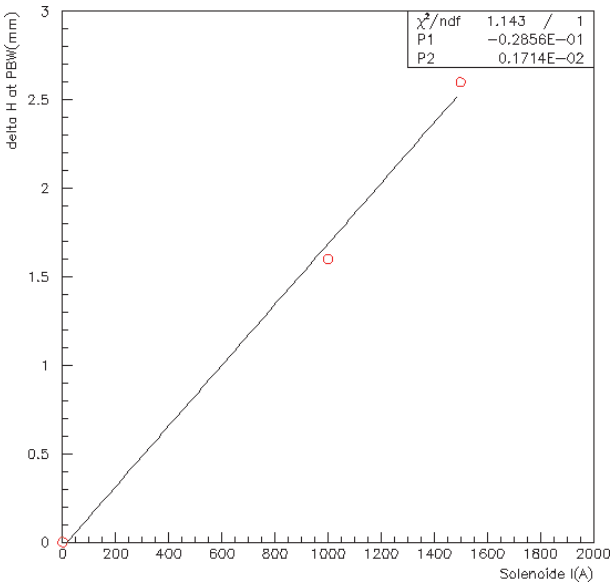

Figure 4. Dependence of the current of the solenoid magnet at H line on the vertical beam position at the proton beam windows.

users, the beam position at the neutron target was changed in the vertical direction as shown in Fig. 4. We developed an automatically controlled beam position compensation system based on the EPICS. By watching the current of the solenoid magnet, the angle of the vertical steering magnet was corrected. Due to the present system, the beam position at the mercury target became more stable.

S. Meigo[1], M. Ooi[1], K. Ikezaki[1], A. Akutsu[1], and H. Fujimori[2,3]

[1]Neutron Source Section, Materials and Life Science Division, J-PARC Center; [2]Muon Science Section, Materials and Life Science Division, J-PARC Center; [3]Institute of Materials Structure Science, KEK

New Mercury Target Vessel with Advanced Design

1. Introduction

The excellent effect of the microbubble injection into mercury to mitigate the pressure waves was demonstrated by the on-beam operation as shown in the previous topics of this report.

As a next step to secure further the target vessel against the pressure waves, we developed a target vessel with a double walled beam window. This structure aims to increase the mercury flow velocity passing across the beam window where it is most severely attacked by the cavitation damage. The effect of mercury flow on the cavitation damage mitigation has been investigated and confirmed both in off-beam tests [1] and in on-beam tests [2]. Moreover, the effect of the double wall to mitigate the cavitation damage was demonstrated in the actual spallation neutron source facility of SNS. Based on these results, we modified the design of the JSNS target to make the double-walled beam window structure, and the fabrication of the new target was completed.

The storage space of the used target vessels is also a serious concern for the long term facility operation, because the storage space capable of handling highly radioactive components is very limited in J-PARC. In order to reduce the volume of used targets, we developed the separate-type target which can be separated into two parts, i.e. the front part and the rear part. This structure allows us to replace only the front part which has much shorter lifetime than the rear part. This new structure was also applied to the design of the new target.

2. Target design with double walled beam window

The effect of the narrow channel to mitigate cavitation damages was investigated experimentally. Figure 1 shows the experimental set-up and one example of the results. Two stainless steel plates were placed face to face closely in stagnant mercury, and impulse forces were applied to the mercury simulating the pressure wave generated by the mechanical striker. The experimental result shows the case of a 1 mm gap between the plates. There is clearly less damage on the narrow channel side than on the bulk side. This indicates that the structure of the narrow channel itself has the effect to mitigate the cavitation damage in addition to the mercury flow effect.

Figure 2 shows the inner structure of the double walled target. A part of the mercury flow is led into the narrow channel at the inlet of the bubbler, and the mercury flow velocity in the narrow channel at

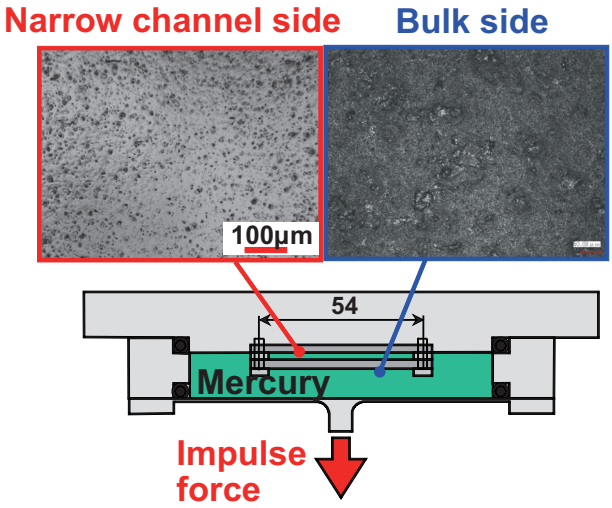

Figure 1. Experiment to investigate the narrow channel effect to mitigate the cavitation damages.

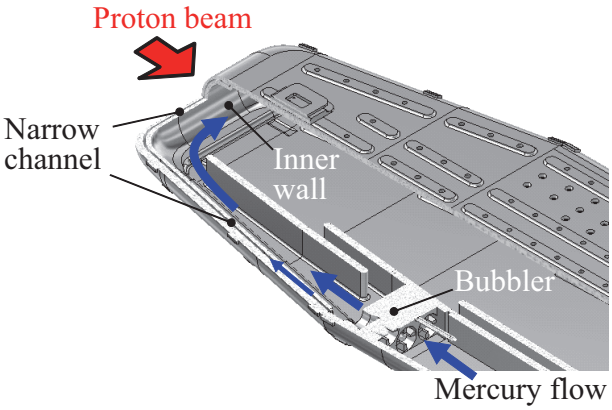

Figure 2. Inner structure of the double walled target.

the beam window is estimated to be almost 4 m/s. The bulk flow side of the inner wall is protected by the micro-bubbling. This structure increased the cooling performance of the inner wall and allowed us to increase the thickness of the inner wall from 3 mm to 5 mm, which increased the safety margin against the cavitation damage. The fabrication of the target was completed and it is ready to be installed during the summer shutdown period in 2013.

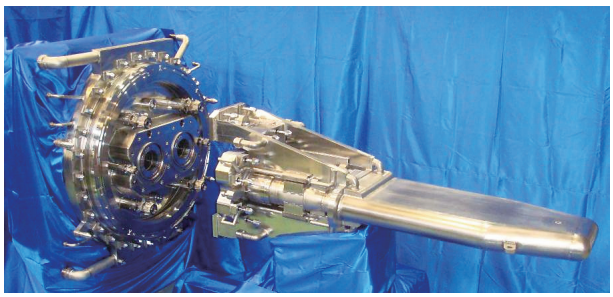

Figure 3. Separate type target vessel with double walled beam window.

3. Separate-type target design

The key technology to realize the separate-type target is keeping seal performance of the complex flange where the front body is detached from the rear body. The complex flange connects all over the three lines of piping, which are two lines of thick mercury piping with diameter of 150 mm and 1 line of thin helium piping with diameter of 10 mm, with a single flange. Thermal hydraulic analyses showed that the temperature difference in the complex flange becomes 80°C at maximum, which causes thermal deformation and deterioration of the seal performance. In order to cope with this issue, we carried out numerical simulations and mock-up tests to cool down the flange effectively using the water flow channel in it. As a result, we could realize the complex flange, which can keep the seal performance even after 1000 cycles of the temperature rising and dropping. The separate-type target vessel was fabricated as shown in Figure 3, and this design was also applied to the fabrication of the double walled target.

References

[1] T. Naoe, M. Ida, M. Futakawa, Nucl. Instr. and Meth. **A 586** (2008) 382.

[2] B. Reimer, J Haines, M. Wendel, G. Bauer, M. Futakawa, S. Hasegawa, H. Kogawa, J. Nucl. Mater. **377** (2008) 162.

K. Haga, T. Wakui, T. Naoe, H. Kogawa, K. Hanano, and M. Futakawa

Neutron Source Section, Materials and Life Science Division, J-PARC Center

Cryogenic Hydrogen System

Introduction

The J-PARC cryogenic hydrogen system provides cryogenic hydrogen at supercritical pressure of 1.5 MPa, whose para-hydrogen concentration is more than “99%” and temperature is less than 20 K, to three moderators so as to provide cold pulsed neutron beams of a higher neutronic performance. This report describes the topics of the cryogenic hydrogen system in JFY2012.

Attainment of stable prolonged operation

It had been difficult to conduct prolonged stable operation of the helium refrigerator due to performance degradation of the heat exchanger, which was caused by adsorption of impurity (mainly moisture) on it. The moisture was adsorbed on an activated charcoal located downstream of the compressor and gradually penetrated to the purified helium stream in the cryogenic operation. In JFY2011, a purification system had been installed. The activated charcoal had been regenerated by flowing heated nitrogen gas (around 373 K) through it. A purification operation was carried out to reduce the dew point below –80°C and nitrogen below 1 ppm during the week before every operation. Accordingly, there was little increase of the pressure difference through the heat exchanger (See Fig.1). We have achieved a three-month prolonged stable operation.

Operational characteristics

An ortho-para hydrogen convertor, which has the catalyst packed-bed volume of 35 L and is filled with a catalyst of hydrous ferric oxide with the porosity of 32%, has been installed to maintain para-hydrogen concentration of more than “99%”. The concentrations of the para-hydrogen in the hydrogen loop were measured at the temperatures of 95 K, 46 K and 20 K during the cool-down process (See Fig.2). It was confirmed that the equilibrium para-hydrogen concentration always existed and the para-hydrogen concentration was maintained more than “99.0%” at the rated condition.

The hydrogen loop is applied to a stepwise huge heat load, which is 3.75 kW for a 1-MW proton beam operation, caused by the proton beam injection. A heater and an accumulator are prepared to mitigate a pressure fluctuation below 0.1 MPa caused by the proton beam injection and stop and always maintain the feed hydrogen temperature constant.

A stable 300-kW proton beam operation, where the nuclear heating was 1.13 kW, has been con-

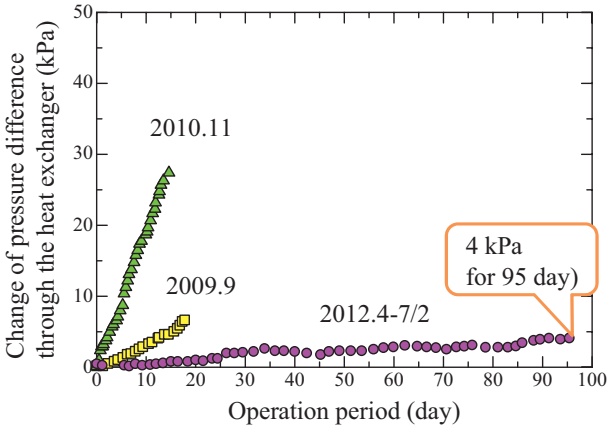

Figure 1. Change of pressure difference through the heat exchanger.

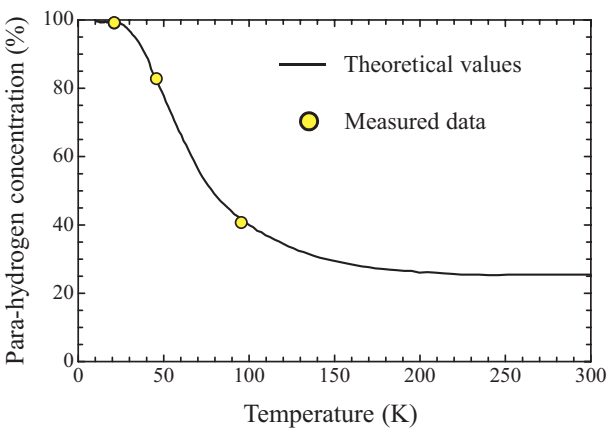

Figure 2. Para-hydrogen concentration during the cool-down process.

ducted since November 2012. It was possible to mitigate the pressure fluctuation caused by the proton beam injection and stop. The feed hydrogen temperature remained unchanged. The 300-kW proton beam operation has been successfully carried out on schedule.

For the first time, the 532-kW proton beam operation was conducted as a trial for the limited time of 40 s in November 2012. A temperature rise of 1.3 K appeared at the outlet of the moderators. The pressure fluctuation was mitigated to the predicted level of 44 kPa. The feed hydrogen temperature was always maintained constant, although it temporarily increased by 0.08 K. It would appear that the stable operation of the cryogenic hydrogen system would be also achieved for the 1-MW proton beam operation based on these results.

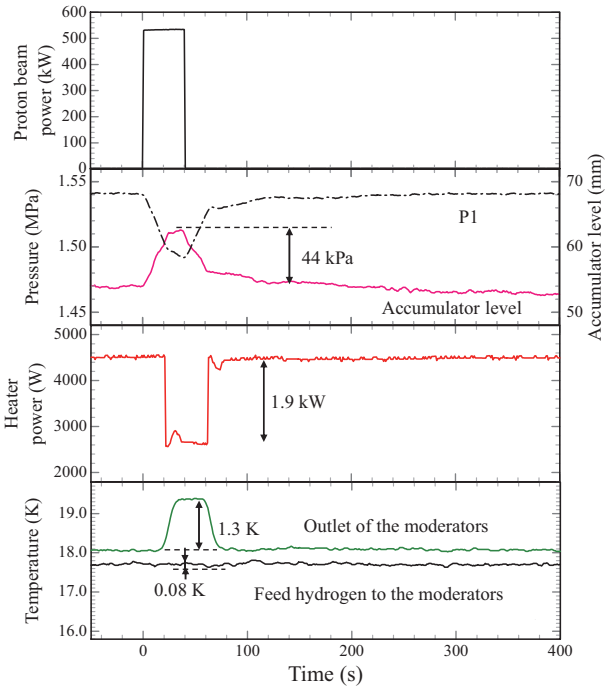

Figure 3. Dynamic behaviors for a 532-kW proton beam operation.

R&D for the welding bellows for the 3rd accumulator

In February 2010, a trouble of the 1st accumulator, which was due to a poor weld in its manufacturing process, was found before the cool-down operation. We have tentatively operated it using the 2nd accumulator, although it has a pressure tightness of 0.9 MPa lower than the required one of 2.0 MPa. The R&D for the welding bellows with the high pressure tightness had been carried out in order to conduct the robust and the stable operation for the proton beam power of 1 MW. A prototype was manufactured and a live test performed. It was confirmed that the developed bellows met the required lifetime of 10,000 cycles at a pressure of 2 MPa. The 3rd accumulator has been designed and we plan to install it in the summer of 2013.

H. Tatsumoto, T. Aso, K. Ohtsu, T. Uehara, Y. Kawakami, and S. Hasegawa
Neutron Source Section, Materials and Life Science Division, J-PARC Center

1. Present states of the 2nd moderator and reflector

According to the proton beam operation schedule, the accumulated irradiation damage to the structural material of the moderator and the reflector, such as aluminum alloy (A6061), will reach the design value (20 DPA) in 2019. Therefore, to replace the moderator and the reflector in 2019, fabrication of a 2nd moderator and reflector will start in 2013. From the experience of the 1st moderator-reflector fabrication, several improvements are taken into account in the 2nd moderator-reflector design. Especially, it is notable that new materials, such as invar alloy and gold-indium-cadmium (Au-In-Cd) alloy, are adopted.

The invar alloy has one order of magnitude lower thermal expansion than aluminum alloy and stainless steel (SS316L). Therefore, the use of the invar alloy as cryogenic pipe material makes it possible to avoid the special fabrication, such as an asymmetrical setting at an elbow-shaped bend in the cryogenic pipe, which was required in the 1st moderator fabrication. However, the development of the invar conversion joints, such as invar-A6061 and invar- SS316L joints are required to utilize it in the cryogenic pipe. We evaluated the mechanical strength of invar-joints with the friction welding method (See Sec. 2).

For the 1st decoupled moderator, a silver-indium-cadmium (Ag-In-Cd) decoupler was developed in order to obtain neutron beam pulse with short tail. However, the Ag-In-Cd decoupler had the disadvantage of high residual radioactivity, such as ^{108m}Ag (half life of 418 years). A combination of Au, In and Cd was selected as the decoupler material, resulting in three orders of magnitude lower radioactivity than the Ag-In-Cd one without sacrificing the pulse characteristics. In order to utilize the Au-In-Cd decoupler, we needed to develop the alloying of Au-In-Cd and to make the bonding between Au-In-Cd and aluminum alloy (A5083) in terms of the heat removal and thermal stress. In the case of alloying of Au-In-Cd, we have already succeeded to make a homogeneous ternary Au-In-Cd alloy. In the next stage, a Hot Isostatic Pressing (HIP) technique is applied to obtain the bonding of the Au-In-Cd alloy to the A5083 (See Sec.3).

2. Examination of the invar joint[1]

For the 2nd moderator fabrication, the bonding strength of the invar joint to SS316L and A6061 was measured at two temperatures, room temperature and 77 K. Figure 1 shows the yield strengths of the invar joint with SS316L. From the results, it is clear that the yield strengths of the invar joint specimens are almost the same as those of the base materials. And it is also clear that the yield strength at low temperature is two times higher than that at room temperature. This result indicates that the invar joint has enough bonding strength as required in the 2nd moderator design. In addition, it is confirmed that the ductility of the invar specimens and their bonding ones at low temperature is higher than that at room temperature.

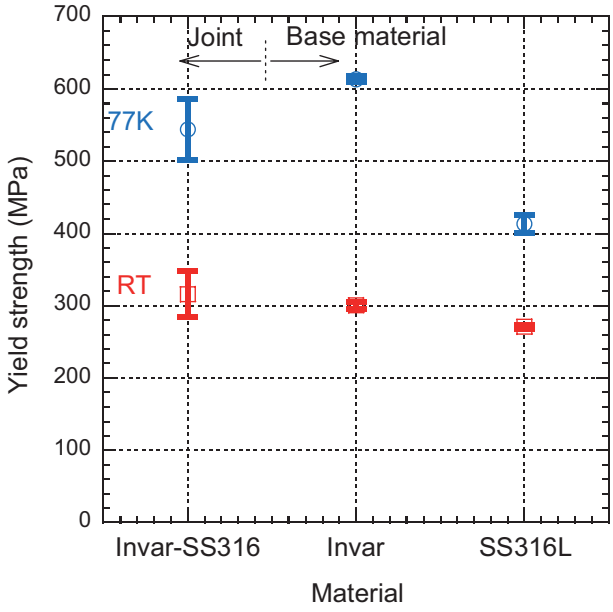

Figure 1. Measured yield strengths of joint specimens (Invar-SS316L) and base material ones (Invar and SS316L).

3. Development of an Au-In-Cd decoupler[2]

We performed a bonding test between Au-In-Cd alloy and aluminum alloy (A5083) by the HIP method. The conditions in the HIP test were: pressure of 100 MPa, holding time of 1 hour, and temperature of 490, 505, 520, 535 and 550°C. As a result, for the first time, we succeeded to bond the two alloys at above 520°C in the HIP temperature. Figure 2 shows cross sectional micrographs at the bonding region with material composition ratio measured by EDX at 535°C in the HIP temperature. Though, in the 520°C case, layers of Au_2Al alloy and Au_2Cd alloy are clearly separated in the diffusion layer, in the 535°C case, the two alloys make an intermetallic matrix in the diffusion layer as shown in the Fig. 2.

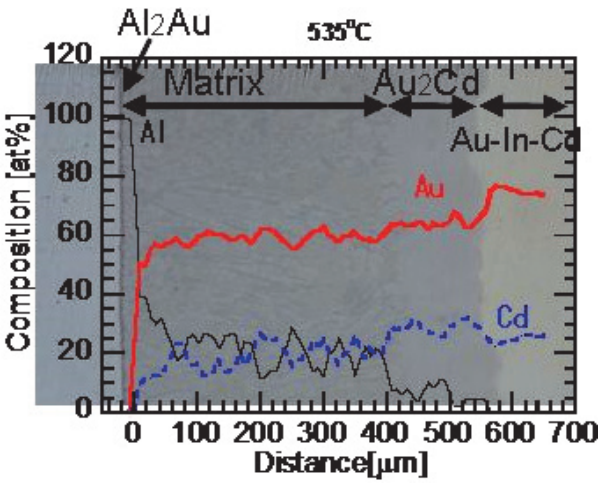

Figure 2. Cross sectional micrographs at the bonding region of the HIP specimen with composition ratio of Al, Au and Cd. The HIP temperature is 535°C.

Then we measured the tensile strength of the HIP specimens. The specimens at 520°C in the HIP temperature were fractured before the tensile test. At 535°C, the tensile strength of 95.2 MPa could be obtained. This value is three times higher than the required strength in the design (30 MPa).

As a result, we found that the intermetallic matrix appearing in the diffusion layer above 530°C in the HIP temperature worked to increase the bonding strength.

References

[1] M. Harada *et al.*, submitted to J. Nucl. Mat. (2013).

[2] M. Ooi *et al.*, submitted to J. Nucl. Mat. (2013).

M. Teshigawara, M. Harada, M. Ooi, and Y. Kasugai

Neutron Source Section, Materials and Life Science Division, J-PARC Center

Radiation Safety

1. Radiological License Update

The radiological license was updated for the following items:

(1) Increasing the proton beam intensity from 320 kW to 350 kW,

(2) Installation of the "U-line" which is a secondary-beam line with ultra-slow muons.

The proton bean intensity in the continuous beam operation to MLF target was increased from 200 kW to 300 kW in November 2012. In order to keep a sufficient margin for 300 kW operations, the proton beam intensity in the licensing was upgraded to 350 kW in advance.

2. Radiological Control of the Experimental Halls

The 1st and 2nd Experimental Halls meet the specifications for contaminated controlled areas in terms of airtightness and negative pressure control. However, at the beginning of our first beam operation in 2008, we determined that the Halls were controlled as "uncontaminated" areas to hold the access easiness such as the followings:

- Experimenters can enter the Halls without wearing special suits and shoes for radiological contamination,
- The contamination checks of their bodies and the items they bring out are not necessary when the experimenters leave the Halls.

On the other hand, there were some issues with the sample handling. Powder and liquid samples may contaminate floors and bodies, if spilled out after neutron irradiation. In order to avoid such kinds of "Radiological Accident", we made rules to handle samples according to the suggestions of the Radiation Safety Office in J-PARC. The rules state:

- Powder and liquid samples must be sealed tightly within metal containers,
- Activated samples must be handled in the "3rd preparation room".

The 3rd preparation room is designated as a contaminated area for handling activated samples. Recently, some experimenters complained about these rules. Practically, some experiments such as the neutron-reflectometry experiment, which was planned at BL16, could not be carried out at first because they needed to use some liquid samples without any enclosures. But, finally, that could be done by evaluating the induced radioactivity of the liquid sample and adjusting the experimental procedure along the rules. We are going to keep the uncontaminated areas as long as possible by considering practical and realistic approaches for each experiment.

Y. Kasugai, M. Ooi, and T. Kai
Neutron Source Section, Materials and Life Science Division, J-PARC Center

Cooling System for Neutron Source

1. Introduction

The cooling system for the neutron source is installed to remove the heat generated by the proton beam and the neutron irradiation. The cooling system is consists of three water systems for the neutron source, two water supply systems for experimental halls, air circulation system for shielding including the neutron shutters, secondary water system and supply and discharge system of gas and water [1].

The components of the cooling system have been maintained periodically to keep the performance and the safety of the neutron source.

The cooling water of the system is directly irradiated by protons and neutrons, and as a result, it will become radioactive. It is necessary to conduct the maintenance to prevent the wide spreading of radioactivity and reduce the radiation impact on the workers.

In this paper, It is shown that the radioactivity in the cooling water of the systems and maintenance for the components of the cooling system for the neutron source.

2. Radioactive Level of the Cooling System

There are three main water systems called 6551, 6552, and 6553 system for neutron source cooling. The 6551 system is connected to the safety hull and the reflector. The 6552 system is connected to the proton beam window (PBW) and three moderators. The 6553 system is connected to a target trolley and shielding in the helium vessel.

Figure 1 shows the tritium density in the cooling water systems from the beam start. And the amount of the proton beam irradiation in the neutron source is also shown in the figure. The tritium density has been increasing with the increase of the proton beam irradiation. There are some points of decreasing density, because the water in the system is exchanged almost completely for the maintenance. But the density decreased by one order through the whole water exchange.

Table 1. Tritium in Cooling Water.

	6551	6552	6553
Meas.	8.3E+04	2.4E+04	1.3E+04
Calc.	5.3E+04	4.6E+04	-

Bq/cm^3

Table 2. Radioactivity in Cooling Water.

	6551	6552	6553
Be7	1.4E+01	4.2E+00	4.8E+00
Na22	3.1E+01	1.6E+00	—
Mn54	4.0E-01	3.2E-02	1.6E-01
Co56	—	—	1.1E-02
Co57	—	—	2.2E-02
Co58	8.4E-02	—	—
Ta182	—	8.0E-02	—

Bq/cm^3

In Table 1, the tritium density in the three systems at Jul. 2013 is shown. In Table 1, the calculated estimation values are also shown. The tritium density in the systems is not so far from the calculated estimation.

In Table 2, the radioactive density in the water is shown. The amounts of Be7, Na22, and etc. increased with the proton beam irradiation.

3. Maintenance of Cooling System Components

The three water systems have two pumps each. The pumps have 100% spec. for the rated system flow rate. The pumps are operated alternately as A system and B system for each operating cycle. The facility operation is continued even in case of the pump trouble.

The pumps are canned pump and the performance is kept by the periodical maintenance including the overhaul with parts exchange.

The radioactive level of the water systems for the neutron source become high and the ordinary maintenance is not easy. Therefore, at the time of separation of the system and disassembly of the pump, the special suits, full-face mask and etc. are

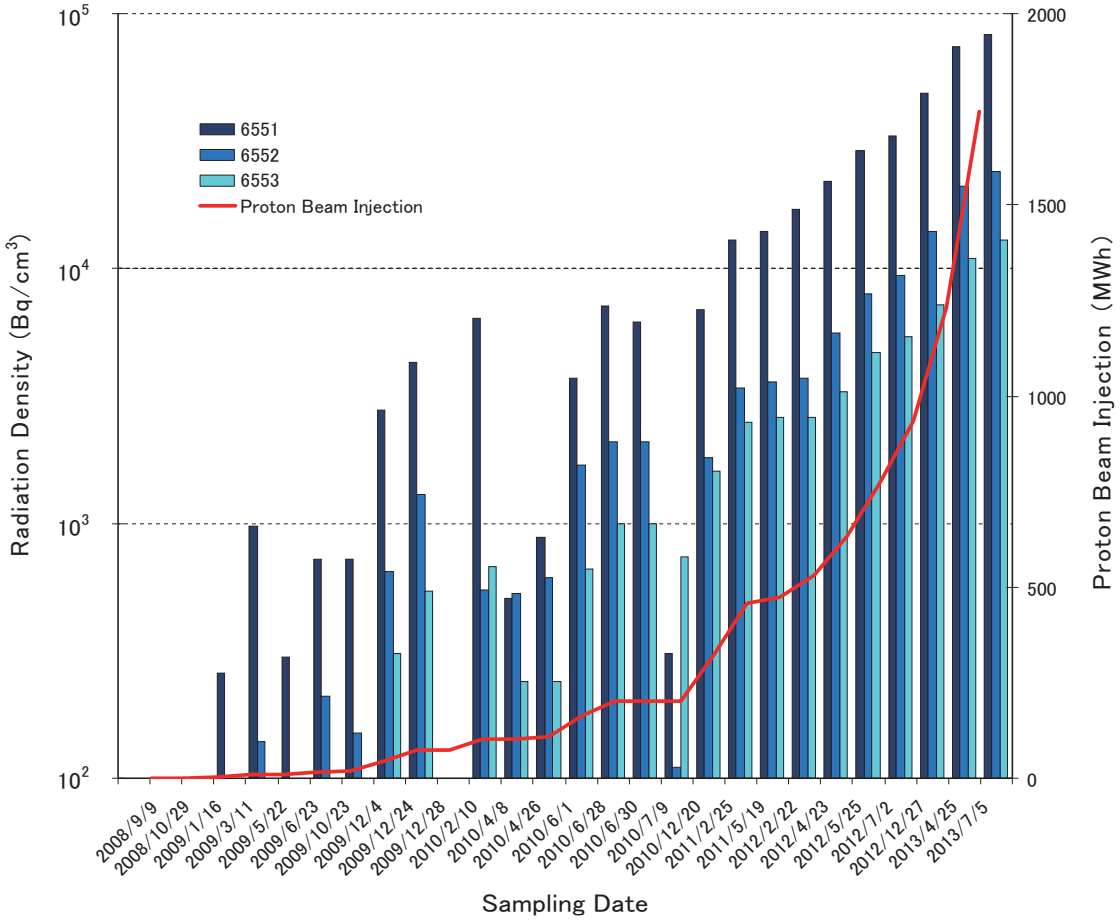

Figure 1. Tritium density in primary cooling water and amount of Proton beam irradiation.

equipped and a local exhaust and air tight house are set to prevent spreading pollution and irradiation. Furthermore, the maintenance work has been conducted while measuring the pollution degree of the components by smears. Therefore, the pollution level at the components area after pump maintenance has been kept very low and changes have not been confirmed. In the case of a future rise in the radioactivity concentration, airline suit and etc. will be used for the cooling system maintenance.

4. Summary

The radiation level in the cooling system was estimated to be increasing with the proton beam power rising. But the periodical maintenance will be needed to keep the facility's performance. Therefore, based on the radioactive protection method, the maintenance plan will be made to work with the appropriate protection. In the future, the cooling system will be kept safe and stable and managed to contribute to the smooth operation of the neutron source facility.

References

[1] Neutron Source Section, Material and Life Science Division, Technical Design Report of Spallation Neutron Source Facility in J-PARC, JAEA Tech., **2011-035** (2011) 417.

H. Kinoshita, M. Seki, T. Suzuki, H. Ueno, and S. Meigo
Neutron Source Section, Materials and Life Science Division, J-PARC Center

General Control System of MLF

1. Introduction

For supplying muon and neutron beams safely and efficiently, a General Control System (GCS) operates within the MLF; it consists of several subsystems of integral control and interlock, network, server, timing distribution systems, and a Personnel Protection System (PPS). It is the advanced and independent system that controls the target stations including a mercury target, neutron moderators with supercritical hydrogen, and so on. It administers the instruments and operating processes of the MLF in various operating states such as the proton beam irradiations and target maintenances. Although the GCS is an independent system, it works closely with the control systems of the accelerators and other facilities in J-PARC [1].

Figure 1 (A) shows the schematic structure of the current Monitor and Operation (MO) system of the GCS. It consists of Personal Computers (PC) and Programmable Logic Controllers (PLC) such as Administrative Control PCs (ACP), General Control Panels (GCP), and Local Control Panels (LCP) connected to the looped optical network systems, named MELSECNET-H (NET -H). The operations of various instruments in the MLF are executed from the ACPs and the PPS operating PCs placed in the MLF control room by operating the LCP of each instrument through the NET-H. Server systems such as a Data Storage (DS) server and a Web Distribution (WD) server, acquire various operation data through the NET-H, then transform, arrange, store, and distribute them. The PCs in Figure 1 (A) are installed with the iFIX-SCADA (Supervisory Control and Data Acquisition) as a framework software and iHistorian for the DB server, where they have been used successfully for the operations of many plant facilities.

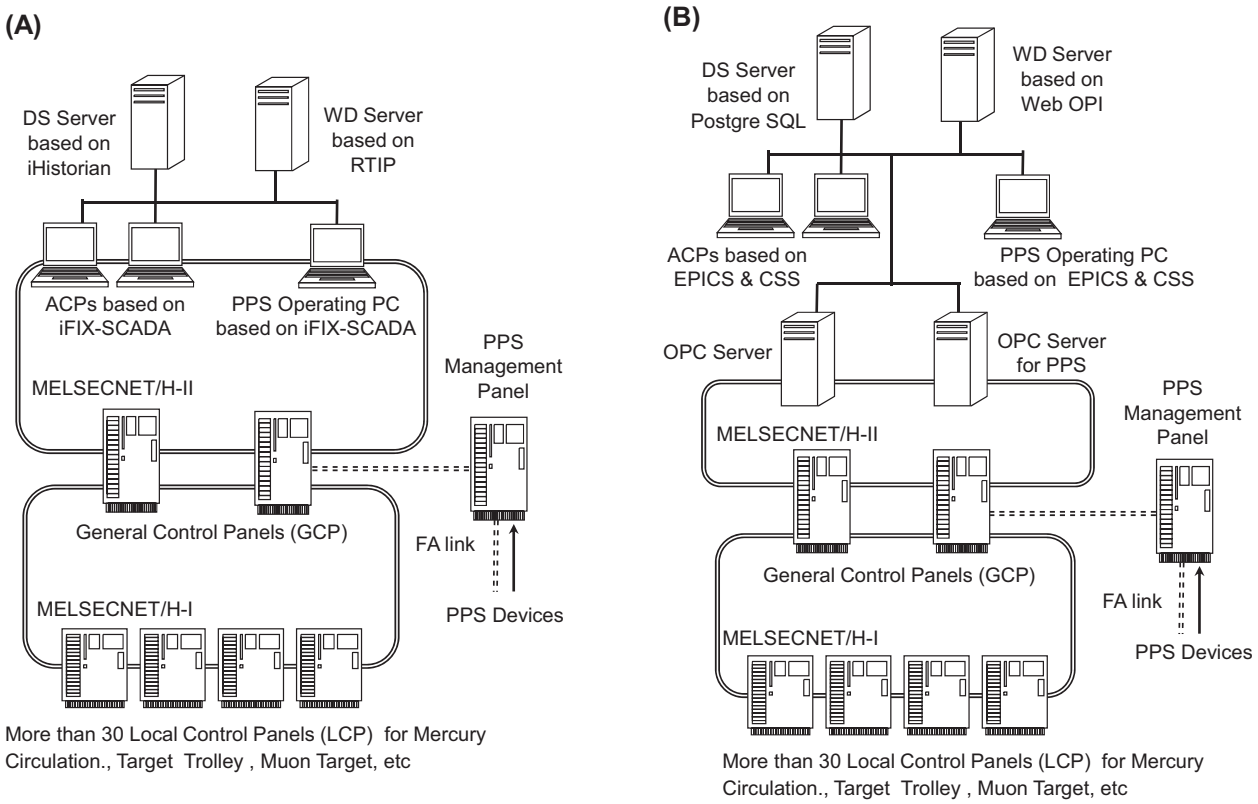

Figure 1. Structure of (A) Current and (B) Upgraded Monitor and Operation (MO) systems.

2. Upgraded MO system in GCS

Since the first proton beam injection in 2008, the GCS has been operated safely and stably without any serious troubles in comparison with upgrades of the target systems for ramping up the proton beam power and increments of the user apparatus year by year. It also behaved according to its safety design during the Great East Japan Earthquake in 2011 [2]. The current MO system based on the iFIX-SCADA has also functioned as expected. However, the downside is its costly maintenance because of its poor flexibility on the Operating System (OS) and software versions. For example, all PCs, which compose the MO system, must be replaced when the OS is upgraded.

Improving the maintenance flexibility of the GCS will result in a sustainable long-term operation; that is why we planned a significant upgrade of the MO system in 2013. According to the plan, we considered the schematic design of the upgraded MO system in 2012, based on the condition of the current functions so as to control all LCPs, acquire, store and distribute operation data of over 7000 items in a suitable data format. Figure 1 (B) outlines the schematic structure of the upgraded MO system. In Figure 1 (B), the following components for the MO system were adopted: Experimental Physics and Industrial Control System (EPICS) as framework software, OPC server as a data input/output module, Control System Studio (CSS) as a user interface window, Postgre SQL for the DS server, and Web OPI for the WD server. Furthermore, we made the prototype of the upgraded MO system, operated it in parallel with the current MO system, and evaluated its concrete performances with true data such as data transmission speed from PLCs, control functions from user interface windows, storage capability of the DS, long-term reliability, and so on. As a result, we were able to demonstrate that it works sufficiently well, as designed.

References

[1] K. Sakai *et al.*, Nucl. Instr. Meth. A **600** (2009), 75.

[2] K. Sakai *et al.*, Proc. of International Collaboration on Advanced Neutron Sources (ICANS-XX), Bariloche, Río Negro, Argentina, March 4–9, 2012, (2012), 113.

K. Sakai, M. Ooi, and A. Watanabe

Neutron Source Section, Materials and Life Science Division, J-PARC Center

Scenes from the Neutron Target Station

Makoto Teshigawara and Hidetaka Kinoshita enjoy a fruitful discussion about test equipment for the tritium reduction gas handling system.

Members of the target group dressed in air-line suits and face masks carefully remove mercury from the target following an irradiation experiment in the hot cell.

Demonstration of the target exchange procedure using the remote handling system.

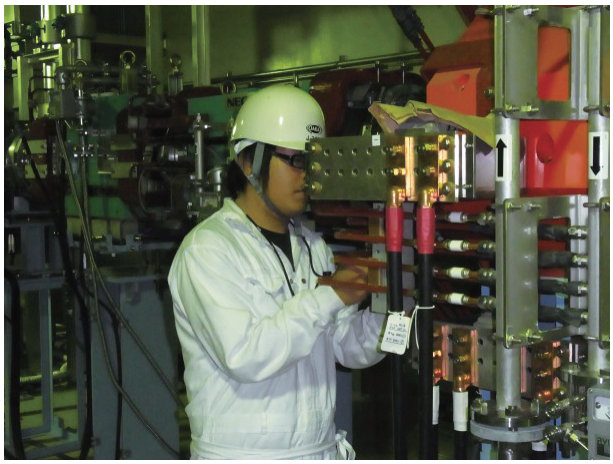

Maintenance work is carried out on the water channel of the quadrupole magnets of the proton beam transport system.

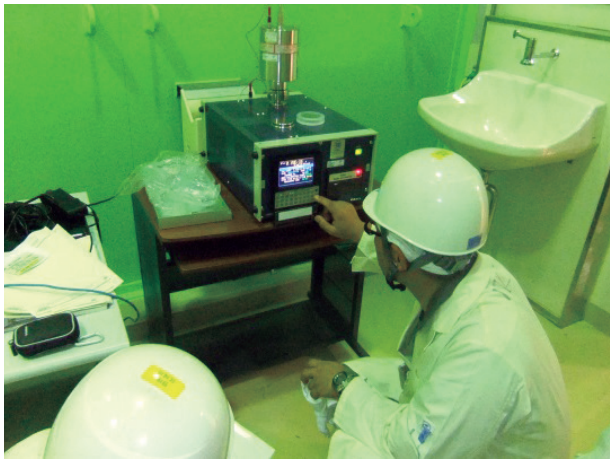

Measurement of tritium gas density during operation of the mercury target cover gas treatment system.

Katsuhiro Haga, Hidetaka Kinoshita, and Hideki Ueno discuss a water flow experiment on the new spallation neutron target.

Neutron Science

BL01: Fermi Chopper Spectrometer 4SEASONS —Improvement in the Background Suppression—

The suppression of unwanted background scattering and improvement of the signal-to-noise (S/N) ratio are obviously important issues for the inelastic neutron scattering instruments. On the Fermi chopper spectrometer 4SEASONS, we have been continuously upgrading the instrument to resolve these issues even after the start of the user program. In 2012, we installed B_4C vanes inside the vacuum scattering chamber and polyethylene plates behind the detector bank. Thanks to these new shielding materials, we successfully reduced the background even further [1].

The vacuum scattering chamber of 4SEASONS houses the detectors on the detector bank which constitutes a downstream part of the wall of the chamber. It consists of 11 panels, each of which can hold 32 pieces of 2.5 m ^{3}He tubes. Currently, 6 detector panels are fully covered by the detectors. The vanes, made of B_4C resin, were installed vertically at the gaps between each of the detector panels [Fig. 1(a)]. They are located parallel to the scattered beam path to block neutrons scattered at the surfaces of the detectors and run across the scattering chamber. Each of the vanes is 20 mm thick and 530 mm long along the beam path. This dimension of the vane does not make any shadow on the detectors.

Most of the outer wall of the vacuum chamber had been covered with 100–200 mm-thick polyethylene plates or polyethylene beads to stop the neutrons coming in from the outside of the chamber. However, the back of the detector bank had been left uncovered. In 2012, we covered this exposed part of the outer wall of the vacuum chamber. We covered the area of 23 m^2 with 80 mm-thick polyethylene plates as shown in Fig. 1(b).

In order to evaluate the effect of the newly installed shielding materials on the background, we performed test inelastic scattering measurements using a single crystal sample of $La_{1.82}Sr_{0.18}CuO_4$, which is one of the copper oxide superconductors. This compound shows very weak magnetic excitations in high energies, and the signal is easily affected by any background or spurious scattering. Figure 2(a) shows the inelastic scattering spectrum at ~5 K observed before the installation of the vanes and the polyethylene plates. By the time we measured these data, we had already installed one B_4C vane at one of the gaps of the detector panels, which corresponds to the position indicated by the arrow in the figure. Though the magnetic excitation signals can be observed at (±0.5, ±0.5), the whole detector

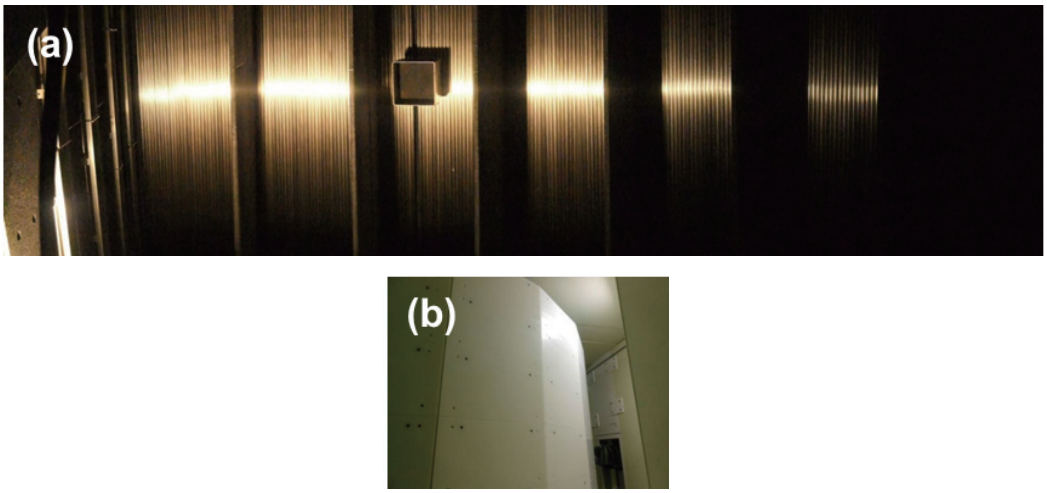

Figure 1. (a) ^{3}He detector tubes and absorbing vanes of B_4C resin inside the vacuum scattering chamber of 4SEASONS. (b) Polyethylene plates behind the detector bank inside the shielding house.

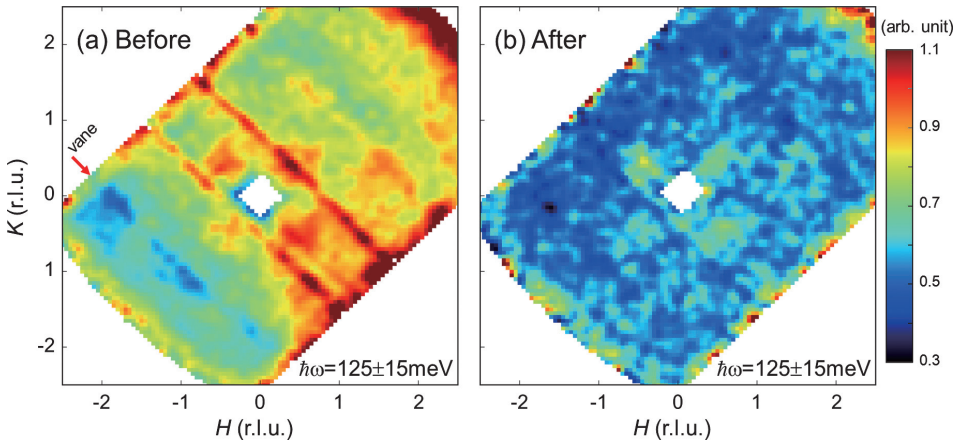

Figure 2. Color maps of the inelastic scattering spectra of $La_{0.82}Sr_{0.18}CuO_4$ at ~5 K measured (a) before and (b) after the installation of the shielding materials. The utilized incident energy is 204 meV. The data are cut at $\hbar\omega = 125\pm15$ meV and is projected onto the (*H*, *K*) plane.

bank, except the area to the left of the vane, shows high intensity. This indicates that most of the detector bank is contaminated by a severe background, while the vane can suppress the background on the detector panel next to the vane. In addition, several streaks are observed at the positions corresponding to the gaps between the detector panels, and some of them superpose the magnetic excitations. These streaks were caused by neutrons that are scattered by the gaps and hit detectors next to the gaps.

Figure 2(b) shows a similar inelastic scattering spectrum observed after the installation of the shielding materials. In contrast to Fig. 2(a), the background clearly decreases in the whole detector bank. Furthermore, the annoying streaks completely disappear. Actually, when we cut the spectra across the magnetic excitations in Fig. 2(a), the obtained profile is asymmetric and the peaks are too sharp due to the overlap of contaminations. On the other hand, in Fig. 2(b), we can obtain symmetric peaks with appropriate widths with lower background [1]. These results proved that the present background suppression work is quite effective for observation of weak excitation signals.

Not only does the improved S/N ratio enable the detection of signals weaker than before, but it also enables a measurement with a shorter time or with a smaller sample. Actually, after this improvement, several nice data in cupurate superconductors, itinerant magnets, multiferroic materials, etc. have been produced on the instrument.

References

[1] R. Kajimoto *et al.*, J. Phys. Soc. Jpn. **82** (2013) SA032.

R. Kajimoto[1], M. Nakamura[2], Y. Inamura[2], K. Ikeuchi[1], S. Ji[1], K. Nakajima[2], S. Ohira-Kawamura[2], W. Kambara[2], M. Sawabe[2], A. Kamiya[2], K. Inoue[2], T. Futagami[1], M. Kobayashi[1], A. Kishi[1], K. Satou[1], K. Aizawa[2], and M. Arai[2]
[1]Neutron R&D Division, CROSS-Tokai; [2]Neutron Science Section, Materials and Life Science Division, J-PARC Center

BL02: Si Crystal Analyzer near Backscattering TOF Spectrometer DNA —Specification and Commissioning Results —

1. Introduction

A Si crystal analyzer near-backscattering spectrometer, called *DNA*, is the first indirect geometry instrument in MLF, which aims to explore, in the nanosecond timescale, the dynamical behaviors of atoms and spins in bio-molecules, soft-materials, and so on. It sees the coupled moderator as a pulsed neutron source and is equipped with a high-speed pulse shaping disc chopper, aiming for a high energy resolution with high intensity. The instrumental overview and the specifications for DNA are shown in Figure 1 and Table 1.

2. Construction works in 2012

Almost all spectrometer components were installed before February 2012, with the exception of the No.1 high speed pulse shaping disc chopper. The No.1 chopper, which is designed as a counter-rotating double-disc chopper with maximum rotational frequency of 300 Hz, was set up with a single disc and commissioned at 225 Hz in early October 2012 by using a long shut-down period.

To evaluate the incident neutron energy distribution at the sample position, and to measure the diffraction pattern from the powder sample, two diffraction-detector-units were installed in this period.

The analyzer coverage was extended to a scattering-angle range from −18 degrees to +126 degrees in the horizontal plain by adding some crystal analyzer units, by the end of December 2012.

3. Beam Commissioning in 2012

The commissioning started from the beginning of February 2012. In this period, the pulse shaping high speed chopper could not be operated, then we operated the DNA spectrometer without the pulse sharpening chopper at energy resolution of ΔE ~ 14 μeV with wide energy transfer range: $-1000 < E / \mu eV < +1500$.

After installing the No.1 high speed chopper, the commissioning of high-resolution measurement was carried out by using single disc with slits of 10 mm and 30 mm widths at 225 Hz in the maximum rotational speed from the end of October 2012. At this point, the energy resolution of 3.0 μeV was achieved.

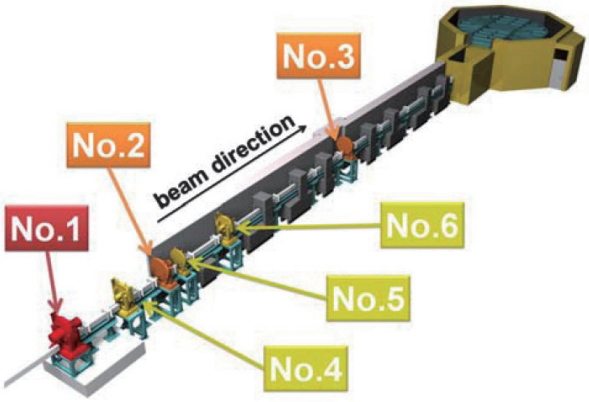

Figure 1. Overview of *DNA*. Each Number indicates a disc chopper installed on the beam line BL02.

Table 1. Instrumental specifications of DNA.

Items	Specification
Neutron source (NS)	Coupled Liquid H_2 Moderator
L_1 (source-sample)	42 [m]
L_2 (sample-analyzer)	~ 2.3 [m]
L_3 (analyzer-detector)	~2.0 [m]
Pulse sharpening chopper (PS-chopper)	
	Max speed: 300Hz at ~7.5m from NS
	(Precent Max speed: 225Hz by 4 slit one disc)
Crystal Analyzer	
Crystal and reflection index	Si(111)
	Si(311) in plan
Bragg angle of analyzers	~87.5 [deg.]
Energy resolution	~3.0 [μeV]: Si(111)
	~14 [μeV]: Si(111)
	Without PS-chopper
	~6 [μeV]: Si(311) expected.
Momentum range	0.07 < Q < 1.70 [A^{-1}]: Si(111)
	0.60 < Q < 3.80 [A^{-1}]: Si(311) in plan
Scan energy range: Si(111)	-40 < E < 100 [μeV]:
	Single pulse scan around E_f
	-500 < E <1500 [μeV]:
	Without PS-chopper in second frame

(the specifications by the end of December 2012)

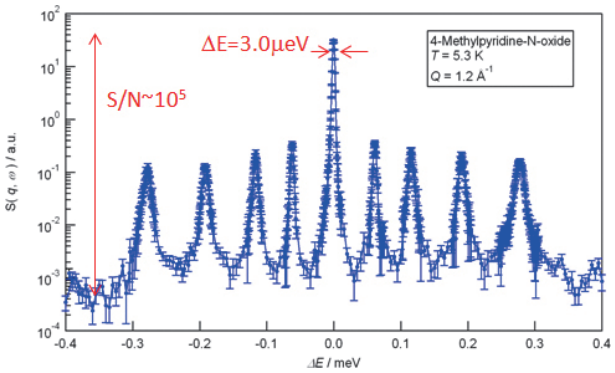

Figure 2. Measurements of the tunnel spectrum for 4-Methylpyridine N-oxide powder with ΔE ~ 3.0 μeV on BL02.

Figure 2 shows the tunneling spectrum for 4-Methylpyridine N-oxide with ΔE ~ 3.0 μeV on BL02. We realized an extremely low contribution of instrumental background.

4. Implementation progress of the user program in 2012A and 2012B

The user program started from May 2012. The user program in 2012A, with 2 experiments, and 2012B, with 5 experiments, was carried out and some of those experiments obtained new findings, which will be reported in near future.

Many experimental applications to the general user program from various scientific fields are expected in the future.

References

[1] N. Takahashi *et al.*, Journal of Physics and Chemistry of Solids **68** (2007) 2199.

[2] N. Takahashi *et al.*, Journal of the Physical Society of Japan **80** (2011) SB007.

K. Shibata[1], N. Takahashi[2], Y. Kawakita[2], K. Kamazawa[1], T. Yamada[1], K. Nakajima[2], W. Kambara[2], M. Kobayashi[1], Y. Inamura[2], T. Nakatani[2], S. Kasai[1], K. Aizawa[2], M. Arai[2], and S. Fujiwara[2,3]

[1]Neutron R&D Division, CROSS-Tokai; [2]Neutron Science Section, Materials and Life Science Division, J-PARC Center; [3]Quantum Beam Science Directorate, JAEA

Upgrading of the IBARAKI Biological Crystal Diffractometer iBIX at BL03

1. Introduction

The IBARAKI biological crystal diffractometer, iBIX, is a TOF neutron single crystal diffractometer to elucidate the hydrogen, protonation and hydration structure of mainly biological macro molecules. Since the end of 2008, the iBIX with 14 detectors has been available to users' experiments supported by Ibaraki University. However, we needed a long time for the measurement of protein samples because the accelerator at J-PARC was not operated at maximum power and the total solid angle of the detector was half of the final planning value. In 2012, we completed the upgrade of the 14 existing detectors and installed the 16 new detectors for the iBIX. This paper reports the results of the iBIX upgrade.

2. Upgrade of the Detectors

Since August 2012, the new detector system has been adapted; the process included the upgrade of the 14 existing detectors and the installation of 16 new detectors for the iBIX. The new detector system improved dramatically the detector efficiency, uniformity of sensitivity, spatial resolution and maintenance method. The following parts of the 14 existing detectors were upgraded: the scintillator packs including scintillators, the wavelength shift fibers strung for x and y direction (256 × 256 pixels), the photomultiplier tubes, the light guide units and the encoder modules.

The total solid angle of detectors subtended by a sample and the average detector efficiencies after upgrading improved by 2 and 3 times respectively (solid angle: 9.1%→19.5% for 4π, efficiency: 19%→58%). The total measurement efficiency of the present diffractometer was on one order of magnitude from the previous one coupled with the increase of the accelerator power (200 kW→300 kW). The uniformity of the detector-sensitivity in the direction of x and y axes before upgrading was about 20% for detector number 3. After upgrading, it was reduced to about 10%.

In December 2012, the commissioning (installation on the diffractometer, noise reduction, determination of the measurement parameter for each detector, measurement test by the data acquisition system with all detectors, etc.) of the new detector system could be succeeded by using a neutron beam. The new diifractometer of the iBIX is shown in Fig. 1.

3. Diffraction measurement with standard samples

We have tried to collect the diffraction dataset of Riboncrease A as a standard protein in order to

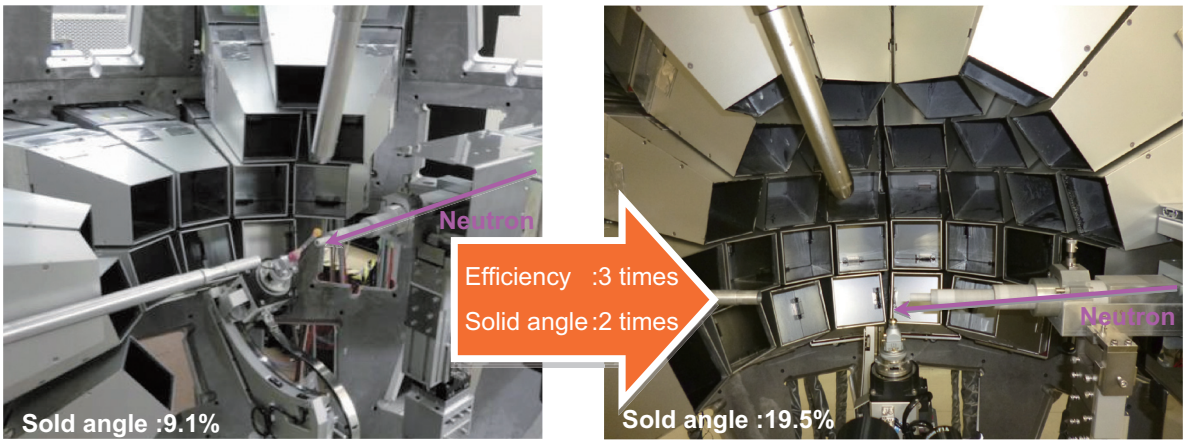

Figure 1. The diffractometer of iBIX before upgrading (Left) and after upgrading (Right) of the detectors.

estimate the performance of the new diffractometer of the iBIX. The data reduction and refinement could be succeeded. The resolution of diffraction data, equivalence among intensities of symmetry related reflections and reliability of the refined structure have been improved dramatically in comparison with these of the data of Riboncrease A obtained by using the iBIX before upgrading. These results imply that a full dataset of standard protein sample can be collected by the new iBIX in about 4 days for a crystal of 2 mm^3 in volume under 1 MW operation of the accelerator power in J-PARC. The new iBIX is expected to reach one of the highest performances of a neutron single crystal diffractometer for biological macro molecules in the world.

4. Feature prospects

In the future, the data reduction software should be upgraded in order to improve the accuracy of the data reduction for the integrated intensities of Bragg reflections, to make the system user friendly and to be available for samples with a large unit cell. For example, background extraction, data correction method, integration method, decentralized processing and peak de-convolution method will be developed in the next five years. In the case of the hardware, we should prepare the utility equipment for sample environment (eg. multi purpose stage, light source, heating device and so on) and a fast and friendly measurement system before an accelerator power reaches 1 MW.

K. Kusaka[1], T. Hosoya[1], T. Yamada[1], T. Ohhara[2], K. Tomoyori[1], M. Katagiri[1], I. Tanaka[1], and N. Niimura[1]
[1]*Frontier Research Center for Applied Atomic Sciences, Ibaraki University;* [2]*Neutron R&D Division, CROSS-Tokai*

Cross-section Measurement of Neutron Capture for Np-237 at ANNRI (BL04)

1. Introduction

Accurate cross section data of the neutron-induced reactions of MAs and LLFPs are required for the study of nuclear transmutations. The cross section at 25.3 meV is important because it is often used as an anchoring point for relative cross section measurements. The systematic uncertainties of the cross section are significantly reduced by normalizing the relative cross sections using the thermal cross section.

The thermal cross sections are in many cases obtained by neutron activation measurements where a sample of interest is irradiated with neutrons having energy distribution such as reactor neutrons. Hence, one can obtain the averaged cross section under this neutron spectrum. Then the averaged cross section is calculated to the thermal cross section using the Westcott's factor [1]. The Westcott's factor is defined as the ratio between the thermal cross section and the Maxwellian averaged cross section. In a recent measurement of ^{237}Np(n, γ) at LANL [2], the Westcott's factor of 0.944 $\pm$ 0.035 was obtained. This value is about 4% smaller than the evaluations such as JENDL-4.0 [3], ENDF/B-VII.1 [4] and Mughabghab [5].

In this measurement, the relative cross section was obtained for ^{237}Np(n, γ) and the Westcott's factor was deduced using the ANNRI-NaI(Tl) spectrometer.

2. Experiment

The sample used in the measurement was a mixture of neptunium dioxide (200 mg of ^{237}Np) and aluminum pressed into a pellet shape of a 1-mm thickness and 20-mm diameter. The pellet was sealed in an aluminum case and placed at a flight length of 28 m. Capture γ rays were detected using the ANNRI-NaI(Tl) spectrometer. Measurements for an aluminum case, carbon and without any sample were also performed to estimate the backgrounds. The obtained TOF spectra are shown in Fig. 1.

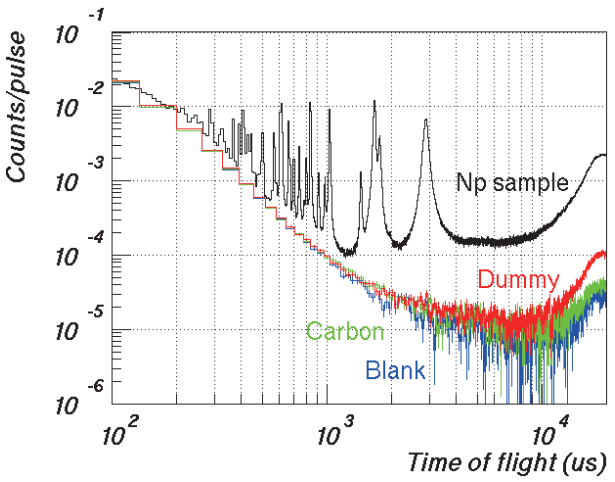

Figure 1. TOF spectra for the measurements of Np sample (black), Al case (red), carbon (green) and no sample (blue).

3. Results

In the data analysis, the dead time was corrected and the backgrounds due to the frame-overlap neutrons, aluminum case and scattered neutrons were subtracted. The effects of the self-shielding and multiple scattering were corrected using the PHITS [6] and JENDL-4.0 [3]. After these corrections, the TOF spectrum was divided by the neutron spectrum which was measured by ^{10}B(n, $\alpha_1\gamma$) reaction. More detailed information could be obtained elsewhere [7].

The relative cross section obtained in the present work was normalized at the first resonance using JENDL-4.0 and the resulting cross section is compared to the JENDL-4.0 in Fig. 2. From the obtained relative cross section, the Westcott's factor was deduced as $0.988 \pm 0.004_{sta} \pm 0.009_{sys}$. The most influential sources of the uncertainty were the frame-overlap background and the thickness of the ^{10}B sample. The Westcott's factor obtained in the present work agrees well with the evaluations of JENDL-4.0 (0.983), ENDF/B-VII.1 (0.986) and Mughabghab (0.982).

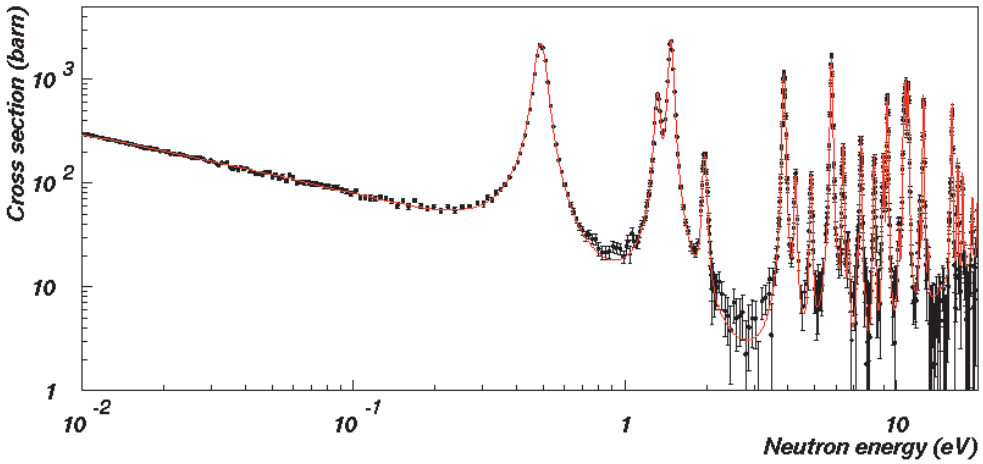

Figure 2. The cross section of ^{237}Np(n, γ) reaction. A red line shows the JENDL-4.0 evaluation.

References

[1] C.H. Westcott, J. Nucl. Energy **2** (1955) 59.

[2] E.-I. Esch *et al.*, Phy. Rev. **C77** (2008) 034309.

[3] K. Shibata *et al.*, J. Nucl. Sci. Technol **48** (2011) 1.

[4] M.B. Chadwick *et al.*, Nucl. Data Sheets **112** (2011) 2887.

[5] S.F. Mughabghab, *"Atlas of neutron resonances"*, Elsevier (2006).

[6] K. Niita *et al.*, JAEA-Data/Code 2010-022 (2010).

[7] K. Hirose *et al.*, J. Nucl. Sci. Technol **50** (2012) 188.

K. Hirose[1,*], A. Kimura[1,2], and H. Harada[1,2] on behalf of the ANNRI collaboration

[1]Research group for Applied Nuclear Physics, Nuclear Science and Engineering Directorate, JAEA; [2]Neutron Science Section, Materials and Life Science Division, J-PARC Center; [*]Present Address: Research group for reactions involving heavy nuclei, Advanced Science Research Center, JAEA

Studies of Neutron Optics for Physics Researches

Introduction

At the NOP beamline (Neutron Optics and Physics) installed at port BL05, the final preparation for neutron lifetime measurement and some other researches and developments are continuing. The time projection chamber (TPC) used to detect neutron beta decay was adjusted precisely for data acquisition with high quality at a high polarization beam branch. Neutron guide tubes were installed upstream of the unpolarization neutron beam branch to extract very slow neutrons for UCN experiments. The chamber for gas scattering experiments was tested at the low divergence beam branch.

Commissioning for neutron lifetime measurement

The recent values of neutron lifetime deviate far beyond the systematic errors claimed in the past and require further improvement to be consistent with the primordial Big Bang nucleo-synthesis.

We are continuing the neutron lifetime measurement at the polarized beam branch of the NOP beamline installed at port BL05. The system consists of a neutron chopper (SFC) and a gas chamber (TPC) for detecting the electrons from the neutron beta decay [1]. The TPC contains diluted ^{3}He and the rate of the ^{3}He(n,p)^{3}H reaction is measured by counting the protons. The neutron lifetime is measured as the ratio of the electron events to the proton events. Commissioning of the system has started with a neutron beam. The electron events and the proton events were found with reasonable signals (Fig.1). The ^{3}He density and the gas pressure, which cause the systematic uncertainty of the measurement, are also studied by using a mass spectrometer. The precise analysis of the data is also in progress.

UCN optics

Ultra-Cold Neutrons (UCNs), which are neutrons with a velocity of less than 7 m/s, are used mainly for particle physics. To research and develop UCN optical devices, a Doppler shifter, which converts incident neutrons of 3.0 nm to pulsed UCNs, is working at the un-polarization beam branch. In order to increase the incident neutrons, we have installed an upstream guide tubes and mirrors. As a result, the intensity of neutrons from the Doppler shifter, which consists of UCNs and faster neutrons, was 49 cps with 300 kW proton beam power. It means that the improvement of the neutron optics increases the intensity by about 20 times.

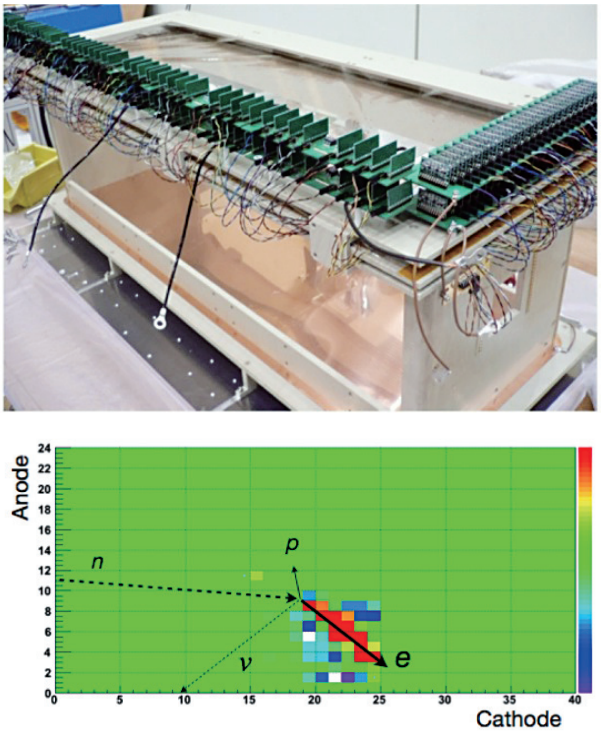

Figure 1. TPC and typical display of beta-decay.

We have also demonstrated the focusing optics of UCNs. The proper acceleration in the middle of the transport reconstructs dense UCN pulse at the experimental apparatus. The acceleration can be controlled by using RF spin flipper with changing its frequency. Figure 2 shows that the reconstructed neutron bunch arrived at the detector at a certain time [2].

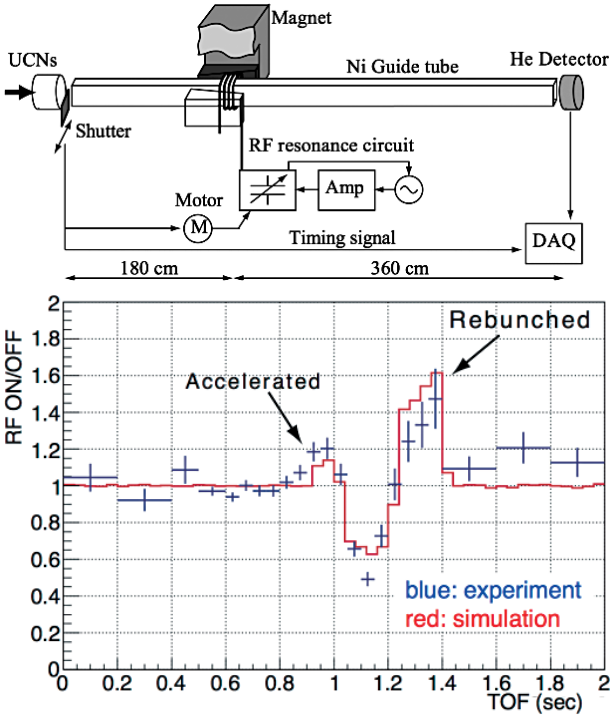

Figure 2. Setup for UCN focusing (up) and the ratio of TOF spectra with and without focusing (bottom).

Precision measurement of scattering from window material

A measurement of the angular distribution of a scattering cross section is planned to be conducted for the search of unknown medium range interactions between neutrons and neutral atoms. The scattering from the window material of the chamber for the neutral atom gas must have large background. We have started the precise studies of the scattering from the window material. A well-collimated neutron beam at the low divergence beam branch was injected into a thick single crystal silicon block to precisely study the neutron scatterings other than the Bragg reflections from a single crystal.

References

[1] H. Otono, Dr. Sc. Dissertation (University of Tokyo, 2012).

[2] Y. Arimoto *et al.*, Phys. Rev. **A 86** (2012) 023843.

Y. Arimoto[1], T. Ino[2,3], S. Muto[2,3], K. Taketani[2,3], H. Oide[3], T. Yoshioka[5], H. Otono[5], T. Yamada[6], K. Mishima[6], S. Yamashita[6], H. Sumino[7], S. Imajo[8], Y. Iwashita[8], M. Yamada[9], Y. Seki[9], Y. Otake[9], Y. Yamagata[9], P. Geltenbort[10], K. Hirota[11], M. Kitaguchi[11], H. M. Shimizu[11], T. Shima[12], H. Funahashi[13], K. Asahi[14], and Y. Kiyanagi[15]

[1]Accelerator Laboratory, KEK; [2]Neutron Science Section, Materials and Life Science Division, J-PARC Center; [3]Institute of Materials Structure Science, KEK; [4]CERN; [5]Department of Physics, Kyushu University; [6]International Center for Elementary Particle Physics, University of Tokyo; [7]Department of Physics, University of Tokyo; [8]Institute for Chemical Research, Kyoto University; [9]RIKEN; [10]Institut Laue Langevin; [11]Department of Physics, Nagoya University; [12]Research Center for Nuclear Physics, Osaka University; [13]Institute for Liberal Arts and Science, Kyoto University; [14]Department of Physics, Tokyo Institute of Technology; [15]Faculty of Engineering, Hokkaido University

Development of SuperHRPD and Structural Study of Functional Materials

After the recovery from the damage by the earthquake on March 11, 2011, we restarted the activity on BL08 SuperHRPD in April 2012. The damage and reconstruction of BL08 was explained in detail in the previous annual report and the KENS report [1]. The most difficult point had been the replacement of the broken mirror and the re-alignment of the beam-line to the experimental hatch. BL08 building moved to the north by 3 cm and to the east by 5 cm and subsided by 9 cm at the expansion joint. The sample position of SuperHRPD moved to the north by 1.25 cm, to the east by 3.39 cm and subsided by 2.77 cm. In addition to the recovery process of the beam-line, we installed a new disk chopper with $^{10}B_4C$ in order to cut the fast neutrons to reduce the background.

The first trial of the measurement and analysis using standard sample CeO_2, taken in April 2012, is shown in Fig.1, in which we can see the successfully performed powder diffraction measurement and Rietveld analysis as it was before the earthquake. The intensity is also at the same level as before the earthquake damage. In the upper panel of the figure, data taken at three different detector banks, backward bank, 90° bank and low-angle bank, are shown. Cleary, the hump in the background due to the scattering of unwanted fast neutrons has diminished and the background level greatly improved. The lower panel shows the Rietveld analysis of the backward bank, and the fitting is satisfactory.

One of the tasks of SuperHRPD is powder diffraction with super-high-resolution experiment and also application to a very complicated organic compound. We have several advancements on these issues. Let us show the status of the resolution of SuperHRPD first. The resolution of the TOF method is simply expressed by the following equation:

$$(\Delta d/d)^2 = (\Delta t/t)^2 + (\Delta L/L)^2 + (\Delta\theta/\tan\theta)^2$$

Shown in Fig.2 is the contribution of each term at BL08. Because of the long distance beam-line and the very short pulse shape at the source, the first two terms for $\Delta d/d$ are very small and it is possible to achieve the final goal of the designed resolution at SuperHRPD; $\Delta d/d$ = 0.035%. However, the current bottleneck is the third term, especially the resolution of the detector pixel size. Since we are still using the old detector of the Sirius diffractometer in KENS, the pixel size is about 12 mm, while the

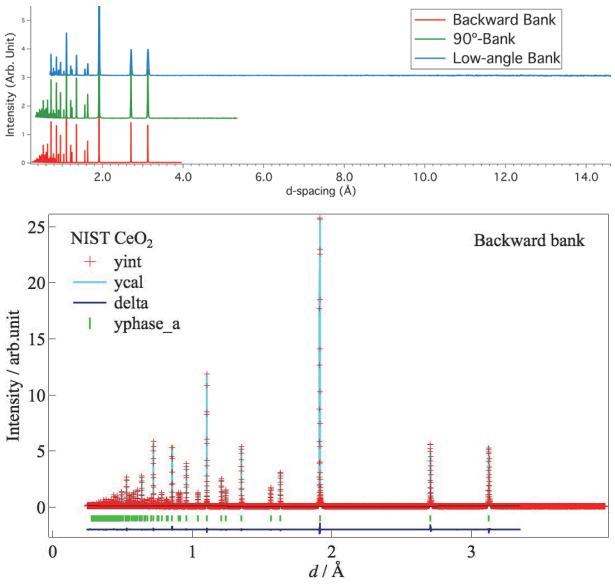

Figure 1. First-trial of the measurement and Rietveld analysis of standard sample CeO_2 after the recovery of SuperHRPD.

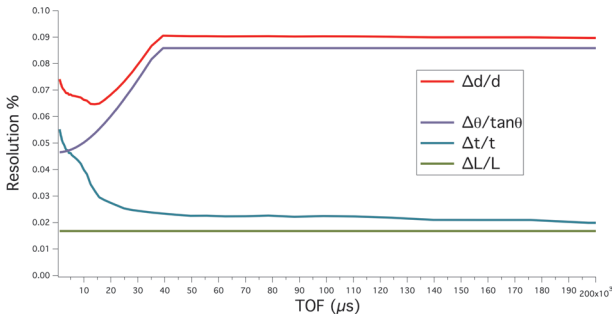

Figure 2. Resolution of BL08 expressed by three different contributions and the total one. 2θ angle is assumed as 165°.

designed parameter for SuperHRPD is assumed to be 3 mm in pixel size. Due to financial problems, the improvement of the detectors at BL08 has been postponed so far, thus we have tried to get better resolution by using only very high angle area data to increase $\tan\theta$ term in the equation. Figure 2 is calculated at $2\theta = 165°$. The calculation tells us that almost all of the resolution at the present BL08 is coming from the detector pixel effect.

In order to overcome the resolution within the present condition, we measured the powder diffraction profile using very high angle region, that is, higher than 175°. The purpose of the study was to pin down the space group of the ferroelectric phase in $SrTi^{18}O_3$ and then the atomic displacement pattern to induce the polarization. $SrTiO_3$ is a special material among the well-known perovskite type structures because the so-called tolerance-factor is almost 1 in this compound so that soft-mode occurs not only at the R and M points at Γ point. Not only that, but also the distortion of the lattice is two order magnitude smaller than those in the other typical perovskite type materials. This is the reason why the structural study of the ferroelectric phase of $SrTi^{18}O_3$ has not been successful in the diffraction experiment yet. Only SuperHRPD has an ability or possibility to complete this task. Figure 3 shows the simulation of the splitting of (200)c Bragg reflection upon the ferroelectric phase transition from tetragonal phase to orthorhombic phase. Note that the unit cell form at the ferroelectric phase is still unknown. If the model as orthorhombic cell is correct and the resolution is 0.035%, the final goal of SuperHRPD, the (200)c profile will change to three peaks shape. At least, when the resolution closes to 0.05%, we can expect the shoulder peaks of three-peak features.

Figure 4 shows the observed profile of (400)c Bragg reflection at 50 K (tetragonal phase) and at 4.8 K (ferroelectric phase). The data is accumulated only at the high angle area, larger than 175°. The resolution is estimated as 0.05%. At the tetragonal phase, we can see two peaks as it is expected from the tetragonal symmetry. On the other hand, at 4.8 K it seems to split further more to form three peaks. Thus, we can say the unit cell is orthorhombic or less symmetrical. We have performed the Rietveld analysis using the all area data since the statistics of the data at only the limited region more than 175° is too poor. Based on the conclusion as shown in Fig.4, we pin down the space group as F2mm with the unit cell size $2a \times 2b \times 2c$. The obtained atomic displacement pattern is the so-called Slater mode plus the anti-phase rotation of TiO_6 molecule.

In order to improve the resolution, we are planning to replace part of the existing position sensitive detectors (diameter of ϕ12.7) at the high angle

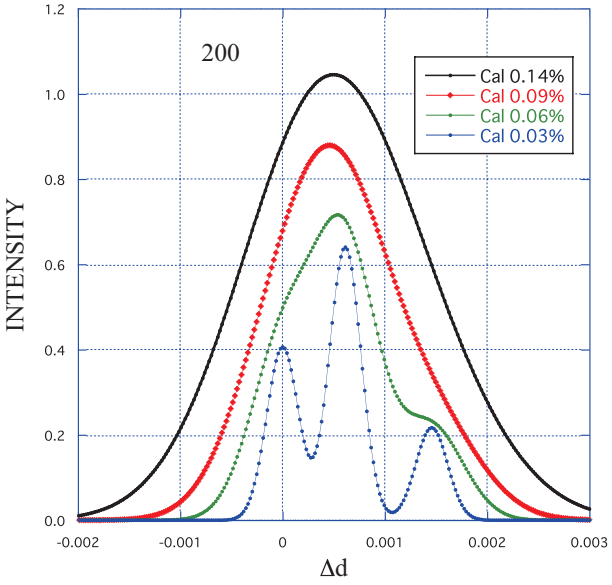

Figure 3. Simulation of the splitting of the (200)c Bragg reflection at various instrumental resolution, by assuming the orthorhombic unit cell.

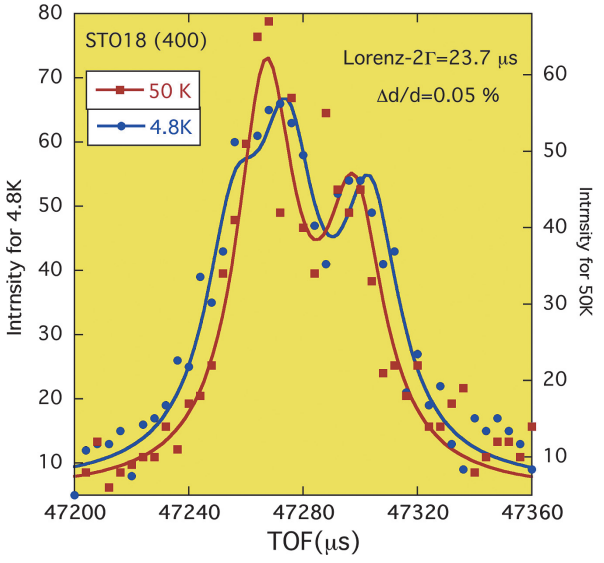

Figure 4. Observed profile of (400)c Bragg reflection at 50 K (tetragonal phase) and at 4.8 K (ferroelectric phase). Data is accumulated only above 175° area.

Figure 5. New position sensitive detector for SuperHRPD. The diameter is ϕ8.

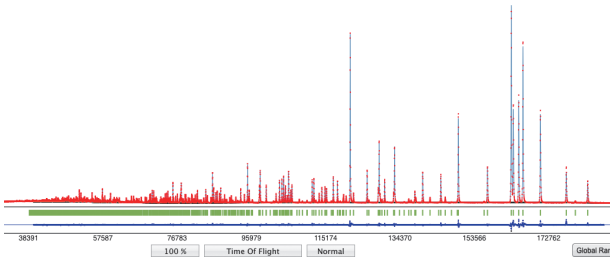

Figure 6. Rietveld fitting of glycyl-glycine based on the $P2_1/c$ model.

region with new detectors with a smaller diameter of ϕ8. Figure 5 shows the new detector; when the present detectors are replaced with these new ones, the resolution will be improved drastically, 2/3 of the $\Delta\theta$ term.

The next issue is the structure analysis of organic compounds. Under the increasing demand of the structure science with complicated structures such as inorganic-organic composite materials, super molecules, pharmaceuticals, biomaterials, *etc*., crystal structure analysis of several small molecules of amino acids and peptides such as glycine, alanine and glycyl-glycine, *etc*., have been performed.

Figure 6 shows the Rietveld fitting of deuterated glycyl-glycine ($P2_1/c$, a = 8.819 Å, b = 9.756 Å, c = 9.782, β = 104.30°). The fitting was satisfactory. Figure 7 shows the crystal structure of deuterated α-glycine obtained from the present analysis together with that of hydrogenated α-glycine [2]. Because of the difference of H and D in the molecule, lattice parameters are different, but the obtained atomic coordinates are almost the same except the differences of H and D atoms. In the figure, the reported

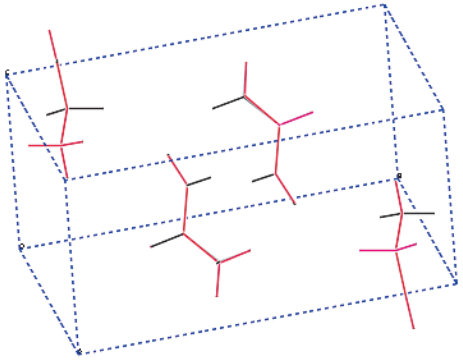

Figure 7. Wire-frame drawings of α-glycine based on the present analysis with that in reference [2]. Two drawings are completely overlapped.

structure and the present result are simultaneously drawn with completely overlapped lines. The details of the activity of organic materials on SuperHRPD will be reported separately.

References

[1] T. Kamiyama *et al*., KENS report **XVIII** (2011) 23.

[2] Per-Gunnar Jonsson and Ake Kvick, Acta Cryst. **B28** (1972) 1827.

S. Torii[1,2], M. Yonemura[1,2], T. Muroya[2], Y. Noda[3], J. Zhang[1,2], Y. Ishikawa[2], M. Ping[2], and T. Kamiyama[1,2]

[1]*Neutron Science Section, Materials and Life Science Division, J-PARC Center;* [2]*Institute of Materials Structure Science, KEK;* [3]*Tohoku University*

Development of an Advanced Special Neutron Powder Diffractometer under Extreme Environment for Materials

1. Introduction

The progress of technological innovation in rechargeable batteries is attracting much attention to overcome the issues of greenhouse gas emissions and to solve the limitation of the fossil energy resources. Despite the impressive growth of the utilization of nickel-metal hydride batteries and lithium ion batteries, the advancement and innovation of the technology is too slow and the scientific understanding underling the battery technology lags.

When the lithium ion battery starts to give electric power to a system, lithium-ions transfer between the positive and negative electrodes. The structural change of the two electrodes after the transformation of lithium ions through the interfaces between each electrode and the electrolyte solution is very important not only from a scientific viewpoint but also from a technological one. The information of the structural changes of the two electrodes and the location of the lithium ions will give us guidelines for improvement of the present lithium ion battery and the invention of an out-of-the-box battery.

In order to clarify the structure of the positive and negative electrodes and the interface between the electrode and electrolyte solution at an atomic level, a new neutron powder diffractometer, SPICA, has been designed and constructed as one of the state-of-the-art measurement apparatuses. It is well known that neutron is a more powerful probe to get information about the location and movement of light elements like hydrogen and lithium atoms in comparison with X-ray.

2. Present status

The SPICA diffractometer is installed at the BL09 beam line with the decoupled-poisoned moderator and the flight path from the moderator to the sample position is L_1 = 52 m to achieve high resolution. The sceneries of the assembling work of the main units of the SPICA diffractometer and the installation operation of the T0 chopper are shown in Figure 1(a), (b) and (c), (d), respectively.

As shown in Figure 2, the diffraction of NIST-TiO_2 powder was measured in order to check up the counter systems (low angle, 90° angle, high angle and back scattering) and their performance. All diffraction profiles indicate good signal-to-noise ratio, that is, low background. The best resolution was recognized to be less than 0.09%. The good performance, low background and high resolution, of the SPICA diffractometer will allow us to analyze the detailed structure and its change of the battery element materials during the discharge and charge cycles in an *in-situ* measurement.

Various kinds of apparatuses have been establishing for *ex situ* and *in situ* measurements of battery element materials under a wide variety of special environments. Figure 3 shows the automatic sample changer that can load 40 samples. Using the equipment, 40 samples can be measured in *ex situ* condition automatically and in continuity.

Figure 1. The construction of the SPICA diffractometer (a), (b) and the installation of the T0 chopper (c), (d).

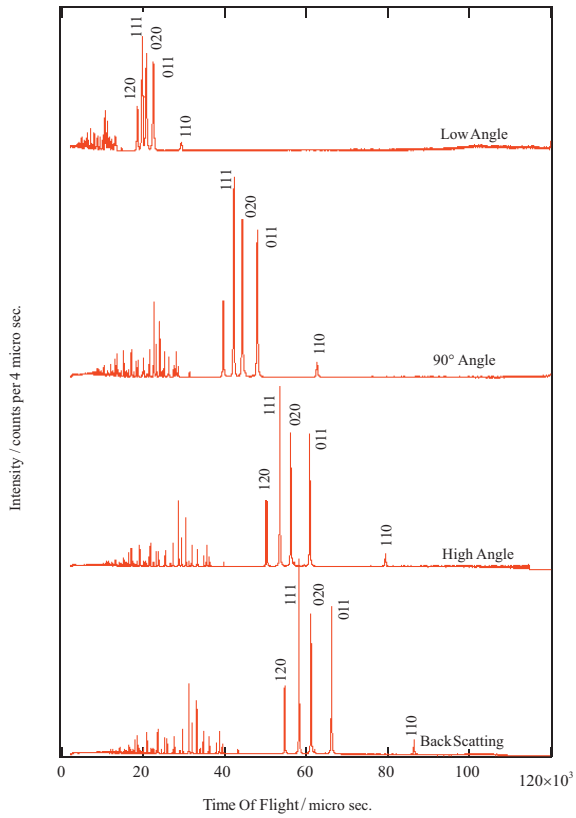

Figure 2. Diffraction profiles of TiO_2 powder at the low angle, 90°angle, high angle and back scattering bank.

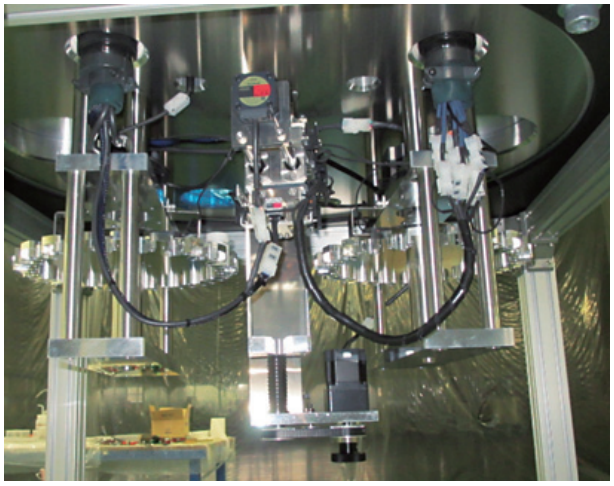

Figure 3. The automatic sample changer for the *ex situ* measurement.

Acknowledgements

This work was supported predominantly by the RISING project, Research and Development Initiative for Scientific Innovation of New Generation Batteries, of NEDO, New Energy and Industrial Technology Development Organization. The neutron scattering experiment was approved by the Neutron Scattering Program Advisory Committee of IMSS, KEK (Proposal No. 2009S10).

M. Yonemura[1,2], T. Fukunaga[3], K. Mori[3], T. Kamiyama[1,2], M. Nagao[1,2], Y. Ishikawa[2], S. Torii[1,2], Y. Onodera[3], R. Tomiyasu[2], H. Asano[2], T. Sakuma[4], T. Ishigaki[5], A. Hoshikawa[5], K. Aizawa[1], S. Harjo[1], K. Kino[6], Y. Idemoto[7], N. Kitamura[7], H. Arai[8], and Y. Uchimoto[9]

[1]Neutron Science Section, Materials and Life Science Division, J-PARC Center; [2]Institute of Materials Structure Science, KEK; [3]Research Reactor Institute, Kyoto University; [4]Institute of Applied Beam Science, Ibaraki University; [5]Frontier Research Center for Applied Atomic Sciences, Ibaraki University; [6]Graduate School of Engineering, Hokkaido University; [7]Faculty of Science and Technology, Tokyo University of Science; [8]Office of Society-Academia Collaboration for Innovation, Kyoto University; [9]Graduate School of Human and Environmental Studies, Kyoto University

BL10: NOBORU

NOBORU was one of the day-1 instruments at MLF, it conducted an user program since 2008. In FY 2012, 19 general use proposals, 2 project use proposals and 1 urgent proposal were approved and carried out at NOBORU. The availability of the beam-line was 100%. Some notable results were obtained using NOBORU this year (see Science Highlights in this report).

The biggest issue of NOBORU was that lack of working space and difficult accessibility for setup and clearance of each experiment. As shown in the top segment of Fig. 1, the delta of BL10 was wedged between BL09 and BL11 with an added large capacitor bank for the experiment using pulsed high magnetic field. We decided to move it under the cable rack of BL10. The operation was completed in September by the MLF stuff, as shown in lower segment of Fig. 1. A minimum depository space for the experimental apparatus was also saved.

NOBORU serves not only the R&D for TOF-imaging, but is also used in conventional radiography. An Electron Multiplying CCD (EM-CCD) camera was purchased and its optical components were investigated. Figure 2 demonstrates the capability of this camera. We confirmed that its best resolution exceeds that of neutron-IP (BAS-2500 system; 50 μm) with a field of view smaller than 5 cm. The CT software for this camera will be available in FY 2013.

Figure 1. Working space of NOBORU in early September (upper) and in the end of September (lower).

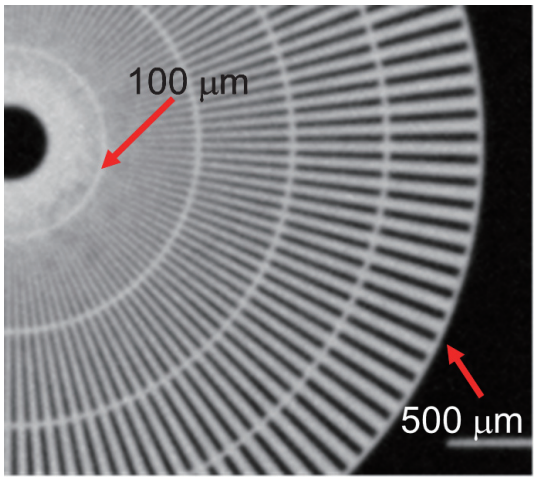

Figure 2. Neutron radiograph of a Siemens star developed in PSI [1]. The values at the red arrows indicate the pitch of the Gd absorber.

References

[1] C. Grünzweig, *et al.*, REVIEW OF SCIENTIFIC INSTRUMENTS **78** (2007) 053708.

K. Oikawa, M. Harada, and T. Kai
Neutron Source Section, Materials and Life Science Division, J-PARC Center

BL11: Performance of High Pressure Neutron Diffractometer PLANET

PLANET is a powder neutron diffractometer built specifically for high-pressure conditions. The construction was finished in March 2012 and the commissioning started from April 2012. Here, we introduce the beamline performance revealed in the commissioning.

Resolution of the diffraction pattern

Figure 1 shows the diffraction pattern of Si powder in standard V capillary. The resolution of the diffraction pattern was found to be $\Delta d/d \sim 0.6\%$ over whole d-range. This value is almost the same as the designed value of $\Delta d/d \sim 0.5\%$.

Elimination of the sample surrounding materials

In the high-pressure experiments, the sample is surrounded by various materials, such as MgO sample container, graphite tube heater and ZrO_2 pressure transmitting medium (see Fig. 2). To analyze the crystal and liquid structures precisely, the elimination of the scattering from the sample surrounding materials is indispensable. For this purpose, PLANET is equipped with the severe collimator system of the incident 4D slit and the radial collimators. This system can confine the gauge volume, typically 3 mm × 3 mm × 3 mm, which enables us to obtain the information almost only from the sample in the high-pressure cell designed for high-pressure and high-temperature experiments (see Fig. 3).

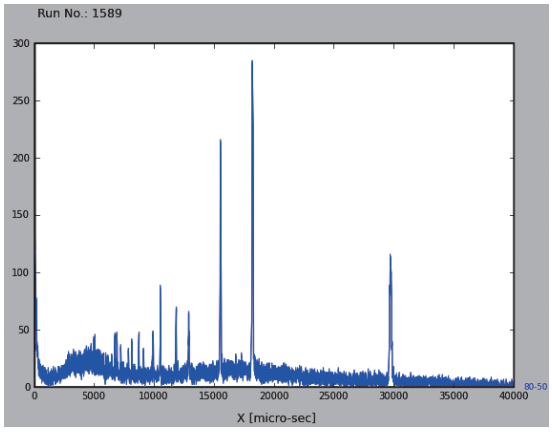

Figure 1. Diffraction pattern of Si powder (NIST #640b) in a V capillary.

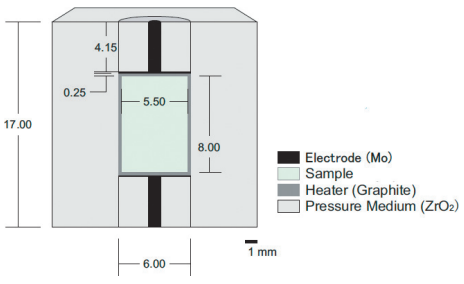

Figure 2. Typical cell assembly to be used in the high-pressure and high-temperature neutron diffraction.

High-pressure experiments

Figure 4 shows the pressure generated with the multi-anvil press "ATSUHIME". By using WC anvils, we can approach the pressure of 7.7 GPa (for Bi III-V transition). This result indicates that we can conduct high-pressure neutron experiments at 10 GPa using a relatively large sample with a volume of 21 mm^3.

Figure 5 shows the pressure dependence of the diffraction pattern of Si powder. When increasing the pressure, the intensity was severely reduced due to the decrease in the anvil gap. The exposure time needed for collecting 20k counts for Si220 is shown in Fig. 6.

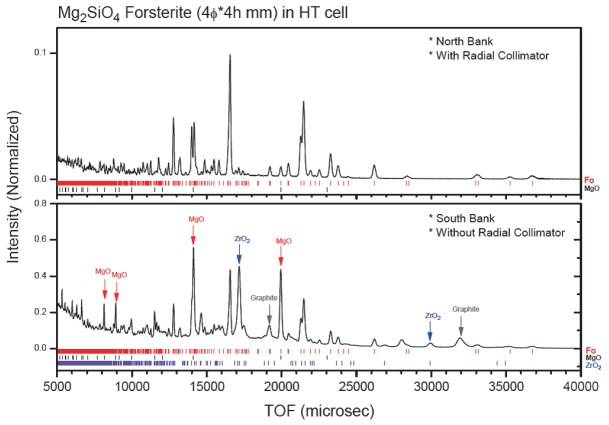

Figure 3. Diffraction patterns of the Forsterite (Mg_2SiO_4) in the high-pressure cell (see Fig. 2) with (upper) and without (lower) the radial collimators. The scattering from the sample surrounding materials completely vanishes with the use of the radial collimator.

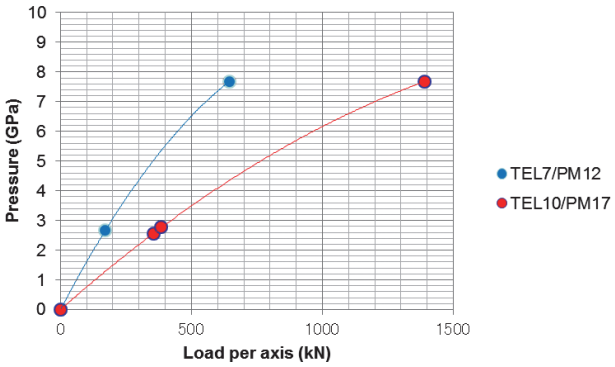

Figure 4. Pressure generation curve of the 6-axis multi-anvil press, where TEL and PM mean the truncation edge length of the anvil and the size of the pressure transmitting medium, respectively.

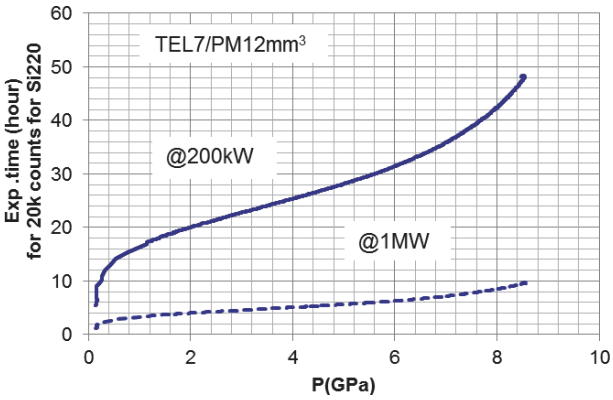

Figure 6. Exposure time needed for collecting 20k counts for Si220, which is estimated from the anvil gap-intensity relation and the pressure dependence of anvil gap. The electric power shown in the figure represents that of the proton beam supplied by the accelerator.

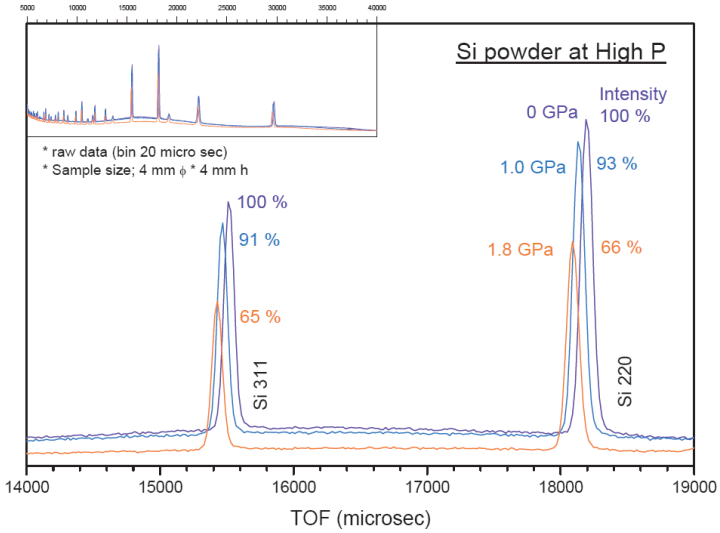

Figure 5. Pressure dependence of the diffraction pattern of Si powder.

This beamline opened for project members in Nov. 2012 and will be opened for general users in Feb. 2013. This project is supported by Grant-in-Aid for Creative Scientific Research (19GS0205) from the Japan Society for Promotion of Science and Grant-in-Aid for Scientific Research on Innovative Areas (No. 20103001) from the Ministry of Education, Culture, Sports, Science and Technology (MEXT) of Japan.

T. Hattori[1,2], A. Sano[1,2], A. Yamada[3], H. Arima[4], W. Utsumi[1,2], H. Kagi[5], and T. Yagi[3]

[1]Neutron Science Section, Materials and Life Science Division, J-PARC Center; [2]Quantum Beam Science Directorate, JAEA; [3]Geodynamics Research Center, Ehime University; [4]Institute for Materials Research, Tohoku University; [5]Graduate School of Science, The University of Tokyo

High Resolution Chopper Spectrometer at BL12

1. Introduction

The High Resolution Chopper Spectrometer (HRC) is being operated at BL12 to study the dynamics in condensed matters with high resolutions using relatively high energy neutrons. A research project using the HRC is being conducted to establish a comprehensive picture of the condensed matter physics by observing a wide range of correlated electron systems. We selected some topics among the experiments and focused on the following four points of view: novel ground states in low dimensional quantum spin systems, interactions among spin, charge, orbital and lattice in electron systems with strong or medium electron correlations, origin of magnetism in ferromagnetic metals, magnetism related to characteristic structures in strongly correlated electron systems. We performed experiments involving these subjects.

2. Instrumentation

For this purpose, we implemented the following improvements in the HRC. As a result, in particular, the neutron Brillouin scattering (NBS) experiments became feasible [1].

A collimator system, composed of slits of vertical cadmium sheets, was installed just upstream of the sample in order to reduce the background noise. The collimators with collimation of 0.3° and 1.5° are mounted in the system, each of the two can be selected by an elevation mechanism with a motor control. On the HRC, position sensitive detectors (PSD) are mounted at the scattering angles $\phi = 3 - 42°$ for conventional inelastic neutron scattering experiments, the background noise for these experiments was successfully reduced by using the 1.5° collimator. Also, PSDs are mounted at low angles down to $\phi = 0.5°$, the 0.3° collimator can reduce the background in this low angle part. This 0.3° collimator is effective for NBS.

The computer environment consists of data analysis software and an experiment control platform. The data analysis software was improved in the following points: the intensity normalization process for the inelastic neutron scattering from powder samples was improved, the analyzed data were transformed to the standard Mslice format for convenience of the users, and the alignment of the sample crystal became very easy. The experiment control platform was also improved, so almost all the hardware on the HRC can be controlled from the computer terminal and these operations can be connected with the data acquisition (begin/end of running). In addition, a conceptual design was performed to improve the analysis software and the experiment control platform .

For conventional inelastic neutron scattering experiments, 128 pieces of 2.8 m-PSDs, which are mounted into two detector banks, cover $\phi = 3 - 42°$ at present. PSDs for the next detector bank were purchased, and will be installed soon.

The cryopump is being operated to provide high vacuum in the scattering chamber. The algorithm of the regeneration process of the cryopump was improved, and so its full pumping capacity became available.

The scattering chamber and its vacuum system were installed in 2009. The maintenance work for them was performed. In particular, the normal property of the large thin Al window on the surface of the chamber, designed on the assumption of a finite lifetime due to permitting the plastic deformation of the window, was confirmed.

To cool the sample down to 4 K stably, a GM-type refrigerator was installed.

Since the cadmium slits were successfully operated for the incident beam collimator, an oscillating radial collimator was manufactured for the collimation of the scattered neutron beam. Its performance will be investigated soon.

A deck connecting the space of BL12 to the mezzanine was constructed, completing the mezzanine in the 1st experimental hall.

3. NBS Experiments

The NBS, which is inelastic neutron scattering in the forward direction, provides a promising way to observe ferromagnetic spin waves in polycrystalline samples. By improving the collimation as mentioned above, the NBS became feasible on the HRC. We successfully determined the spin wave dispersion relations of $La_{0.8}Sr_{0.2}MnO_3$ and $SrRuO_3$, by using polycrystalline samples [1], as shown in Fig. 1.

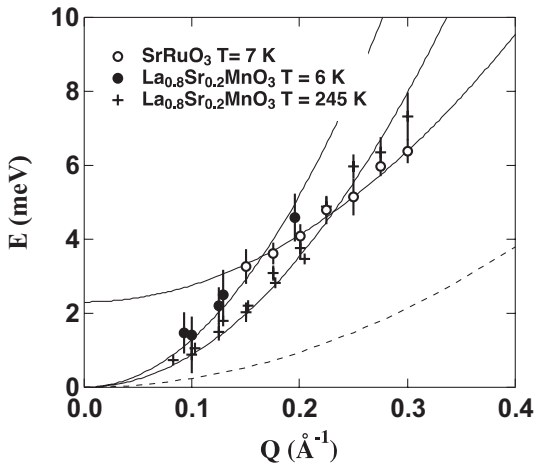

Figure 1. Spin-wave dispersion curves for $La_{0.8}Sr_{0.2}MnO_3$ and $SrRuO_3$ determined on the HRC. The solid lines are fitted curves. The dashed line is the upper boundary accessible with a conventional spectrometer.

References

[1] S. Itoh, Y. Endoh, T. Yokoo, D. Kawana, Y. Kaneko, Y. Tokura, and M. Fujita, J. Phys. Soc. Jpn. **82** (2013) 043001.

S. Itoh[1,2], T. Yokoo[1,2], T. Masuda[3], H. Yoshizawa[3], D. Kawana[3], M. Soda[3], and Y. Ikeda[3]

[1]Neutron Science Section, Materials and Life Science Division, J-PARC Center; [2]Institute of Materials Structure Science, KEK; [3]The Institute for Solid State Physics, The University of Tokyo

BL14 AMATERAS

1. Introduction

JFY2012 was the 4th year since AMATERAS [1] (Fig. 1) has been opened to users. Fortunately, AMATERAS did not suffer any serious after effects from the earthquake in 2011. However, we encountered several problems, which caused a certain amount of beam time loss in JFY2012. In the course of the instrumental activities, we performed maintenance, tests and development of the auxiliary devices and made efforts to improve the spectrometer. It should be also reported that Dr. Yukinobu Kawakita has joined our group since the end of this fiscal year.

2. Instrumental Activities

In JFY2012, 36 days of beam-time were spent as instrument-group-use. In the end of JFY2011, we found deformation of one of the disks of the high-speed disk-choppers, and had to stop the operation of this disk, which caused limitation of the achievable resolution and loss of intensity. A new disk was delivered in the beginning of JFY2012, and we carried out the replacement and commissioning of the new disk. Other maintenance works involving the detector electronics and other devices have been also done.

We also made efforts to develop auxiliary devices and improve the spectrometer performance. An oscillating radial collimator (ORC) was developed by the MLF in-house staff. After off-beam and on-beam tests (Fig. 2), the ORC was used in an actual experiment in January, 2013. The further efforts to reduce the background continued. The time-independent background became a serious problem in some users' experiments. We spotted the floor under the scattering chamber as one of its sources. Additional shielding on the floor is under preparation. In the course of the study of the beam transport to increase the flux at the sample position, we have replaced the end section of the guide mirror with higher-performance one. The increase in the flux was as expected. As a response to this result, we ordered 8.6 m of new mirror, which will be installed

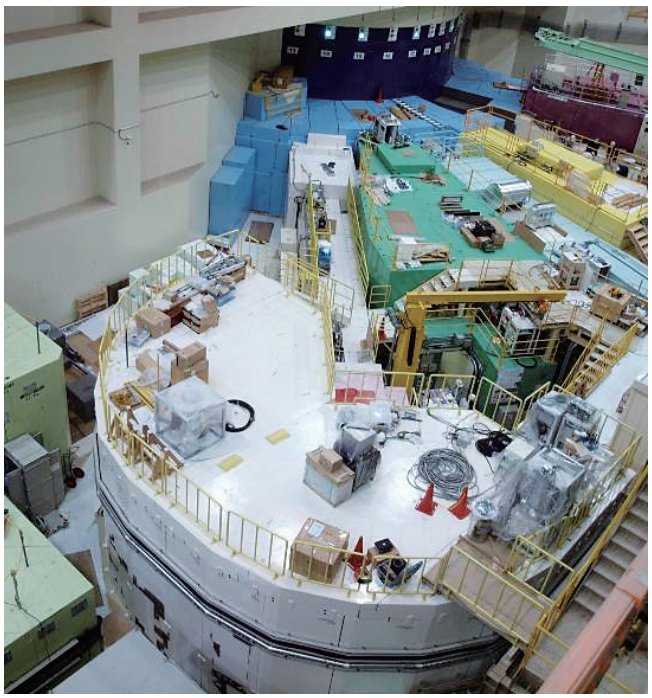

Figure 1. AMATERAS in November, 2012.

Figure 2. Test of a new oscillating radial collimator.

in 2013 together with the re-alignment work of the full beam-transport.

AMATERAS experienced series of problems. During one of the users' experiments, a sample stick was unexpectedly blown out from user carry-in Orange cryostat due to a sudden evaporation of the condensed air inside the sample space. Fortunately, there were neither injuries nor serious damage of the instruments. However, the investigation of this accident stopped the AMATERAS operation for three days. Also, the user program was interrupted twice due to troubles of a cryostat and the beam shutter controller. These problems caused beam-time loss. The main part of the loss was covered by the instrument-group-use beamtime to minimize the effect to the user activities. Some of the planned instrumental study and commissioning were cancelled or postponed to JFY2013.

3. User Program

AMATERAS accepted two project use proposals, 27 general use proposals, including four reserved ones, and one urgent use proposal in JFY2012. The accepted project use proposals are 'Research on structure and electronic properties of functional materials by AMATERAS spectrometer' (PI: T. Masuda) and 'Project research on structure and dynamics of protonic, superionic and amorphous functional materials' (PI: Y. Kawakita). The general use proposals reflect the wide variety of their research fields. It is notable that more than 2/3 of them were in the field of condensed matter physics. Two proposals of them were cancelled because of problems in the sample preparation. Two other proposals were interrupted or had their beam time reduced due to the problems mentioned in Section 2.

We have used a bottom-loading ^{4}He closed-cycle refrigerator for most experiments as a standard sample environment (SE) equipment of AMATERAS. In this fiscal year, other SE equipments such as user's carry-in and BL-common use ones were required more than before. A project use experiment used a high-temperature furnace by setting into the ORC to cut off neutrons scattered at niobium heaters, radiation shields and outer vacuum chamber. An Orange cryostat, which was used for a general use experiment, is quite useful for low-temperature experiments. Since some safety problems were pointed out on its sample stick through the investigation of the accident, we will improve the design for the stick and make a new one in JFY2013.

References

[1] K. Nakajima, S. Ohira-Kawamura, T. Kikuchi *et al.*, J. Phys. Soc. Jpn. **80** (2011) SB028.

K. Nakajima, S. Ohira-Kawamura, Y. Kawakita, and T. Kikuchi
Neutron Science Section, Materials and Life Science Division, J-PARC Center

Development and Commissioning of TAIKAN

The small and wide angle neutron scattering instrument TAIKAN (BL15) has been developed to characterize microstructures or hierarchical structures precisely and efficiently with a 1 MW spallation neutron source at the J-PARC.

TAIKAN's main set of components includes: optical devices, 4 choppers (3 disk choppers and a T0 chopper), a sample stage, a vacuum scattering chamber, 4 detector banks (small-, middle-, and high-angle, and backward detector banks) with ^{3}He PSD tubes with 8 mm in diameter and about 0.6 MPa in ^{3}He gas pressure, and a ultra-small-angle detector bank with a high-resolution 2-dimensional detector.

Figure 1 shows the small-, middle-angle detector banks in the vacuum scattering chamber, and the high-angle detector bank in the atmosphere. The ^{3}He PSD tubes were added on the middle-angle detector bank in FY2012. The numbers of ^{3}He PSD tubes were increased to 632, 304, and 104 for the small-, middle-, and high-angle detector banks, respectively.

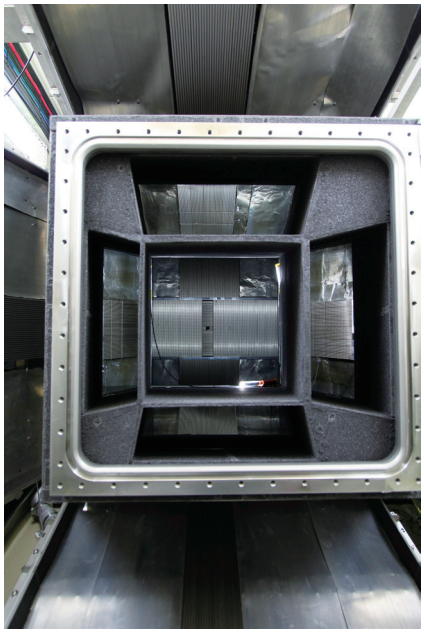

Figure 1. Small-, middle-, and high-angle detector banks.

Figure 2 shows the backward detector bank and a sample changer on the sample stage. On the detector bank 48 ^{3}He PSD tubes were installed to make the maximum q value, q_{max}, 250 nm^{-1} at the maximum scattering angle of $2\theta_{max} = 160^{o}$ and 0.05 nm in neutron wavelength.

Figure 3 shows a chamber of an ultra-small-angle detector and a N_2 neutron beam monitor on an exchanger in the vacuum scattering chamber. A high-resolution 2-dimensional scintillation detector with an active size of about 5 inch in diameter and a spatial resolution of about 0.5 mm will be installed in the chamber in FY2013. The N_2 neutron

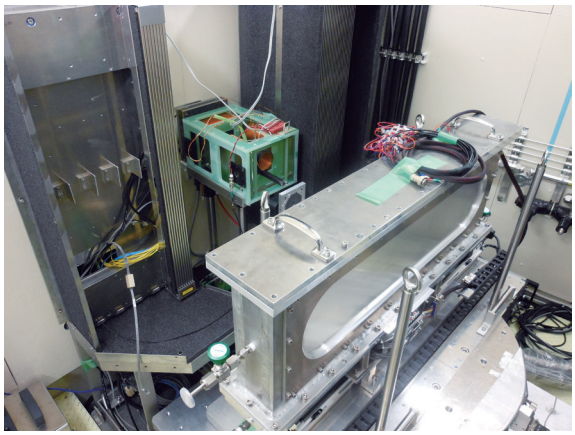

Figure 2. A backward detector bank and a sample stage.

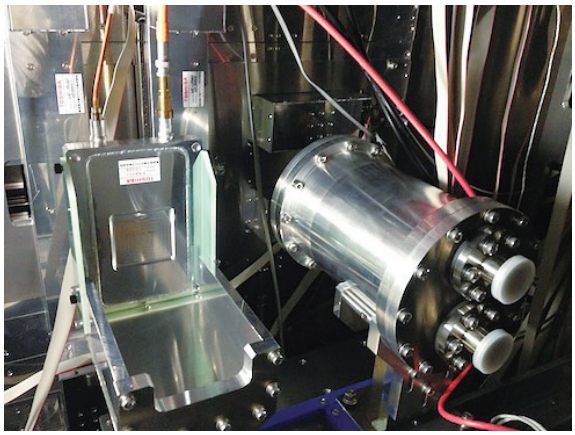

Figure 3. A chamber of an ultra-small-angle detector (right) and a N_2 neutron beam monitor (left).

beam monitor is a low efficiency detector developed for monitoring an intense neutron beam produced by the spallation neutron source at the J-PARC. In TAIKAN two N_2 neutron beam monitors are installed. One is installed at the position shown in Fig. 3, and the other is installed directly upstream of the sample stage. These N_2 neutron beam monitors are used to measure the neutron flux of an incident beam and the transmission of a sample for normalizing the neutron scattering intensity.

The characteristic of TAIKAN was evaluated with a neutron beam. Figure 4 shows a neutron scattering profile of a standard sample of glassy carbon with thickness of 1 mm, which was obtained with the small- and middle-angle detector banks, and the backward detector bank. The beam size at the sample position is 10 mm × 10 mm. The neutron wavelength used in data analysis is from 0.07 to 0.76 nm. Both Guinier region and Porod region had been observed with only the small-angle detector bank so far, but a diffraction profile was also observed successfully in the q region of about 6 - 160 nm^{-1} with the middle-angle and backward detector banks. It was confirmed that the diffraction originated from the glassy distribution of carbon atoms. On the figure an USAXS profile measured by Dr. Ilavsky of APS is also plotted in arbitrary unit as a reference.

The sample changer shown in Fig. 2 has been mostly used by users. A 10-sample set in sample holders can be mounted simultaneously on the sample changer. The temperature of the samples can be controlled between 5 and 80°C. Figure 5 shows a 1Tesla-electromagnet for the experiment of magnetic materials. In order to cool a sample, a 4K-cryostat can be installed into the electromagnet.

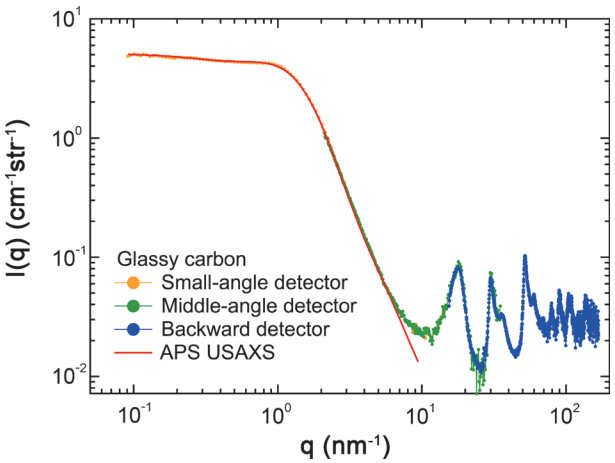

Figure 4. Scattering profiles of glassy carbon.

Figure 5. A 1Tesla-electromagnet with a 4K-cryostat.

J. Suzuki[1], S. Takata[2], K. Ohishi[1], H. Iwase[1], T. Tominaga[2], T. Shinohara[2], T. Oku[2], T. Nakatani[2], Y. Inamura[2], T. Ito[1], K. Suzuya[2], K. Aizawa[2], M. Arai[2], T. Otomo[2,3], and M. Sugiyama[4]

[1]Neutron R&D Division, CROSS-Tokai; [2]Neutron Science Section, Materials and Life Science Division, J-PARC Center; [3]Institute of Materials Structure Science, KEK; [4]Research Reactor Institute, Kyoto University

Free Liquid Interface Measurement Using Horizontal Type Neutron Reflectometer SOFIA

Neutron reflectometry (NR) is greatly valid for investigations on structures of surfaces and buried interfaces composed of soft materials. A beam line (BL) 16 in J-PARC/MLF is dedicated for a horizontal type neutron reflectometer. At BL16, two downward neutron beams (2.22° and 5.71°) are transported from a coupled hydrogen moderator to irradiate free surface such as air-water interface. In order to realize a neutron reflectivity measurement with a high flux neutron beam at J-PARC/MLF as early as possible, we started to accept the neutron beam with "ARISA-II" reflectometer relocated from the KENS facility in 2008 [1]. However, the motion range of the slits, sample and detector stages were so short that only the 2.22° beam line at BL16 was used, because the components of ARISA were not designed for this beam line. This is a serious disadvantage in an air-liquid interface measurement to observe high-q region with a high incident angle.

To overcome this problem, ARISA-II was replaced with a brand-new reflectometer "SOFIA (SOFt-Interface Analyzer)" in 2011 through the collaboration between JST/ERATO and KEK [2, 3]. Figure 1 shows a schematic drawing of SOFIA in the experimental hutch. With the new slit, sample, and detector stages, we can accept the 5.71° beam line as well as the 2.22° beam line. This enables us to measure NR over wide scattering vector (q) region on free liquid surfaces. Also, the slit system can finely collimate to irradiate an area of 10 mm × 10 mm, a typical sample size for synchrotron light sources, with an angular resolution of 3%.

The regulation to treat liquid sample was, however, very strict and it was not allowed to measure air-liquid interface in J-PARC/MLF. This year, this regulation was drastically relaxed and the air-liquid interface measurement was permitted. For this measurement, a Langmuir trough was newly installed to create a monolayer on a free water surface (Fig. 2). The result of the test measurement shows a clear

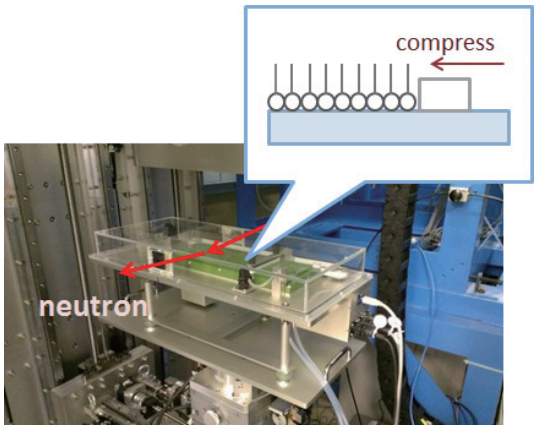

Figure 2. New Langmuir trough to create a monolayer on a free water surface for neutron reflectivity measurement.

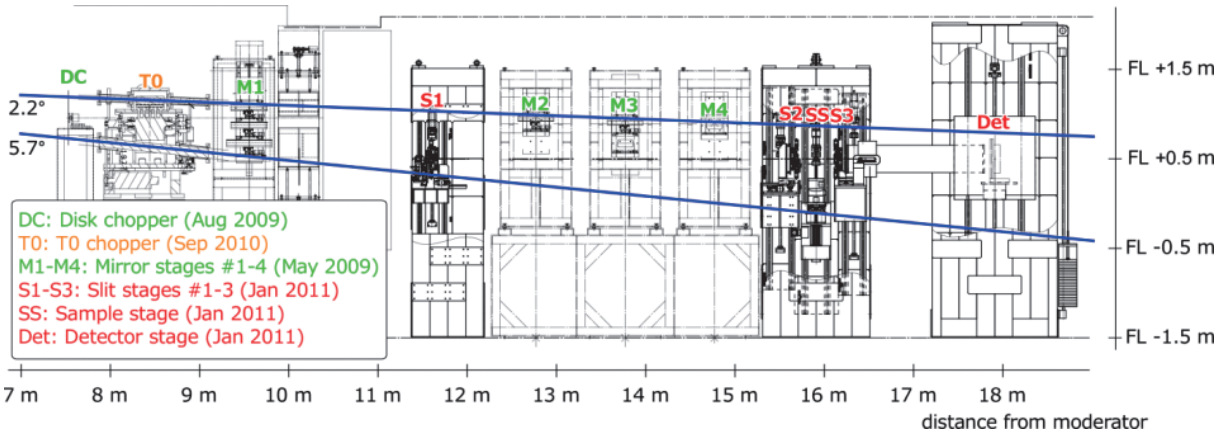

Figure 1. Side view of SOFIA reflectometer placed at BL16 in J-PARC/MLF.

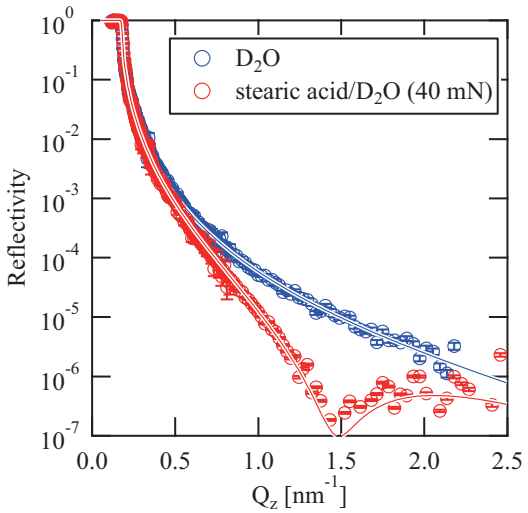

Figure 3. Neutron reflectivity profiles from air/heavy water interface and from air/stearic acid/heavy water interface.

fringe, which originated from a partially deuterated stearic acid monolayer (Fig. 3). Thanks to the high flux beam of J-PARC/MLF, only 30 minutes are enough to take good statistics, which is 10 times less than that of KEK-PS. The background level is, however, still high due to neutrons hitting at the trough. To solve this problem, we are developing a neutron absorber to suppress the background.

References

[1] K. Mitamura *et al.*, J. Phys. Conf. Ser. **272** (2011) 012017.

[2] N. L. Yamada *et al.*, Euro. Phys. J. Plus **126** (2011) 108.

[3] K. Mitamura *et al.*, Polymer J. **45** (2013) 100.

N. L. Yamada[1,2], K. Mitamura[3,4], N. Torikai[5], H. Sagehashi[1,2], S. Sato[1,2], H. Seto[1,2], T. Oda[6], M. Hino[6], M. Furusaka[7], and A. Takahara[3,4]

[1]Neutron Science Section, Materials and Life Science Division, J-PARC Center; [2]Institute of Materials Structure Science, KEK; [3]JST, ERATO, Takahara Soft Interfaces Project; [4]Institute for Materials Chemistry and Engneering, Kyushu University; [5]Graduate School of Engineering, Mie University; [6]Research Reactor Institute, Kyoto University; [7]Department of Quantum Science and Engineering, Hokkaido University

BL17: Polarized Neutron Reflectometer SHARAKU

1. Introduction

SHARAKU （写楽), named after the famous Japanese ukiyo-e printer, is a polarized neutron reflectometer [1]. The installation was completed at the end of 2011, and the user program started in 2011B. Twelve general researches and four project researches were conducted in fiscal year 2012, although we were still working to upgrade the reflectometer especially for the polarized neutron reflectometry [2].

2. The basic performance of the reflectometer

2.1 Specular Reflectivity down to 10^{-7}

We achieved a measurement of the specular reflectivity down to the 10^{-7} order using unpolarized neutrons without any background subtraction (Fig. 1). The sample is a Ni/Ti multilayer on a Si substrate. The thickness of both Ni and Ti layers in the bilayer is approximately 5 nm each, and the number of the stacks is 20. Fringes are clearly observed in the q-region between q_c of the total reflection and the 1st Bragg peak.

2.2 Performance of the polarizing devices (polarizer, analyzer, and spin flipper)

The key devices of the polarized neutron reflectometers are a polarizer, an analyzer, and a spin-flipper. The polarizer of this reflectometer consists of $4q_c$ Fe/Si polarizing supermirrors which align with double-transmission geometry, and a stack of the same $4q_c$ Fe/Si polarizing supermirrors are used for the analyzer. Both devices were fabricated by Swiss Neutronics. Two-coil spin flippers are employed to flip the polarized neutron spin before and after the sample.

Wavelength dependences of flipping ratios are plotted in Fig. 2, and those of a product of polarizing efficiency of the polarizer and the analyzer, *pp*, and flipping efficiencies of the flippers, *f*1, and *f*2 are shown in Fig. 3. The efficiencies indicated in Fig. 3 are calculated using the values in Fig. 2. Figure 3 indicates that the polarizer, the analyzer, and the two spin flippers, all work very well. The maximum flipping ratio is approximately 50 for the 0.3 nm neutron, and linearly decreases with increasing the wavelength. There is no additional fine structure in

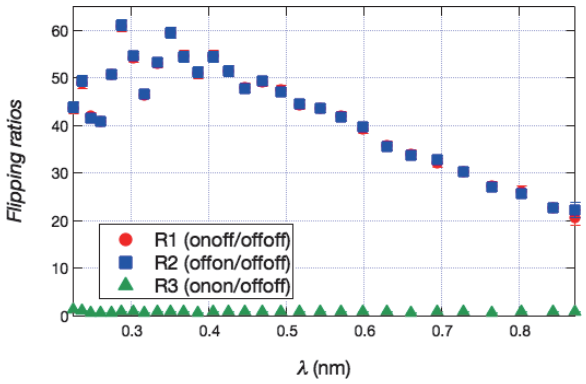

Figure 2. Flipping ratios according to status (active or inactive) of each spin-flipper.

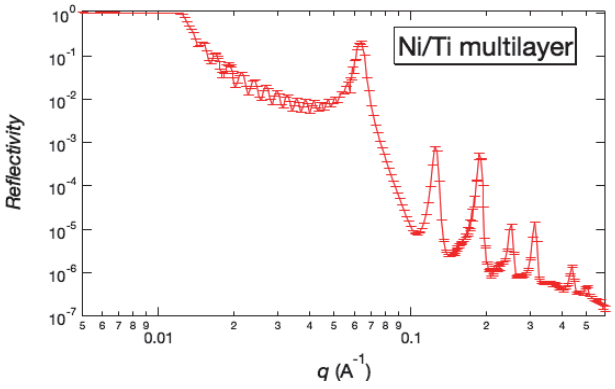

Figure 1. Specular reflectivity of a Ni/TI multilayer using unpolarized neutrons.

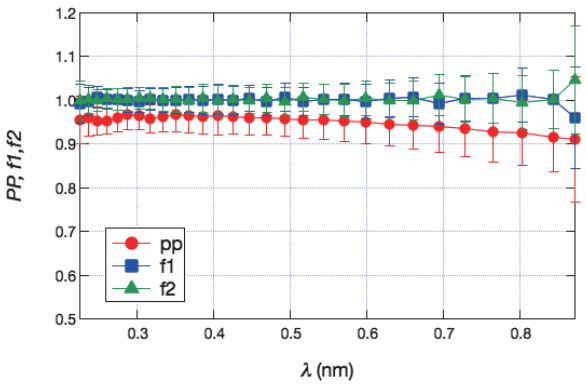

Figure 3. Polarizing efficiency, and flipping efficiencies of the devices for polarized neutrons.

the flipping ratios and the efficiencies. It enables us to do a simple data correction.

3. Sample environment equipment

An external magnetic field is indispensable to the reflectometry of magnetic multilayers. A conventional electromagnet is usually used for the experiments. This magnet is water cooled and produces magnetic fields of up to 10 KOe. We have a cryocooler which can control the sample temperature between 3 K and the ambient temperature. A superconducting magnet that produces a magnetic field of up to 70 kOe has been introduced to MLF. This magnet is also available. Reflectivity measurements can be performed down to 50 mK under magnetic fields up to 70 kOe in combination with a ^{3}He variable temperature insert.

As the first user of the 7T magnet, we conducted the initial performance test in collaboration with the sample environment (SE) team of MLF. The magnet successfully generated magnetic fields of up to 70 kOe. Then, polarized neutron reflectivity measurements in a general use program were performed using this SM at low temperatures.

Figure 4. The 7 T superconducting magnet on the sample table of SHARAKU.

References

[1] M. Takeda *et al.*, *Chinese J. Phys.* **50** (2012) 161.

[2] H. Hayashida, M. Takeda, D. Yamazaki, R. Maruyama, K. Soyama, M. Kubota, T. Mizusawa, N. Yoshida, Y. Sakaguchi, Physica B **42** (2013) 130.

M. Takeda[1,2,3], D. Yamazaki[1,4], K. Soyama[1,3,4], R. Maruyama[4], H. Hayashida[4], M. Kubota[1,2], H. Asaoka[1,2], K. Aizawa[2], M. Arai[2], Y. Inamura[2], W. Kambara[2], K. Kaneko[1,2], T. Nakamura[4], T. Nakatani[4], K. Oikawa[5], T. Ohhara[6], K. Sakasai[4], T. Shinohara[2], K. Suzuya[2], N. Takahashi[2], S. Takata[2], I. Tamura[2,3], K. Toh[4], H. Yamagishi[4], T. Hirano[7], N. Yoshida[6], Y. Sakaguchi[6], M. Mizusawa[6], J. Sato[6], S. Kasai[6], T. Ito[6], K. Kiriyama[5], and M. Katagiri[8]

[1]Quantum Beam Science Directorate, JAEA; [2]Neutron Science Section, Materials and Life Science Division, J-PARC Center; [3]Department of Research Reactor and Tandem Accelerator, JAEA; [4]Neutron Instrumentation Section, Materials and Life Science Division, J-PARC Center; [5]Neutron Source Section, Materials and Life Science Division, J-PARC Center; [6]Neutron R&D Division, CROSS-Tokai; [7]Hitachi Research Laboratory, Hitachi Ltd., Hitachi; [8]Frontier Research Center for Applied Atomic Science, Ibaraki University, Hitachi

BL18: Status of SENJU

SENJU is a new TOF single-crystal neutron diffractometer designed for precise crystal and magnetic structure analyses under multiple extreme environments such as low-temperature, high-pressure and high-magnetic field, and also capable of taking diffraction measurements of small single crystals, less than 1.0 mm^3 in volume.

Just after the launch of SENJU in March, 2012, primary conditionings and test diffraction measurements were undertaken as shown in the MLF annual report for 2011. Subsequently, we determined several instrumental parameters by diffraction measurement of a standard sample, tested newly installed devices (7T magnet and high-pressure cell), and undertook a structure analysis of a very small organic crystal in order to present the performance of SENJU.

1. Determination of instrumental parameters

Instrumental parameters such as the flight path (L_1 and L_2) and the positions of detectors have to be established initially to successfully do any measurements on the instrument. The angular positions of the detectors were determined by observing some Bragg reflections on each detector and rotating an NaCl single crystal several times little by little (Fig. 1). From these data, the scattering plane and the vertical angles of the detectors from the scattering plane were determined. These values were confirmed to coincide well with the designed values.

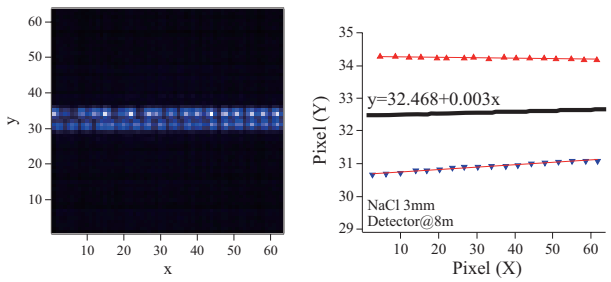

Figure 1. Observed Bragg reflections from a NaCl single crystal for the determination of the detector parameters.

2. On-beam tests of new devices

On-beam commissioning of newly installed sample environment devices, a 7T longitudinal magnet and a high-pressure cell, were carried out on SENJU.

The magnet (empty) was set in the vacuum chamber of SENJU and exposed by a neutron beam at room temperature. Figure 2(a) shows a diffraction image of all detectors. Although the upper and lower detectors were hidden by the magnet, all equatorial plane detectors and the bottom detector are available for diffraction measurement with the magnet. Figure 2(b) shows the 1st frame (0.4~4.4 Å) time-of-flight neutron spectrum of the detector #14 from the magnet. As expected, many Bragg peaks from the magnet were observed. On the other hand, as shown in Fig. 2(c), there is no Bragg peak from the magnet in the spectrum of the 2nd frame (4.4~8.8 Å), an important wavelength region for measurement of magnetic reflections in the field of materials science.

A compact clamp type high-pressure piston-cylinder cell (< 2 GPa) made from copper-beryllium alloy (Fig. 3(a)) was also tested on SENJU. A taurine single crystal (3 mm^3 in volume) was enclosed in the pressure cell together with deuterated glyc-

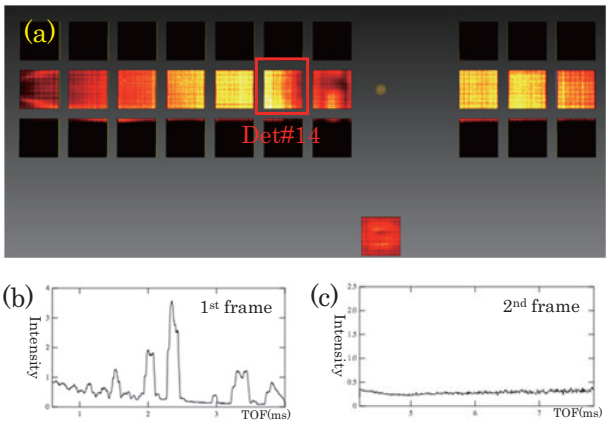

Figure 2. (a) Diffraction image of the empty magnet. (b) 1st frame TOF spectrum of the Det. #14. (c) 2nd frame of the Det. #14.

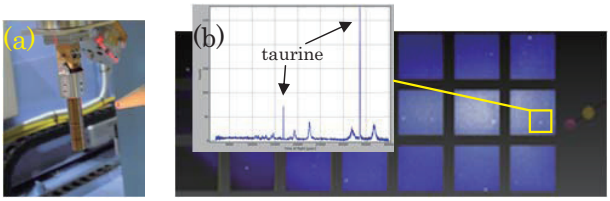

Figure 3. (a) Photo of the piston-cylinder cell. (b) Diffraction image and a TOF profile of the taurine crystal in the cell.

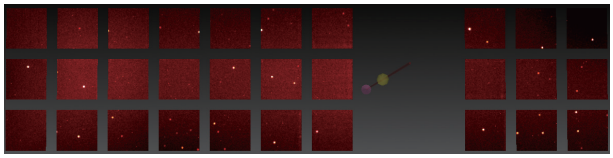

Figure 4. Diffraction image of a sub-millimeter size taurine single crystal.

erol and pressurized up to 1 GPa. The accelerator power was 300 kW and the exposure time was 6 hours. Even through the pressure cell, many distinct Bragg reflections from the taurine were observed as shown in Fig. 3(b). The result shows that this piston-cylinder cell is available enough as one of the high-pressure environments of SENJU.

3. Structure analysis of a sub-millimeter size organic single crystal

Structure analysis of sub-millimeter size crystals is one of the most important purposes of SENJU. We tried a structure analysis of a taurine crystal with 0.1 mm^3 (ϕ0.6 mm) volume by using SENJU. The measurement temperature was room temperature and the accelerator power was 260 kW. The total exposure time was 7.5 days (6 crystal orientations $\times$ 30 hours exposure). Figure 4 shows a diffraction image. Finally, 980 reflections ($I > 4\sigma(I)$) were observed and the d_{min} value was 0.7 Å. In structure refinement, the atomic positions and anisotropic displacement parameters of all hydrogen and non-hydrogen atoms were refined. The number of refined parameters was 129 and all of them had reasonable values. The final R-value was 7.14% ($I > 4\sigma(I)$). This result suggests that structure analysis of a 0.1 mm^3 size will be available by few days measurement when the accelerator power achieves 1 MW.

4. User program

The user program of SENJU started from the 2012A period. Three general proposals were conducted in 2012A, and another seven in 2012B. In addition, one trial use and six project uses were also carried out.

T. Ohhara[1], R. Kiyanagi[2], T. Kawasaki[2], K. Oikawa[3], I. Tamura[2,4], K. Kaneko[2,5], A. Nakao[1], T. Hanashima[1], and K. Munakata[1]

[1]Neutron R&D Division, CROSS-Tokai; [2]Neutron Science Section, Materials and Life Science Division, J-PARC Centeri; [3]Neutron Source Section, Materials and Life Science Division, J-PARC Centeri; [4]Department of Research Reactor and Tandem Accelerator, JAEA; [5]Quantum Beam Science Directorate, JAEA

BL19-TAKUMI
Engineering Materials Diffractometer

1. General Information

2012 FY was a fruitful year for TAKUMI after its recovery from the damages caused by the Tohoku earthquake. The re-commissioning after the earthquake was performed continuously while implementing the user programs. TAKUMI thanked repeated users and new users with their amazing research themes. They conducted experiments related not only to the residual strain mapping, but also to various kinds of in situ measurements which covered loading experiments at RT, high temperatures and low temperatures, thermal treatments and trials of thermo-mechanical simulation.

Typical topics carried out at TAKUMI during 2012 FY, which received attention from their related fields, were internal strains in an ITER central solenoid conductor sample [1], internal strains in a rebar embedded in an air-cured concrete, nano bainite transformation behavior associated with pre-martensite transformation, TRIP steels deformation behavior [2] and deformation behavior of LPSO Mg-Zn-Y alloys. An ITER conductor sample, in a shape as used in a performance test of cyclic current at high magnetic fields, was used in the experiment to fix the origins of the performance degradation during the test. Careful analyses successfully elucidated the role of martensite in TRIP steels during plastic deformation.

2. Sample Environments & Software

Development of new sample environment (SE) devices and software upgrades were performed besides re-commissioning of the present SE devices. Loading experiments are now able to be controlled by strain data measured using strain gauges or extensometers. The development of software for link-automatic control of several goniometers and the data acquisition system has also been completed.

3. User Programs

During 2012 FY, TAKUMI accepted and operated

Figure 1. Users enjoy their studies; Prof. Fukuda is setting his shape memory alloy sample for low temperature loading (up), while Prof. Kusunoki is discussing the acquired data with his colleagues (bottom).

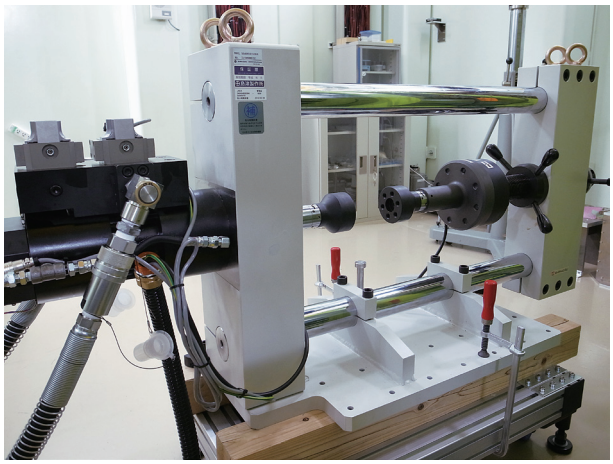

Figure 2. A new fatigue machine has been delivered during 2012 FY.

user programs as the way it did before the earthquake. There were 42 approved proposals including project researches and one instrumental use, while the number of unapproved and reserved proposals was only 8. Four proposals for propriety uses were included in the approved proposals. MLF operated approximately 200 days during 2012 FY, and the beam time allocations in TAKUMI are shown in Figure 3.

As shown in Figure 3(a), the beam time for the instrumentation, including re-commissioning after the earthquake, maintenances, upgrading works etc., was only about 15% of the total, while the rest of the beam time was used for the user programs. When the beam time allocation is classified according to the type of experiment, as shown in Figure 3(b), the percentage of strain mapping is only 24%, while that of various kinds of in situ studies is more than 50%. The percentage of studies related to the earth science using high pressure devices is about 10%, even the project research related to the neutron diffraction under high pressure condition has been finished in 2011 FY.

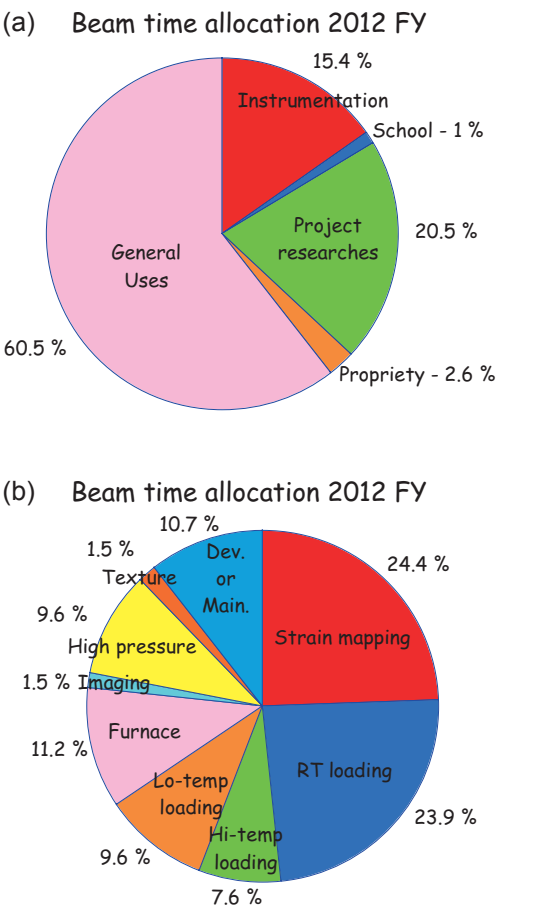

Figure 3. Beam time allocation in TAKUMI for the approved proposals.

References

[1] T. Hemmi *et al.*, Supercond. Sci. Technol. **26** (2013) 084002 (6pp).

[2] S. Harjo *et al.*, Mater. Res. Soc. Symp. Proc. **1528** (2013) (7pp).

K. Aizawa, S. Harjo, J. Abe*, W. Gong, and T. Iwahashi

*Neutron Science Section, Materials and Life Science Division, J-PARC Center; *present affiliation: Neutron R&D Division, CROSS-Tokai*

The Current Status of the Versatile Neutron Diffractometer, iMATERIA

1. Introduction

Ibaraki prefecture, the local government in Japan in the area where the J-PARC sites are located, has decided to build a versatile neutron diffractometer (IBARAKI Materials Design Diffractometer, iMATERIA [1]) to promote industrial applications for the neutron beam in J-PARC. iMATERIA is planned to be a high throughput diffractometer so that materials engineers and scientists could use it like the chemical analytical instruments in their materials development process.

This diffractometer is designed to look at a decoupled-poisoned liquid hydrogen moderator (36 mm, off-centered) (BL20), and to have the incident flight path (L1) of 26.5 m with three wavelength selection disk-choppers and straight neutron guides with a total length of 14.0 m. The instrumental parameters are listed in Table 1. There are four detector banks including a low angle and a small angle scattering detector bank. The angular coverage of each detector bank is also shown in Table 1. The rotation speeds for the disk-choppers are the same with a pulse repetition rate (25 Hz) for the most applications (normal mode). In this case, the diffractometer covers $0.18 < d\ (Å) < 2.5$ with $\Delta d/d = 0.16\%$ and covers $2.5 < d\ (Å) < 800$ at three detector banks of 90 degree, low angle and small angle with gradually changing resolution. When the speed for the wavelength selection disk-choppers is reduced to 12.5 Hz (wide-d mode), we can access a wider d-range, $0.18 < d\ (Å) < 5$ with $\Delta d/d = 0.16\%$, and $5 < d\ (Å) < 800$ with gradually changing resolution.

The automatic sample changer system [2] is most important sample environment for high throughput experiments. The automatic sample changer system consisted of large number of sample storage and two lines of elevating system, pre-vacuum chambers and sample rotating tables. So, this we can handle more than 600 samples continuously at room temperature without breaking a vacuum of sample chamber.

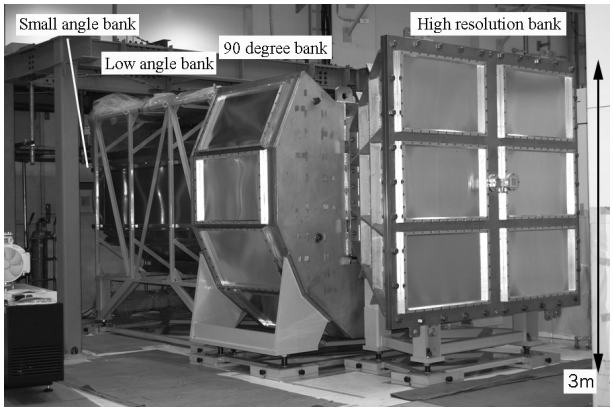

Figure 1. IBARAKI Materials Design Diffractometer, iMATERIA without detector for each bank and instrument shielding. The high-resolution bank, special environment bank (90 degree bank), low angle bank, can be seen from right to left. The small angle detector bank, which is not shown in picture, is situated in the low angle vacuum chamber (left hand of the picture).

Table 1. Instrumental parameters of iMATERIA. L2 is the scattered flight path. The d-range for each bank is the maximum value for 2-measurement mode.

L1		26.5 m
Guide length		Total 14 m (3 section)
Position of Disk choppers		7.5 m (double) 11.25 m (single) 18.75 m (single)
High Resolution Bank	2θ L2 d-range	$150^\circ \le 2\theta \le 175$ 2.0 - 2.3 m $0.09 \le d(A^\circ) \le 5.0^\circ$
Special Environment Bank	2θ L2 d-range	$80^\circ \le 2\theta \le 100^\circ$ 1.5 m $0.127 \le d(A^\circ) \le 7.2$
Low Angle Bank	2θ L2 d-range	$10^\circ \le 2\theta \le 40^\circ$ 1.2 - 4.5 m $0.37 \le d(A^\circ) \le 58$
Small Angle Bank	2θ L2 d-range	$0.7^\circ \le 2\theta \le 5^\circ$ 4.5 m $1.69 \le d(A^\circ) \le 800$

2. Current status

The three banks (high resolution bank (BS bank), special environment bank (90 degree bank) and low angle bank) are user operational. It takes several

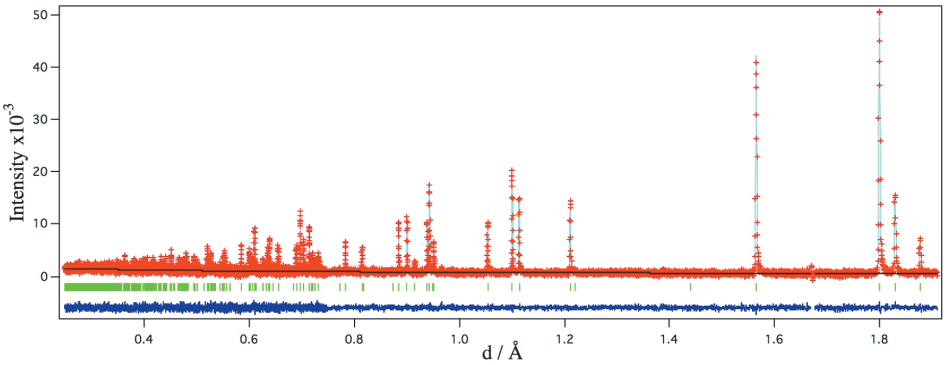

Figure 2. Rietveld refinment pattern of 4.5 mg $LiCoO_2$ by high resolution bank of iMATERIA using Z-Rietveld. The measurement time was 20 h for 4.5 g samples at 300 kW.

minutes to obtain a 'Rietveld-quality' data for the X-ray laboratory sized sample measured at 1 MW. Currently, the beam power is limited for tuning the accelerator (~300 kW), so that the measuring time is about 10 to 20 min for about 1 g of standard oxide samples.

In 2012, 81 user groups include 17 of urgent use used iMATERIA (60% are industrial users include proprietary and urgent use).

The beam power became higher than before, it is possible to measure the small quantities (few mg) samples and the sample containing large neutron absorption elements for about one day beamtime. Fig.2 shows the Rietveld fitting pattern of for 4.5 mg $LiCoO_2$ sample for 20 h at 300 kW beam power. The good fitting in Fig.2. is supported that the neutron diffraction experiment from 4.5 mg sample is succeded.

3. Conclusion

iMATERIA with four detector banks design for wide d range coverage. The wide d coverage and the short measuring time for this diffractometer will lead to the holistic understanding of materials structure and their function for materials development.

References

[1] T. Ishigaki *et al.*, Nucl. Instr. Meth. Phys. Res. A **600** (2009) 189.

[2] A. Hoshikawa *et al.*, J. Phys.: Conf. Ser. **251** (2010) 012083.

T. Ishigaki[1], A. Hoshikwa[1], M. Yonemura[2,3], K. Iwase[1], D. S. Adipranoto[1], and T. Kamiyama[2,3]

[1]Frontier Research Center for Applied Nuclear Sciences, Ibaraki University; [2]Neutron Science Section, Materials and Life Science Division, J-PARC Center; [3]Institute of Materials Structure Science, KEK

Status of the High Intensity Total Diffractometer (BL21, NOVA)

1. Overview

NOVA has been opened for general proposals since FY2012. Beside upgrading of the sample environments, the capability of the small sample measurements was improved.

2. Background reduction

As this is a high-intensity instrument, it is essential to reduce the intrinsic background to realize smaller sample measurements. Upstream from the sample position, Boron-containing concrete (neutron shielding concrete), boric acid resign and iron shield (1 m thick along the neutron beam direction) were installed to reduce the neutron backgrounds (Fig. 1). Inside the vacuum tank and neutron detectors were covered by B_4C resign. By improving the detector shielding, the background reduction of NOVA reached satisfactory level. In Fig. 2, the intensities of silica glass, silicon power and the intrinsic background of the 90-deg detector bank of NOVA were plotted. The neutron wavelength range of NOVA is from 0.12 Å to 8 Å. The intrinsic background was measured at the same condition of the incident beam without anything at the sample position. All the intensities were normalized by counts of the incident neutron monitor (GEM monitor in Fig. 1). The level of the intrinsic background was less

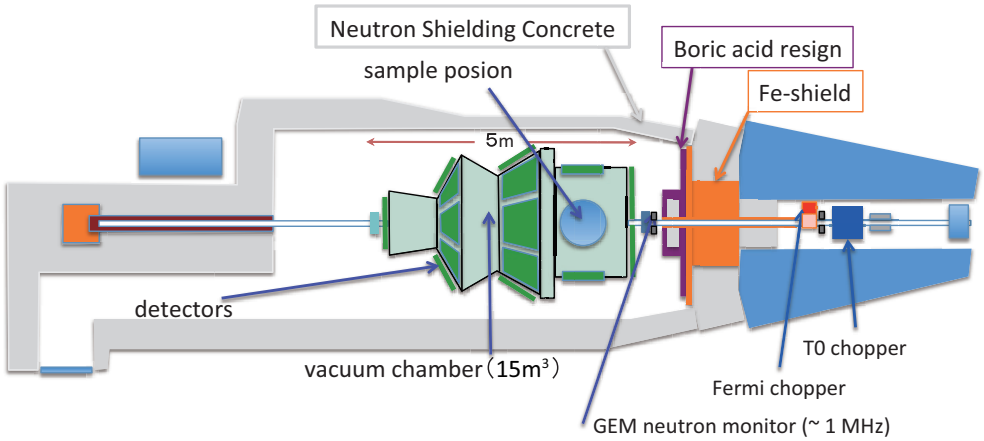

Figure 1. Shields of NOVA.

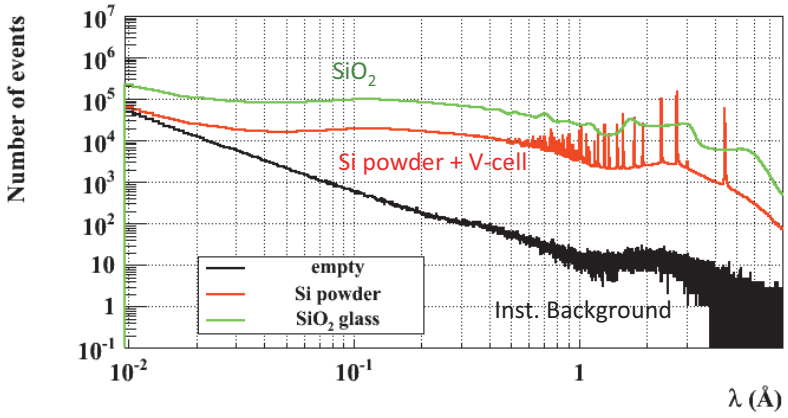

Figure 2. Intrinsic background of the 90-deg detector bank of NOVA compared with silica glass and silicon powder. "Empty" corresponds to the intrinsic background.

than 0.1% of the silica glass intensity and less than 1/10000 of the Bragg peak intensity. Compared to the base line of silicon power, which is mainly caused by a vanadium cell (0.1 mm thickness), the background level is less than 1%. In other words, the background of the cell should be reduced.

The backgrounds of other detector banks tend to be larger. To reduce the background, the reduction of the max beam size of NOVA, 20 mm × 20 mm, should be reconsidered and the optimized collimator should be replaced.

3. "1 mg sample" measurement

The low background of NOVA realizes measurement of 1 mg sample. Figure 3 shows the diffraction pattern of $YLiFeH_6$ provided by Orimo group of Institute of Materials Research, Tohoku University. This is a new iron based hydride synthesized at 6 GPa, 600-800ºC. The size of the sample is 800 μm in diameter and 200 μm in height. The weight is about 1 mg. The diffraction patterns of each detector bank obtained by 8 hrs of measurements are consistent with the simulated diffraction pattern of $YLiFeH_6$ (space group: F-43m). So far, the quality of the data is not good for Rietveld refinement but it is promising in obtaining better quality data improvement of the cell, neutron beam size and additional radial collimator.

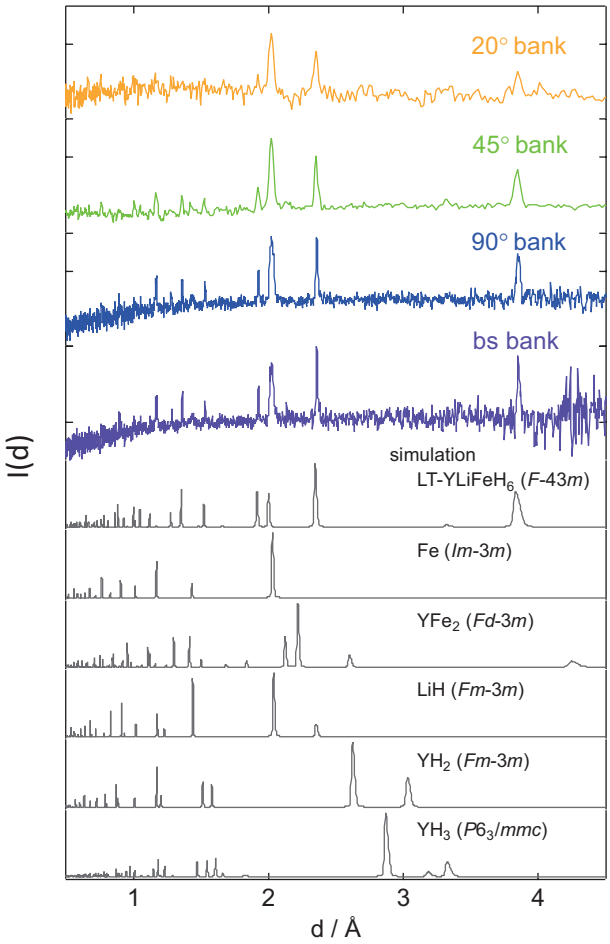

Figure 3. Neutron diffraction of $YLiFeH_6$ (1 mg).

T. Otomo[1,2], K. Ikeda[2], H. Ohshita[1,2], N. Kaneko[1,2], T. Seya[1,2], and K. Suzuya[1]

[1]Neutron Science Section, Materials and Life Science Division, J-PARC Center; [2]Institute of Materials Structure Science, KEK

Development and Application of an in-situ SEOP ^{3}He Neutron Spin Filter at J-PARC/MLF

1. Introduction

We have been developing an in-situ SEOP ^{3}He neutron spin filter (NSF) to apply it to pulsed neutron experiments at J-PARC/MLF. The ^{3}He NSF works for neutrons in a wide energy range, and has a large angular acceptance while contributing little scattering in a small-angle region. Therefore, the ^{3}He NSF could be used as a polarization analyzer for small angle scattering and reflectometry with pulsed neutrons. In this study, we performed demonstration of the polarization analysis experiments with our developed ^{3}He NSF at the small angle scattering instrument TAIKAN (BL15) and polarized neutron reflectometer SHARAKU (BL17).

2. A polarization analysis experiment at TAIKAN (BL15)

In this study, we aimed to divide coherent scattering from incoherent scattering from a hydrogenous sample by polarization analysis using the ^{3}He NSF [1]. The sample was silver behenate ($C_{22}H_{43}AgO_2$). The incident neutrons were polarized by the magnetic supermirror, and the neutron spin polarity was controlled by the spin flipper before the sample. The polarization of neutrons scattered from the sample were analyzed by the ^{3}He NSF. The sample was put just before the ^{3}He NSF, where the distance from the sample to the ^{3}He NSF was 160 mm. The ^{3}He spin filter was located in a position to cover the scattering angles between 0 and 6 degrees.

The ^{3}He polarization, P_{3He} = 68.4%, and the polarity was fixed during the experiment. We measured the scattering intensities by controlling the spin flipper on and off. The radial averages of the measured intensities are shown in fig. 1 (a). The Bragg peak at $q = 1.06$ nm^{-1} was observed both with the spin flipper on and off (Fig. 1 (a)), since the polarization efficiency of the ^{3}He NSF was not 100% for the neutrons. By correcting the effect of finite efficiencies of the polarizer, analyzer and spin flipper, we could successfully obtain the coherent and incoherent scattering intensities from the hydrogenous sample of silver behenate (Fig. 1 (b)).

3. A polarization analysis experiment at SHARAKU (BL17)

In this study, we tried to measure the specular and off-specular reflections from a magnetic multilayer sample by the polarization analysis with the ^{3}He NSF. The sample was a Fe/Cr multilayered thin film with giant magneto-resistance effect [2]. The incident neutron beam was polarized with Fe/Si supermirrors and the polarity was controlled with the spin flipper. The neutrons reflected from the sample were analyzed

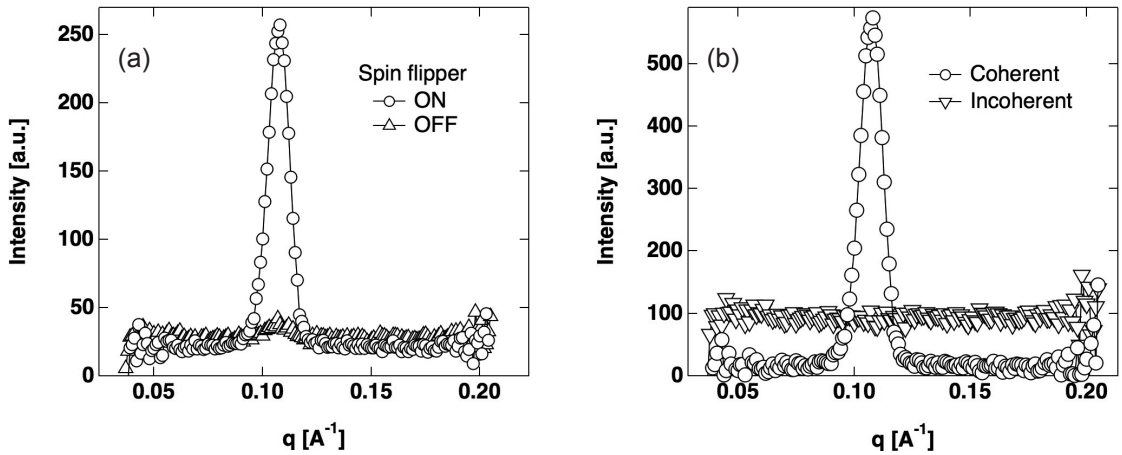

Figure 1. (a) Observed intensities, (b) Coherent and incoherent components.

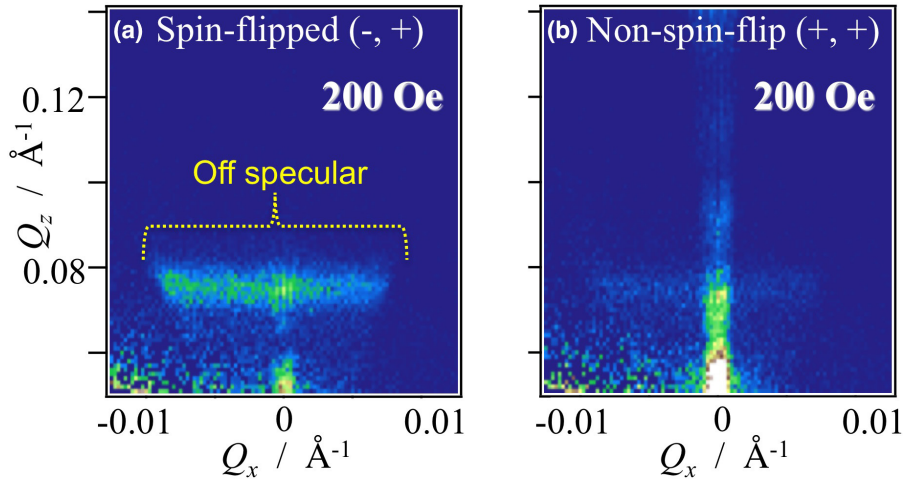

Figure 2. The measured reflected intensity with (a) the spin-flipped and (b) non-spin-flipped conditions.

and detected with the ^{3}He NSF and two-dimensional position sensitive detector. The ^{3}He NSF worked stably for 5 days during this experiment with P_{3He}~0.68.

Figures 2 (a) and (b) show the measured reflected intensities obtained with the applied magnetic field condition of 200 Oe with the spin-flip and non-spin-flip conditions. The specular peak and off-specular reflection around $Q_z = 0.08$ Å^{-1} are clearly observed in the spin-flip condition, indicating the existence of the antiferromagnetic correlations in the low magnetic field condition. These results are consistent with those reported in ref. [2].

References

[1] J.C. Dore, J.H. Clarke, J.T. Wenzel, Nucl. Instrum. Meth. **138** (1976) 317.

[2] M. Takeda *et al.*, Physica B **213-214** (1995) 248.

T. Oku[1], H. Hayashida[2], K. Sakai[3], T. Shinohara[1], M. Nakamura[1], S. Takata[1], K. Soyama[2], D. Yamazaki[2], K. Aizawa[1], M. Arai[1], M. Takeda[1,4,5], Y. Endoh[4], K. Kakurai[4], H. Kira[6], Y. Sakaguchi[6], K. Ohishi[6], H. Iwase[6], J. Suzuki[6], T. Ino[1,7], and K. Ohyama[8]

[1]Neutron Science Section, Materials and Life Science Division, J-PARC Center; [2]Neutron Instrumentation Section, Materials and Life Science Division, J-PARC Center; [3]Neutron Source Section, Materials and Life Science Division, J-PARC Center; [4]Quantum Beam Science Directorate, JAEA; [5]Department of Research Reactor and Tandem Accelerator, JAEA; [6]Neutron R&D Division, CROSS-Tokai; [7]Institute of Materials Structure Science, KEK; [8]Institute for Material Research, Tohoku University

Progress of Manyo-Library

1. Introduction

A data analysis environment has been developed to provide a software framework for neutron scattering experiments in MLF. The framework, Manyo-Library, has common and generic data analysis functionalities for neutron scattering experiments. Manyo-Library provides many kinds of functions, for example, data containers, data input/output functions, data-analysis operators and a distributed parallel data processing method.

Data analysis software applications built on the first version of Manyo-Library, ver. 0.1, were applied to the experiment data. The applications have been used in MLF from the day-one [1, 2]. The second version of Manyo-Library, ver. 0.2, has been installed to the neutron scattering instruments in MLF and utilized as an infrastructure of data analysis environment in each instrument. Data analysis efficiency has been improved and many analysis operators were developed and appended to the framework.

2. New release

In FY2012 we reviewed the framework. The obsolete functions in the framework were removed and the strategy for software development was modified. The functions of the framework were divided into two parts, the core-library and the MLF-library. The core-library consists of the data containers, the data input/output functions and the templates for data analysis operators, etc. The MLF-library contains the data analysis, especially data reduction, and operators, which are commonly used among the MLF instruments. The common data correction functions are going to be joined in the MLF-library. The applications for the inelastic instruments, Utsusemi, and the engineering diffractometer, Emaki, etc., were clearly separated as the add-on packages from the framework. The reviewed structure of Manyo-Library is shown in Fig.1. The latest version of Manyo-Library, ver. 0.3, was prepared in last October [3]. It is the first release version and consists of the core- and the MLF-library. Users can develop add-on packages for users' purposes on the framework.

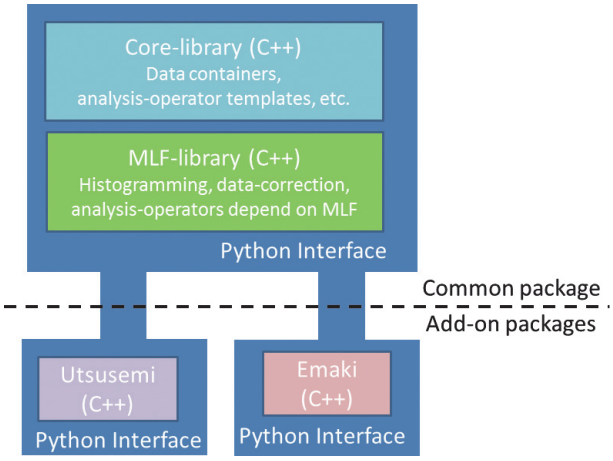

Figure 1. The structure of Manyo-Library released this year. The data analysis functions of Manyo-Library developed in C++ and python languages can be shared and called from the add-on packages, Utsusemi [4] and Emaki on Python environment.

3. Monitoring system with Manyo-Lib.

Here, we introduce a new application of the released Manyo-Library. The on-line monitoring system, which executes data reduction and visualization in the middle of a measurement, is strongly required by users. However, we had only a simple on-line monitoring provided by the DAQ-Middleware [5], which gives users just graphical plots or text data with a poor flexibility. On the other hands, the off-line analysis codes in Manyo-Library provide a lot of flexible and useful functions, for example time-dependent data analysis or higher dimension visualization. But these codes are not suitable for the on-line monitoring because they require a whole event data file at a time to analyze, so the data access process overloads the DAQ system and takes a lot of time to visualize data, especially on a long measurement.

To realize the on-line monitoring, we developed successfully a system to read and analyze only event data newly acquired by DAQ by means of repeated

observations of data files. This system is made possible by two developments. One is a new component of DAQ-Middleware to make indexes at the same time as neutron event recoding in order to enable fast access to a part of the event data files. The other one is a new function to make histogram by reading repeatedly incremental events using the index information of the event data files. As a result, a mount of events analyzed at a time is minimized and its processing time, including the visualization, shortens. This system can serve as an on-line monitor.

Not only does this system make it possible to take incremental events at a moment but it also summarizes all of them. In addition, we can change freely the interval time to obtain incremental events and the conditions for histogram making, data reduction and visualization during measuring. By using this method, various applications in measurement can be carried out on this system. For example, we can see the transformation of signal peaks at detectors on scanning measurements with drifting sample temperature or with moving slits window. In addition, the data analysis of the on-line monitoring condition finishes when the measurement ends.

This monitoring system has already been installed at BL17, SHARAKU, as shown in Fig.2. This is utilized to see the histogram data from the beam monitor detector at the beam line by using easy histogram viewer, which works almost like an on-line monitoring. We will expand this as a common system to be used at any instrument in MLF.

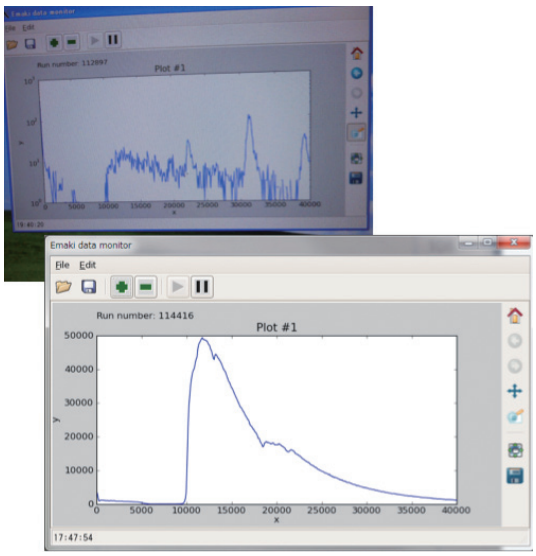

Figure 2. Screen shots of the on-line monitoring system in BL17.

4. Future Plans

We will continue to work on the refining of Manyo-Library. Some common functions for data correction and fitting developed in add-on libraries are going to be joined in the MLF-library. And now we prepare manuals and binary installation packages for Linux and Windows systems. Furthermore, we are discussing how to collaborate with the similar framework Mantid [6] used in other facilities. These tasks are needed to expand further the use of Manyo-Library.

References

[1] J. Suzuki *et al.*, Nucl. Inst. and Meth. Phys. Res. **A534** (2004) 175.

[2] J. Suzuki *et al.*, Nucl. Inst. and Meth. Phys. Res. **A600** (2009) 123.

[3] http://wiki.kek.jp/display/manyo/Manyo+Library+Home

[4] Y. Inamura, T. Nakatani, J. Suzuki and T. Otomo, Supplement of J. Phys. Soc. Jpn., to be published (Proceedings of QENS/WINS2012).

[5] K. Nakayoshi, Y. Yasu, E. Inoue, H. Sendai, M. Tanaka, S. Satoh, S. Muto, J. Suzuki, T. Otomo, T. Nakatani, T. Ito, Y. Inamura, M. Yonemura, T. Hosoya and T. Uchida, Nucl. Instr. and Meth. **A623** (2010) 537.

[6] http://www.mantidproject.org

J. Suzuki[1,2], Y. Inamura[3], T. Ito[4], and T. Nakatani[3]

[1]Computing Research Center, KEK; [2]Information System Section, J-PARC Center; [3]Neutron Science Section, Materials and Life Science Division, J-PARC Center; [4]Neutron R&D Section, CROSS-Tokai

Activity Report of the Sample Environment at J-PARC/MLF

1. Introduction

Sample environment (SE) plays an indispensable role in achieving the aims of the researchers' experiments and share of technical expertise. In this fiscal year, the SE technical team was well organized and not only started supporting the user experiments in utilizing the SE equipment but also joined various experiments to acquire specialized knowledge and accumulate experience. In addition, the utilities in the SE areas have been equipped completely, and the working circumstances have been improved.

2. SE equipment and Lending Service

The SE team has already equipped three pieces of SE equipment for common use in FY2011: a 7 T vertical-field superconducting magnet with an asymmetric coil pair (Fig. 1(a)), a ^{3}He-^{4}He dilution refrigerator insert, which can achieve 50 mK (Fig. 1(b)), and a high-temperature furnace with a niobium heater, which can be heated up to 1600°C in common use (Fig. 1(c)). In addition to them, a new top-loading ^{4}He cryostat with aluminum window (Fig. 1(d)) was purchased in FY2012. This cryostat can be fitted to both goniometers and vacuum scattering chambers in various BLs. The system is designed to be cooled down to 2 K by pumping the liquid helium, and even the dilution refrigerator insert can be set into the inner vacuum chamber.

The SE technical staff supported the operation of the superconducting magnet at BL17 in 2012A and at BL18 in 2012B, and the high-temperature furnace at BL14 and BL15 in 2012B. Since the SE technical staff had little experience and opportunity to operate the SE equipment, we took part in some users' experiments through the operation of an Orange cryostat, and ^{3}He cryostat, to acquire efficiently skills and experience.

We have lent SE peripheral apparatus and parts such as vacuum pumps, temperature sensors, cryogen containers, vacuum components, and so on.

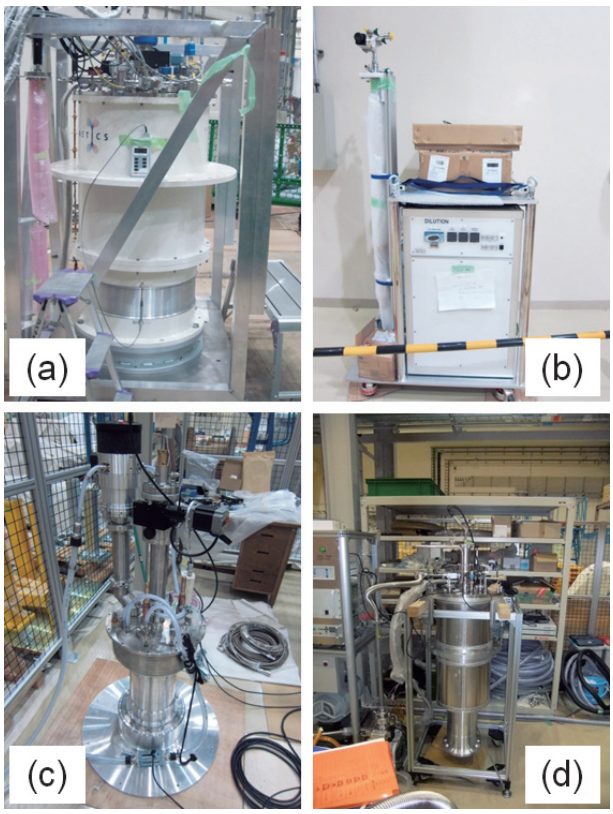

Figure 1. Common SE equipment managed by the SE team: (a) superconducting magnet, (b) dilution refrigerator insert, (c) high-temperature furnace and (d) ^{4}He cryostat.

The lending service information such as the lending procedure and specifications of each apparatus can be found on the MLF internal website.

3. KENS SE Equipment

Some of the SE equipment such as cryostats, furnaces, sample changers and goniometers, which used to be operated in the KEK neutron facility (KENS), were transported to J-PARC in 2011. Since we did not have most of the manuals, drawings, and peripheral apparatus and parts such as the cables and controllers, we had to investigate their structures, make up for the missing parts, and then check their safety in a test run. They can be reused, for instance as equipment for calibrating the tem-

perature sensors or as spare machines, after repair and modification to comply with the SE protocol.

3. SE Area

We have SE preparation areas in the MLF 1st and 2nd experimental halls to prepare and repair the SE equipment and to maintain its performance. Their utilities were obviously insufficient to do the tasks, because only electric power supplies, equipped as utilities at the first stage in FY2011, were available. In this fiscal year, we have equipped the other utilities such as water cooling, helium recovery, compressed air and exhaust gas line systems as well. Though the working circumstances are gradually being improved, the SE areas must be enlarged enough to manage the SE equipment whose number will increase in the future.

4. SE Workshop

The 7th International Workshop on Sample Environment at Neutron Scattering Facilities was held in Sydney, Australia, 17-20 September 2012. There were 52 participants including 6 members from J-PARC/MLF. S. Ohira-Kawamura reported on the current status of SE in MLF, and K. Munakata gave a talk about the introduction of CROSS and a high-pressure apparatus for neutron diffraction at low temperature. In this workshop, it was proposed to newly organize an international society for SE (ISSE) to activate collaborations and information sharing among the facilities. The site tour on ANSTO (Australian Nuclear Science and Technology Organisation) was scheduled at the final day of the workshop, and we visited the neutron experimental hall. The next SE workshop will be held near ISIS, UK, in 2014.

Y. Yamauchi[1], T. Yokoo[1,2], S. Ohira-Kawamura[1], Y. Kawakita[1], and W. Kambara[1]

[1]Neutron Science Section, Materials and Life Science Division, J-PARC Center; [2]Institute of Materials Structure Science, KEK

Activity Reports of the Chemical Safety Group in MLF

Working safety groups in MLF such as radiation, chemical, equipment, electricity, gas, and laser have been organized, to assure the safety and to support users. The chemical safety group has been designated to be one of them. The group is composed of thirteen members from J-PARC (JAEA and KEK), CROSS, and IBARAKI prefecture. Figure 1 shows the tasks of our group and the application process for a user experiment in MLF. We have four main tasks consisting of double review of samples' chemical safety, information management of samples, support of user's sample preparation, and maintenance of the sample preparation rooms in MLF. The 1st chemical safety review is performed on the samples in the experiment proposal submitted by users. We confirm their safety and the reactivity of samples and cells in the condition of the user experiments. If it is necessary to get any more information about the user's samples and each experiment's conditions to estimate the safety, we contact the user through the users office in J-PARC. The 2nd chemical safety review is conducted on the actually carry-in samples in the application form submitted by users with the above-mentioned viewpoints in mind. The information of all samples is managed according to the use of the application. Please note that the deadline for submitting the application is ten days before of the user's experiment day. We also check the status of all samples on each beam line after the user's experiments. In addition, we maintain the sample preparation room and support the user's sample preparation. There are two sample preparation rooms in MLF. One is the radiation controlled area of category 1 for treating the radioactivated samples by neutrons and the other is that of category 2 for treating the non-radioactivated samples. Those rooms have some necessary devices for the user's sample preparation and measuring the sample physical properties such as concentration, density, pH, and humidity. The manual for utilizing those devices is also prepared in English for foreign users.

Figure 2 shows the transition on the number of user's application form of carry-in samples in MLF

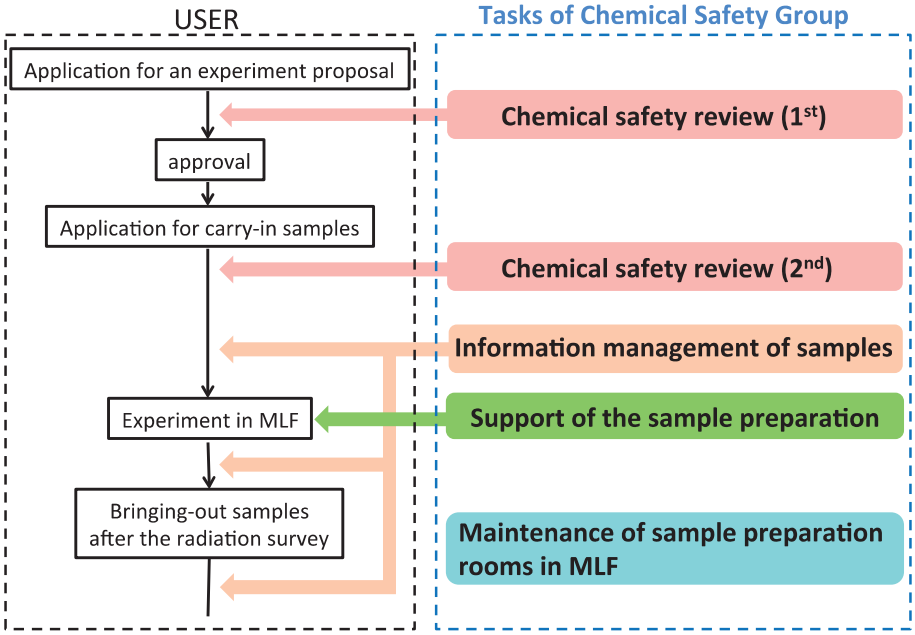

Figure 1. Tasks of chemical safety group.

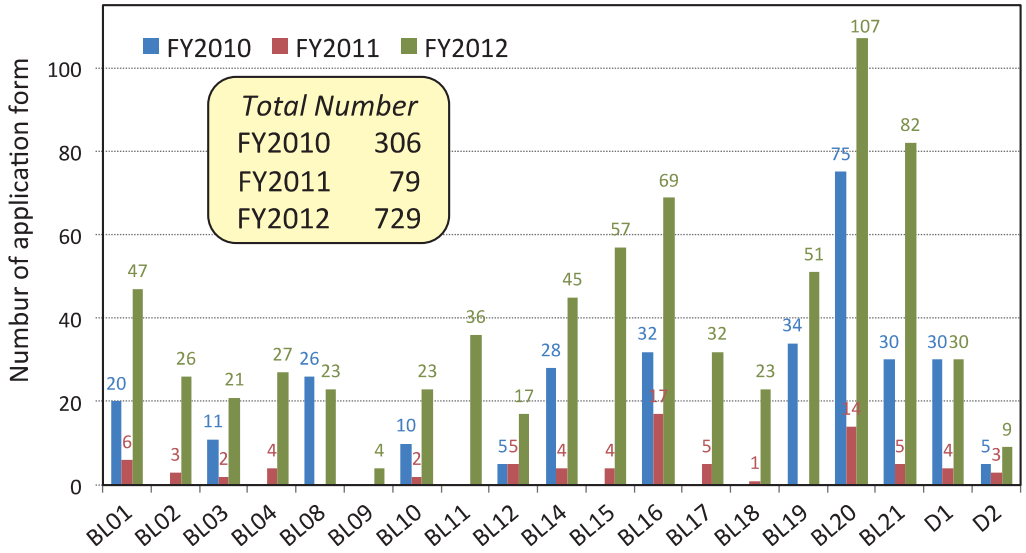

Figure 2. Transition on the number of user's application forms of carry-in samples in MLF for the last three years.

on each beam lines for three years from FY2010. In FY2012, BL20 received the largest number of user proposals, and the next was BL21. The reason why both beam lines are popular is because of the neutron diffractometers, also the measurement time for a sample is quite short so that they can accept so many users. As shown in the insert in Figure 2, the total number of application forms was 306 in FY2010, 79 in FY2011, and 729 in FY2012. If we exclude FY2011 when J-PARC was affected by the Great East Japan Earthquake, the total number in FY2012 had more than doubled since FY2010. This is due to the seven newly-constructed neutron instruments and the increase of the beam power from about 100 kw to 200 kW. We plan to increase the beam power up to 1 MW within a few years. It should follow that the number of the application forms and our group's amount of work will drastically increase.

We keep on working so that the users can perform their experiments safely and comfortably.

S. Ono[1], S. Takata[1], N. Takahashi[1], H. Kogawa[2], K. M. Kojima[3,4], M. Sakaguchi[4], M. Kobayashi[5], K. Akutsu[5], and S. Tanaka[6]

[1]Neutron Science Section, Materials and Life Science Division, J-PARC Center; [2]Neutron Source Section, Materials and Life Science Division, J-PARC Center; [3]Muon Science Section, Materials and Life Science Division, J-PARC Center; [4]Institute of Materials Structure Science, KEK; [5]Neutron R&D Division, CROSS-Tokai; [6]Science and Technology Promotion Foundation of IBARAKI

$ZnS/^{10}B_2O_3$ Ceramic Scintillator Contributing to Nuclear Security

In the recent years, there has been a severe shortage in the supply of ^{3}He gas. Thus there is an urgent need to develop detector technologies alternative to the conventional ^{3}He-gas-based detector. Our scintillation detector developed in the J-PARC/MLF may ameliorate the present situation in fields where neutrons need to be measured.

We have developed two-dimensional scintillator detectors using a new material ($ZnS/^{10}B_2O_3$) for detection of high-intensity neutrons in the past and a numbers of the detectors have been delivered and in service at the beamlines of BL03 (iBIX), BL17 (Sharaku) and BL18 (SENJU).

The $ZnS/^{10}B_2O_3$ ceramic scintillation detectors are planned to be implemented to a non-destructive measurement equipment for nuclear safeguard demonstration testing [1]. The scintillator material was originally developed for neutron scattering instruments in the J-PARC/MLF. The scintillator contains no organic materials, and its properties, high detection efficiency and fast temporal response, are also useful to measure neutrons from substances such as U and Pu contained in a mixed oxide nuclear canister. The plan calls for 60 or more of these detectors to be installed in the equipment designed by the Nuclear Science and Engineering Directorate of the JAEA, and the neutron measurement should proceed with high detection efficiency.

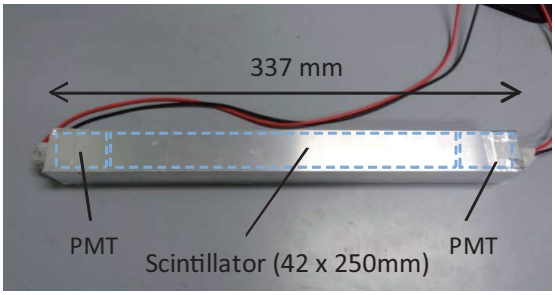

Figure 1. A prototype detector equipped with a $ZnS/^{10}B_2O_3$ ceramic scintillator for a nuclear security application.

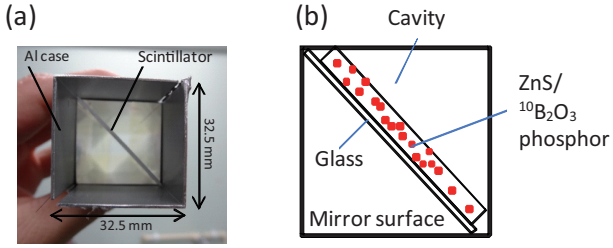

Figure 2. (a) Photograph and (b) schematic view of the detector (cross sectional view).

References

[1] T. Nakamura *et al.*, in the proceedings of the 54th Annual Meeting of the Institute of Nuclear Materials Management (INMM54).

T. Nakamura[1], K. Toh[1], K. Honda[2], K. Suzuki[3], H. Yamagishi[3], K. Sakasai[1], K. Soyama[1], and M. Katagiri[4]

[1]Neutron Instrumentation Section, Materials and Life Science Division, J-PARC Center; [2]Japan Radiation Engineering Co. Ltd.; [3]Nippon Advanced Technology Co. Ltd.; [4]Frontier Research Center for Applied Atomic Sciences, Ibaraki University

High Pressure MWPC Neutron Detector for Pulsed Neutrons

A two-dimensional position-sensitive neutron detection system that can read out individual signal line and consists of a multiwire-type detector element was fabricated for J-PARC/MLF BL17 and the first irradiation test was performed using a collimated neutron beam. Neutron irradiation was carried out using a CN-3 cold neutron beam line at KUR. The irradiated neutron detection system consists of a 256 channel multiwire detector element (x: 128 lines, y: 128 lines) equipped into a pressure vessel, amplifier-shaper-discriminator (ASD) boards, optical signal transmission devices, position encoders with field-programmable gate arrays (FPGAs), and a fast data acquisition device. The pitches of each axis are 1 mm and the conversion gap is 25 mm.

An imaging experiment was performed to verify an operation of the position encoder. As an example of the experimental results, a measured two-dimensional image is shown in Fig. 1. In this experiment, 9 collimated neutron beams with a size of 0.7 x 1.0 mm^2 were irradiated to the detector. It was confirmed that the position encoder works well and can be used in a neutron detection system. The spatial resolution of our detector was less than 2 mm FWHM in both directions. Considering the Monte Carlo simulation results [1], this value appears to be reasonable. Fig. 2 shows the reactor power dependence to the measured counts of the developed detector system. The developed detector showed a linear response up to the full power, 5 MW, of KUR reactor and the counting rate at 5 MW was approximately 45 kcps. The linear response for counting rate greater than 45 kcps can be observed easily by irradiating with a higher flux of neutrons, because the counting rate of our system was not saturated.

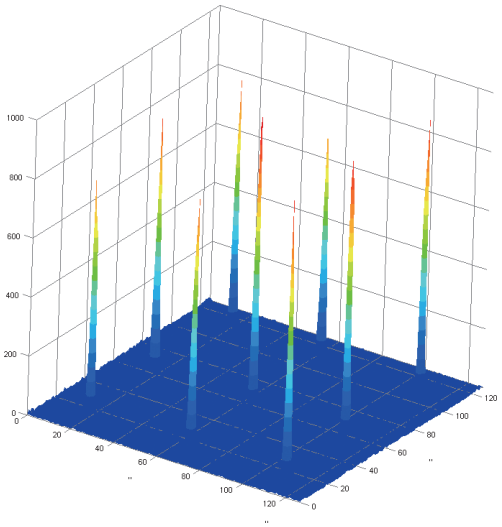

Figure 1. Two-dimensional response obtained using a collimated beam with a size of 0.7 × 1.0 mm^2.

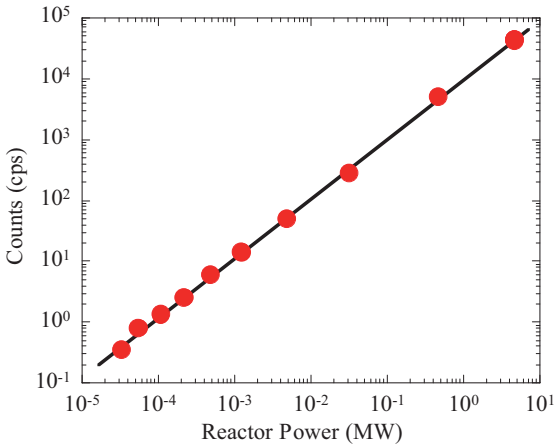

Figure 2. Measured counts of developed system under neutron irradiation as a function of KUR reactor power.

References

[1] H. Yamagishi, K. Toh, T. Nakamura, K. Sakasai and K. Soyama, J. Instrum. **6** (2011) C12025.

K. Toh[1], T. Nakamura[1], K. Sakasai[1], K. Soyama[1], M. Hino[2], M. Kitaguchi[2], and H. Yamagishi[3]

[1]Neutron Instrumentation Section, Materials and Life Science Division, J-PARC Center; [2]Research Reactor Institute, Kyoto University; [3]Nippon Advanced Technology, Co. Ltd.

Focusing Supermirrors on Precisely Figured Elliptical Surfaces

1. Introduction

Reflective optics is one of the most useful techniques for focusing a neutron beam with a wide wavelength range since there is no chromatic aberration.

We have been developing aspherical supermirror optics by using an ion beam sputtering technique to coat high performance supermirrors [1] and a numerically controlled local wet etching (NC-LWE) technique [2] to figure aspherical mirror substrates.

Previously, we fabricated a plano-elliptical supermirror with a clear aperture with size of 90 × 40 mm^2 by applying these techniques and obtained a focusing gain of 6 and a reflectivity of 0.64-0.7 in the critical-angle region for $m = 4$ [3]. Increasing the mirror size is essential for increasing the focusing gain. We report the fabrication result of an elliptical supermirror with large clear aperture size and the focusing performance of the neutron beam.

2. Mirror Fabrication

We fabricated a 400-mm-long elliptical neutron-focusing supermirror by a combined fabrication process consisting of precision grinding, HF dip etching, NC-LWE figuring, low-pressure polishing and ion beam sputtering deposition. We succeeded in obtaining a figure error of 0.43 μm p-v with a surface roughness of less than 0.2 nm rms.

3. Experimental setup and result

The focusing performance of the fabricated elliptical supermirror was evaluated at BL10 NOBORU. We show a schematic of the setup for measuring the neutron beam profile in Figure 1. A flat supermirror with $m = 4$ is used to reflect the neutrons into the focusing device to reduce the background and the gamma radiation from the direct beam. The wavelength of the neutron beam varied from 3.5 to 10 Å. Two-dimensional images of focused and non-focused direct neutron beams were measured using an imaging plate (Fujifilm BAS-ND; resolution: 50 μm). The width of the slit in this experiment was 0.10 mm. The magnification of the optical design was 1.

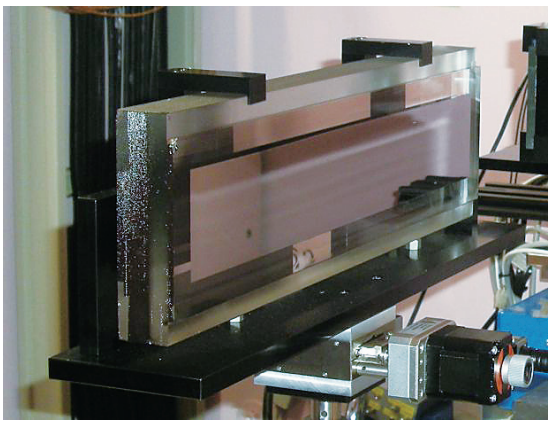

Figure 2. A photograph of the 400-mm-long elliptical neutron-focusing supermirror.

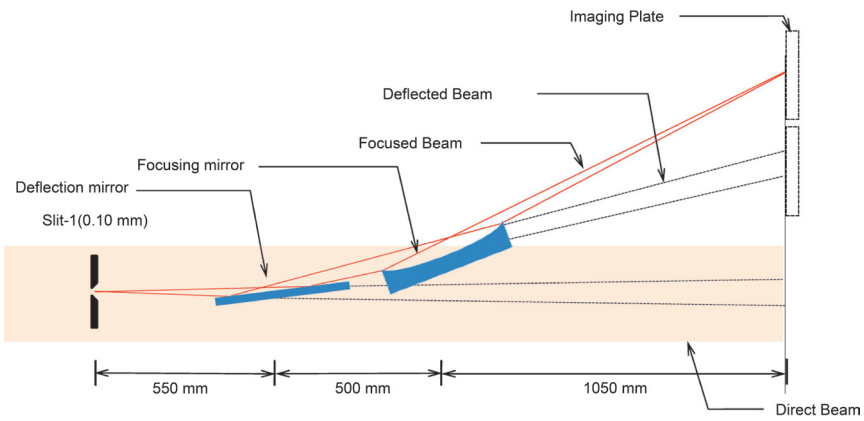

Figure 1. A schematic of the setup for measuring the neutron focusing profile.

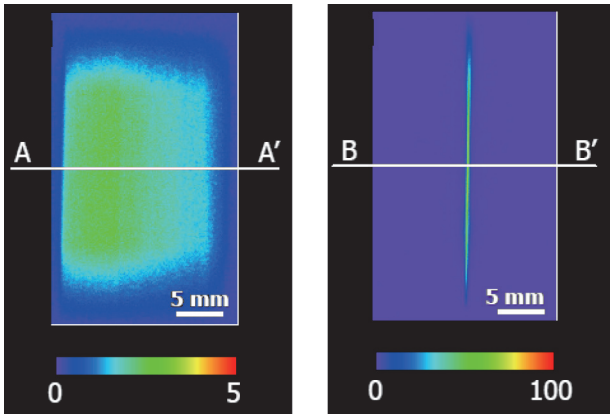

Figure 3. 2-d images of focused beam.

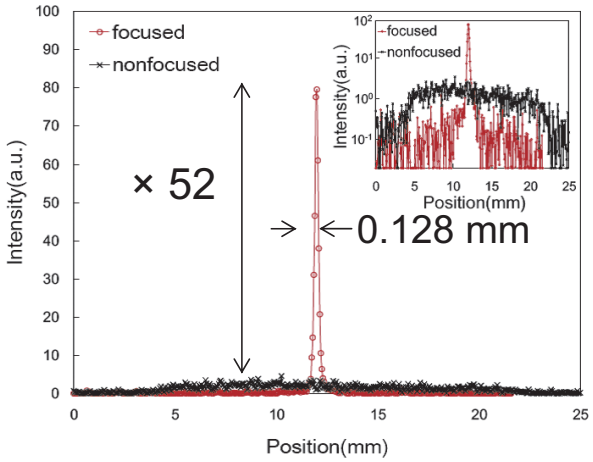

Figure 4. Neutron profiles of focused beam.

Figure 3 (A) and (B) shows two-dimensional images of focused and non-focused direct neutron beams, the neutron beam detected using the imaging plate. A neutron beam with a wide wavelength range was uniformly focused on the mirror where it had an effective width of 30 mm. The neutrons detected beyond the mirror were due to the horizontal divergence of the neutron beam.

Figure 4 shows detail profiles of (A) and (B). The full width at half maximum (FWHM) of the focused beam was 0.128 mm, and a focusing gain of 52 in terms of the peak intensity was achieved compared with the non-focused direct beam. At the peak intensity for a neutron beam, the wavelength range is 3.5-10 Å.

References

[1] R. Maruyama, D. Yamazaki, T. Ebisawa, M. Hino, K. Soyama, Thin Solid Films, **515** (2007) 5704.

[2] R. Maruyama, D. Yamazaki, T. Ebisawa, K. Soyama, J. Appl. Phys. **105** (2009) 083527.

[3] K. Yamamura, Ann. the CIRP **56/1** (2007) 541-4.

[4] D. Yamazaki *et al.*, J. Phys.: Conf. Ser. **251** (2010) 012076.

D. Yamazaki[1], R. Maruyama[1], H. Hayashida[1], K. Soyama[1], M. Nagano[2] , F. Yamaga[2], and K. Yamamura[2]

[1]*Neutron Instrumentation Section, Materials and Life Science Division, J-PARC Center;* [2]*Graduate School of Engineering, Osaka University*

Development of a Multi-Channel Spheroidal Focusing Mirror

1. Introduction

Some focusing devices are well used to increase neutron intensity for a minute area such as a small sample. Focusing mirror is the major focusing device and several types of it have been developed. In general, coating the surface of the focusing mirror with high-Q_c supermirror and enlarging the size of the mirror are an effective method to increase the gain of neutron intensity by covering a wide divergence of neutron beams. However, in some instruments, many other devices have already been installed and narrow space is allowed for setting the docusing device and a compact one should be required. A multi-channel focusing mirror enables us to cover a wide divergence of neutron beams even in a narrow space. In this study we tried to develop a multi-channel spheroidal (MS) focusing mirror.

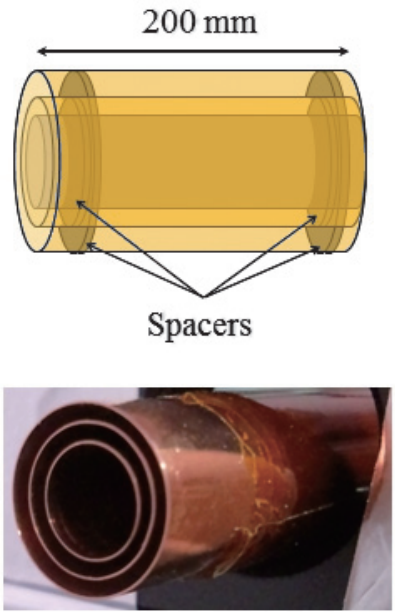

Figure 1. The conceptual diagram and picture of the prototype MS focusing mirror.

2. Experimental setup and result

Figure 1 shows a conceptual diagram and picture of a prototype MS focusing mirror. The prototype MS mirror consists of cupper uncoated by supermirror with 200 mm length. The MS mirror is fabricated by three spheroidal mirrors with different diameters. The diameters at the center are 5.512 mm, 7.348 mm and 9.186 mm from inside, respectively. These three spheroidal mirror are held coaxially using ring shape of aluminum spacers as shown in fig. 1.

Figure 2 shows a schematic diagram of a performance test of the MS mirror at BL10 NOBORU. A pinhole slit with diameter 0.1 mm was set at the focal point position which is 300 mm downstream of the MS focusing mirror. A 2D-detector was set after the pinhole slit. A supermirror was set at upstream of the MS focusing mirror in order to protect the detector from high-energy direct beams.

Figure 3 shows a result of the performance test of the MS mirror. The red (circle) and blue (square) lines correspond to TOF spectrum with and without

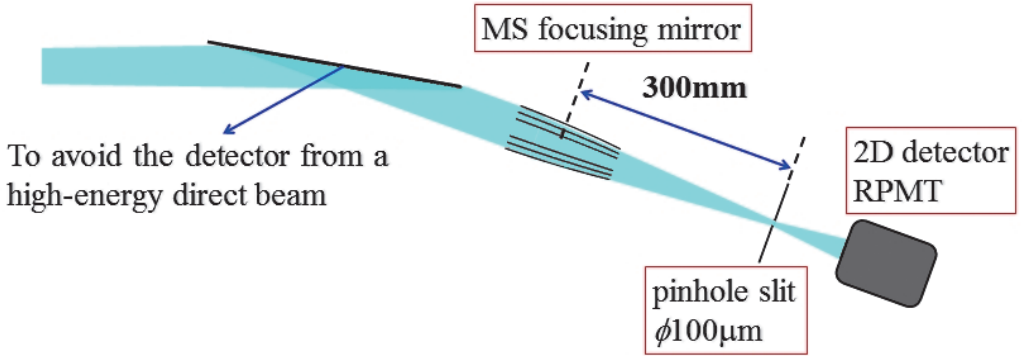

Figure 2. Schematic diagram of the experimental setup at BL10 NOBORU.

the MS focusing mirror. The black line shows the intensity ratio of these spectrums. The result shows that the intensity gain of neutron beam is about 6 for wavelength longer than 0.5 nm, which is about 70% of expected spec. Since the alignment precision of the three spheroidal mirrors affects directly the neutron gain, the alignment method and precision has to be improved.

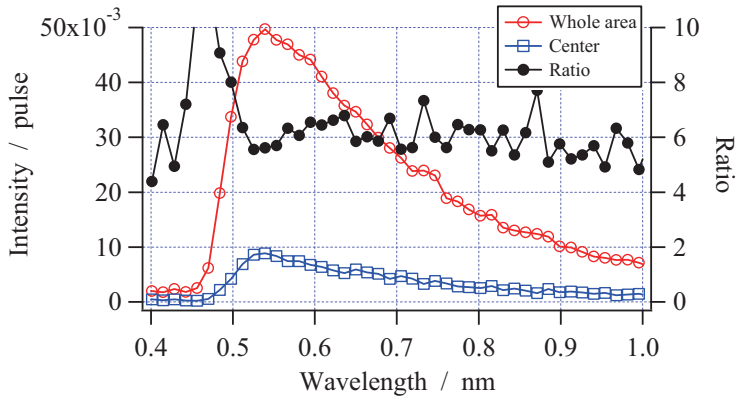

Figure 3. The result of the performance test of the MS mirror.

H. Hayashida, K. Soyama, D. Yamazaki, and R. Maruyama
Neutron Instrumentation Section, Materials and Life Science Division, J-PARC Center

Scenes from the Neutron Experimental Hall

Manuel Angst, Joerg Voigt, and Hailey Williamson from FZJ discuss their experimental data in the BL01 cabin.

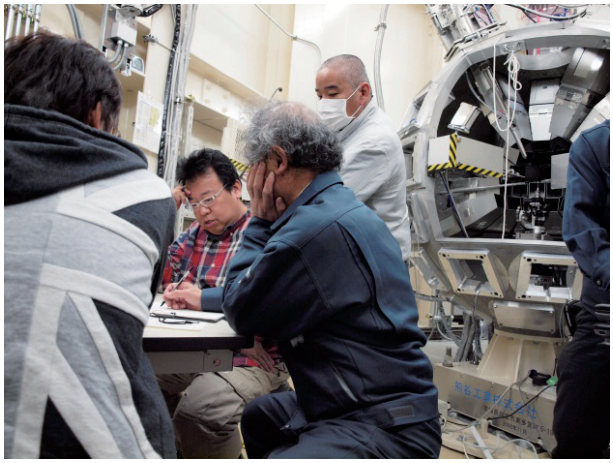

Takaaki Hosoya, Katsuhiro Kusaka, Masaki Katagiri, and Seiji Ninomiya (Ibaraki Univ.) discuss detectors at BL03.

Users and beamline staff – shown in the BL11 cabin - enjoy the first high-pressure neutron experiment.

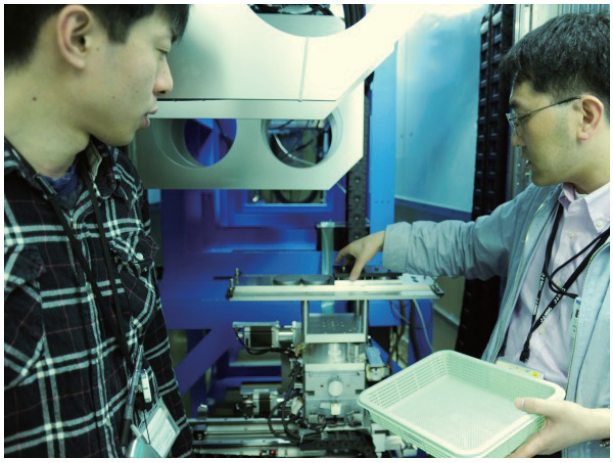

Norifumi L. Yamada (KEK) and Motoyasu Kobayashi (JST/ERATO) position samples at BL16.

Keitaro Kuwahara (Ibaraki Univ.) loads a sample in the refrigerator at BL14.

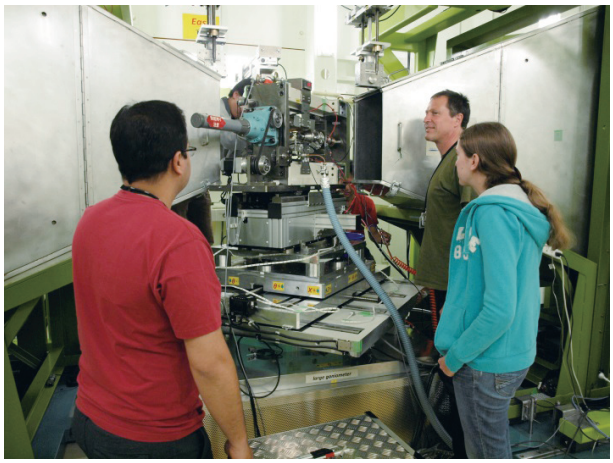

Klaus Dieter Liss (ANSTO), Saurabh Kabra (ISIS), and Lisa Thoennessen (ANSTO, Wollongong Univ.) discuss thermal and loading schedules for their in-situ experiments at BL19.

Muon Science

Status of J-PARC MUSE

At MUSE, we have had a steady operation at the D-line in the fiscal year of 2012. At the U-line, we managed to install a new axial focusing muon beamline components to extract intense surface muons dedicated for the ultra slow muon production. Also, we completed the installation of front-end magnets in the vicinity of the muon target during a shut-down period in the summer of 2012 under an intense radiation field.

1. D-line Operation

Consequently, we managed to operate users' run at the D-line with proton intensity of up to 300 kW. We installed a switch yard, a kicker and septum magnets to allow a single bunched muon beam up to 60 MeV/c towards D1 and D2 areas in the D-line. Everything worked successfully, delivering a single pulse towards the D1 area, with negligibly small S/N ratio appeared in the μSR spectrum. At the D1-area, a dilution refrigerator which had been used at KEK-Tsukuba, was brought to MUSE, fixed and installed, enabling us to perform μSR measurements as low as 25 mK.

2. Installation of the U-line

We were funded to install a second muon beamline, the so called U-line, which consists of a large acceptance solenoid made of mineral insulation cables (MIC), a superconducting curved transport solenoid magnet and a superconducting axial focusing magnets system. There, we can collect surface muons with a large acceptance of 400 mSr. Compared to the conventional beamlines such as the D-line, the large acceptance of the front-end solenoid allows us to capture 10 times more intensity pulsed surface muons of 5×10^8 /s, when the proton beam intensity reaches 1 MW. The U-line components of the superconducting curved and axial focusing magnets were already fabricated and their commissioning was performed in October, 2012. Fig.1 (Up) shows a picture of the celebration of the delivery of the superconducting curved transport solenoid magnet. Fig.1 (Down) shows a picture of the superconducting axial focusing magnets associated with three sets of ±400 kV DC separators.

In the commissioning works, we succeeded in extracting the world's highest intensity pulsed muons, 2,500,000 muons per pulse (6.4×10^8 /s at 212 kW, corresponding to 3×10^8 /s at 1 MW) to the U1 experimental area. This intensity achieved at the U-line exceeds the previous intensities, 72,000 muons per pulse (120 kW) and 180,000 muons per

Figure 1. (Up), picture of the celebration of the delivery of the superconducting curved transport solenoid magnet. (Down), picture of the superconducting axial focusing magnets associated with three sets of ±400 kV DC separators.

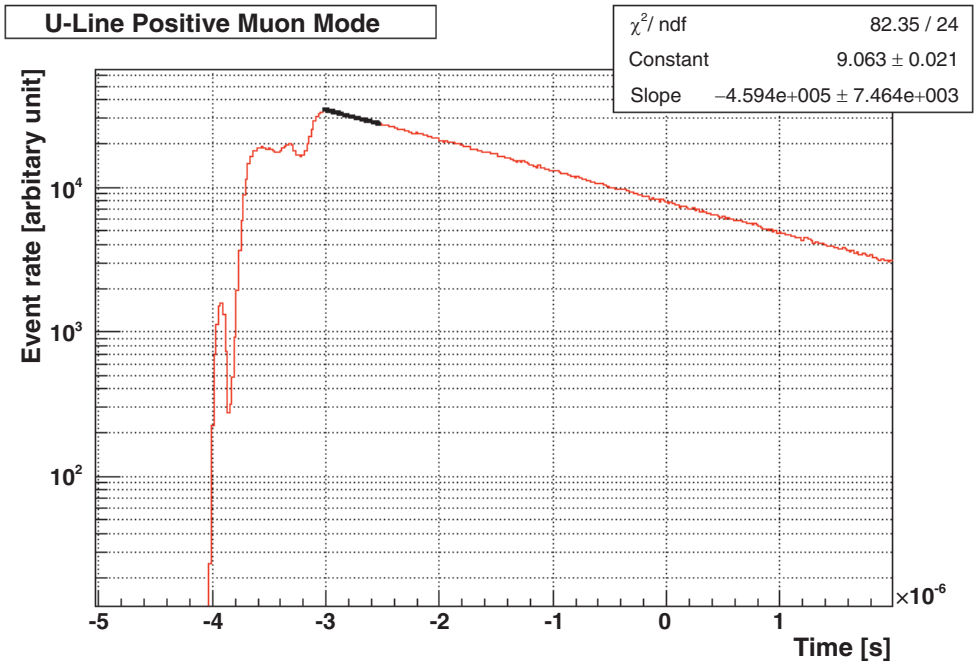

Figure 2. Lifetime spectrum of the surface muons extracted to the U1 area, showing 2 bunched structure of the surface muons and electrons. It demonstrated that surface muons as much as 6.4 × 10^7/s @212 kW were extracted to U1 shielding area, corresponding to 20 times stronger than D-line.

pulse (300 kW), which were achieved at the D-line of this facility in 2010, respectively. It means that for the first time globally we achieved the world's strongest pulsed muon intensity. The achieved intensity not only shortens the measurement time to one-twentieth compared with the present measurement, but it also may open a new era to capture novel information that could not be recognized before. According to the simulation, we could extract 2 × 10^8 /s surface muons (at the 1 MW operation) to the experimental area, with an approximate transport efficiency of 40%. It demonstrates that the beam line design concept adopting axial focusing extraction for the first time is working very well. Fig. 2 shows a lifetime spectrum of the surface muons extracted to the U1 area on Al target, showing 2-bunched structure of the surface muons and electrons. It demonstrated that very intense surface muons as much as 6.4 x 10^7/s @212 kW were extracted to the U1 shielding area, which was 20 times stronger than the D-line.

As a next step, we are planning to stop such intense pulsed muons towards a hot tungsten target for generating intense ultra-slow muon beams in order to realize "ultra-slow muon microscopes". When the production of an intense ultra-slow muon source is realized, the use of its short-range penetration depth (eg. 1 nm resolution at a penetration of 1 nm, and 10 nm at a penetration of 6 nm in gold) will allow the muon science to expand into a variety of new scientific fields, such as,

1) Surface/boundary magnetism utilizing its spin polarization and unique time-window.
2) Surface chemistry, utilizing a feature of a light isotope of hydrogen, such as catalysis reactions.
3) Precise atomic physics such as QED,
4) Ion sources towards possible μ^+ μ^- collider experiments in high-energy physics.

3. Installation of the front-end magnets for the S-line and H-line in the vicinity of the muon target

During a shut-down period in the summer of 2012, we worked on the installation of front-end magnets for the S-line, which is a surface muon beam line dedicated for the materials science with a modest-acceptance (about 50 mSr), and the H-line at which various problems of the fundamental phys-

ics research will be studied, for instance, the precise measurement of the hyperfine splitting of Muonium, implying the existence of new physics laws beyond the Standard Model, or the precise measurement of the anomalous magnetic moment (g-2) of muons,. Although the radiation level in the vicinity of the muon target was very high to be in the order of Sv/h, we finally managed to install the SQ4,5,6 and HS1, HS2, HS3 and HB1 associated with guide shields and pillow seals between those elements. Fig.3 shows a picture of the installation of the HS1,-HS2, HS3 and HB1 under a severe radiation environment in the vicinity of the muon target.

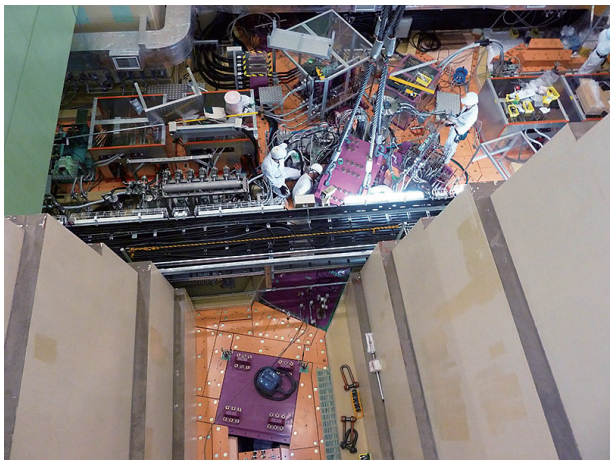

Figure 3. A picture of the installation of the HS1,-HS2, HS3 and HB1 in the vicinity of the muon target.

Y. Miyake[1,2], N. Kawamura[1,2], K. Shimomura[1,2], P. Strasser[1,2], A. Koda[1,2], H. Fujimori[1,2], S. Makimura[1,2], Y. Kobayashi[1,2], J. Nakamura[1,2], Y. Ikedo[1,2], T. Nagatomo[1,2], K. Nishiyama[1,2], K. M. Kojima[1,2], M. Miyazaki[1,2], R. Kadono[1,2], W. Higemoto[1,3], and T. U. Ito[1,3]

[1]*Muon Science Section, Materials and Life Science Division, J-PARC Center;* [2]*Institute of Materials Structure Science, KEK;* [3]*Advanced Science Research Center, JAEA*

Commissioning Test for the Remote-Controlled Replacement of the Muon Rotating Target

The most intense pulsed muon beam will be generated by a 3-GeV 333-μA proton beam on a muon target made of 20-mm thick isotropic graphite (IG-430) in J-PARC/MUSE (Muon Science Establishment). At present, the fixed edge-cooling method has been adopted for cooling the muon target [1]. However, it is predicted that the graphite will break down in six months due to radiation damage [2]. To extend the lifetime of the muon target, we are planning to adopt the rotating target method, which can distribute the radiation damage of graphite to a wider area. Figure 1 shows a picture of the rotating target. In the M2 primary proton beamline, some of the components will be so highly irradiated that it would make it impossible to perform hand-on maintenance. Therefore, the muon rotating target with a plug shield, called rotating target assembly, must be handled in a remote handling room, the *Hot cell* [3]. In this report, a commissioning test for the remotely controlled replacement of the muon rotating target during the summer-shutdown of 2012 is described.

Both the rotating target and the fixed-edgecooling target can be replaced by almost the same procedure as described below. Figure 2 shows a picture of the respective apparatuses used for the replacement in the *Hot cell*. Figure 3 shows a schematic drawing of the replacement. The *Target rod* consists of a stainless-steel rod with two joints, the muon target (the rotating target or the fixed edge-cooling target) and a profile monitor. The signal cables, the thermo-couples, and the water pipes go through the stainless rod. In the case of the rotating target, the rotating shaft must also go through it. When the used target is replaced, the whole *Target rod* is discarded. The *Target rod* is positioned by a horizontal pin and some guides to the plug shield and fixed by 4 bolts, which are handled by a remote-controlled power-manipulator. The exchange device ensures the up-down motion, the right-left motion, the forward-backward motion and the rotation to replace the *Target rod* from the plug shield. The

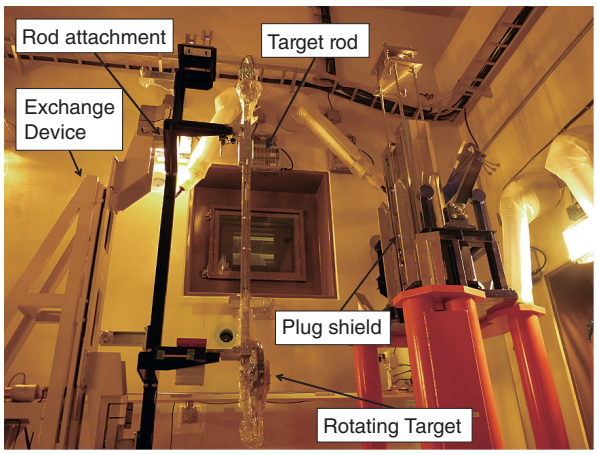

Figure 2. Apparatuses for replacement in the *Hot cell*.

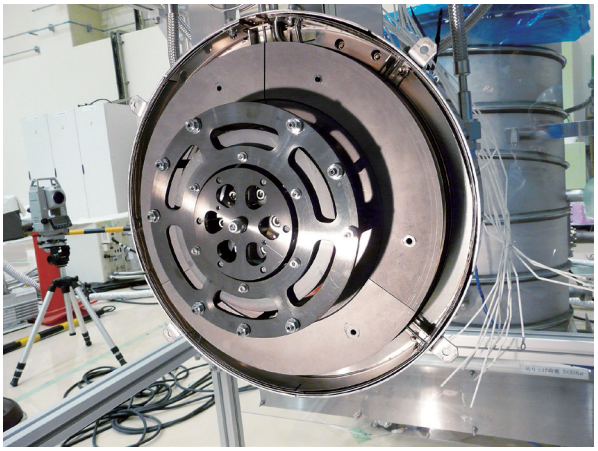

Figure 1. A picture of the muon rotating target.

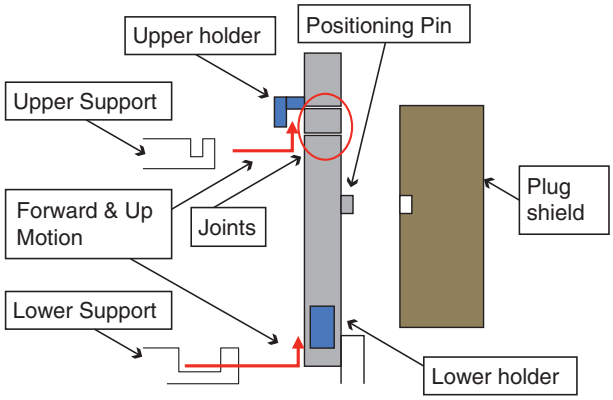

Figure 3. Schematic drawing of the replacement.

loads for each motion can be monitored. Because the exchange device is used in common with several other apparatuses for the neutron source, a rod attachment for our assemblies is necessary. At first, the empty rod attachment is attached to the exchange device. Then the upper and lower holders of the used *Target rod* are held by the upper and lower supports of the rod attachment, respectively. The fixing bolts are loosened by the power-manipulator, which can handle the bolts through remote control. Finally, the *Target rod* is dismounted from the plug shield by the upward and backward motion of the exchange device. The attachment with the used *Target rod* is remotely transported to the attachment rack by an overhead crane in the *Hot cell*. Then another attachment with a new *Target rod* is set on the exchange device by the crane. Finally, the new *Target rod* is fixed on the plug shield and the power-manipulator tightens the bolts.

The *Target rod* must be equipped with two weaker sections to be cut, so that it can be divided into three parts for volume reduction of the highly radioactive waste. These weaker sections will be elastically distorted under a load of 700 N at the positions of the holders. To avoid an excess load, we paid attention to how the misalignment of the attachment against the *Target rod* was detected and absorbed in the design of the rod attachment. In the case of the fixed target, there are two loose joints to facilitate the manufacturing and to absorb the misalignment. On the contrary, in the case of the rotating target, the joints need to be manufactured precisely, because several bearings supporting the rotating shaft must be coaxially and rigidly located. Furthermore, because the exchange device leans 3-mm forward when not sustaining the weight of the *Target rod*, the upper support against the lower support with the *Target rod* must be located 3-mm forward than the position without the *Target rod*. Therefore, several important features were implemented to the rod attachment. Positioning guides were used to the upper support to correct the slight left-right misalignment. A dial gauge was utilized to measure the relative position precisely between the plug shield and the rod attachment. Sustaining parts were also used to sustain the lean of the exchange device and the excess load due to the forward motion of the exchange device. On the lower support, the spring buffer is equipped to absorb the misalignment between the upper and lower support. The spring constant of the buffer is carefully designed not to exceed the elastic distortion of the

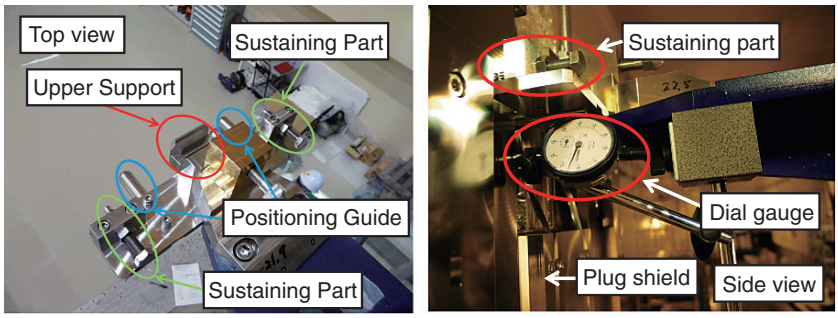

Figure 4. Pictures of the upper support.

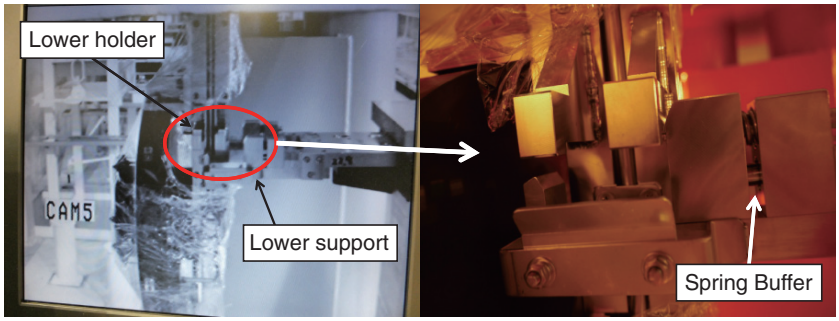

Figure 5. Pictures of the lower support.

Target rod. Simultaneously, the spring constant is also designed to give a load to fix the *Target rod* into the plug shield firmly. Figure 4 shows pictures of the upper support. On the left, the upper support can be seen. On the right, the upper support holds the upper holder while measuring the relative position against the plug shield. Simultaneously, the sustaining parts prevent it from going forward too much. Figure 5 shows pictures of the lower support.

The commissioning tests of the remotely controlled replacement of an un-irradiated rotating target were performed in August and September of 2012. After some preliminary tests outside of the *Hot cell*, the tests in *Hot cell* were performed from the 7th to 25th of September, 2012. The air radiation dose of our working area in the *Hot cell* depends on the cooling period after the proton-beam has stopped, the drainage status of the highly radioactive mercury from the neutron target vessel, and the existence of an additional shield. As a reference, the dose in 2012 at our working area, in the case of a cooling period of one month and without the additional shield, was 140 μSv/h. The dose was reduced to 2 μSv/h after a two months cooling period and with the additional shield. A half-face respirator mask with filters was required when we worked in our working area. Finally, the rotating target could be successfully replaced by remote handling. Figure 6 shows a picture of us before entering the *Hot cell*.

Figure 6. Picture of us before entering the *Hot cell*.

References

[1] S. Makimura *et al.*, Proceedings of the 8th Annual Meeting of Particle Accelerator Society of Japan (2011) 1188.

[2] S. Makimura *et al.*, Nuclear Instruments and Methods in Physics Research A **600** (2009) 146.

[3] S. Makimura *et al.*, Proceedings of the 7th Annual Meeting of Particle Accelerator Society of Japan (2010) 479.

S. Makimura[1,2], S. Onizawa[3], M. Ito[4], Y. Matsuzawa[3], R. Shimizu[3], and J. Nakamura[1,2]

[1]Muon Science Section, Materials and Life Science Division, J-PARC Center; [2]Institute of Materials Structure Science, KEK; [3]Nippon Advanced Technology Co., LTD; [4]ATOX Co., LTD

H Line Installation Work

A brand new beam line, H-line, is planned to be constructed as the 4th beam line in MUSE. The new beam line is designed to have a large acceptance, momentum tune-ability, and the ability to use a kicker magnet and Wien filter. This beam line will provide an intense beam for experiments which require high statistics and need to occupy the experimental areas for a relatively long period. Several experiments in the field of fundamental physics study have been proposed in the H-line [2-4].

From the muon production target, it is possible to extract 4 muon beam lines. The H-line is extracted to the south east direction.

At the primary stage of MUSE construction, only the D-line and the front-end magnets in the S-line were installed, and then the front-end magnets in the U-line were installed in 2009, as shown in Fig. 2. In the H-line, temporary radiation-shield blocks were placed. J-PARC has been operated since 2008, and thus the activation around the muon production target becomes more serious with every passing year. According to the evaluation using a Monte-Carlo code [5], the dose rate beside the target chamber was estimated to be close to 1 Sv/h, and the summer shutdown in 2012 would be the last chance for the installation of front-end magnets in the H-line.

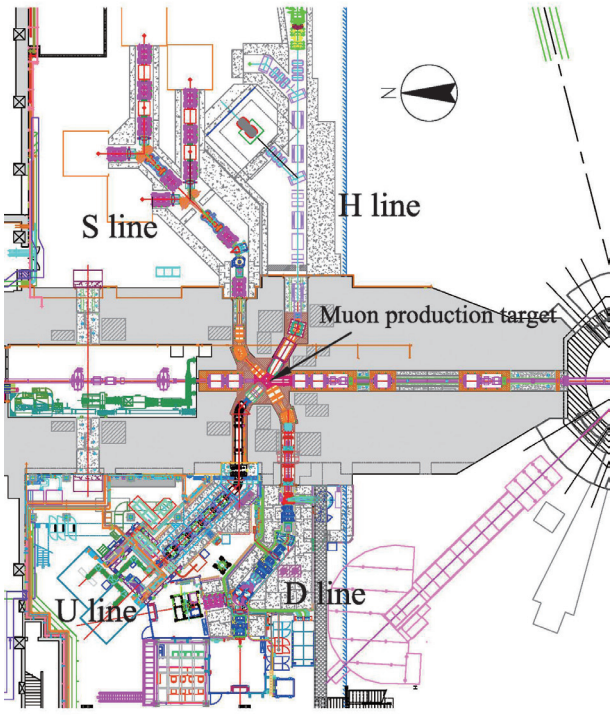

Figure 1. A layout plan of MUSE.

The frontend magnets, *i.e.* the muon-capture solenoid, HS1, and the first bending magnet, HB1, were fabricated and ready to be installed in June, 2012. The period of the shutdown was three months, from July to September. In addition to the H-line construction, a quadrupole triplet in the S-line had to be installed during the shutdown. The workplaces of these tasks are adjacent to each other, which required time sequential task management. In order to prolong the radiative cool time, the muon facility operation was terminated a week earlier than the J-PARC operation. Just after the beam stop, the S-line construction was started; it was estimated that the radiation dose rate at the work place was much lower than that of the H-line. The period of the S-line construction was effective for radiative cooling in the H-line. At the end of July, the H-line construction was started.

Taking into account the effect of the residual activity and the joint to the existing surrounding de-

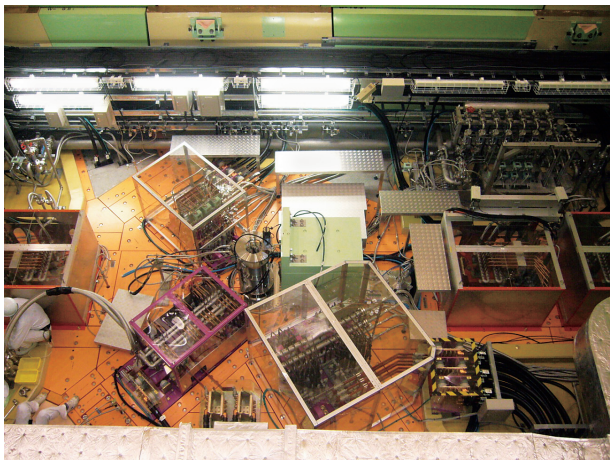

Figure 2. Picture around the muon target in 4/Jul before starting the construction.

vices, the scenario of the construction was well considered. The downstream half of HS1, HS1b, was installed under the irremovable existing cable ruck and cooling water pipes. At first, HS1b was placed on the special truck placed at around the position of HB1, and then the truck was pushed by a jack to be inserted into the proper position. By a special hanging tool, HS1b was slightly lifted up to remove the truck. After the installation of HS1b, HB1 was placed. The first gate valve, HGV1, is located at a position inaccessible by the crane. Thus, a special hanging tool was prepared. Finally, the upstream half of HS1, HS1a, was installed. Before the installation of HS1a, the activated iron blocks were removed, and were transported remotely to the temporary storage pit. All the devices shown in Fig. 4 were successfully installed, and the construction of the front-end part of the H-line was completed in early October, as shown in Fig. 5.

Because the H-line has a large acceptance, *i.e.* its aperture is large; the duct streaming neutrons is expected to increase. Thus, the radiation shield in experimental area #1 was reinforced. The magnets and the devices to be installed in the experimental

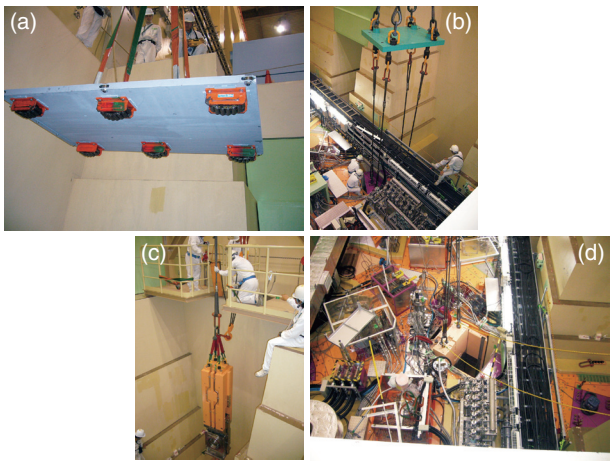

Figure 3. (a) the truck for HS1b; (b) the hanging tool for HS1b; (c) the hanging tool for HGV1; (d) removal of the activated iron blocks.

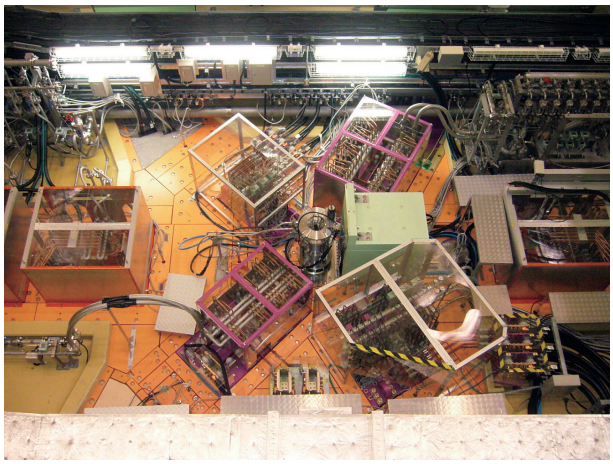

Figure 5. Picture in 4/Oct after completing the installation of major devices.

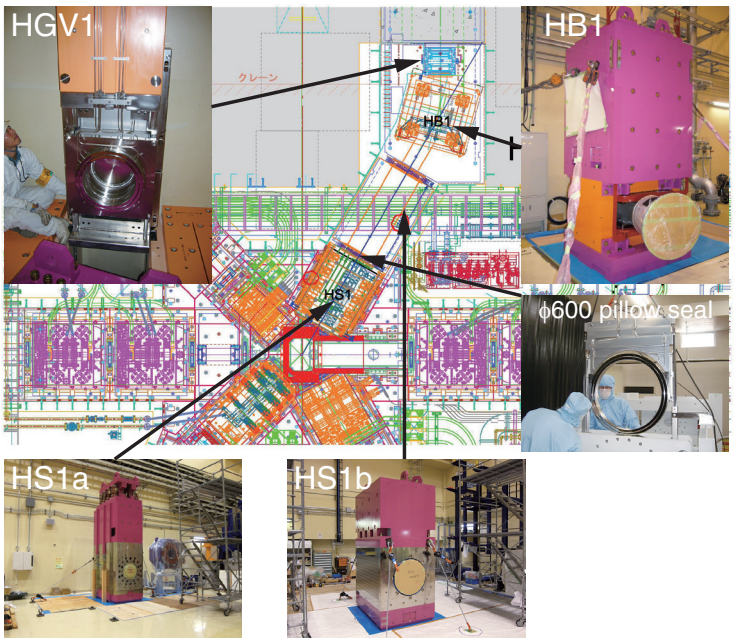

Figure 4. The installed devices.

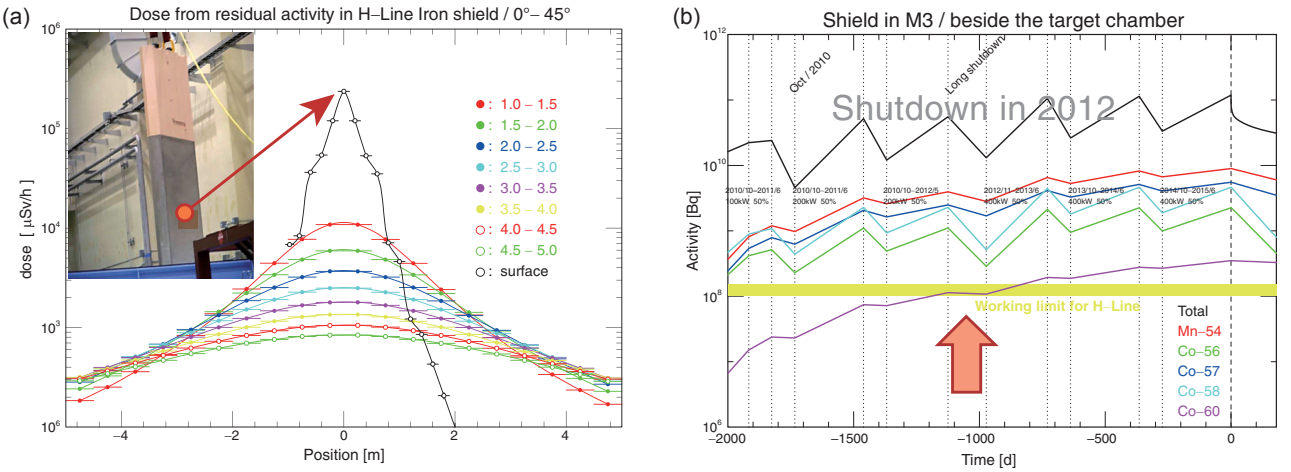

Figure 6. (a) the estimated radiation dose from the residual activity in the iron block beside the target chamber; (b) accumulation of the residual activity.

area are being designed as part of the installation work, which will start in 2014.

The highest measured radiation dose rate was about 250 mSv/h in the iron block placed just beside the target chamber. This is consistent with the prior evaluation. Thus, the construction scenario based on this estimation was confirmed to be reasonable.

References

[1] N. Kawamura *et al.*, *2013 Journal of Physics: Conference Series* **408** 012072.

[2] K. Shimomura *et al.*, *ibid*.

[3] N. Saito *et al.*, *ibid*.

[4] S. Mihara *et al.*, *ibid*.

[5] N. Kawamura *et al.,* 2009 *NIM A* **600** 114.

N. Kawamura[1,2], P. Strasser[1,2], A. Koda[1,2], and Muon Sci. Sec., J-PARC

[1]Muon Science Section, Materials and Life Science Division, J-PARC Center; [2]Institute of Materials Structure Science, KEK

Installation of Front-end Magnets for the S-Line

The construction of the surface muon beamline (S-line) in experimental hall No.1 of the Materials and Life science experimental Facility (MLF) building, which is designed to serve high intensity muon beams with a momentum of 28.5 MeV/c, has just started. When the construction of the S-line is completed, the S-line will consist of 4 beam legs and 4 experimental areas, sharing double pulsed muon beam by utilizing 2 electric beam kickers as shown in Fig. 1. The primary goal of the initial construction stage is to deliver a surface muon beam to one of the planned experimental areas (S1) in FY2013.

At the early stage of the construction of the M1/M2 primary proton beamline, a triplet magnet (SQ1-2-3), a bending magnet (SB1) and 4 pillow seals, adjacent to the muon production target chamber, were installed at the S-line. To extract the muon beam toward experimental hall No.1, a triplet magnet (SQ4-5-6), a beam duct (SVD2), and a pillow seal (SPS5) have been newly installed in the M2 beamline tunnel. Since these equipments are situated under the ceiling concrete shields at one of the *branching valleys* from the muon target, the utilities like the cable connection, the piping for the cooling water, the gas handling lines for the pillow seal, must be completed simultaneously. Moreover, the installation for the S-line must finish before the installation of the front-end magnet for the H-line starts, because both installations were scheduled during the summer shutdown in 2012. Due to the limited space in the handling area of the concrete shields, it was not possible to proceed simultaneously with these works.

Fig. 2 shows the installation of SQ4-5-6. The concrete shields at the beamline level were removed, and the guiding shield for SQ4-5-6 was installed, which is designed to provide both functions of the pillow seal guide and the duct support for SVD2. Before the installation of SQ4-5-6, SVD2 was attached from the inside of the M2 tunnel, and was aligned carefully. Fortunately, the residual radioactivity level of SQ4-5-6 position was not very

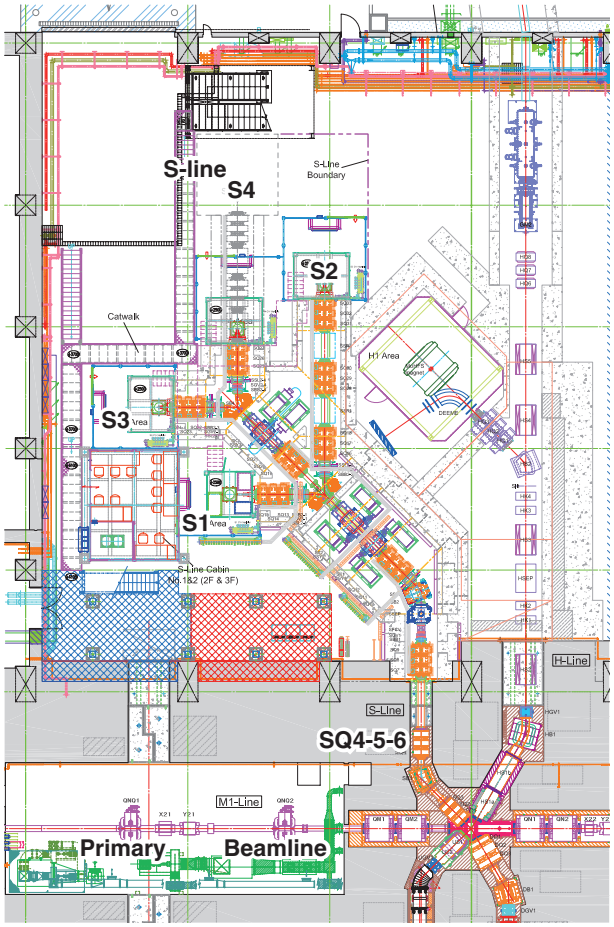

Figure 1. Beamline layout of the S-line (plan).

Figure 2. Installation of the SQ4-5-6 triplet magnet.

high despite its location relative to the muon production target. On the other hand, the concrete 5-ton shield at the exit of the secondary beamline tunnel , which was slightly moved due to the East Japan Earthquake in 2011, was re-aligned and securely fixed to the MLF building wall. Besides, as it was planned, the type-310 pillow seal, which was previously used at the front-end of the U-line as UPS1, and then stowed in a storage pit at FL10m after removal from the U-line, was re-installed at the S-line as SPS5. However, it turned out that the pillow diaphragm was partially damaged. Therefore, we decided to install a spare type-310 pillow seal as SPS5.

The main part of the construction was successfully completed in July, 2012. The construction of the S-line in experimental hall No.1 is expected to continue in FY2013, with the aim to conduct a beam test at the S1 experimental area.

A. Koda[1,2], P. Strasser[1,2], N. Kawamura[1,2], and J-PARC Muse staff
[1]*Muon Science Section, Materials and Life Science Division, J-PARC Center;* [2]*Institute of Materials Structure Science, KEK*

Installation of Superconducting Curved Solenoid for the U-line

In Japan Proton Accelerator Research Complex (J-PARC), installation of a new muon beamline, called Superomega muon beamline, was completed on the U-line in the Materials and Life Science Experimental Facility (MLF) in October 2012. The Superomega muon beamline is the second muon beamline among the four planning beamlines in the MLF/J-PARC. The Superomega muon beamline is a new type of muon beamline, since all beamline magnets in Superomega beamline consist of solenoid coils. The Superomega muon beamline consists of three parts: normal conducting capture solenoid, superconducting curved transport solenoid and superconducting axial focusing magnet. The capture solenoid has a large solid angle acceptance of 400 msr, so that a large number of muons can be captured and transported to the experimental area. The details of the properties and installations of the capture solenoid and the axial focusing magnet were already reported elsewhere [1, 2]. Here, we mainly report the properties and the installation of the superconducting curved solenoid.

The curved solenoid transports the captured muons through the secondary beamline tunnel into experimental hall No. 2. The solenoid consists of a 6-m long straight section placed between two 45° curved sections. The curved section is divided into seven segmented thin solenoids with an angle between each solenoids of 5.625°. In order to compensate a stray field from the straight section, matching solenoids are placed at the entrance and the exit of the curved solenoid. To satisfy the feasibility of fabrication of the solenoid, the straight section is divided into five 1.1.2-m long solenoids. These sixteen solenoids, except for the exit solenoid, are connected in series, while the exit solenoid can be adjusted separately. On the straight section, two dipole coils, which produce vertical opposite fields, with integrated fields of 0.2 Tm, are located near the center of the straight section. They provide charge selection required by the use of only positive muons or negative muons. For steering the beam direction and position of the beam center at the exit of the curved solenoid, two dipole correction coils with vertical and horizontal fields are located at the center of the exit solenoid.

A superconductor is commonly used for the solenoids and the dipoles. The solenoid coils use 85 A in series and the dipoles use 77 A individually. All of the cold masses, superconducting solenoids and dipoles, are designed to be conductively cooled by five Gifford-McMahon (GM) refrigerators with capacity of 1.5 W at 4.2 K (2nd stage) and 35 W at 50 K (1st stage).

The muon transport rate of the capture and the transport solenoids was simulated using G4Beamline. Captured muons by the capture solenoid are estimated to be 5×10^8 muons/s when the 3 GeV primary proton beam is incident on the muon production target. The simulation results show that the total transport rate of the captured muons with momentum of 30 MeV/c (surface muon) is 82% at the exit of the curved

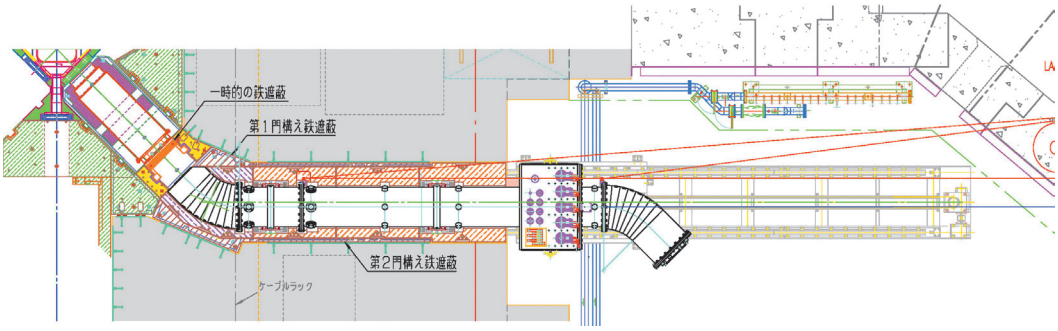

Figure 1. Top View of the solenoid insertion device and curved solenoid.

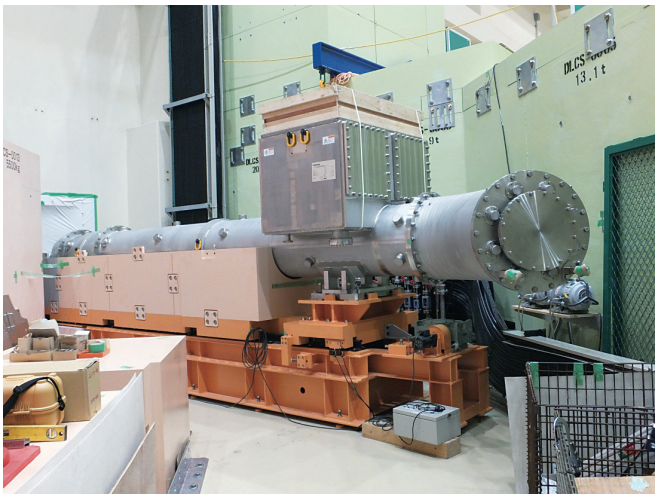

Figure 2. The curved solenoid and insertion device. The lower part of the iron radiation shield is also shown.

solenoid. This corresponds to 4×10^8 muons/s which are extracted into the experimental area. The main beam loss occurs at a gate valve located between the capture and the curved solenoids. This means that almost all muons incident on the curved solenoid are transported to experimental hall No. 2.

For the installation of the curved solenoid, we also developed an insertion device, because it will be set between the M2 tunnel and the experimental hall, as shown in Fig. 1-3. Six iron blocks, with a total weight of about 65 tons, are also set on the insertion device for the radiation protection from the M2 line. Therefore, we adopted two sets of linear guides for the horizontal transport motion to keep good reproducibility.

Figure 3. The curved solenoid was set proper position. A part of linear guide at the experimental area was also shown.

References

[1] K. Nakahara *et al.*, Nucl. Instr. Meth. Phys. Res. A **600** (2009) 132.

[2] Y. Ikedo *et al.*, MLF Annual Report 2012 145.

K. Shimomura[1,2], Y. Ikedo[1,2], Y. Miyake[1,2], P. Strasser[1,2], N. Kawamura[1,2], K. Nishiyama[1,2], S. Makimura[1,2], H. Fujimori[1,2], A. Koda[1,2], J. Nakamura[1,2], T. Nagatomo[1,2], Y. Kobayashi[1,2], T. Adachi[3], A. D. Pant[4], T. Ogitsu[5], T. Nakamoto[5], K. Sasaki[5], H. Ohata[5], R. Okada[5], A. Yamamoto[5], Y. Makida[6], M. Yoshida[6], T. Okamura[6], R. Okubo[6], W. Higemoto[1,7], T. U. Ito[1,7], K. Nakahara[8], and K. Ishida[9]

[1]Muon Science Section, Materials and Life Science Division, J-PARC Center; [2]Institute of Materials Structure Science, KEK; [3]Graduate School of Science, University of Tokyo; [4]Interdiscplinary Graduate School of Medicine and Engineering, University of Yamanashi; [5]Cryogenics Science Center, KEK; [6]Institute of Particle and Nuclear Studies, KEK; [7]Advanced Science Research Center, JAEA; [8]Department of Physics, University of Maryland; [9]Advanced Meson Science Laboratory, Nishina Center, RIKEN

Installation of Superconducting Axial Focusing Magnet for U-line

In the Japan Proton Accelerator Research Complex (J-PARC), the installation of a new muon beamline, called Superomega muon beamline, was completed on the U-line in the Materials and Life Science Experimental Facility (MLF) in October 2012. The Superomega muon beamline is the second muon beamline among the four planned beamlines in the MLF/J-PARC. The Superomega muon beamline consists of three parts: normal conducting capture solenoid, superconducting curved transport solenoid and superconducting axial focusing magnet. The details about the properties and installations of the capture solenoid and the curved solenoid were already reported elsewhere [1, 2, 3]. Here, we mainly report the properties and the installation of the axial focusing magnet.

The muon beam from the muon production target is extracted by the capture and curved solenoids to the experimental hall No. 2 of the MLF. The axial focusing magnet is located on the downstream of the curved solenoid. The major purpose of the axial focusing solenoid is to further transport the muon beam in the experimental hall (about 6 m long) and to efficiently focus on the ultra slow muon production target [4]. Furthermore, the axial focusing solenoid is equipped with functionalities required for the muon beamline, such as beam blocker, positron separator and beam slit. The beam blocker has a copper block of 600 mm in diameter and 50 mm in thickness. When experimenters work in the experimental area, the copper block can be inserted into the beamline by two air cylinders for reducing radiation exposure of the experimenters from mainly neutral particles, neutrons and gamma rays, in the beamline. The three stage Wien filter type of the positron separators can be applied $\pm$ 400 kV of electric field and 0.05 T of central peak dipole field. Since the positrons, which have the same momentum as the muons, are simultaneously transported in the muon beam, and their intensity is expected to be a hundred times larger than that of the muons, the positrons must be eliminated to allow precise measurement of the various purposes of the muon experiments [5]. The beam slit is located between the last two cryostats, in order to trim the edge of the muon beam, and to cut off the residual positrons through the separators.

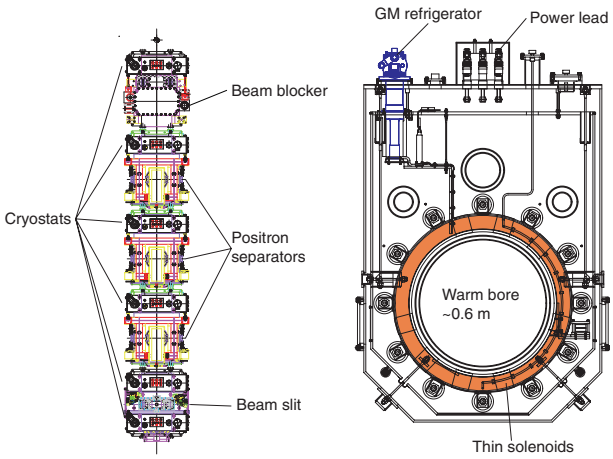

Figure 1. (a) Axial focusing magnet, (b) cryostat for superconducting solenoid.

Figure 1(a) shows a whole sketch of the axial focusing solenoid, and (b) is cryostat for the superconducting solenoid. The axial focusing solenoid is composed of six cryostats and five beamline vacuum ducts.The distance between the cryostats is 1.6 m, except for that between the fifth and sixth cryostats, which is 0.8 m. Each cryostat has two superconducting thin solenoid coils, and a warm bore of 600 mm in diameter for the beamline duct. The cryostat is cooled down by the thermal conducting method using a Gifford-McMahon refrigerator. The two solenoids in the cryostat can be individually excited up to 82.5 A, and the peak magnetic field of the two solenoids is about 1.2 T. The muon beam is transported with repeating cycle of focusing and defocusing by magnetic field of superconducting thin solenoids.

The installation and the alignment of the axial focusing solenoid were started from the end of August

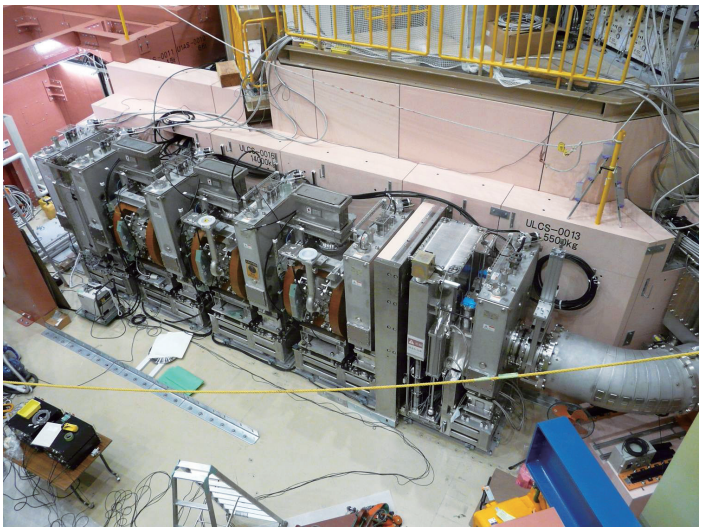

Figure 2. A picture of axial focusing solenoid.

of 2012. Firstly, five position adjustable base plates were aligned on the beamline with accuracy of less than 0.1 mm. The cryostat and beamline duct were placed on the same mounting, and then the mounting was set on base plate by positioning pins. Figure 2 shows the picture of the installed axial focusing magnet in the end of September. Electric cabling, cooling water and pressurized air piping were done after finishing the installation of the beamline apparatus, and the concrete shieldings were covered on the beamline. The Superomega muon beamline was ready to operate for the beam commissioning in the beginning of October.

According to our beam transport simulation using Geant4 based Monte-Carlo program G4Beamline [6], and the beam commissioning [7], the Superomega muon beamline can transport 6.4×10^7 positive muons /s to the end of the axial focusing magnet at 212 kW of the primary proton intensity, and more than 50% of them are incident on the ultra slow muon target (Tungsten foil: 70(W) × 50(H) × 0.05(T)) placed downstream of 700 mm from the last solenoid. At present, we proceed the project of the production of the ultra slow muon beam using the surface muon beam of the Super omega muon beamline and the vacuum ultra violet laser system [8].

References

[1] K. Nakahara *et al.*, Nucl. Instrum. Methods Phys. Res., Sect. A **600** (2009) 132.

[2] K. Shimomura *et al.*, MLF Annual Report 2012 143.

[3] Y. Ikedo *et al.*, KEK Progress Report 2012 18.

[4] T. Nagatomo *et al.*, MLF Annual Report 2012 162.

[5] T. Adachi *et al.*, in preparation.

[6] Muons Inc. 552 Nm Batavia Avenuue, Batavia, IL, available at http://www.muonsinc.com.

[7] Y. Ikedo *et al.*, MLF Annual Report 2012 182.

[8] J. Nakamura *et al.*, MLF Annual Report 2012 164.

Y. Ikedo[1,2], Y. Miyake[1,2], K. Shimomura[1,2], P. Strasser[1,2], N. Kawamura[1,2], K. Nishiyama[1,2], S. Makimura[1,2], H. Fujimori[1,2], A. Koda[1,2], J. Nakamura[1,2], T. Nagatomo[1,2], Y. Kobayashi[1,2], T. Adachi[3], A. D. Pant,[4], T. Ogitsu[5], T. Nakamoto[5], K. Sasaki[5], H. Ohata[5], R. Okada[5], A. Yamamoto[5], Y. Makida[6], M. Yoshida[6], T. Okamura[6], R. Okubo[6], W. Higemoto[1,7], T. U. Ito[1,7], K. Nakahara[8], and K. Ishida[9]

[1]Muon Science Section, Materials and Life Science Division, J-PARC Center; [2]Institute of Materials Structure Science, KEK; [3]Graduate School of Science, The University of Tokyo; [4]Interdisciplinary Graduate School of Medicine and Engineering, University of Yamanashi; [5]Cryogenics Science Center, KEK; [6]Institute of Particle and Nuclear Studies, KEK; [7]Advanced Science Research Center, JAEA; [8]Department of Physics, University of Maryland; [9]Advanced Meson Science Laboratory, Nishina Center for Accelerator-Based Science, RIKEN

Performance of the DC-separator at the U-line

In the Japan Proton Accelerator Research Complex (J-PARC), the installation of a new muon beamline, called Superomega muon beamline, was completed on the U-line in the Materials and Life Science Experimental Facility (MLF) in October 2012. The basic properties and the installation of the Superomega muon beamline were already reported elsewhere [1, 2, 3]. The last part of the Superomega is an axial focusing solenoid. One of its major purposes is the reduction of positron contamination from the muon beam. Three sets of Wien filter type separator combined with a superconducting axial focusing magnet were installed for this purpose.

For a short period before the installation, conditioning and performance tests were done for a single separator with a superconducting magnet at the U1 area. The results were not satisfactory. Without magnetic field, it was possible to apply stable high voltages of $\pm$ 320 kV on the electrodes under an argon gas environment with 2-5 $\times$ 10^{-2} Pa in pressure. The pressure was regulated with a mass flow controller and by steady pumping by turbo molecular pumps. Without the argon flow, the vacuum pressure was around 10^{-5} Pa and a stable operation was achieved at –230 kV for the cathode and +230 kV for the anode. Magnetic fields from the superconducting magnets had a strong influence on the discharge phenomena of the separator. The current of solenoid magnets reduces the applicable anode voltage, due to increase of the dark currents such as 175 kV at 40 A and 20 kV at 60 A. Contrarily, the cathode voltage can be slightly increased by solenoid magnetic field. The magnetic field of the correction coils for the separator affects less than that of the solenoid, and even with 340 A of the correction coil current $\pm$ 320 kV can be applied. For further investigation on the discharge phenomena, an acrylic blank flange was attached to the separator chamber and the inside view of the chamber was monitored through a large mirror by video camera. According to the observations of several days until the sudden interruption due to the video camera damage, the following information was obtained. By applying the high voltage, a continuous discharge illumination was observed on the surface of the ceramic bushings at both the cathode and the anode. High-voltage break-down due to an over-current interlock at the anode and successive overcurrent at the cathode were clearly observed. The video picture will be analyzed more systematically.

After the completion of the installation of the axial focusing solenoid, the performance of the three sets of separators was tested. As a general impression, the high voltages in the axial focusing solenoid were much more unstable than that of a single separator with single solenoid axial focusing magnet. A strong correlation between neighboring separators was observed, i.e., high-voltage break-down at neigh-

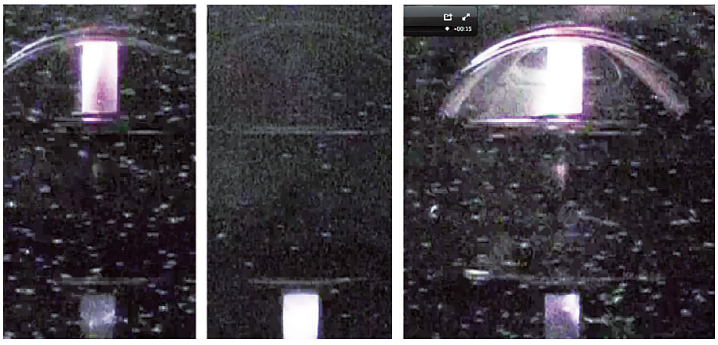

Figure 1. Pictures of the separator discharge. Break down at the anode (left) and successive dark current at the cathode (middle). Simultaneous break down on both electrodes (right).

boring separators was always caused even at low voltage excitation. Similar correlation was noticed even between the first and the third separators. The high voltage was successfully applied only on the center separator without magnetic field from the neighboring axial focusing magnets.

To avoid these difficulties, modified transport parameters for the axial focusing magnets were chosen. Instead of applying a periodic magnetic focus ing field over the separator region by the axial focusing magnets, we decided not to excite the neighboring solenoids of the second separator, and only the second separator was operated to eliminate the positrons.

According to our simulations, the beam transport efficiency of the axial focusing magnet is lower (60%), but the final beam profile is not affected by these parameter changes. However, expected positron separation is sufficient with one separator. In the original case, due to a magnetic field component along the beamline, the positron separation is less effective and three sets of separator are necessary.

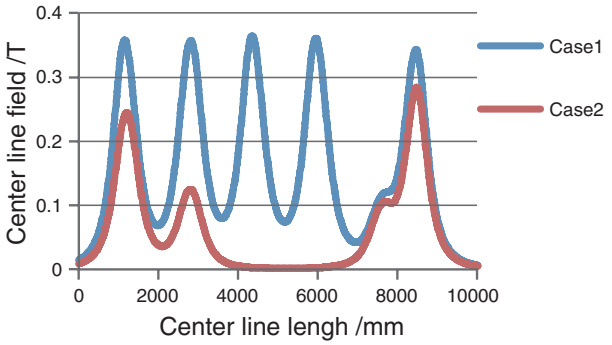

Figure 2. Magnetic field distribution of the original design parameters (case1) and the modied parameters (case2).

In the operation test using the new parameters of the axial focusing magnets, ± 350 kV was achieved at the center separator. However, frequent interruptions due to sudden discharge and shut down of the high voltage power supply by overcurrent interlock occurred. A procedure for an automatic recovery of high voltages was established. At first, the negative high voltage is started to sweep and after it reaches 100-150 kV, the sweep of the positive high voltage begins to rise.

As reported elsewhere, commissioning tests for the separator were successfully performed with the new parameters of the solenoid magnets. The positrons were sufficiently separated by a single separator as shown in Fig. 3 and Fig. 4. Fig. 3 shows the scintillation signal from a beam profile monitor at the focal position of the axial focusing magnet. The sufficiently reduced positron signals before the prominent muon signals can be seen in this picture.

A time spectrum of the μ-e decay positron counter is shown in Fig. 4. The spectrum clearly shows a μ^+ decay curve with a life time of 2.2 μs. The double bunch structure of the muon beam is also clearly seen in this spectrum. The positron prompts composed of scattered positrons by the target are sufficiently suppressed by the positron separator, although the intensity of the positrons in the muon beam was estimated to be 100 times larger than that of the muons [3].

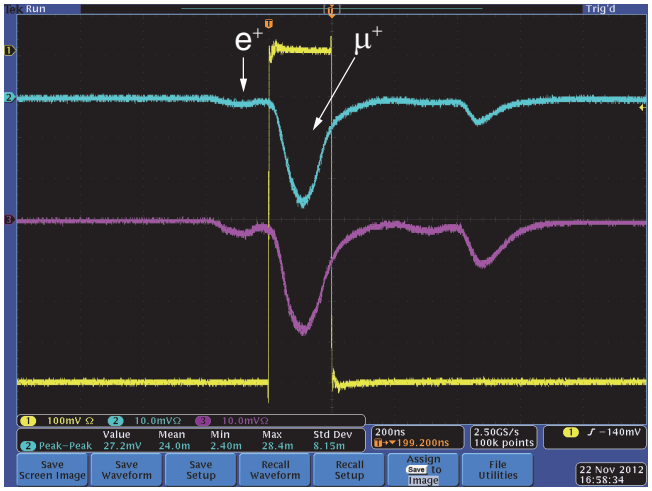

Figure 3. Beam structures seen on an oscilloscope.

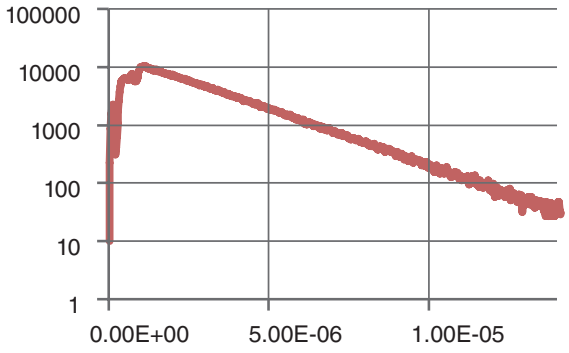

Figure 4. Time spectrum of the μ-e decay positron.

For a more efficient muon transport and smaller beam profile at the ultra slow muon target [4], an operation mode with three separators is necessary. Now we start to analyze the reason of the separator discharge under magnetic field. Also even for one separator mode, studies to find the conditions to achieve a more stable operation is needed, i.e., gas mixture and pressure optimization, insertion of foils between separator chambers, etc.

References

[1] K. Shimomura *et al.*, MLF Annual Report 2012 143.
[2] Y. Ikedo *et al.*, MLF Annual Report 2012 145.
[3] T. Adachi *et al.*, in preparation.
[4] T. Nagatomo *et al.*, MLF Annual Report 2012 162.

K. Nishiyama[1,2], Y. Ikedo[1,2], Y. Miyake[1,2], K. Shimomura[1,2], P. Strasser[1,2], N. Kawamura[1,2], S. Makimura[1,2], H. Fujimori[1,2], A. Koda[1,2], J. Nakamura[1,2], T. Nagatomo[1,2], Y. Kobayashi[1,2], T. Adachi[3], A. D. Pant[4], T. Ogitsu[5], T. Nakamoto[5], K. Sasaki[5], H. Ohata[5], R. Okada[5], A. Yamamoto[5], Y. Makida[6], M. Yoshida[6], T. Okamura[6], R. Okubo[6], W. Higemoto[1,7], T. U. Ito[1,7], and K. Ishida[8]

[1]Muon Science Section, Materials and Life Science Division, J-PARC Center; [2]Institute of Materials Structure Science, KEK; [3]Graduate School of Science, The University of Tokyo; [4]Interdisciplinary Graduate School of Medicine and Engineering, University of Yamanashi; [5]Cryogenics Science Center, KEK; [6]Institute of Particle and Nuclear Studies, KEK; [7]Advanced Science Research Center, JAEA; [8]Advanced Meson Science Laboratory, Nishina Center for Accelerator-Based Science, RIKEN

Kicker System – Noise Reduction at D-line –

1. Introduction

The muon kicker system is used to separate the muon pulses and feed them to two experimental areas (D1, D2) simultaneously. The beam operation with a kicker system started in the winter of 2011. Dividing the muon beam into two single-pulsed beams was successful, but anti-noise measures were required. Later, the kicker noise level was drastically improved through refining both the ground lines of the kicker system and the detectors. Figure 1 shows μe-decay spectra with kicker on/off. However, the kicker noise level is still high according to the S/N ratio of some detectors. Further measures to reduce the kicker noise were necessary.

2. Trial-and-error to reduce the kicker noise

First, the noise level of the feed-through terminals, which was the highest noise source of the kicker system, was reduced after being enclosed with copper sheets as shown in Fig. 2.

Then, the kicker chamber, which contains the two kicker magnets, the two switchyards and the two oil tanks with matching electric circuits, was completely covered with 2 mm thick aluminum plates. The kicker chamber, neatly fitted in an aluminum box in a narrow space sandwiched between concrete shields, is shown in Fig. 3.

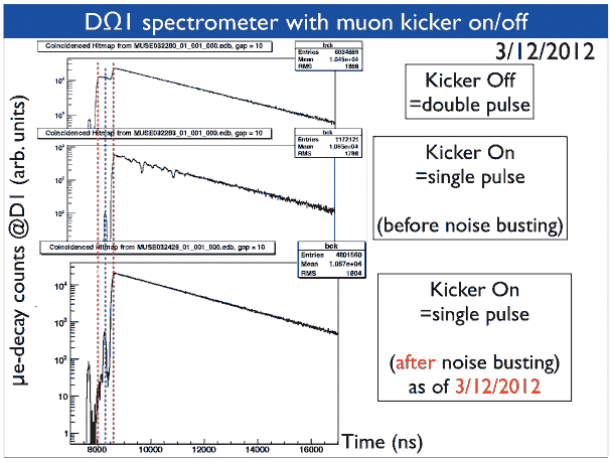

Figure 1. μe-decay spectra with kicker on/off.

Figure 2. The feed-through terminals enclosed with copper sheets.

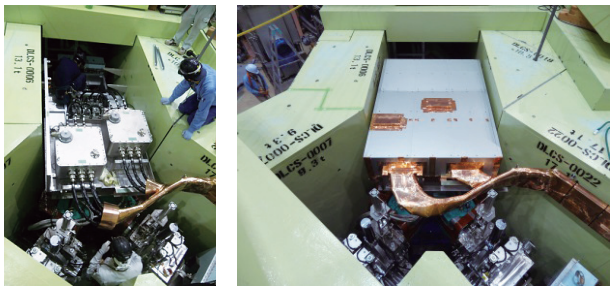

Figure 3. The kicker chamber fitted in an aluminum box.

Figure 4. Cable rack for the power cables shielded with copper sheets.

Furthermore, the whole cable rack for the power cables was also overlaid with 0.2 mm thick copper sheets, without any break point along its length, to shield the kicker noise as shown Fig. 4.

The noise levels were drastically improved after taking the above measures. Figure 5 shows a comparison between the noise levels using a radio wave detector [1] before and after taking these new noise reduction measures.

There was a remarkable improvement of 1/100 of the noise level at around the top of the kicker chamber. However, further improvements are re-

quired for experiments with negative muons and muoniums at the D2 area. Any conceivable means to reduce the RF noises can be employed, therefore insulating the kicker chamber from the beam ducts and their base is planned as the next trial-and-error project.

3. Summary

A kicker system was installed to separate the double-pulsed muon beam in the summer of 2011. The kicker system directed the two single-pulsed muon beams to the two existing experimental areas D1 and D2 simultaneously in March 2012. Now experiments with the spectrometer in D1 area can be performed with kicker-on without any problems, but the kicker noise level is still high to carry out experiments in D2 area simultaneously. Further measures to reduce the kicker noise are in progress for the next beam operation.

References

[1] H. Fujimori *et al.*, KEK-MSL Report 2011 (2012) 9.

[2] H. Fujimori *et al.*, Proceedings of the 8th Annual Meeting of Particle Accelerator Society of Japan, August 1-3, 2011, Tsukuba, Japan.

[3] P. Strasser, H. Fujimori *et al.*, Physics Procedia **30** (2012) 65.

[4] H. Fujimori *et al.*, KEK-MSL Report 2010 (2011) 10.

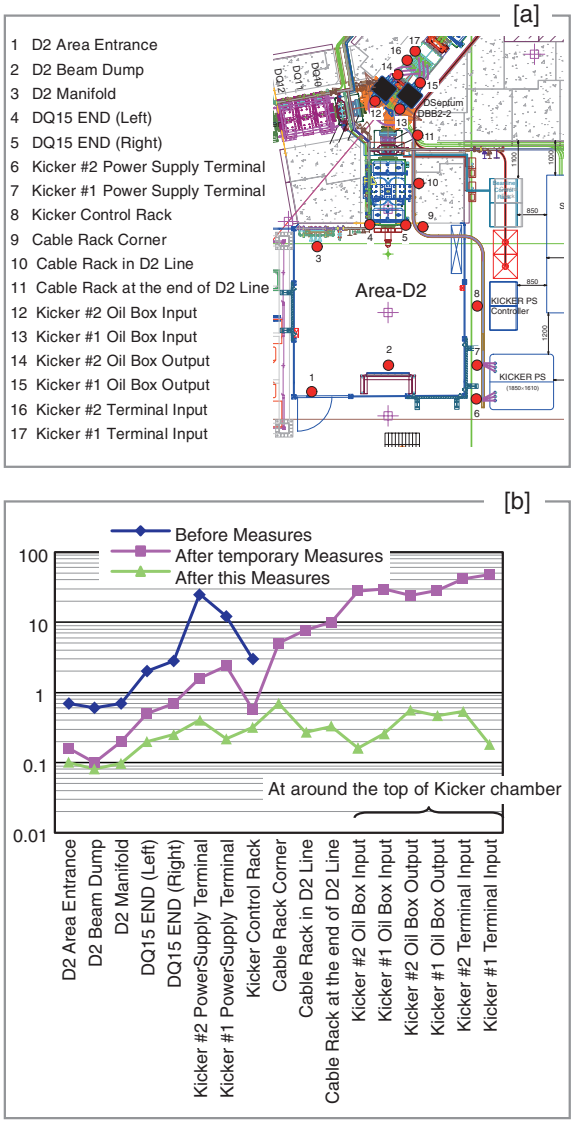

Figure 5. [a] Survey points around the kicker system. [b] Distribution of RF noise levels corresponding to local points around the kicker system.

H. Fujimori[1,2], Y. Irie[1,2], T. Nagatomo[1,2], S. Sakata[3], M. Meguro[3], N. Kurosawa[3], K. M. Kojima[1,2], P. Strasser[1,2], and Y. Miyake[1,2]

[1]Muon Science Section, Materials and Life Science Division, J-PARC Center; [2]Institute of Materials Structure Science, KEK; [3]Nippon Advanced Technology Co. Ltd. (NAT)

U-line Interlock System

We introduced an ultra-slow muon (USM) beamline as an extension of the U-line in the MUSE facility of J-PARC MLF. In this report, we describe the interlock system introduced to perform safety management of the USM beamline.

The interlock systems for the U-line

There is an area named U1 at the beam exit of the U-line where the USM beam is generated using an intense surface muon beam. The U1 area is isolated by radiation shield walls with limited access from a side door and from the top upon removal of a cell shield (see Fig.1).

The USM beam is transported to the U1 experimental area (U1A/B) adjacent to the shielded area. The human access to the U1 shielding area or U1 experimental area is allowed only when the muon beam is not supplied to those areas.

In order to protect the personnel working in these areas against radiation hazard, a muon blocker, a capture solenoid magnet and an access door are interlocked to the beam [personnel protection system (PPS)]. For further improvement of safety, the PPS system has fail-safe apparatus for stopping the muon beam.

The PPS devices for U1 shielding area consist of a capture solenoid US1 and the U-line muon blocker. Those for the U1 experimental area are two U1 area muon blockers (see Fig.2). The operation modes are summarized in Tables 1 and 2.

Table 1 shows the requirement for muon beam supply to the U1 shielding area and the U1 experimental area. And Table 2 shows the requirement for access to both areas.

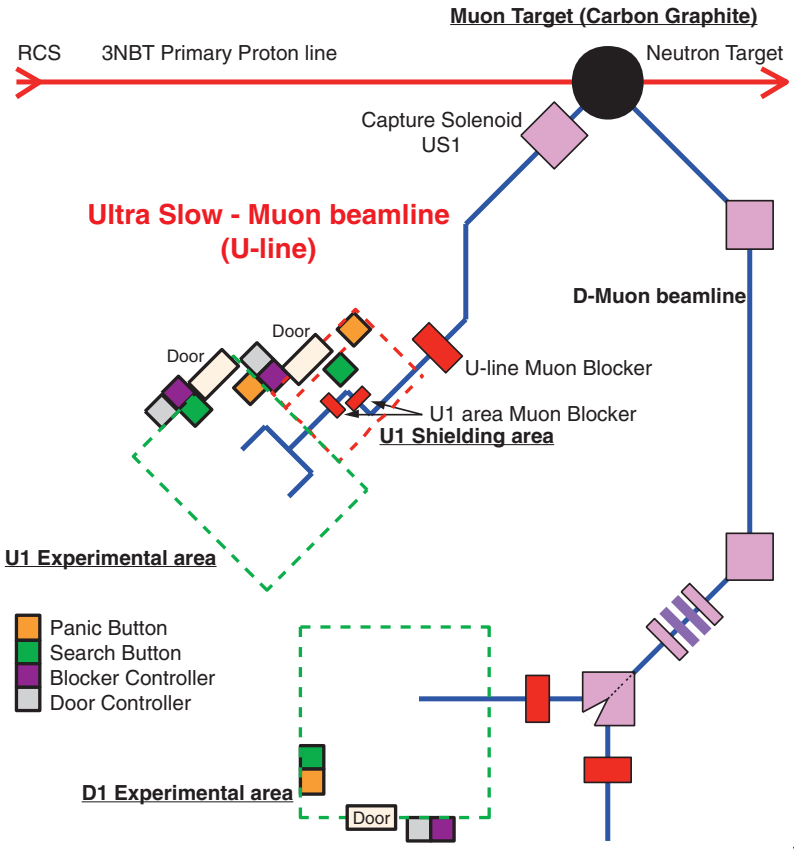

Figure 1. Schematic diagram of interlock devices for the U-line and the ultra-slow muon beamline.

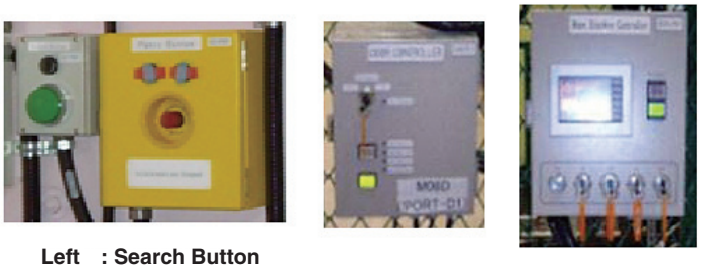

Left : Search Button
Right : Panic Button

Door Controller

Blocker Controller

Figure 2. PPS Interlock system controllers.

Table 1. Conditions for beam supply to the U1 shielding area and the U1 experimental area.

U1 shielding area muon beam "ON". (allowing to open U-line muon blocker and turn ON US1 power supply)	• U-line muon blocker controller all keys locked in. (U1 shielding area door closed and locked)
U1 experimental area muon beam "ON" (allowing to open two U1 area muon blockers)	• U1 area muon blocker controller all keys locked in. (U1 experimental area door closed and locked)

Table 2. Conditions for access to the U1 shielding area and the U1 experimental area.

U1 shielding area	• US1 OFF • U-line muon blocker closed
U1 experimental area	• Two U1 area muon blockers closed

Y. Kobayashi[1,2], N. Kawamura[1,2], K. Shimomura[1,2], W. Higemoto[1,3], and Y. Miyake[1,2]

[1]Muon Science Section, Materials and Life Science Division, J-PARC Center; [2]Institute of Materials Structure Science, KEK; [3]Advanced Science Research Center, JAEA

Magnetic Shields for W-target Chamber in U-line

In the Japan Proton Accelerator Research Complex (J-PARC), the installation of a new muon beamline, called Superomega muon beamline, was completed on the U-line in the Materials and Life Science Experimental Facility (MLF) in October 2012. The Superomega muon beamline is the second beamline out of the four planned beamlines in the MLF/J-PARC. The basic properties and the installation of the Superomega muon beamline were already reported elsewhere [1, 2, 3]. The final purpose of the Superomega muon beamline is the surface muon source for the ultra-slow muon beam. The ultra-slow muon beam is an innovative beam with significant characteristics of tunable energy, small beam size, *etc*. The production method of the ultra-slow muon was reported in this issue [4, 5]. At present, the ultra-slow muon beamline is under construction at the downstream of the Superomega muon beamline. The residual magnetic field from the Superomega muon beamline at the ultra-slow muon production target (W target), which is a tungsten foil of 70 mm in width, 45 mm in height and 0.05 mm in thickness, has a crucial influence to the ultra-slow muon beam properties, such as the extraction and the focusing of the beam [4]. Furthermore, the magnetic field normal to the beam direction, significantly reduces the spin polarization of the muon. To avoid these, we decided to construct a magnetic shield for the W target, which encloses the W target vacuum chamber. Here, we report on the magnetic shield for the W target placed 700 mm downstream from the last solenoid of the Superomega muon beamline.

In order to reduce the stray magnetic field at the W target from the solenoids of the Superomega muon beamline, we installed the magnetic shield surrounded W target vacuum chamber. This is made mainly of an extra-low carbon steel (SUYP1) plate of 20 mm in thickness. There are three plates normal to the beam axis of the Superomega muon beamline, and their dimensions are 1.2 m in width and 2.2 m in height for the first plate, 1.0 m in width and 2.4 m in height for the second and third one. The first plate which is made of ordinary iron, is placed right downstream of the last cryostat of the axial focusing solenoid, the second one is located at 100 mm apart from the first plate, the last one is 200 mm further downstream of the second one. Each plate has a hole for the beamline duct from the central axis of the beamline, and their diameters are 500, 400, 300

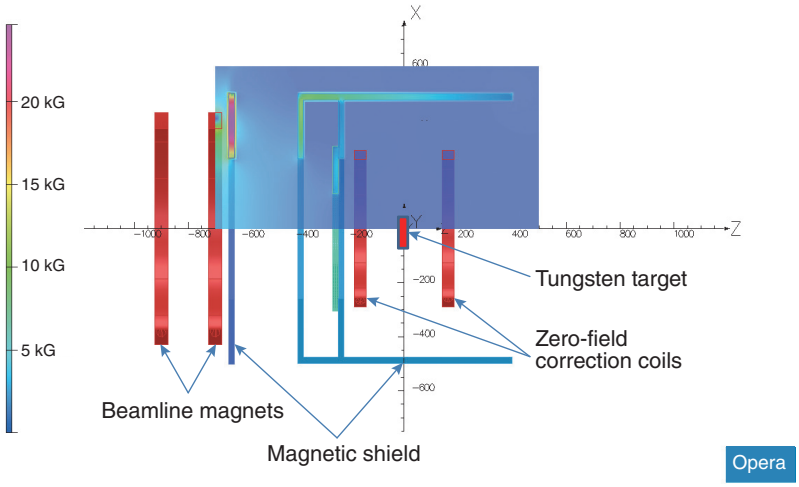

Figure 1. A top view of the magnetic shield for the ultra-slow muon production target. The upper region in the figure represents the magnetic field distribution by the superconducting solenoids.

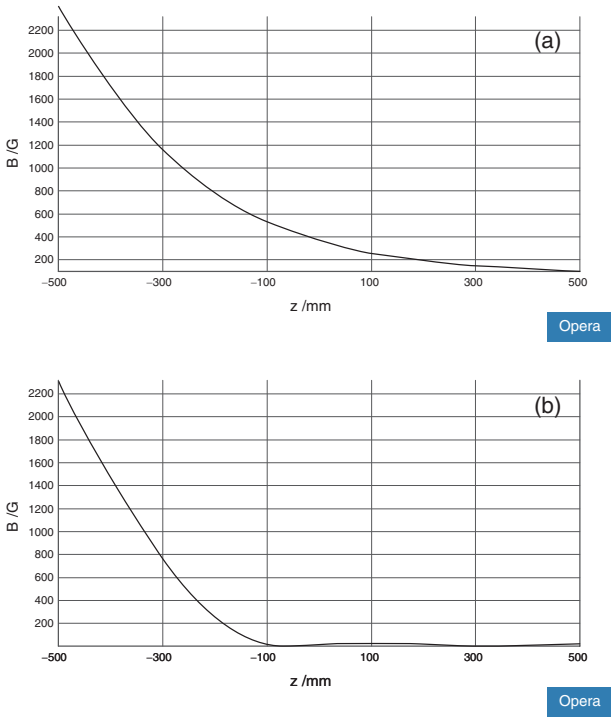

Figure 2. The calculations of the stray magnetic field distribution along the beam axis (a) without magnetic shield, (b) with magnetic shield. The tungsten target is located at $z = 0$.

mm, respectively. The side plates of the magnetic shield are 2.4 m in height and 1.0 m in width. They are placed on the both sides of the W target chamber 1.0 m apart from each other. Figure 1 shows a top view of the magnetic shield, the last two superconducting solenoids of the Superomega muon beamline, and two zero-field correction coils. The muon beam is coming from the left to the right side, and is incident on the W target located in the center position between the two zero-field correction coils.

The stray magnetic field at W target from the solenoids of the Superomega muon beamline and effectiveness of the magnetic shield were calculated using simulation code, TOSCA. Figure 2(a) shows the magnitude of the stray magnetic field without magnetic shield along the beam axis of the Superomega muon beamline. The curve shows that the magnetic field decreases with increasing the length from the last solenoid of the Superomega beamline. The magnitude of the stray magnetic field is 370 G at the W target ($z = 0$). The effectiveness of the magnetic shield is shown in Fig 2. As clearly seen in these figures, the stray field along the beam

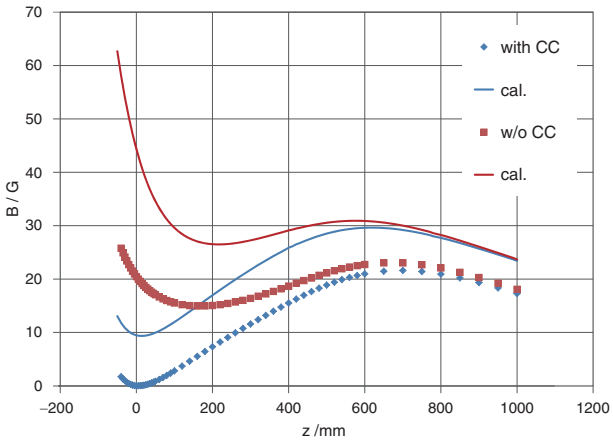

Figure 3. The measured and calculated magnetic field distributions along the beam axis with/without the zerofield correction.

axis is drastically reduced by the magnetic shield in the range over the W target chamber. The magnitude of the residual stray field is less than 20 G at the W target. The residual stray field is originated from the large hole of the magnetic shield for the beamline duct, and the field can be canceled by using the three-direction zero-field correction coils equipped on the W target chamber.

The measurements for the stray magnetic field in the vicinity of the W target were performed after the installation of the W target chamber and the magnetic shield downstream of the Superomega muon beamline using three-dimensional Hall probe on the three-direction positioning equipment. The measured and calculated stray magnetic field along the beam axis are shown in Fig. 3. Although there exists offsets between measured and calculated fields, the measured field exhibits a good agreement with that of the calculated one. The offsets between fields are probably originated from the effect of the magnetization of the magnetic shields. We tried to cancel the residual stray magnetic field by using zero-field correction coils in three directions. The curve with zero-field correction coils exhibit 0 G at $z = 0$ and gradually increases with increasing z. And then, it shows peak structure of 20 G at around $z = 700$ mm, and decreases with increasing z. As a result, the residual stray field is suppressed less than 1.5 G over the region of the W target. The major component of the residual stray field is the beam axis direction, and in the direction normal to the beam

axis, the residual stray field is less than 0.2 G. Since the direction of the muon spin polarization is along the beam axis, the field along the beam axis does not affect the spin depolarization of the muons. And the residual stray field normal to the beam axis is sufficiently reduced by the magnetic shield for the change of the muon spin. It is concluded that the magnetic field environment around the W target is ready to start the experiment for extracting the ultra-slow muon.

References

[1] K. Nakahara *et al.*, Nucl. Instrum. Methods Phys. Res., Sect. A **600** (2009) 132.

[2] K. Shimomura *et al.*, MLF Annual Report 2012 143.

[3] Y. Ikedo *et al.*, MLF Annual Report 2012 145.

[4] T. Nagatomo *et al.*, MLF Annual Report 2012 162.

[5] J. Nakamura *et al.*, MLF Annual Report 2012 164.

Y. Ikedo[1,2], H. Fujimori[1,2], T. Nagatomo[1,2], R. Ohkubo[3], K. Nishiyama[1,2], Y. Miyake[1,2], K. Shimomura[1,2], P. Strasser[1,2], N. Kawamura[1,2], S. Makimura[1,2], A. Koda[1,2], J. Nakamura[1,2], Y. Kobayashi[1,2], A. D. Pant[4], T. Ogitsu[5], T. Nakamoto[5], K. Sasaki[5], H. Ohata[5], R. Okada[5], A. Yamamoto[5], Y. Makida[6], M. Yoshida[6], T. Okamura[6], T. Adachi[7], W. Higemoto[1,8], T. U. Ito[1,8], K. Nakahara[9], and K. Ishida[10]

[1]Muon Science Section, Materials and Life Science Division, J-PARC Center; [2]Institute of Materials Structure Science, KEK; [3]Mechanical Engineering Center, KEK; [4]Interdisciplinary Graduate School of Medicine and Engineering, University of Yamanashi; [5]Cryogenics Science Center, KEK; [6]Institute of Particle and Nuclear Studies, KEK; [7]Graduate School of Science, The University of Tokyo; [8]Advanced Science Research Center, JAEA; [9]Department of Physics, University of Maryland; [10]Advanced Meson Science Laboratory, Nishina Center for Accelerator-Based Science, RIKEN

Development of a Manufacturing Method of Highly Pure Tungsten Foil for Thermal Muonium Generation

The Ultra-Slow Muon Microscope (USMM) will be utilized for promoting various advanced researches by using ultra-slow muons, which have been developed at KEK-MSL and RIKEN/RAL since 1995 [1,2]. Positive muons, generated in the primary proton beamline and transported to a vacuum chamber for generation of ultra-slow muons, are introduced into a hot tungsten foil at 2000 K. Positive muons will capture electrons and will be converted into muonium atoms. Then the thermal muonium atoms would be evaporated into an ultra-high vacuum and ionized by a laser ionization method.

A highly pure tungsten foil is essential, because a clean tungsten surface is required to obtain an intense muonium emission. The thickness, the height, and the width of the foil are determined by the beam parameters of the introduced positive muons, and they are evaluated to be 50 μm in thickness, 54 mm in height and 70 mm in width, respectively. Unfortunately, the companies, which had supplied in the past highly pure (6N, 99.9999%) tungsten foils, discontinued the manufacturing. It used to be manufactured by a hot rolling technique of highly pure tungsten bulk material. However, the hot rolling apparatus for highly pure tungsten material must be specialized to tungsten, because the hot rolling needs to be performed at a much higher temperature than in the case of other materials. Therefore the development of different manufacturing methods was started instead of fabricating a new and expensive hot rolling apparatus.

There are two categories of techniques to manufacture a foil. One is piling up the material on a basal plate, such as a Chemical Vapor Deposition (CVD) method or a Physical Vapor Deposition (PVD) method, and the other is reducing the thickness of bulk material, for example, by mechanical polishing or etching. However, because piling up the material up to 50 μm is time-consuming, the manufacturing apparatus must be continuously and exclusively operated. Therefore, the thickness-reducing technique was investigated first. Because the 6N-tungsten bulk material is expensive, ordinary pure tungsten material (3N, 99.95%) was utilized to evaluate the feasibility of the manufacturing process. Since it is well-known that tungsten bulk material can be cut by electric discharge machining (EDM) into 1-mm thick plates, commercially available tungsten plates with a thickness of 1 mm were utilized in these investigations. These plates were mechanically polished into 0.2-mm thick plates. Continuously, the thickness was reduced up to 50 μm by two methods, etching and mechanical polishing, respectively. The aiming thickness accuracy is 5%, which corresponds to 2.5 μm.

The etching of tungsten material is performed under the following exothermic reaction:

$$2ClF_3 + W \rightarrow WF_6(\uparrow) + Cl_2(\uparrow)$$

The chlorine trifluoride was supplied into a vacuum vessel at a rate of 500 standard-cc/min and the pressure was kept at 2.6 kPa by evacuating with a dry pump. The temperature was maintained at 80°C by a heater. Then the reaction speed was experientially evaluated to be 20 μm/hour for the first hour and 40 μm/hour subsequently. To reduce the thickness from 0.2 mm to 50 μm, the etching process was performed for 4 hours. The tungsten plate was set on a quartz table and the reaction had to take place on only one surface. However, because the tungsten plate was distorted by the reaction heat, the reaction did not take place just on one surface. Also, it was found out that it is difficult to keep the etching speed uniform on the whole area. This is because the reaction speed depends on the temperature. To keep the temperature precisely uniform on the whole area under the exothermic reaction, more segmented temperature control by individual heaters is required. Consequently, the thickness varied from 48 μm to 108 μm. Figure 1 shows pictures of the etching apparatus and the distorted tungsten foil.

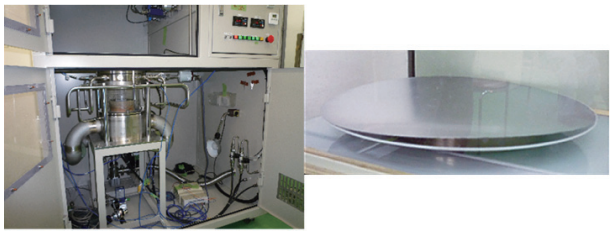

Figure 1. Pictures of the etching apparatus and the distorted tungsten foil.

At the same time, mechanical polishing was performed. The tungsten plate was firmly bonded to a base with beeswax or solid wax and polished into a foil. At the beginning, the tungsten foil came out during polishing, because the foil was delaminated beyond the bonding force. The reason of this delamination can be recognized as a processing strain. Then the conditions of polishing, such as feed rate, grinding margin, count of spark-out and so on, were investigated by reference to a research by Y. Nagatomo [3]. As a result, uniform 50-μm thick foils could be successfully obtained. The obtained thickness accuracy was 10%.

As a next step, the successfully-performed mechanical polishing was applied to a sintered tungsten bulk material, which is commercially available and made of nearly 6N-99.9999% tungsten. The 6N-tungsten is not as ductile as the 3N-tungsten, because impurities are functionally doped to the 3N-tungsten for increased ductility. Before polishing, the tungsten block was sliced to 20 plates with a thickness of 1 mm by the EDM. Then the tungsten plate was polished under almost similar conditions to 3N-tungsten polishing pattern. However, in this case, it was found out that the load from the delamination was much larger than for the former polishing. Indeed, the foil easily came out and broke into pieces. By observing the breaking behavior and the broken pieces, we could deduce the following facts: (1) the specification of the tungsten plates itself, (2) the effect of the generated heat and the thermal stress during the polishing, and (3) the lack of bonding force. The details and the measures taken are described below. (1) The specification of the tungsten plates was not completely suitable to our polishing. When the bulk material was obtained, the grain size in the sintered process had not been checked carefully. The average grain size was 20 μm, which seemed to be somehow large in comparison with the thickness of the foil, 50 μm. The EDM had to be performed more carefully. The processing strain by the EDM was considered to be large, because a change in color was observed at the surface of the tungsten plates after the EDM. Therefore, the tungsten plates were annealed before polishing. As a result, we reduced the distortion, though some cracks occurred during polishing. (2) During the polishing, both ends were gradually delaminated. The mechanical polishing was performed by a surface grinding machine. Figure 2 shows pictures of the surface grinding machine and the polishing of the 6N-tungsten foil. Even if the tungsten plates were set in any direction, the delamination occurred at the end of the longitudinal travel of the grinding (i.e., as the tungsten foil was twisted). Here, a green carborundum whetstone and a diamond whetstone were respectively used for a comparison. Also, copper alloy and iron alloy were used for a comparison as materials for the basal plate. As a result, no differences could be observed. (3) The bonding was not rigid enough, so delamination of the foil occurred. Successively, the polished tungsten powders or the ground whetstone slid into the gap between the foil

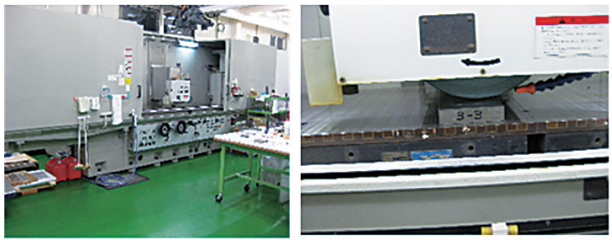

Figure 2. Pictures of the surface grinding machine and the polishing of the 6N-tungsten foil.

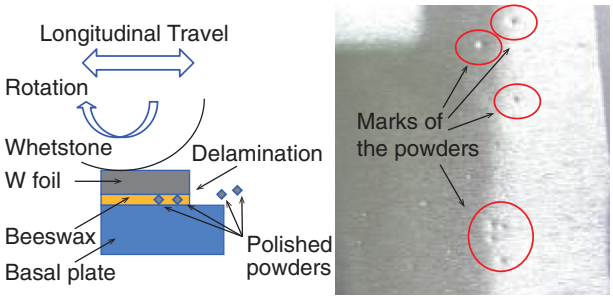

Figure 3. Schematic drawing of the powders-sliding into the gap and a picture of the foil under polishing.

Figure 4. Pictures of the broken tungsten foils.

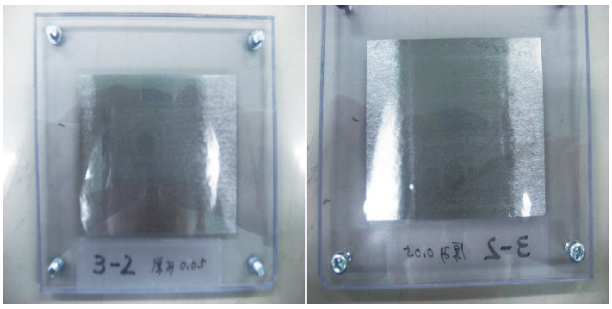

Figure 5. A picture of the manufactured 6N-tungsten foil.

and the basal plate. Figure 3 shows a schematic drawing of the powders-sliding into the gap, and a picture of the foil under polishing where the marks left by the powders can clearly be seen. As a result, the foil came away and broke into pieces. Figure 4 shows pictures of the broken foils. To increase the bonding force, the beeswax was replaced with an epoxy bonding agent. Finally, one 6N-tungsten foil with the aimed dimensions was obtained. The foil bonded to the basal plate was exposed to organic solvents, and was detached from it successfully. The thickness accuracy was less than 5%. Figure 5 shows a picture of the manufactured 6N-tungsten foil. The residual organic solvents on the tungsten foil were measured by a Fourier transform infrared spectroscopy. Consequently, no organic solvent was observed.

In the future, the tungsten bulk material will be manufactured by tungsten powders with a smaller grain size. The conditions for EDM will be investigated carefully. Then manufactured foil will be utilized for a generation of ultra-slow muons.

References

[1] K. Nagamine *et al.*, Phys. Rev. Lett. **74** (1995) 4811.

[2] P. Bakule *et al.*, Nucl. Instrum. Methods Phys. Res. B **266** (2008) 335.

[3] Y. Nagatomo *et al.*, Report of Miyazaki Prefecture Industrial Technology Center **47** (2002) 43, written in Japanese.

S. Makimura[1,2], M. Onoi[3], M. Wakasugi[3], T. Nagatomo[1,2], Y. Ikedo[1,2], P. Strasser[1,2], K. Shimomura[1,2], J. Nakamura[1,2], K. Nishiyama[1,2], and Y. Miyake[1,2]

[1]Muon Science Section, Materials and Life Science Division, J-PARC Center; [2]Institute of Materials Structure Science, KEK; [3]Metal Technology Co., LTD.

Construction of the J-PARC/MUSE Ultra-Slow Muon Beamline

At the J-PARC Muon Science Facility (MUSE), located in the Materials and Life Science Facility (MLF) building, we are now constructing a new ultra-slow muon beamline to extend the scope of the μSR technique from bulk material to thin films, multilayers, surfaces and extremely small samples. The new Super-Omega muon beamline (U-Line), which produces now the world's strongest pulsed surface muon beam, will be used to generate intense ultra-slow muons by the re-acceleration of thermal muons regenerated by the laser resonant ionization of muonium atoms evaporated from a hot tungsten foil, a method that originated from the Meson Science Laboratory at KEK. The re-accelerated beam (ultra-slow muon beam) has better energy resolution, time resolution and space distribution compared to the initial surface muon beam.

The design of the new ultra-slow muon beamline was already reported in the previous KEK-MSL Report (2011). During this fiscal year, the beamline components were constructed by Irie Koken Co., Ltd. Figure 1 shows a picture of the completed ultra-slow muon beamline during the factory inspection. In the foreground, one can distinguish the two branches of the beamline leading to the two experimental areas: U1A on the left (Ultra-Slow Muon μSR) and U1B on the right (Reacceleration and Microbeam μSR), respectively. A closer view of some of the optical elements is shown in Fig. 2. Figure 3 shows pictures of the beam monitor and slit assembly. There are five such assemblies located along the ultra-slow muon beamline for monitoring and tuning purposes. Both horizontal slit mechanisms (left and right) are remotely activated from the same side, while the vertical slits (top and bottom) are both mounted from below. This compact arrangement leaves space for a beam monitor transfer mechanism to be placed at the top of the vacuum chamber. At the moment either a standard MCP detector (micro channel plate, 40-mm in diameter, single anode) or a two-dimensional MCP detector (with delay-line anode for high resolution 2D-imaging from RoentDek Handels GmbH.) can be mounted. The detector is lowered behind the slits that can also be used to evaluate the beam profile with a single-anode MCP.

The ultra-slow muon beamline was delivered to MLF in November 2012, and the installation and alignment started in January 2013. The first ultra-slow muon beam is expected by the end of the spring of 2013.

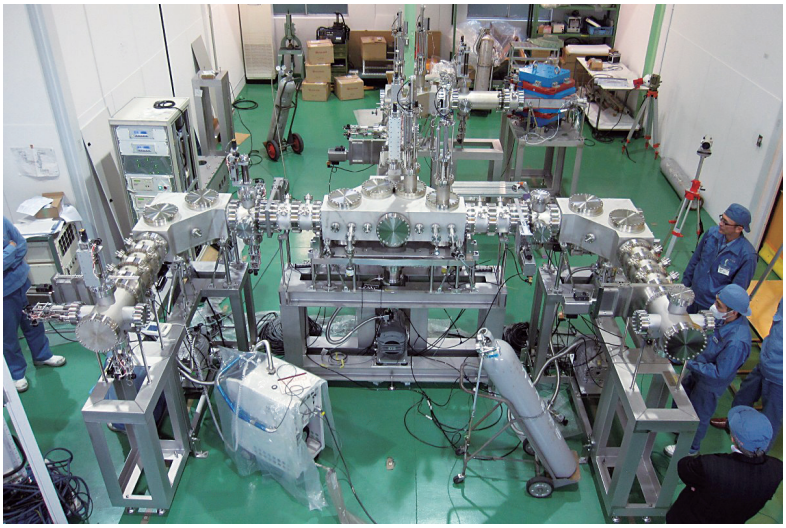

Figure 1. The new ultra-slow muon beamline during the inspection at the factory.

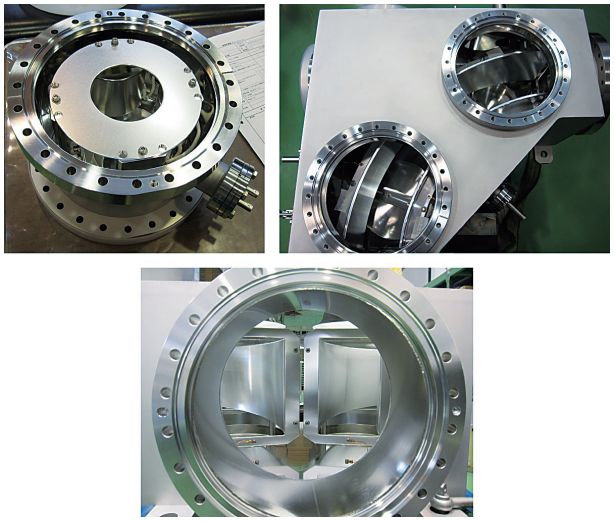

Figure 2. Optical elements: electric quadrupole (top left), 90° electric bend (top right), and entrance of the double electric bend (bottom), respectively.

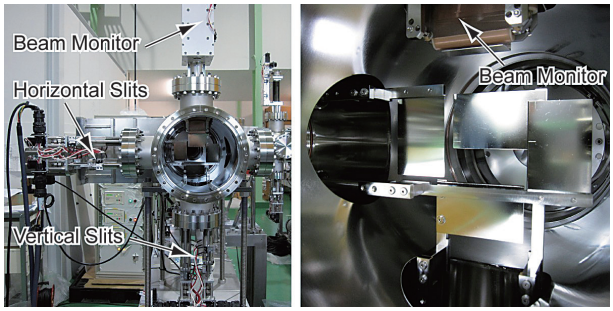

Figure 3. Beam monitor and slit assembly.

The full Geant4 beamline transport simulation of the ultra-slow muon beam is also in progress using the PSI simulation package. The magnetic and electric field distributions of each individual component were calculated using the code OPERA-3D (TOSCA), and incorporated in the simulation code.

P. Strasser[1,2], S. Makimura[1,2], T. Nagatomo[1,2], Y. Ikedo[1,2], J. Nakamura[1,2], K. Nishiyama[1,2], K. Shimomura[1,2], A. Koda[1,2], N. Kawamura[1,2], H. Fujimori[1,2], W. Hegemoto[1,3], R. Kadono,[1,2] and Y. Miyake[1,2]

[1]*Muon Science Section, Materials and Life Science Division, J-PARC Center;* [2]*Institute of Materials Structure Science, KEK;* [3]*Advanced Science Research Center, JAEA*

Installation and Simulation of Ultra-Slow Muon Beam Line

At the J-PARC Muon Science Facility in the MLF building, we installed the ultra-slow muon beam line at the end of the Super-Omega beam line of the U-Line [1]. Highly intense surface muons with energy of ~4 MeV are provided from the Super-Omega beam line and implanted into a hot tungsten foil as a source of ultra-slow muons. The ultra-slow muons are produced by combination of the thermal muonium evaporation from the surface of the 2000-K tungsten foil and the resonant ionization by utilizing a VUV Laser [2]. After the ionization, the ultra-slow muons are accelerated to 30 keV and are focused by cylindrical electrostatic lens, so-called SOA Lens. The extracted ultra-slow muon beam is transported to two experimental ports; one is utilized for the ultra-slow μSR research and the other for realizing a micro radius beam by re-acceleration to several hundred keV. The beam line consists of a magnetic bend for mass analysis, several electrostatic bends and lenses. All of the power sources for these devices are controlled by PLC. A remote control system operating through the Internet was constructed. A power source to heat up the tungsten target with the pulsed interrupt function to suppress the magnetic field induction was also installed.

Investigation of the beam optics parameters was performed based on the Monte Carlo simulation [3].

Table 1. beam optics parameters for 15-keV muons transported to the μSR setup.

Devices / unit	Value
EQ1 / kV	-0.250
MB / Gauss	125.04
EQ2 / kV	-0.300
EQ3 / kV	+0.150
EB1 / kV	3.7176
EQ4 / kV	+1.145
EQ5 / kV	-2.075
EQ6 / kV	-2.000
EQ7 / kV	+1.100
ED / kV	2.450
EB2 / kV	3.7250
EQ8 / kV	0.900
EQ9 / kV	-1.400
EB3 / kV	3.7500
EQ10 / kV	1.000
EQ11 / kV	-1.613
EQ12 / kV	0.755

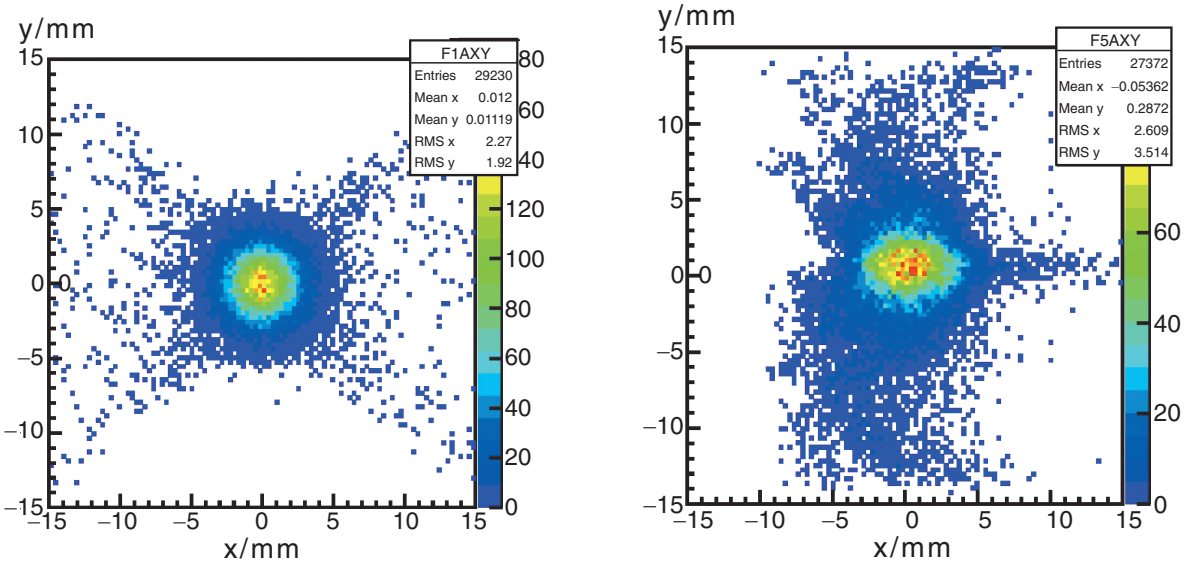

Figure 1. Estimated x-y plots of beam spots at the first (left) and last focal planes (right) in unit of mm.

The three dimensional static electric and magnetic fields, applied to the simulation, were calculated with the finite element method (OPERA-3D) where the contents such as the shape of electrodes, supports and surroundings were reproduced as closely as possible. The maximum transportation rate was more than 90% from the first focal plain to the last focal plane (just before the Einzel lens) with the parameters listed in Table 1. And the estimated beam spots at the first and the last focal plane are shown in Fig. 1.

Early in the next fiscal year, we are first planning a commissioning of the ultra-slow muon beam line with $^{6,7}Li^{+}$ ions that the natural tungsten foil contains as impurities. By heating up the tungsten, the Li ions are spontaneously evaporated and that can be utilized as a pilot beam. After the commissioning with the Li ions, we will start the resonant laser tuning. We steadily advance the preparation of the first ultra-slow muon beam as early as possible.

References

[1] Y. Ikedo *et al.*, MLF Annual Report 2012 182.

[2] J. Nakamura *et al.*, MLF Annual Report 2012 164.

[3] the “musrSim” package developed by LMU group of PSI (http://lmu.web.psi.ch/simulation/index.html)

T. Nagatomo[1,2], Y. Ikedo[1,2], P. Strasser[1,2], S. Makimura[1,2], J. Nakamura[1,2], R. Ohkubo[3], K. Nishiyama[1,2], K. Shimomura[1,2], N. Kawamura[1,2], A. Koda[1,2], H. Fujimori[1,2], Y. Kobayashi[1,2], T. U. Ito[1,4], W. Higemoto[1,4], A. D. Pant[5], R. Kadono[1,2], E. Torikai[5], and Y. Miyake[1,2]

[1]Muon Science Section, Materials and Life Science Division, J-PARC Center; [2]Institute of Materials Structure Science, KEK; [3]Mechanical Engineering Center, KEK; [4]Advanced Science Research Center, JAEA; [5]Interdisciplinary Graduate School of Medicine and Engineering, University of Yamanashi

Transport System of Laser Pulses

The transport system of laser pulses [1] introduces laser waves to the muonium (Mu, μ^+e^-) production vacuum chamber [2] on a new-muon beamline (U-line) in J-PARC [3]. The Ultra-Slow Muon Beam [4] is produced by laser resonant ionization of thermal (*E*~0.3 eV) muonium. In this laser resonant ionization process, thermal Mu is excited (1S→2P) by a coherent vacuum ultraviolet wave (VUV, 122 nm, Lyman-α) and ionized by a 355-nm wave (UVA). This coherent VUV wave, a pulsed resonance radiation, is generated in a Krypton (Kr) gas cell by sum-difference frequency mixing of a 212-nm wave (UVC, two-photon resonant excitation) and a tunable difference wave (near infrared, NIR, 820 nm) [5]. These coherent radiation sources, based on a diode-pumped fiber laser and solid-state laser technologies, have been developed by Saito *et al.* at RIKEN [6], and installed in a laser cabin [7].

These vacuum chambers for the transport system (manufactured by AVC Co., LTD. [8]) consist of a VUV steering vacuum chamber and a nitrogen monoxide (NO) gas cell (Fig. 1). The VUV pulse generated in the Kr gas cell goes sequentially through the VUV steering chamber, the Mu production chamber, and the NO gas cell. In the VUV steering chamber, two "bright" fundamental waves (212 nm, 820 nm) can be separated from the VUV wave by wavelength dispersion of the refractive index at a LiF wedge plate. The 355-nm wave has nearly the same incident angle to the Mu production chamber as that of a VUV wave. At the NO gas cell, there are parallel plates that accumulate nitrogen monoxide molecules ions for measuring the intensity of the VUV pulse [9].

The VUV steering chamber has two mirror control units (Fig. 2). High vacuum (<10^{-6} Pa) can be achieved in the VUV steering chamber, since the mirrors equipped in this chamber, are steered from outside of the chamber, by magnetic coupling mechanism, and no other drive mechanisms, such as piezoelectric system, etc., are adopted in it.

Since mirror control units were prepared for each VUV pulse and 355-nm pulse, individually, we can easily control the distance between these pulses and the Mu production target (tungsten foil). By monitoring the ionization rate of the thermal Mu with changing this distance, it will be revealed whether the thermal Mu follows a Boltzmann distribution.

For the design of the VUV steering chamber, calculations of the ultimate pressure and optics were carried out.

Since, the thermal Mu production requires ultra-high vacuum (10^{-7} Pa~10^{-8} Pa), the VUV steering chamber is differentially pumped from the Mu production chamber (Fig. 3). The calculation of differential pumping is as follows:

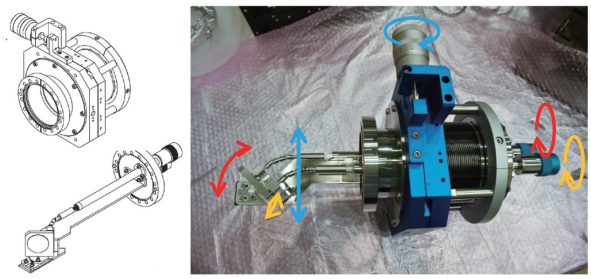

Figure 2. Mirror control unit.

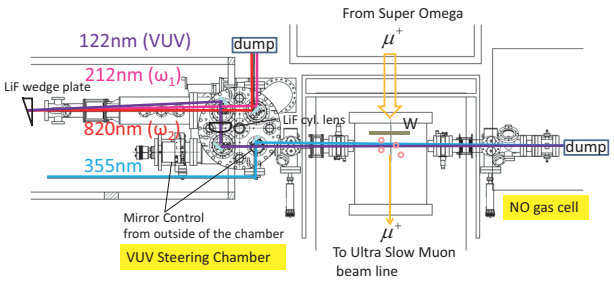

Figure 1. Transport system of laser pulses.

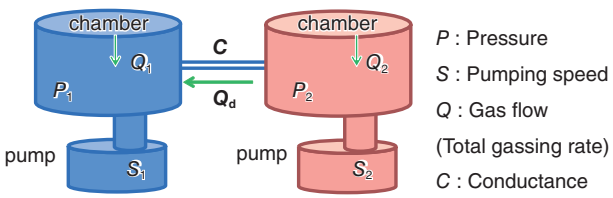

Figure 3. Diagram of a differential pumping.

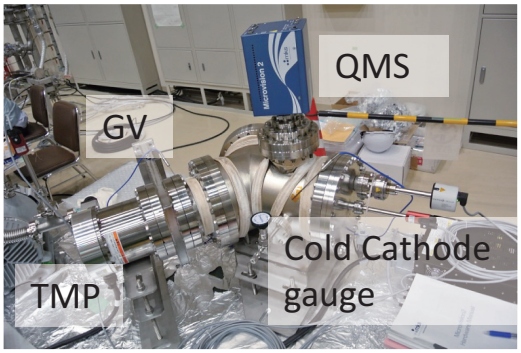

Figure 4. Test chamber for outgassing measurement.

$$P_2 - P_1 = Q_d \frac{1}{C}, \quad P_1 = \frac{Q_1 + Q_d}{S_1}, \quad P_2 = \frac{Q_2 - Q_d}{S_2}$$

$$\Rightarrow \begin{cases} P_1 = \dfrac{(C+S_2)Q_1 + CQ_2}{C(S_1+S_2) + S_1S_2} \\ P_2 = \dfrac{(C+S_1)Q_2 + CQ_1}{C(S_1+S_2) + S_1S_2} \end{cases}$$

Conductance C of the thin tube (whose length is 12 cm, and the section is of rectangle shape of 5 × 2 cm for vertically long radiation profile of VUV pulse) is 0.04m³/s. Then, the pressure of the Mu production chamber P_2 reaches less than 1 × 10^{-7} Pa, when that of the VUV steering chamber P_1 is around 1 × 10^{-6} Pa.

For measurements of the total outgassing rate, a bench test chamber was prepared (Fig. 4). The chamber has a Pirani and cold cathode vacuum gauge and a quadrupole mass spectrometer (QMS).

The calculation of the total outgassing rate by the equation of buildup is as follows: (V: volume of the chamber)

$$P(t) = P_0 + \frac{Q}{V}t \Rightarrow Q = \frac{dP}{dt}V$$

According to this calculation, (Table 1. shows the results) the total outgassing rate and the ultimate pressure of the VUV steering chamber are estimated to be less than 1 × 10^{-7} Pa m³/s, 1 × 10^{-7} Pa, respectively.

In order to investigate the components of the outgassing, QMS measurements were also performed. The existence of the usual gases was confirmed for the residual gas components, such as H_2O, O_2, and CO_2, and no specific gas, such as hydrocarbon,

Table 1. Total outgassing rate.

	Q / (Pa m³/s)
Test chamber (empty)	3.6 × 10^{-9}
Mirror mount (1 in.)	1.1 × 10^{-9}
Control unit for mirror 3	3.1 × 10^{-9}
Mirror(Al plane mirror, 2in.)	2.8 × 10^{-9}

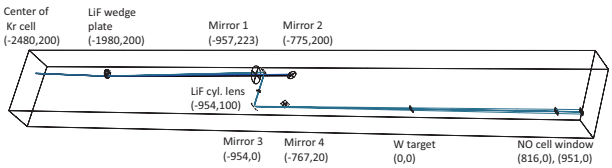

Figure 5. Coordination of Ray trace.

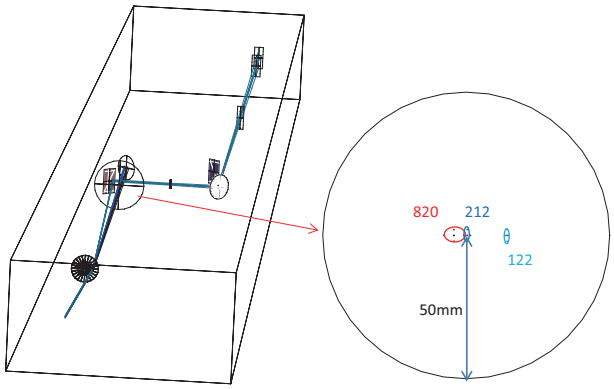

Figure 6. Ray trace for separation of pulses.

which is thought to reduce the yield of the Mu, was registered. In addition, the pressure changes while moving the mirror control unit in the test chamber were examined using a pressure gauge. The pressure of the chamber increases from 7.5 × 10^{-7} Pa to 1 × 10^{-6} Pa, and decreases to its original value in a few minutes.

Radiation profiles and the separation of laser pulses are calculated by a ray-tracing, *Optica* (Fig. 5).

Although a cylindrical lens of MgF_2 was used for pulse separation at RIKEN-RAL muon facility [10], a wedge plate of LiF is planned to be used for horizontal pulse separation (Fig. 6), and the vertex angle of this wedge plate is 6°. At present, a new way of focusing in Kr gas is extensively studied in RIKEN to adapt high intense laser pulses.

Next, the vertically long profile of VUV pulse is suitable for effective ionization of Mu. A cylindrical lens of LiF is used for making vertical profile (Fig. 7). The radius of the curvature of this lens is -100 mm, now.

The transport system of laser pulses was temporary set on the shielding of the D-line (Fig. 8). Then, it was confirmed that there was no leak in the chamber.

Fig. 9 shows the current status at the U1 shielding area. We are also in the process of improving the laser safety.

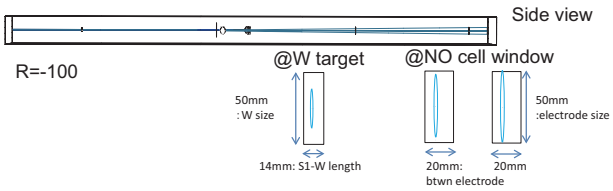

Figure 7. Ray trace for the profile of VUV pulse.

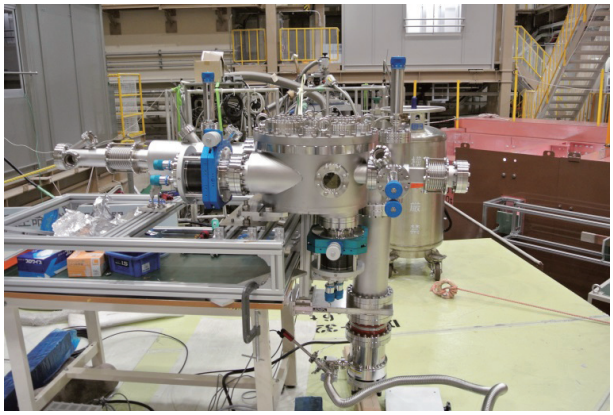

Figure 8. Temporary setting of the VUV steering chamber.

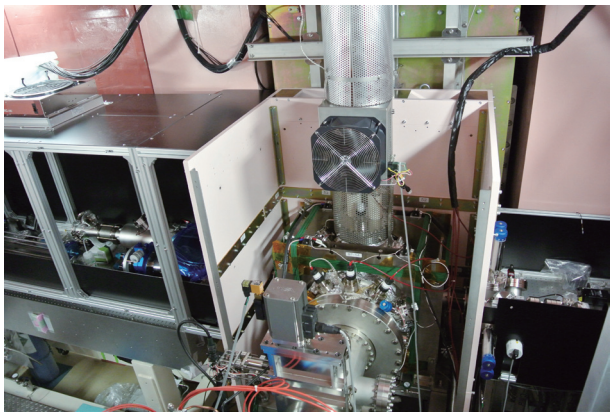

Figure 9. Transport system of laser pulses and Mu production chamber.

References

[1] J. Nakamura *et al.*, 68th Annual Meeting of the Phys. Soc. of Jpn. (2013) 26pXZB-7.

[2] T. Nagatomo *et al.*, 68th Annual Meeting of the Physical Society of Japan (2013) 26pXZB-8;
P. Strasser *et al.*, KEK Progress Report 2012-2 KEK-MSL REPORT 2011 (2012) 14.

[3] Y. Ikedo *et al.*, KEK Progress Report 2012-2 KEK-MSL REPORT 2011 (2012) 18.

[4] Y. Miyake *et al.*, Nucl. Instrum. Methods Phys. Res., Sect. B **95** (1995) 265.

[5] O. A. Louchev *et al.*, Phys. Rev. A **84** (2011) 033842.

[6] N. Saito *et al.*, Reports on the Topical meeting of the Laser Soc. of Japan **427** (2012) 49.

[7] J. Nakamura *et al.*, KEK Progress Report 2012-2 KEK-MSL REPORT 2011 (2012) 17

[8] http://www.a-vc.net/

[9] T. Kajiwara et al., Rev. Laser Eng. **12** (1984) 367;
J.A.R. Samson, *et al.*, Vacuum ultraviolet spectroscopy, Academic Press, London, (2000)

[10] P. Bakule *et al.*, Nucl. Instrum. Methods Phys. Res., Sect. B **266** (2008) 335;
Y. Matsuda *et al.*, Physica B **326** (2003) 217.

J. Nakamura[1,2], Y. Oishi[3], N. Saito[4], K. Miyazaki[4], K. Yokoyama[3], K. Okamura[5], S. Makimura[1,2], Y. Miyake[1,2], T. Nagatomo[1,2], P. Strasser[1,2], Y. Ikedo[1,2], D. Tomono[3], K. Shimomura[1,2], S. Wada[4,5], N. Kawamura[1,2], A. Koda[1,2], and K. Nishiyama[1,2]

[1]Muon Science Section, Materials and Life Science Division, J-PARC Center; [2]Institute of Materials Structure Science, KEK; [3]Advanced Meson Science Laboratory, RIKEN Nishina Center; [4]Photonics Control Technology Team, RIKEN Center for Advanced Photonics; [5]Megaopto Co., LTD.

Coherent Lyman-α Resonance Radiation Source for Ultra-Slow Muon Microscope

A coherent light source is one of the important devices to advance various branches of science, and the accelerator-based science is no exception. We are going ahead with the development of high-energy coherent muonium Lyman-α resonance radiation source towards the realization of high-intensity, low-temperature, high-time resolution, and high-spin polarized ultra-slow muon source. Such a muon source is required for the ultra-slow muon microscope at the Muon Science Laboratory [1]. The energy-level spacing between 1S and 2P in muonium corresponds to a wavelength of 122.09 nm and the wavelength is called Lyman-α resonance line. And our aim is to realize output energy of 100 μJ/pulse at 122.09 nm.

Muonium Lyman-α resonance radiation is generated in a four-wave mixing process involving two photons at 212.556 nm and a third photon at near 820.649 nm [2, 3]. The frequency $\omega_1 = c/(212.556 \times 10^{-9}$ m) is resonant with the two-photon transition 4p-5p[1/2,0] of Kr. We designed coherent 212.556 (Omega 1) and 820.649 nm (Omega 2) light sources based on the most-advanced techniques of all-solid-state lasers, fiber lasers, and nonlinear frequency conversion as shown in Fig. 1.

A distributed feedback laser was used for the purpose of determining the oscillation wavelength, which is fundamental in the nonlinear frequency conversion. The frequency ω_1 is the fifth harmonic of the fundamental at a frequency of $c/(1062.78 \times 10^{-9}$ m) Hz and a two-photon resonance frequency in order to excite Kr. The all-solid-state amplifier is composed of two types of optical amplifiers: regenerative amplifier and side-pumped amplifier. The regenerative amplifier produced 2 mJ optical pulses at a repetition rage of 25 Hz. The output pulses were amplified up to 80 mJ after amplification through the side-pumped amplifier. The duration of the pulses was approximately 2 ns. We expect that the output power at 1062.78 nm will increase up to 1 J with the use of power amplifiers.

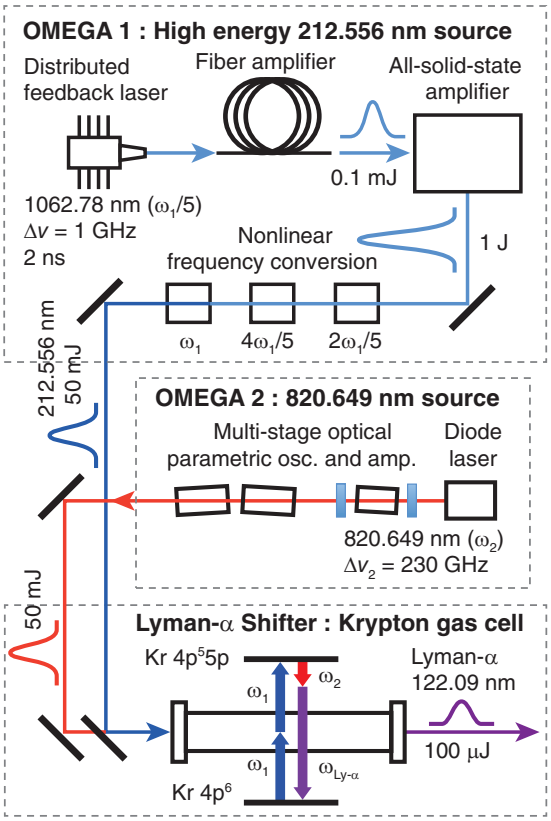

Figure 1. Lyman-α resonance radiation source.

The fundamental is incident on a 20-mm-long, uncoated LiB_3O_5 crystal and generates a wave at the second harmonic frequency in the condition of non-critical phase matching. The fourth harmonic ($4\omega_1/5$) is produced in frequency doubling of the second harmonic wave in a 7-mm-long BaB_2O_4 crystal. The fifth harmonic is generated in sum-frequency mixing using the fundamental and the fourth harmonic in another 7-mm-long BaB_2O_4. Omega 1 can currently increase the pulse energy up to a maximum of 8 mJ.

Omega 2 is a coherent 820.649 nm light source based on optical parametric oscillation and amplification. We developed a spectrum-broadened diode laser, which was used as an injection seeder to determine the center wavelength and spectrum bandwidth in the optical parametric processes. The output spectrum linewidth emitted from the diode laser was determined to be 235 GHz.

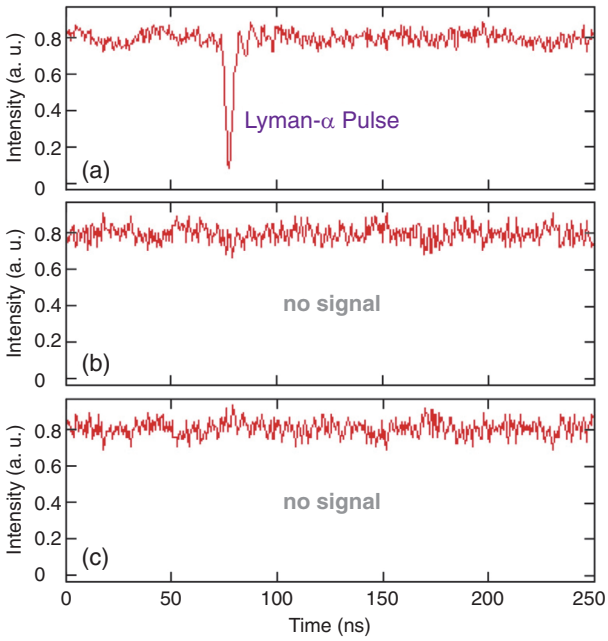

Figure 2. (a) Lyman-α pulse generated in two-photon resonance four-wave mixing. In the four-wave mixing (b) ω_1 was blocked and (c) ω_2 was blocked.

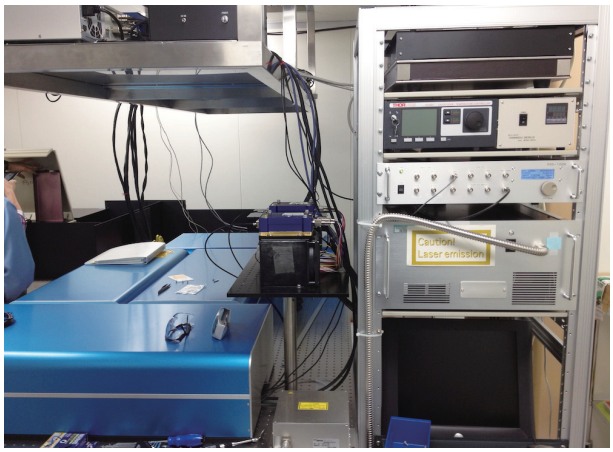

Figure 3. System of coherent Lyman-α resonance radiation source at the muon U-line.

Omega 2 was pumped with a flashlamp-pumped frequency-doubled Nd:YAG laser. The pulse width was approximately 7 ns. A maximum output energy of 2.3 mJ with a duration of 6 ns was emitted from the optical parametric oscillator using a 15-mm-long, uncoated KTP crystal in a resonator. The optical parametric amplifier consists two 15-mm-long, uncoated KTP crystals. The constitution of walk-off compensation amplified output pulses produced in the optical parametric oscillator up to an output energy of 13 mJ at 820.649 nm.

Output pulses at 212.556 and 820.649 nm were simultaneously and coaxially input to a Lyman-α shifter. The wave-vector mismatch is negative for vacuum ultra violet wavelengths shorter than the Kr resonance line at approximately 124 nm. Generally, a positively dispersive buffer gas such as Ar is mixed to satisfy the phase matching condition. The pressure of Kr-Ar gas ($P_{Ar}/P_{Kr} \approx 3$) gas cell was set to a pressure of 2.6×10^{-1} Pa. Fig. 2 (a) shows a temporal pulse of Lyman-α resonance radiation generated in two-photon resonance four-wave mixing in a Kr gas cell. We observed the increase of output intensity at 122.09 nm with the decrease in pressure up to 1.0×10^{-1} Pa.

In conclusion, we have successfully generated muonium Lyman-α resonance radiation. We carried the coherent Lyman-α resonance radiation source in muon U-line on March 22, 2013 and constituted it for a principle experiment of ultra-slow muon generation as shown in Fig. 3.

References

[1] Y. Miyake *et al.*, Hyperfine Interact **216** (2013) 79.
[2] G. Hilber *et al.*, J. Opt. Soc. Am. B **4** (1987) 1753.
[3] O. A. Louchev *et al.*, Phys. Rev. A **84** (2011) 033842.

N. Saito[1], Y. Oishi[2], K. Miyazaki[1], K. Okamura[1], M. Iwasaki[2], and S. Wada[1]
[1]Photonics Control Technology Team, RIKEN Center for Advanced Photonics, RIKEN; [2]Advanced Meson Science Laboratory, Nishina Center for Accelerator-Based Science, RIKEN

Installation of Kalliope additional positron detectors to DΩ-1 spectrometer

In FY2010 and FY2011, we developed the prototype of a new positron detector system called Kalliope [1,2]. In FY2012, we installed 12 Kalliope modules to the existing μSR spectrometer DΩ-1 to double the detector solid angle [3]. We also developed an auto-tuning program of the threshold level to adjust the efficiency of the individual pixel positron counters. The commissioning and the application to the user measurement have revealed a problem, which requires an improvement of the detector photodiodes.

Kalliope, which stands for KEK Advanced Linear and Logic-board Integrated Optical detectors for Positrons and Electrons, is a high-density positron detector array necessary for pulsed muon facilities. It consists of (1) plastic scintillator telescope on the scintillator board, (2) analog front-end board with an application specific Integrated Circuit (ASIC), which makes a digital pulse from the analog input signals, and (3) digital board with field-programmable gate array (FPGA), which stores the timing information of the digital pulses and transfers it to the DAQ computers. In FY2012, we developed a Kalliope module (v1.0-DΩ-1plus design), which could be installed to the existing DΩ-1 spectrometer. The specifications of the module are summarized in Table 1.

The photo of the developed Kalliope module is shown in Fig.1. By placing a scintillator board, which is separated from the analog board and connected by coax cables, the scintillator telescope may point to any angle, independently from the analog board orientation.

These Kalliope modules are installed to DΩ-1 spectrometer as shown in Fig.2. The upstream installation is particularly challenging due to the limited space: Kalliope modules are installed between the existing PMT-based detectors and the beam duct. The detector solid angle of the Kalliope units installed is almost the same like that of the existing PMT-based detectors, which is 8%. After the installation, the overall detector solid angle of DΩ-1 yields 18% approaching to the standard solid angle (20-25%) available in the conventional μSR spectrometers used around the world.

Table 1. Specifications of Kalliope v1.0-DΩ-1plus design.

component	specification
Scintillator block	16 pairs of plastic scintillators (1 × 1 × 1.2 cm), installed on GN1274-1 board
Analog board	Volume 2011 ASIC on GN1186-3 board
Digital board	BBT x-027 = GN1078-2 board

GN-XXXX is the catalog number of the manufac-turer, GND (Tateyama, Japan)

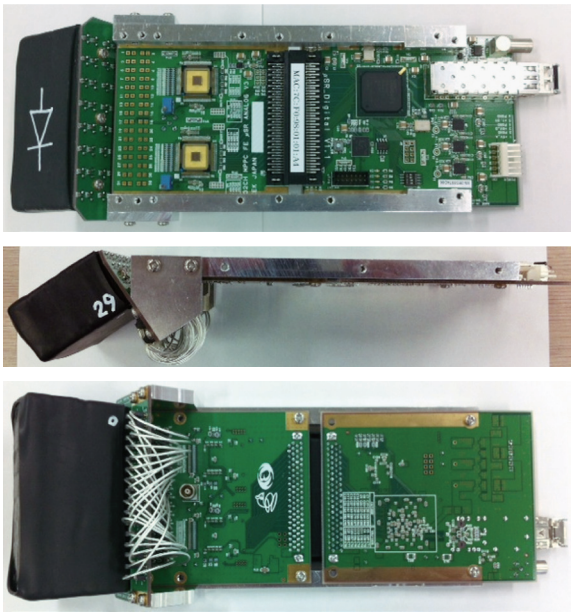

Figure 1. Kalliope-v.1.0-DΩ-1plus design. It consists of scintillator block on scintiboard, analog board and digital board. The coax cable connecting the scintiboard and analog board is Nihon-IF CJP series.

Fig.3 shows the μ-e decay time spectra with and without the Kalliope contributions. With the Kalliope modules installed, the μ-e decay count rate doubled due to the increased detector solid angle.

One achievement in FY2012 was the development of an auto-tuning script of the threshold level of the Kalliope modules, which was necessary to have before proceeding with a mass installation. The procedure was originally planned to search for an ap-

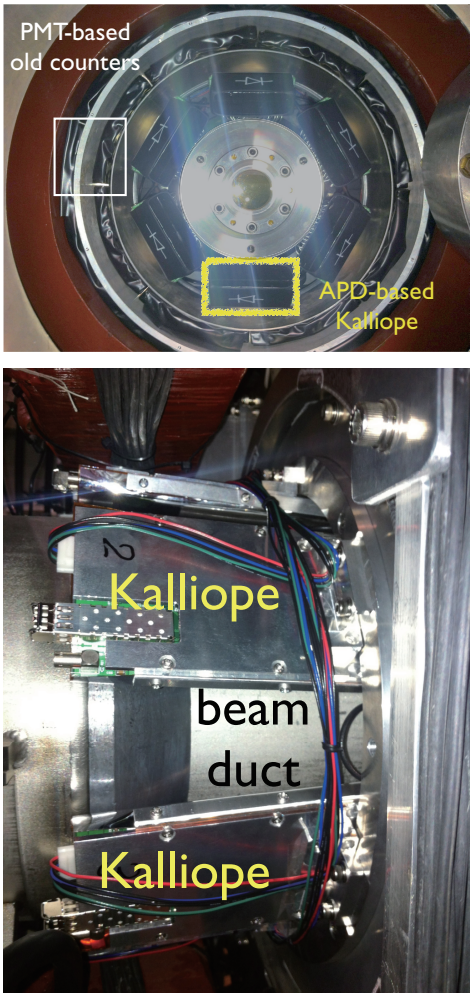

Figure 2. Kalliope modules installed to DΩ-1 spectrometer. They are installed into the free space between the existing PMT-based counters and the beam duct.

propriate count rate of each counter by changing its threshold level. However, the cross correlation of the threshold levels between the channels prohibited a straight-forward calculation of the threshold level. We adapted a simplified algorithm of a common threshold level for all counters and made a convergence. The cross-correlation originated from a bug in the ASIC internal circuit, and was reflected in the design of the following Volume-2012 ASIC.

Another problem, which became evident after

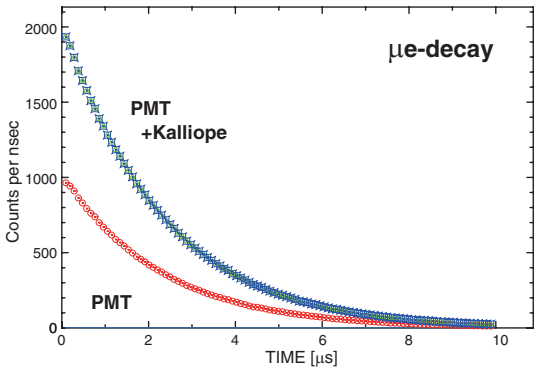

Figure 3. The μ-e decay time spectrum with and without Kalliope.

mass and actual installation of the Kalliope modules, was a rate-dependent deformation of the μSR spectrum. The μ-e decay time spectra, which appears to be fine in Fig.3 was deformed in the early stages beyond the level explained by the usual accidental pile-ups of positron signals. The reason was the combination of (1) instantaneous high count-rate associated with the after-pulse from the multi-pixel avalanched photo diode MPPC and (2) the saturation of the input amplifier of Volume-2011. Although the latter is inevitable with the current design of the ASIC, the former may improve with the new design of MPPC (Hamamatsu) which is going to be released in mid-2013.

As a result of the installation of Kalliope to the real spectrometer, tools and tips necessary for the operation were accumulated in FY2012. We also encountered new problems, which became evident after the actual application of the modules in μSR. We indent to solve these problems and aim to manufacture full-sized spectrometers in FY2013.

References

[1] K. M. Kojima *et al.*, KEK-MSL Annual report (2010).
[2] K. M. Kojima *et al.*, KEK-MSL Annual report (2011).
[3] KEK highlight (in Japanese)
http://www.kek.jp/ja/NewsRoom/Highlights/20130124170000/

K. M. Kojima[1,2,3,7], T. Murakami[4,7], S. Kanda[5,6,7], Y. Takahashi[1,2,7], Y. Fukao[4,7], S. Y. Suzuki[6,7], A. Koda[1,2,3,7], M. Miyazaki[1,2,7], M. Hiraishi[1,2,7], R. Kadono[1,2,3,7], N. Saito[4,5], M. Ikeno[5,7], M. Saito[4,7], T. Uchida[4,7], and M. Tanaka[4,7]
[1]Muon Science Section, Materials and Life Science Division, J-PARC Center; [2]Institute of Materials Structure Science, KEK; [3]Department of Materials Structure Science, The Graduate University for Advanced Studies (Soken-Dai); [4]Institute of Particle and Nuclear Studies, KEK; [5]Graduate School of Science, University of Tokyo; [6]Advanced Meson Science Laboratory, Nishina Center for Accelerator-Based Science, Riken; [7]Open Source Consortium of Instrumentation (Open-It), KEK

Installation of Dilution Refrigerator at J-PARC MUSE

Low temperature electronic and magnetic properties are often very important to clarify an intrinsic property of the material. To meet the strong demands from the users for experiments below 1 K, we installed a dilution refrigerator (DR) at D1 area, MUSE. The DR was previously used at KEK-MSL, which could achieve a temperature lower than 20 mK. The main feature of the DR is a "top-loading" system. For an ordinary dilution refrigerator, the dilution unit should be warmed up to room temperature to change a sample. Therefore, it takes a few days to change and cool down a sample. Meanwhile, in our top loading DR, a sample can be changed by unloading or loading just the sample holder. This feature is quite useful for a μSR experiment.

In February 2010, we transported the DR system from Tsukuba to Tokai, and started the installation at J-PARC MUSE. We also constructed the new stage for the DR at D1 area. Figure 1 shows the DR, and the stage at D1 area.

The cooling down of the DR is carried out by the following procedures:

1. Evacuation of the outer and inner vacuum can to high vacuum (12 h)
2. Pre-cooling by liquid nitrogen (24 h)
3. Preparation of liquid helium transfer (6 h)
4. Liquid helium transfer (12 h)
5. Cooling down to 4 K (3 h)
6. Cooling down of 1 K pot to 1.5 K (1 h)
7. Condensation of ^{3}He/^{4}He mixture (2 h)
8. Circulation of ^{3}He/^{4}He mixture (8 h)

At least, 3 days are required to cool down to 4 K and another 12 h is necessary to cool down to lowest temperature (20-30 mK). For exchanging and re-cooling down of the sample, it takes roughly 12 h.

In the beginning of the installation, we found out that there was a serious leakage at the plate heat exchanger and the indium seals of the DR unit. Additionally, several problems of the thermometers, the heaters and the vacuum sealing were found. These problems have been already fixed and now DR is used for several users' experiments. These results will be published elsewhere.

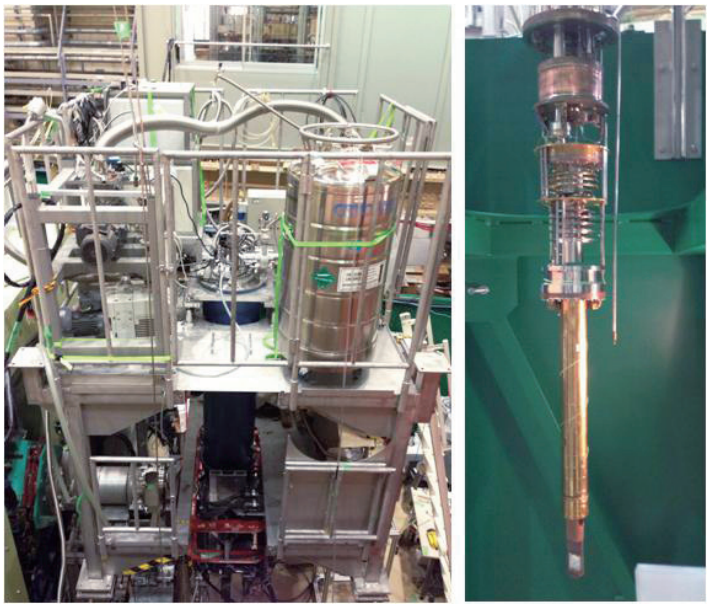

Figure 1. (Left) Dilution refrigerator at D1 area. Top flange of the DR is ~3 m from floor. (Right) Dilution unit.

We have carried out test experiments by using blank silver sample holder without sample. As shown in Fig.2, no significant muon spin relaxation was seen under TF of 20G. This result indicates that the implanted muon stopped just on silver plate.

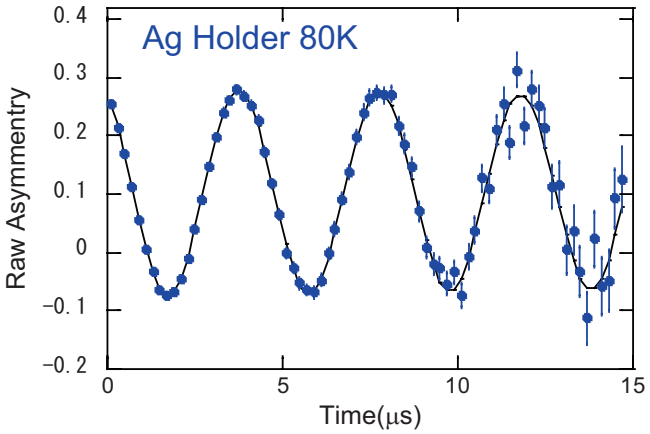

Figure 2. Test experiment with blank silver holder.

W. Higemoto[1,2], T. U. Ito[1,2], K. Yamauchi[2,3], and A. Koda[2,3]

[1]Advanced Science Research Center, JAEA; [2]Muon Science Section, Materials and Life Science Division, J-PARC Center; [3]Institute of Materials Structure Science, KEK

Scenes from the Muon Experimental Hall

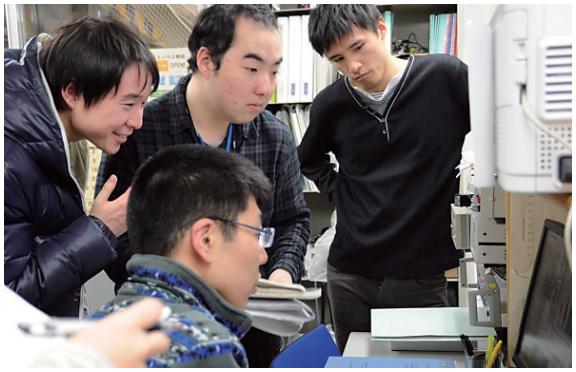

Masanori Miyazaki and Masatoshi Hiraishi explain the basics of muon spin relaxation to MLF school participants, Kenji Tsutsumi and Kentaro Sato, from Tohoku University.

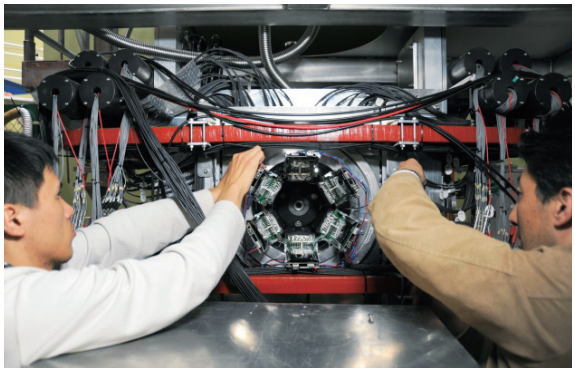

Masatoshi Hiraishi and Kenji M. Kojima work on the newly-installed 'Kalliope' detector system of the DOmega-1 spectrometer at the D1 experimental area.

Shunsuke Makimura with the rotating muon production target that he designed.

Koichiro Shimomura with the SuperOmega curved solenoid installed at the U-line – the world's highest intensity surface muon channel.

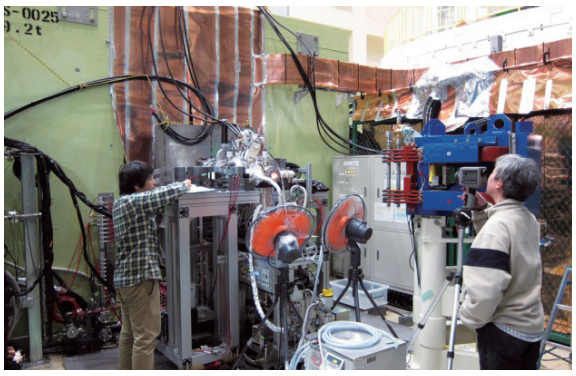

Yutaka Ikedo and Takashi Nagatomo align the vacuum chamber used to generate thermal muonium for ultra-slow muon formation at the U1 area.

Patrick Strasser and Yutaka Ikedo work with contractor technicians on the Mu production chamber in the U1A area.

Yu Oishi, Koji Miyazaki, Kotaro Okamura, Norihito Saito and Masahiko Iwasaki from RIKEN work with Jumpei Nakamura to prepare an intense VUV laser system used to ionize Mu in the laser cabin.

What's new at the MLF in 2012?

Advance Neutron Beam Line for VIllage of Neutron ResOnance Spin Echo Spectrometers (VIN ROSE) at BL06

The neutron spin echo (NSE) technique is an essential spectroscopic method, which enables us to achieve the highest neutron energy resolution. NSE with a pulsed neutron source makes it possible to scan a wide dynamic range of Fourier time.

Kyoto University and KEK are installing two types of NSE spectrometers at BL06, which are a neutron resonance spin echo (NRSE) instrument and a modulated intensity by zero effort (MIEZE) instrument. Both NRSE and MIEZE make use of neutron resonance spin flippers. Since NSE with neutron resonance spin flippers makes it possible to design compact spectrometers, multiple machines can be installed in a narrow space. In Figure 1, the schematic top view of the BL06 beam line is shown. Two curved supermirror guide tubes for each spectrometer will be installed. The space at BL06 is very limited, therefore the role of these curved guides is to create experimental space for two spectrometers and transport the optimized neutron beam efficiently. By using curved guide tube, fast neutrons and gamma rays from the source are stopped by an iron beam dump.

NRSE is suitable to study slow dynamics of soft condensed matter with high energy resolution, while MIEZE has the big advantage of flexible sample environments with the potential to open new fields of study such as spin dynamics in strongly correlated systems. Thus we have named BL06 "VIN ROSE" (Village of Neutron Resonance Spin Echo Spectrometers) [1]. In the VIN ROSE, neutron optical devices are key component and many of those are present in the spectrometers. Some of the devices, such as the focusing mirror and the related devices have been developed and improved step by step. All the supermirrors for these guides are deposited on silicon wafers with thickness of 3 mm by using the ion beam sputtering machine at KURRI (KUR-IBS) [1, 2]. The supermirrors are hold precisely and covered by iron shields to reduce the

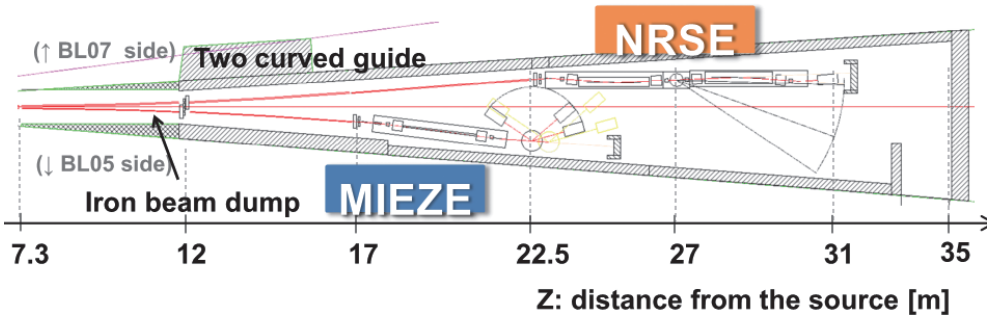

Figure 1. Schematic top view of MIEZE and NRSE beam line at BL06.

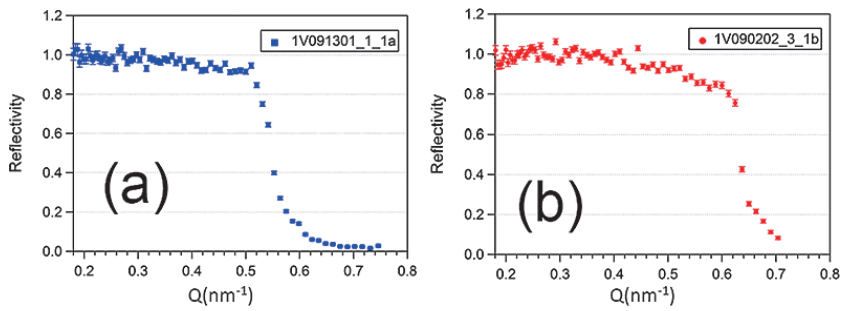

Figure 2. Reflectivity of typical m=2.5 and 3 supermirror for (a) NRSE and (b) MIEZE spectrometer, respectively.

Table 1. Planning instrumental specifications of VIN-ROSE.

Spectrometer	Wavelength	Q range [Å^{-1}]	Fourier Time
MIEZE	3 < λ < 13 [Å]	0.2 < Q < 3.5	1 [ps] < t < 2 [ns]
NRSE	5 < λ < 20 [Å]	0.02 < Q < 0.65	0.1 [ns] < t < 0.1 [μs]

dose level. The NRSE and MIEZE guides use m = 2.5 and 3 supermirrors, respectively. Their high performance has been proven by neutron reflectivity measurements etc., which is shown in Figure 2.

Currently, upstream concrete shielding has been installed on the BL06. The guide mirrors and downstream concrete shielding will be installed in FY2013, and the commissioning of the instruments will start from FY2014. In Table 1, the planning instrumental specifications of VIN-ROSE are listed.

References

[1] M. Hino, T. Oda, M. Kitaguch, N. L. Yamada, H. Sagehashi, Y. Kawabata, H. Seto, Physics Procedia **42** (2013) 136.

[2] M. Hino, H. Sunohara, Y. Yoshimura, R. Maruyama, S. Tasaki, H. Yoshino and Y. Kawabata, Nucl. Inst. Meth. A **529** (2004) 54.

H. Endo[1,2], M. Hino[3], T. Oda[3], N. L. Yamada[1,2], H. Seto[1,2], M. Kitaguchi[4], and Y. Kawabata[3]

[1]Neutron Science Section, Materials and Life Science Division, J-PARC Center; [2]Institute of Materials Structure Science, KEK; [3]Kyoto University Research Reactor Institute; [4]Department of Physics, Nagoya University

Construction of The Pulsed Neutron Imaging Beam Line at J-PARC

1. Introduction

The neutron radiography technique has been utilized as an essential non-destructive inspection method in various fields due to its distinctive characteristics such as high transmittance and high sensitivity to light elements. Recently, a new imaging technique, using unique features of the neutron energy dependence of transmission rate, has been attracting attention, because it enables us to visualize spatial distributions of more physical quantities inside the objects as follows: crystallographic information by the Bragg edge method [1], elemental compositions and temperature by the resonance absorption method [2] and magnetic fields inside and outside of objects by the polarized neutron method [3]. The pulsed neutron beam is very effective for such measurements to analyze the neutron energy dependences through the time-of-flight method with a broad neutron energy range. To provide the new methods to the general users, we have started the construction of a pulsed neutron imaging instrument at BL22 in MLF of J-PARC. This is the world's first instrument dedicated to the neutron imaging at pulsed sources.

2. Characteristics of the instrument

The imaging instrument has been designed by taking into account the requirements for each imaging technique. The Bragg edge imaging requires a wavelength resolution of 0.2% for strain measurements, and neutron wavelength longer than 5 Å to cover the 1st Bragg edge. The resonance absorption imaging needs a neutron energy range of up to several tens of keV, and an energy resolution lower than 1% for the resonance peak analysis. The conventional neutron radiography experiment, which is an indispensable technique even in the cutting-edge instrument, demands the highest neutron flux and the highest spatial resolution with a large beam size.

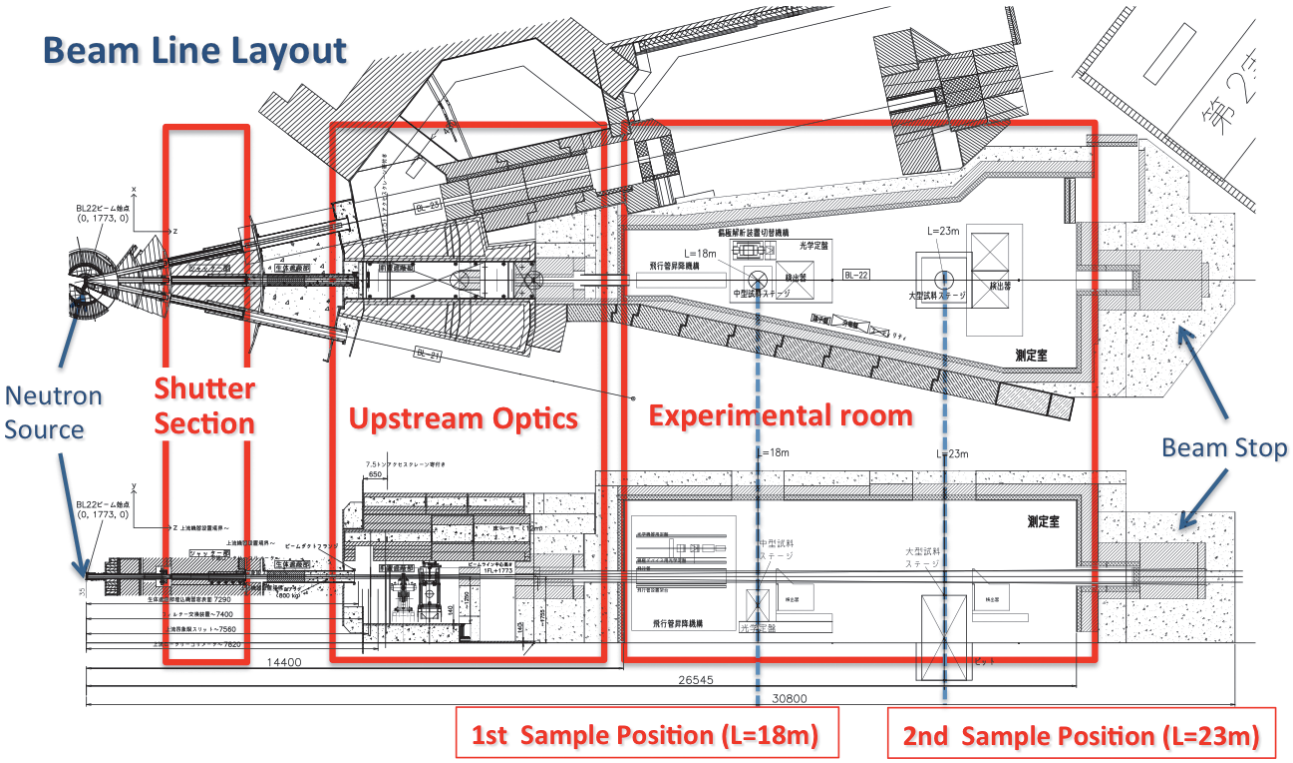

Figure 1. Illustration of the pulsed neutron imaging instrument at J-PARC.

To satisfy all requirements, we introduce a selectable beam divergence (L/D values) and two sample positions as shown in Fig.1. One is located at 18 m from the source to obtain the highest neutron flux of about 10^8 n/sec/cm^2 and a wavelength of up to 8.8 Å. The other is at 23 m to achieve enough high wavelength resolution for the Bragg edge imaging and the highest spatial resolution by the largest L/D value of 7500. The beam size of 300 mm × 300 mm is brought about by installing beam collimators inside the beam shutter.

3. Beam line components

In the upstream optics section, neutron optical devices such as filters, T_0 and disk choppers, a light shutter, rotary collimators, and B_4C slits, are installed to provide suitable neutron beam to a sample. Inside the experimental room, a large sample stage with the load capacity of 1,000 kg is placed at the 2nd sample position to conduct observation of large samples or to handle large sample environments.

The two-dimensional detectors are the most important components of the instrument. The detectors need to obtain time dependent images for the time-of-flight analysis. Therefore we have been developing counting type neutron detectors with high-time resolution (Δ t = 10 nsec) and camera type detectors with high spatial resolution ($\Delta > 10$ μm).

The installation of the instruments started in the summer of 2013. The first beam derivation and the start of the commissioning are planned to begin in 2014.

References

[1] H. Sato *et al.*, J. Phys.: Conf. Ser. **251** (2010) 012070.

[2] K. Kaneko *et al.*, J. Phys. Chem. Solids **60** (1999) 1499.

[3] T. Shinohara *et al.*, Nucl. Instr. And Meth. A **651** (2011) 121.

T. Shinohara[1], T. Kai[2], K. Oikawa[2], M. Ooi[2], M. Harada[2], K. Sakai[2], T. Nakatani[1], M. Segawa[1,3], H. Iikura[1,4], T. Kamiyama[5], H. Sato[5], H. Yokota[6], T. Sera[7], Y. Saito[8], K. Mochiki[9], T. Sakai[4], M. Kureta[3], K. Aizawa[1], M. Arai[10], and Y. Kiyanagi[5]

[1]Neutron Science Section, Materials and Life Science Division, J-PARC Center; [2]Neutron Source Section, Materials and Life Science Division, J-PARC Center; [3]Nuclear Science and Engineering Directorate, JAEA; [4]Quantum Beam Science Directorate, JAEA; [5]Faculty of Engineering, Hokkaido University; [6]Advanced Science Institute, RIKEN; [7]Faculty of Engineering, Kyushu University; [8]Research Reactor Institute, Kyoto University; [9]Faculty of Engineering, Tokyo City University; [10]Materials and Life Science Division, J-PARC Center

Polarized Inelastic Neutron Spectrometer POLANO

1. Introduction

In the Materials and Life Science Experimental Facility (MLF), three chopper type spectrometers are now part of the research program. One of the remaining technical issues that should be realized in MLF is the use of a polarization neutron technique with a pulsed neutron beam. The polarized neutron experiments are quite significant for the material science, particularly for the research on magnetism, hydrogen materials, and strongly correlated electron systems entangled with multiple physical degrees of freedom. Therefore, new spectrometers that enable us to conduct polarization analysis are very much expected as forthcoming instruments. A joint project between the Institute of Materials Structure Science (IMSS), KEK, and the Institute of Materials Research (IMR) of Tohoku University was initiated with the aim of future construction of the spectrometer and research program for functional magnetic materials in 2009. Now, the POLANO (Polarization Analysis Neutron Spectrometer with Correlation Method) project has begun [1].

2. Conceptual Design of Spectrometer

Our principal concept is to achieve higher-energy polarization analysis of inelastic scattering beyond a reactor-based neutron source. The suite of inelastic spectrometers involving an inverted geometry spectrometer and a spin-echo instrument in MLF can cover a relatively wide area in momentum (Q) and energy (E) space with various Q and E resolutions. Slow dynamics in soft matter to electron band excitation are targeted in the dynamical range of 10^{-9} eV $\leqq E \leqq 2 \times 10^{0}$ eV. For detailed dynamical studies in advanced material science, polarization analysis is an inevitable technique in addition to the wide Q-E coverage. Hence, we propose a chopper-type polarized neutron spectrometer which enables us to carry out inelastic experiments with reasonable intensity for research of the dynamical properties in materials.

Table 1. Basic instrumental parameters in POLANO.

Parameters	
Moderator	H_2 decoupled
L1 - L2 - L3	17.5 - 2.0 - 1.85 m
Energy resolution	3~5% at elastic position
Momentum resolution	1~2%
Sample size	20 × 20 mm
Detector angle (hor.)	3 – 120°
Detector angle (ver.)	±7°

The basic instrumental parameters of the POLANO spectrometer are summarized in Table 1. Since the designing concepts of POLANO are compact with reasonably wide sample space design, higher neutron flux, higher neutron energy polarization up to 100 – 150 meV, and medium resolution, the geometrical condition, $L_2 = 2.5$ m and $L_3 = 1.85$ m were chosen.

3. Beam Transport

A 3D representation of POLANO is shown in Fig. 1. The 23rd beam line, where POLANO will be installed, is viewing decoupled moderator with a known pulse width of $\Delta t_m = a/\sqrt{E_i}$ with $a = 2.5$. After the moderator neutrons are transported by $m = 4$ supermirror guide tubes optimized for 110 – 120 meV neutron intensity. An elliptical guide optimized section by section (section length = 50 cm) can yield a neutron flux of 3.9×10^5 [n/sec/meV/cm^2/MW], which is almost comparable with a coupled moderator beam line at $E = 100$ meV.

4. Mechanical Choppers

Below the exit of a biological shield, several types of choppers are placed. T_0 chopper is the first chopper to eliminate fast and epithermal neutrons with a massive metal blade rotating with a maximum speed of 100 Hz [2]. The blade is made of Inconnel X750, which is known for having high strength without using radiological elements with long lives such as cobalt. Though the weight of the blade is over 120 kg, at 100 Hz of rotating speed, less than ±5 μs

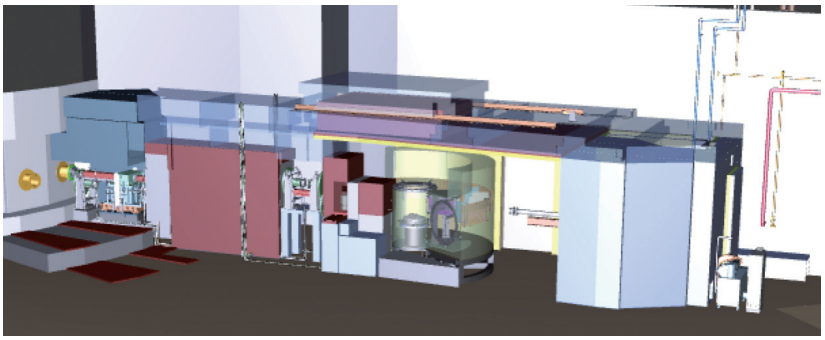

Figure 1. Schematic view of the POLANO spectrometer.

of jitter (phase control accuracy) was achieved. In order to avoid the frame overlap of a 25 Hz proton (neutron) pulse in MLF, a slow rotating disk chopper will be installed in the beam line. Two disk choppers synchronized with neutron pulse are placed at L = 7.5 and 13.9 m. A Fermi chopper will be used for monochromizing the incoming neutron energy. It is the same type of Fermi chopper developed for High Resolution Chopper spectrometer in MLF [3], which has a 600 Hz maximum speed with 0.3 μs jitter enabling high resolution and transmission experiments. For more effective measurements, we adopt the cross correlation method that utilizes multiple wavelengths of neutrons for one inelastic measurement. Hence, we have intensity gains of a factor of ten or higher in principle. A special type of disk chopper (correlation chopper) is required to realize this correlation method. The disk diameter is ideally over 1000 mm with a rotational speed of 350 Hz. Additionally, 255 (2^N-1) open and close sequences are required to be on the disk [4]. These conditions are quite difficult to realize mechanically because the maximum stress evaluated is almost 4000 MPa.

5. Schedule

We have almost completed the design of the spectrometer and have already started the manufacturing of several components, such as the T_0 chopper, detectors, guide tubes and so forth. The construction of a large beam line shielding will start in September of this year. Also, we have started contracts for building the vacuum chamber, correlation chopper, part of the supermirror analyzer, and other utilities. Most parts of the instrument will be completed by March 2015. On the other hand, some crucial polarization devices still require R&D, and will take considerable time to be completed. Polarization devices in POLANO are described in a Ref. [5].

References

[1] T. Yokoo, K. Ohoyama, S. Itoh, J. Suzuki, K. Iwasa, T.J. Sato, H. Kira, Y. Sakaguchi, T. Ino, T. Oku, K. Tomiyasu, M. Matsuura, H. Hiraka, M. Fujita, H. Kimura, T. Sato, J. Suzuki, M. Takeda, K. Kaneko, M. Hino and S. Muto, J. Phys. Soc. Jpn. in press.

[2] S. Itoh, K. Ueno, R. Ohkubo, H. Sagehashi, Y. Funahashi and T. Yokoo, Nuclear Instruments and Methods in Physics Research A **654** (2011) 527.

[3] S. Itoh, K. Ueno and T. Yokoo, Nuclear Instruments and Methods in Physics Research A **661** (2012) 58.

[4] S. Rosenkranz and R. Osborn, Pramana Journal of Physics **71** (2008) 705.

[5] K. Ohoyama, T. Yokoo, S. Itoh, J. Suzuki, K. Iwasa, T.J. Sato, H. Kira, Y. Sakaguchi, T. Ino, T. Oku, K. Tomiyasu, M. Matsuura, H. Hiraka, M. Fujita, H. Kimura, T. Sato, J. Suzuki, H.M. Shimizu, T. Arima, M. Takeda, K. Kaneko, M. Hino, S. Muto, H. Nojiri, C.H. Lee, J.G. Park, S. Choi, J. Phys. Soc. Jpn. in press.

T. Yokoo[1,2], K. Ohoyama[3], S. Itoh[1,2], J. Suzuki[4], M. Nanbu[5], N. Kaneko[1,2], K. Iwasa[6], T.J. Sato[7], H. Kimura[7], and M. Ohkawara[3]

[1]Neutron Science Section, Materials and Life Science Division, J-PARC Center; [2]Institute of Materials Structure Science, KEK; [3]Institute for Materials Research, Tohoku University; [4]Mechanical Engineering Center, KEK; [5]Center of Neutron Science for Advanced Materials, IMR, Tohoku University; [6]Department of Physics, Tohoku University; [7]Institute of Multidisciplinary Research for Advanced Materials, Tohoku University

Beam Commissioning of the U-line and Update of the World Record of the Strongest Pulsed Muon Source

In the Japan Proton Accelerator Research Complex (J-PARC), the installation of a new muon beamline, called Superomega muon beamline, was completed on the U-line in the Materials and Life Science Experimental Facility (MLF) in October 2012. The Superomega muon beamline is the second muon beamline among the four planned beamlines in the MLF/J-PARC. The basic properties and the installation of the Superomega muon beamline were already reported elsewhere [1, 2, 3]. Here, we report on the results of the first extraction experiment and the beam commissioning for the Superomega muon beamline.

In order to optimize the currents of the beamline magnet of the Superomega muon beamline, we started to perform the surface muon extraction experiment and beam commissioning for the U-line right after the installation of the Superomega muon beamline. The experimental setup of the muon beam commissioning is shown in Fig. 1. The transported muon beam profile was observed by the muon beam profile monitor using plastic scintillation fiber array or by the circular plate of the plastic scintillator taken by an image intensifier tube (IIT) camera placed on the focal point of the Superomega muon beamline. The diameter of the scintillation fiber of the muon beam profile monitor is 2 mm, and 15 fibers are aligned with 10-mm step for the both vertical and horizontal directions. The scintillation light excited by the muon beam from the fiber array counter is converted to electrical pulse signals by multi anode photo multiplier tubes individually, and then their integral intensity within the common gate signal adjusted the first pulse of the muon beam (muon beam in J-PARC has a double-bunched beam structure) are recorded by the 16channel charge to a digital converter (QDC). The number rate of the positive muon was detected by μ-e decay

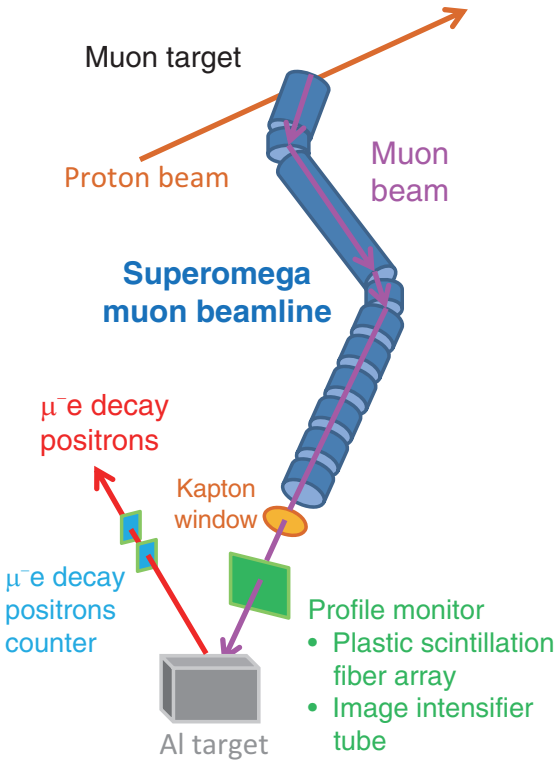

Figure 1. Schematic diagram of the experimental setup for the beam commissioning of the U-line.

positrons emitted from the aluminum target placed behind the muon beam profile monitor. The μ-e decay positron counter is a conventional hodoscope, which includes a set of two plastic scintillation counters. They are placed away from the target by 2.5 m and 3.5 m in distance in the direction normal to the beam axis. A coincidence of the two signals of the μ-e decay positron counters are taken and then send to time to digital converter (TDC) for making time spectrum of μ-e decay positrons.

Figure 2 shows a photo of the muon beam profile at the focal point of the Superomega muon beamline. The muon beam was incident on the plastic scintillation plate in the target vacuum chamber. The light from the plate was taken by the IIT camera through the window of the chamber. The larger circle in this photo represents the edge of the scintillation plate(the diameter is 130 mm). An ellipsoidal part seen in the center of photo, whose major axis is in vertical direction, indicates the muon beam profile. Although the origin of the distortion of this beam profile is still unknown, it was seen that this distortion of the profile appears in the optimized condition of the muon beam, *i.e.* the highest peak and integral intensities, and the narrowest beam size.

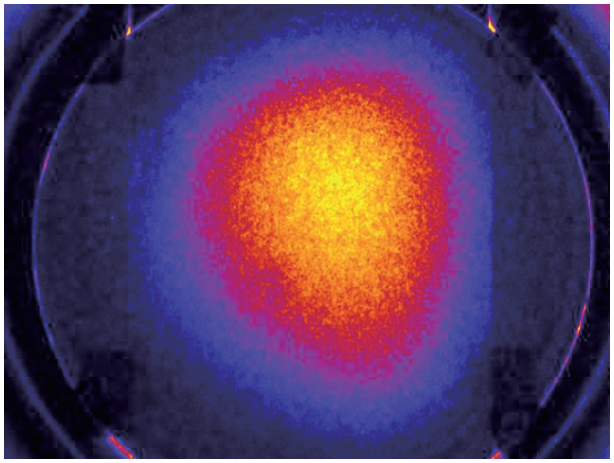

Figure 2. A picture of axial focusing solenoid.

A time spectrum of the μ-e decay positron counter is shown in Fig. 3 (a). The spectrum clearly shows a μ^+ decay curve. According to the fitting result of the decay curve, the life time is estimated to be 2.2 μs. This is in good agreement with the reference number of the average life time of the positive muons. The double bunch structure of the muon beam is also clearly seen in this spectrum. The positron prompt that is composed of scattered positrons by the target is sufficiently suppressed by the positron separator, although the intensity of the positrons in the muon beam was simulated 100 times larger than that of the muons [4]. A number rate of the muon beam was 6.4×10^7 positive muons/*s*, when the primary proton beam power was 212 kW. This corresponds to 3×10^8 positive muons/*s* at 1 MW proton beam power. Figure 3(b) shows the beam profiles of vertical and horizontal directions at the focal position of the Superomega muon beamline detected by a plastic scintillation fiber array counter, after optimization of the beam intensity and the width at the focal position by scanning the currents of the beamline magnets of the Superomega muon beamline. The results of the Gaussian fit for the vertical and horizontal profile show that the widths (1σ) of the muon beam are 34 mm for the vertical direction and 30 mm for horizontal direction. As seen in the beam profile photo taken by the IIT camera, this results show that the muon beam profile represents the ellipsoi-

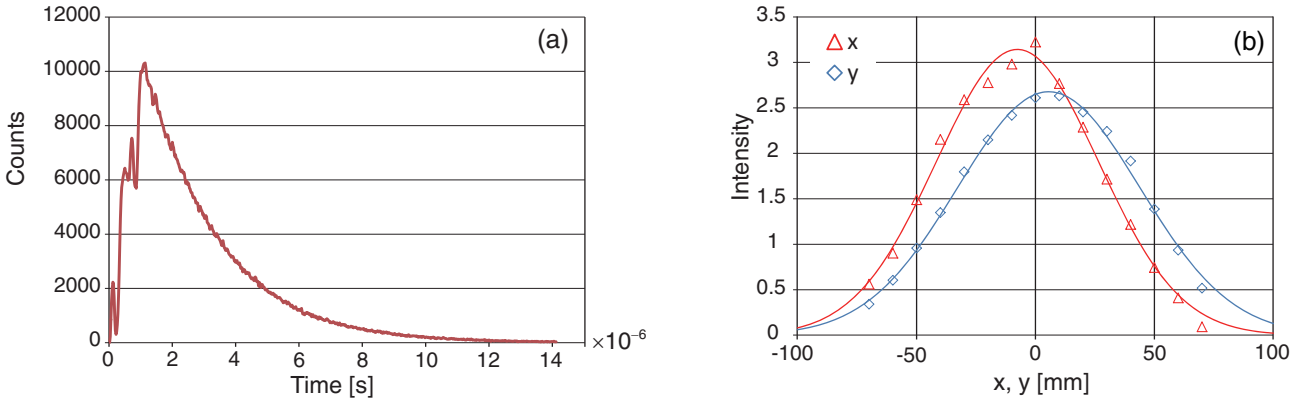

Figure 3. (a) μ-e decay time spectrum from aluminum target, (b) muon beam prole at target position detected by ber array counters.

dal shape with the major axis of vertical direction. Since our final goal for this beamline is the surface muon source for the ultra-slow muon beam, and the ultra-slow muon production target is the tungsten foil of 70 mm in width, 45 mm in height [5], this results indicate that more than fifty percent of the muons transported by the Superomega muon beamline is incident on to the target. We now started to construct the ultra-slow muon beamline and after that, we are planning to perform the extraction experiment of the ultra-slow muon beam as soon as possible.

References

[1] K. Nakahara *et al.*, Nucl. Instrum. Methods Phys. Res., Sect. A **600** (2009) 132.

[2] K. Shimomura *et al.*, MLF Annual Report 2012 143.

[3] Y. Ikedo *et al.*, MLF Annual Report 2012 145.

[4] T. Adachi *et al.*, in preparation.

[5] T. Nagatomo *et al.*, MLF Annual Report 2012 162.

Y. Ikedo[1,2], Y. Miyake[1,2], K. Shimomura[1,2], P. Strasser[1,2], N. Kawamura[1,2], K. Nishiyama[1,2], S. Makimura[1,2], H. Fujimori[1,2], A. Koda[1,2], J. Nakamura[1,2], T. Nagatomo[1,2], Y. Kobayashi[1,2], T. Adachi[3], A. D. Pant[4], T. Ogitsu[5], T. Nakamoto[5], K. Sasaki[5], H. Ohata[5], R. Okada[5], A. Yamamoto[5], Y. Makida[6], M. Yoshida[6], T. Okamura[6], R. Okubo[6], W. Higemoto[1,7], T. U. Ito[1,7], K. Nakahara[8], and K. Ishida[9]

[1]Muon Science Section, Materials and Life Science Division, J-PARC Center; [2]Institute of Materials Structure Science, KEK; [3]Graduate School of Science, The University of Tokyo; [4]Interdisciplinary Graduate School of Medicine and Engineering, University of Yamanashi; [5]Cryogenics Science Center, KEK; [6]Institute of Particle and Nuclear Studies, KEK; [7]Advanced Science Research Center, JAEA; [8]Department of Physics, University of Maryland; [9]Advanced Meson Science Laboratory, Nishina Center for Accelerator-Based Science, RIKEN

Strategic Use

In keeping with our mandate to promote facility utilization, grow the user community and actively support national research priorities, CROSS-Tokai launched in JFY 2012 the Trial Use access system and the Elements Strategy Initiative on the Public Beamlines at the MLF within the science program area of Strategic Use.

- **Trial Use Access System**

A key component of the CROSS-Tokai mission is to promote the use of, and facilitate access to, the neutron Public Beamlines at J-PARC MLF. With this motivation, CROSS-Tokai began this year the Trial Use Access System that aims to encourage and support first-time and novice users of neutron-based experimental techniques.

The specific objectives of the Trial Use System are:

- To grow the user community and,
- To promote the use and utility of pulsed neutrons through the development and demonstration of innovative new applications

Accordingly, up to a maximum of five percent (5%) of the total beamtime on each of the Public Beamlines at the MLF will be set aside for Trial Use experiments in each round.

The Trial Use system is targeted at:

- First time and novice users of neutron-based experimental techniques and,
- First time users of pulsed neutron beams who wish to establish experimental feasibility and the capability of the instruments at J-PARC MLF.

Employing the specialist expertise and experience of the CROSS-Tokai Science Coordinators and other appropriate staff, the Trial Use system offers support to prospective users through the whole process of facility utilization including:

- Instrument selection and feasibility assessment
- Proposal preparation
- Experiment design, planning and execution
- Data analysis and interpretation
- Publication of results

The Trial Use Access System applies only to the six Public Beamlines of J-PARC MLF that are supported by CROSS-Tokai. Anyone wishing to learn more about the Trial Use access system should contact CROSS-Tokai via the CROSS*help* hotline at http://www.cross-tokai.jp/en/contact/crosshelp.shtml.

- **Elements Strategy Initiative**

The Elements Strategy Initiative (ESI) is an integrated strategic research program of the Japanese government that is designed to bring together industry, government, and academia in a coordinated way that streamlines the process of translating fundamental discoveries into real-life applications so as to maintain and promote the international competitiveness of the Japanese economy and industry.

The ESI has established four core research centers (CRCs) to lead the development of innovative materials and alternative technologies that have reduced or no reliance on rare earth or precious metals in the target research areas of:

- Magnetic Materials
- Catalytic and Battery Materials
- Electronic Materials
- Structural Materials

As part of this integrated approach, the Public Neutron Beam Facility at J-PARC has been identified as one of the key pieces of national research infrastructure that should work in collaboration with the CRCs towards the goals of the program. Accordingly, a proportion (15%) of the total beamtime on the Public Beamlines at the MLF has been ear-marked by the Selection Committee of CROSS-Tokai to support these research activities.

In addition, members of the CROSS-Tokai and MLF staff have been appointed to work as expert advisors to the CRCs to assist with the process of identifying areas in which neutron scattering can contribute to the research effort and to assist with the preparation of proposals and experimental planning.

We look forward to reporting many exciting research outcomes from our collaboration with the ESI in coming years.

JASRI – CROSS-Tokai Complementary Use Proposal Program

As part of their respective roles as Registered Institution responsible for the promotion of Public Beamline utilization at J-PARC MLF and SPring-8, CROSS-Tokai and JASRI commenced in the 2013A proposal round a trial of a Complementary Use Proposal Program.

By encouraging and supporting the simultaneous and complementary use of pulsed neutrons (J-PARC MLF) and synchrotron radiation (SPring-8), the program aims to enhance the quality, scope and impact of research outcomes from the Public Beamlines at both facilities.

In the first trial phase of the program, applicants wishing to have their proposals considered within the Complimentary Use framework are asked to submit separate proposals through the General Use access systems of both J-PARC MLF and SPring-8. These applications are considered separately within the normal proposal assessment mechanisms and, if approved by both facilities, are recognized as “Complementary Use” proposals.

SPring-8

It is hoped that the Complementary Use program will develop in coming years to the point where a single research proposal will qualify the applicant to receive beamtime allocations from multiple facilities. Similarly, it is expected that the scope of the Complementary Use program will soon expand beyond the Public Beamlines at SPring-8 and J-PARC MLF to include other instruments at these facilities and even other organizations.

MLF Operations in 2012

CROSS-Tokai - 2012 Update

About CROSS-Tokai

In July 2009, the Japanese government established at J-PARC the Public Neutron Beam Facility consisting of the accelerators used to generate the neutron beams and a proportion of the beamlines that exploit them for research purposes.

In order that open access to major publicly-funded research facilities be guaranteed, the policy framework within which the Public Neutron Beam Facility was created required that an independent third-party organization be responsible for the administration and support of the science program on the so-called Public Beamlines.

CROSS-Tokai was appointed to this role by the Ministry of Education, Culture, Sports, Science and Technology in March 2011 and soon after began operations out of its newly-established offices within the J-PARC precinct.

CROSS-Tokai and J-PARC

Although CROSS-Tokai is structurally independent of JAEA and KEK – the co-owners and operators of J-PARC – it maintains a high level of cooperation and collaboration with the two founding organizations that is driven by the common scientific objectives of all the stakeholders. Figure 2 shows a schematic representation of the operational and functional relationship between CROSS-Tokai and J-PARC.

The Public Beamlines at J-PARC・MLF

The MLF has capacity to accommodate up to 23 neutron beamlines around the present target station. There are currently 17 neutron and 2 muon beam instruments in operation, 1 neutron instrument in commissioning and 3 new beamlines under construction. Of these, 5 beamlines have been designated as Public Beamlines as part of the Public Neutron Beam Facility and are supported by CROSS-Tokai.

Though not exhaustive in their experimental capability, the Public Beamlines cover a wide range of neutron scattering techniques and research applications. The Public Beamlines at J-PARC・MLF are:

- BL01 *4SEASONS* - 4D-Space Access Neutron Spectrometer
- BL02 *DNA* - Biomolecular Dynamics Spectrometer
- BL15 *TAIKAN* - Small and Wide Angle Neutron Scattering Instrument
- BL17 *SHARAKU* - Polarized Neutron Reflectometer
- BL18 *SENJU* : Extreme Environment Single Crystal Neutron Diffractometer

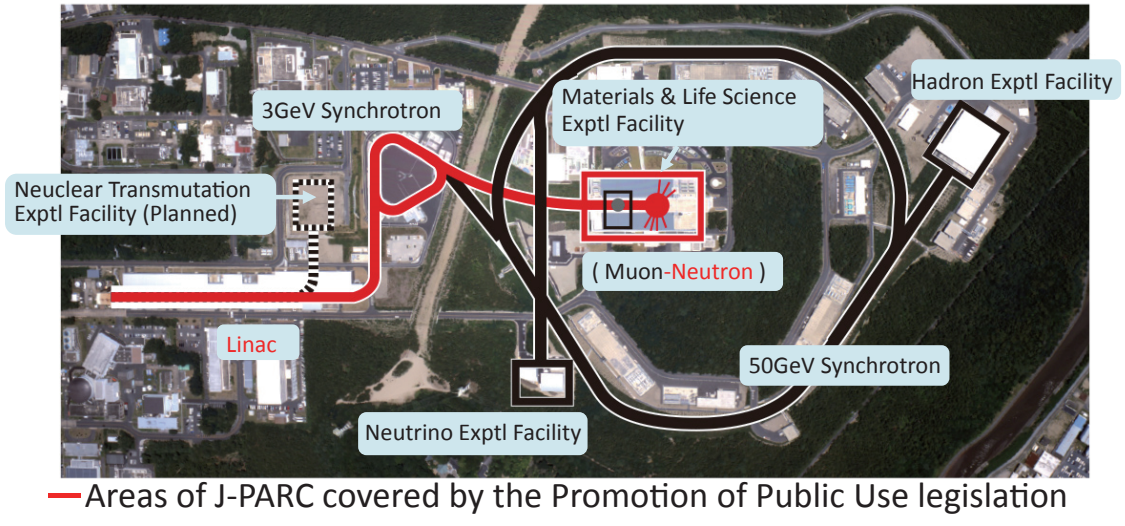

Figure 1. The Public Neutron Beam Facility at J-PARC (shown in red).

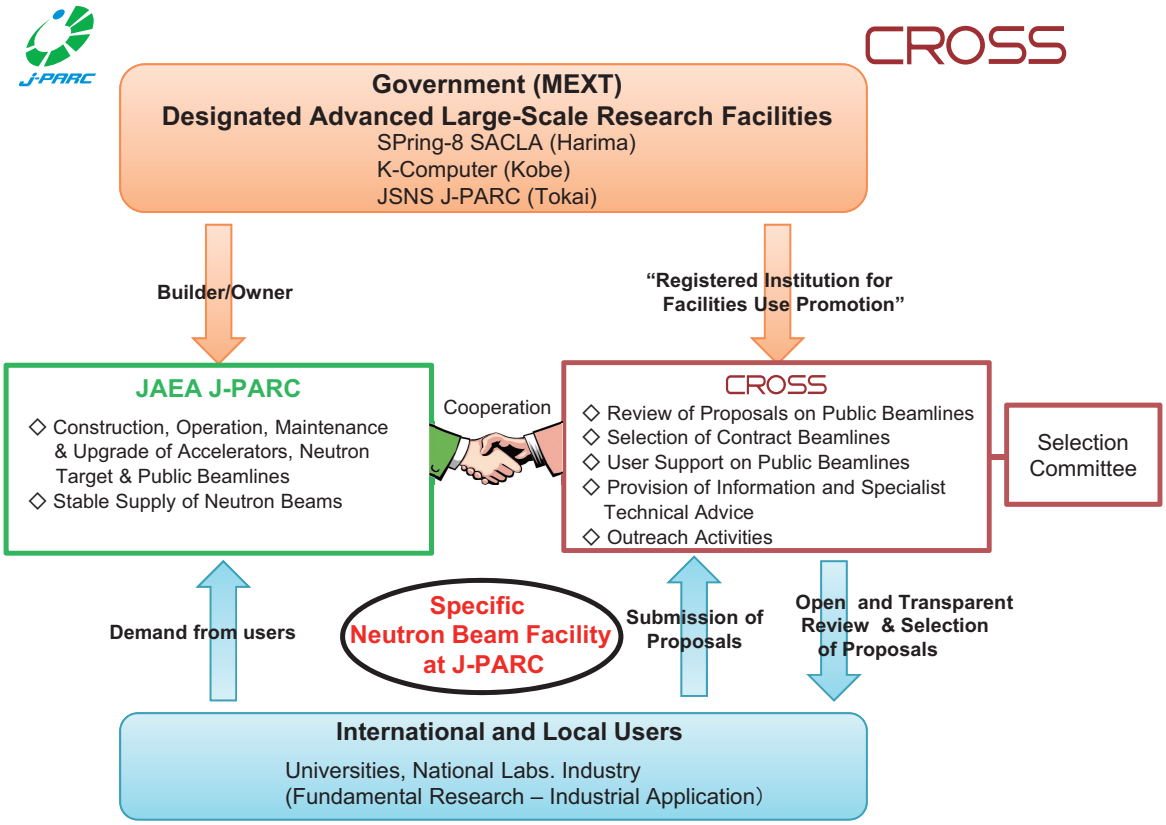

Figure 2. The relationship between and respective functions of JAEA and CROSS-Tokai.

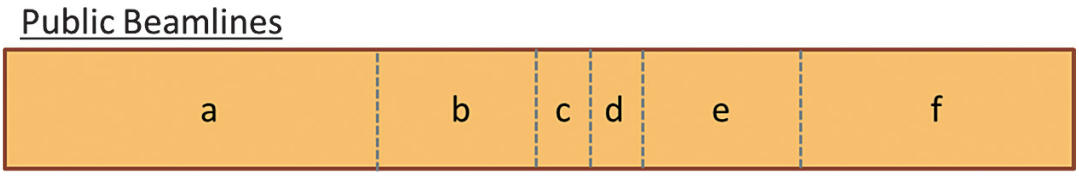

(a) General Use
(b) Elements Strategy Initiative (up to 15%)
(C) Trial Use (up to 5%)
(d) Director's Discretion (up to 5%)
(e) CROSS-Tokai Research (up to 15%)
(f) Facility Use (up to 25%)

Figure 3. Beamtime Distribution on the Public Beamlines.

Distribution of Beamtime on the Public Beamlines

The Selection Committee of CROSS-Tokai regularly reviews and sets policies for the distribution of beamtime on the Public Beamlines at the MLF. Governed by the legislative framework within which the Public Neutron Beam Facility was established and in response to the operational requirements of the beamlines, beamtime is currently distributed in approximately the following ratios:

The Role of CROSS-Tokai

Under the terms of the legislation that supports the Public Neutron Beam Facility, CROSS-Tokai is entrusted with specific responsibilities. In practical terms, the core functions of CROSS-Tokai can be summarized as follows:

- *Proposal Selection and Beamtime Allocation on the Public Beamlines*
- *User Support on the Public Beamlines*
- *Establishment of an Information Resource for Facility Users*

- *Outreach and Facility Utilization Promotion*
- *Contract Beamline Assessment and Selection*

CROSS-Tokai in 2012

Overview

Two years have now passed since CROSS-Tokai commenced operations in support of the Public Beamlines at J-PARC. Though the start of direct user support activities was delayed by about 10 months due to the Great East Japan Earthquake of March 2011, CROSS-Tokai continued to expand the scope and scale of its activities during the recovery period and is now fully engaged in its core business of managing the proposal selection process for the Public Beamlines, delivering high-quality user support and promoting facility utilization.

CROSS-Tokai 2012 Highlights

- ***PLANET* becomes the 6th Public Beamline**

During JFY2012, the suite of Public Beamlines consisted of five fully-operational instruments: BL01 *4SEASONS*, BL02 *DNA*, BL15 *TAIKAN*, BL17 *SHARAKU* and BL18 *SENJU*. From JFY2013, the sixth Public Beamline at J-PARC・MLF – BL11 *PLANET* – will become available to users.

With the addition of *PLANET* to the fold, the range of science enabled on the Public Beamlines will be extended to include the study of liquids and solids under extreme temperature and pressure conditions with particular application in the Earth and Materials Sciences.

For more information about *PLANET* and its capabilities, please see the detailed beamline update in this report.

Figure 4. BL11 PLANET.

- **Strategic Use**

In keeping with our mandate to promote facility utilization and actively support national research priorities, CROSS-Tokai initiated two new user programs on the Public Beamlines in JFY2012:

- **Trial Use** – a program that promotes the use of neutrons by first-time or novice users from both the industrial and academic sectors; and,
- **Elements Strategy Initiative** – a Japanese Government program that aims to promote the development of alternative materials and technologies in the target areas of permanent magnets, catalysis and batteries, and electronic and structural materials.

Please see the “What’s new at the MLF in 2012” section in this report for more details about Trial Use and the Elements Strategy Initiative.

- **JASRI – CROSS-Tokai Complementary Use**

In the area of facility utilization promotion, we have in the last year joined with JASRI – our sister organization at SPring-8 – to develop a system of Complementary Use proposals. This system aims to encourage and facilitate complementary and collaborative use of multiple large-scale facilities – initially neutron and synchrotron radiation sources – in a single research project. We hoped that, ultimately, the system will develop to a stage where users can make a single research proposal to multiple facilities.

Other Key CROSS-Tokai activities and milestones in JFY2012

- **Proposal Selection**
  - 2012B Call for Proposals – May-Jun 2012
  - 2013A Call for Proposals – Oct-Nov 2012
  - Supported the work of committees associated with proposal selection:
    - Selection Committee –20 Aug 2012 at TKP Ochanomizu Conference Center, Tokyo,
      13 Feb 2013 at TKP Tamachi Conference Center, Tokyo
    - Proposal Evaluation Committee & Expert Panels
      2 Aug 2012 at KEK-Tokai, Ibaraki (Expert Panels)
      3 Aug 2012 at KEK-Tokai, Ibaraki

31 Jan 2013 at KEK-Tokai, Ibaraki (Expert Panels)
1 Feb 2013 at KEK-Tokai, Ibaraki

- CROSS Development Proposal Evaluation Panel
  26 – 27 Dec 2012 at KEK-Tokai, Ibaraki

- **User Support**

CROSS-Tokai is now supporting user operations and ongoing instrument development activities on the five Public Beamlines with a Neutron R&D team of 28 scientists, programmers, engineers and technicians.

Figure 5. Selection Committee 20 Aug 2012.

Complementing these human resources, CROSS-Tokai continues to develop and maintain user facilities in the Ibaraki Quantum Beam Research Center including:

- ✧ User Experiment Preparation Laboratory I – Hard Matter
- ✧ User Experiment Preparation Laboratory II – Soft Matter & Biomaterials
- ✧ User Data Analysis Room
- ✧ User Lounge and "Refresh Rooms"

Contract Beamline Review

Also starting this year, CROSS-Tokai is undertaking the task of reviewing the operation and performance of contract beamlines at the MLF. Specifically, during JFY2012, we established and set terms of reference for the Contract Beamline Evaluation Committee that will carry out the interim review of two Ibaraki Prefecture beamlines (BL03 iBIX and BL20 iMATERIA) during JFY2013.

- **Outreach and Facility Promotion**

Workshops

- **3rd CROSSroads Workshop : Structure and Function of Chiral Magnetic Materials** 17-18 Dec 2012, Ibaraki Quantum Beam Center, Tokai

User Experiment Preparation Laboratory I

User Experiment Preparation Laboratory II

User Data Analysis Room

User Lounge

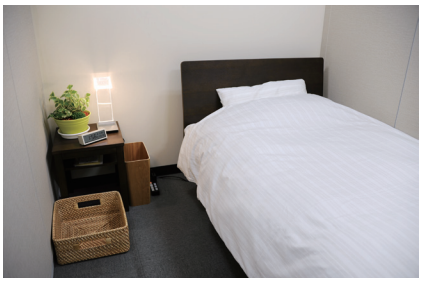

Refresh Rooms

Figure 6. User facilities in the Ibaraki Quantum Beam Research Center.

- **4th CROSSroads Workshop : Progress in Thin Film and Interface Science at J-PARC** 10 Jan 2013, Kenkyusha, Tokyo
- **5th CROSSroads Workshop : Structure and Properties of Materials using the Single Crystal Diffractometers at J-PARC** 25-26 Feb 2013, Ibaraki Quantum Beam Center, Tokai
- **6th CROSSroads Workshop : Leading Edge Research using Dynamics Spectrometers** 14-15 Mar 2013, Tokyo Office of Kyoto University, Tokyo

Public Lectures

- **Applications of Synchrotron Radiation and Neutrons in Cultural Heritage** 28 Sept 2012, Kenkyusha, Tokyo

Seminars

- **1st Seminar on Neutron Scattering at RIKEN** 24 Apr 2012, RIKEN, Wako, Saitama
- **Industrial Applications of Neutron Scattering** 27 Jul 2012, Mitsui Mining and Smelting Co., Saitama
- **Industrial Applications of Neutron Scattering in Osaka** 8 Aug 2012, Osaka Science & Technology Center, Osaka
- **Industrial Applications of Neutron Scattering** 9 Aug 2012, Sumitomo Chemical Co., Osaka
- **Industrial Applications of Neutron Scattering** 19 Oct 2012, TOYOTA Central R&D Labs, Aichi
- **Industrial Applications of Neutron Scattering** 28 Nov 2012, TORAY Research Center, Shiga
- **Industrial Application Seminar (at JSNS Annual Meeting 2012)** 10 Dec 2012, Kyoto University, Kyoto
- **1st Synchrotron Radiation・Neutron Linkage Use Seminar** 22 Mar 2013, LMJ Tokyo, Tokyo

Status of Beam Operations at the MLF

In Japanese Fiscal Year (JFY) 2012, the beam operation at the MLF started with a beam power of 200 kW. Figure 1 shows the trend of the beam power from the first beam to the end of May 2013. Although the accelerator already demonstrated its capability for beam operation with power of 300 kW, the mercury target had a pitting damage issues on the target vessel so the beam power for users had to be limited to less than 200 kW. After installation of the helium bubbler system in the mercury target, the power of the beam operation increased to as high as 300 kW. For the accelerator study, a high power beam of up to 500 kW operated shortly for less than one minute.

The time schedule in JFY2012 is shown in Fig. 2. Because of the strong demand from the neutrino facility in J-PARC, a long beam time was planned in JFY 2012 for all facilities. Since the ion source of the accelerator was found to have a long life time, the period for each beam run became longer than the previous. According to the plan, the beam was stopped for a short time only for the MLF in the end of April and the beginning of January because of the maintenance of the cryogenic system at the neutron source. In Table 1, the scheduled time and availability are shown. We succeeded in supplying beam for users with long duration and considerably high availability, such as 95%.

Table 1. Run cycle, scheduled time and availability.

Run#	Scheduled Time (h).	Availability
42	967	96.4
43	775	96.7
44	516	94.1
45	801	92.4
46	886	93.8
47	636	94.5
Overall	4581	94.7

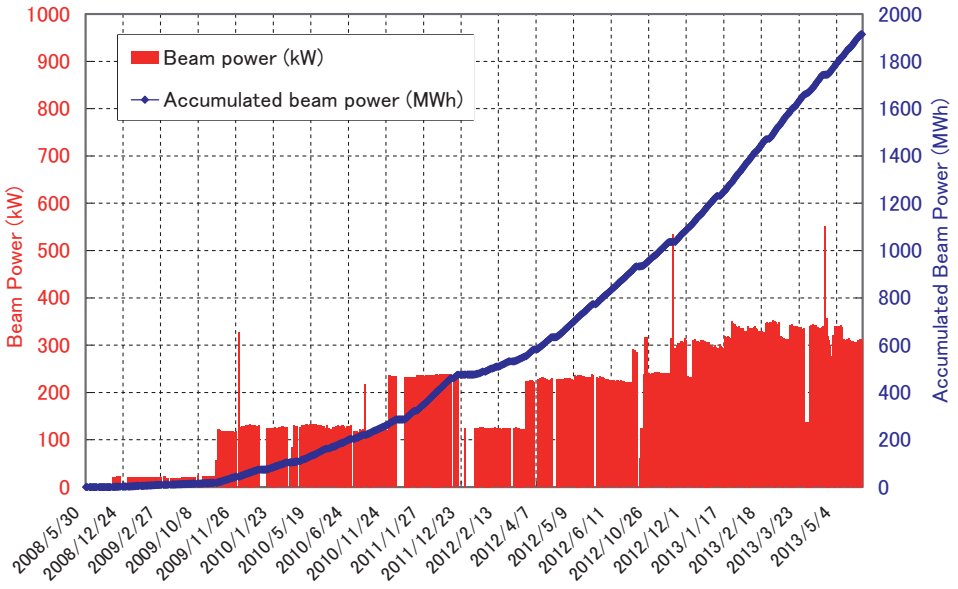

Figure 1. Beam power trend at MLF and cumulative beam power from the first beam to the summer 2013.

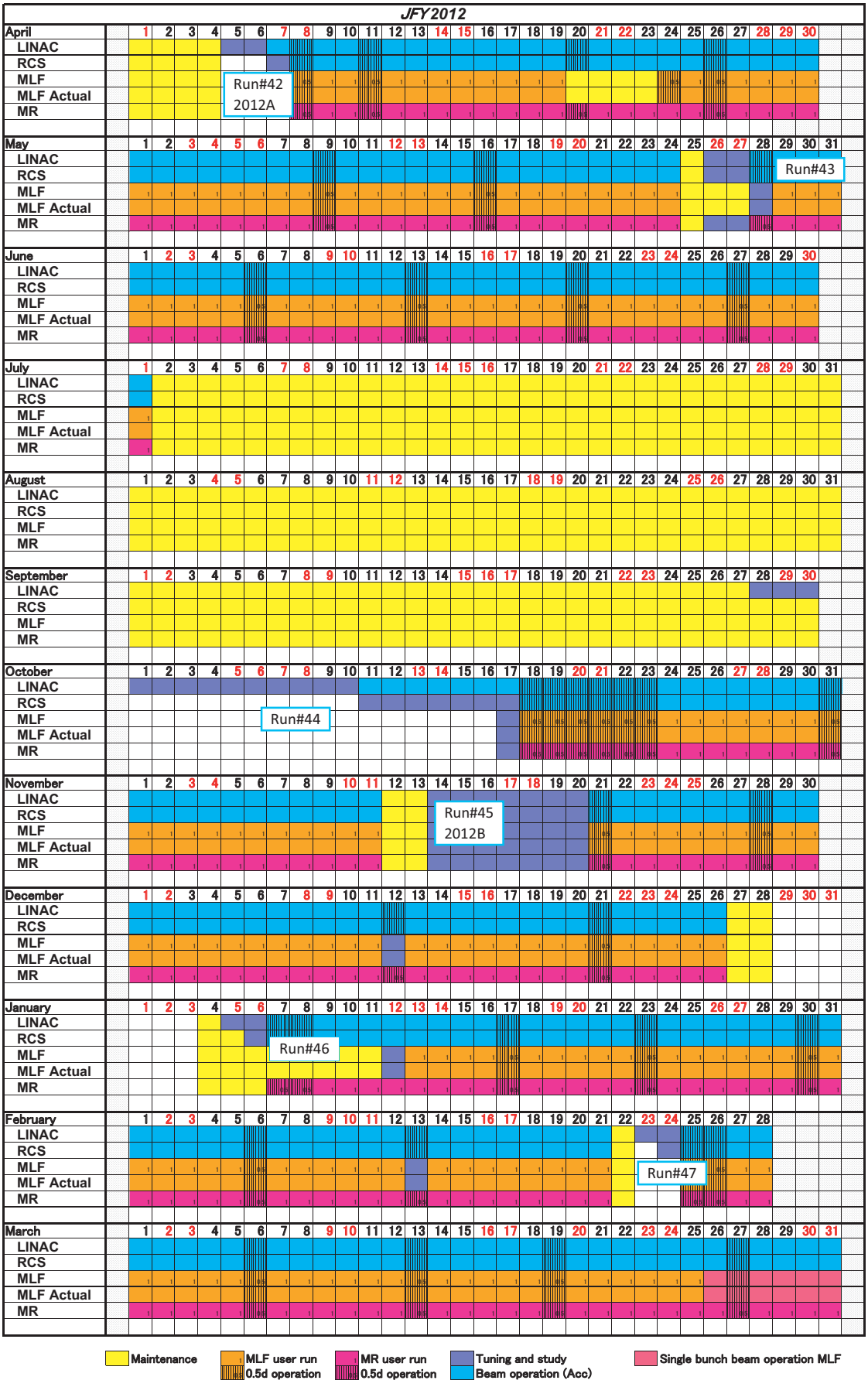

Figure 2. Scheduled plan and actual results for the beam operation in JFY2012 at J-PARC.

Users at the MLF

The number of users at MLF in fiscal year 2012 hit a record high. After recovering from the damages caused by the March 11th earthquake in 2011, the MLF was fully operational in fiscal year 2012, and the number of MLF users in each category had significantly increased from those in the previous fiscal year. The number is not expected to increase in fiscal year 2013 since a long period of accelerator shut down is planned for the upgrade of the linear accelerator to increase the beam energy from 180 MeV to 400 MeV. After the upgrade, more users than ever will come to MLF. The transition of the number of users at MLF is summarized in Table and Figure for domestic and foreign users of the neutron and muon experimental facilities.

Table. The number of domestic and foreign users in the period of fiscal year

	FY2008		FY2009		FY2010		FY2011		FY2012	
	Domestic Users	Foreign Users	Domestic Users	Foreign Users	Domestic Users	Foreign Users	Domestic Users	Foreign Users	Domestic Users	Foreign Users
Neutron	182		378		529		222		735	
	161	21	353	25	485	44	198	24	650	85
Muon	12		57		55		30		72	
	12	0	55	2	48	7	28	2	62	10

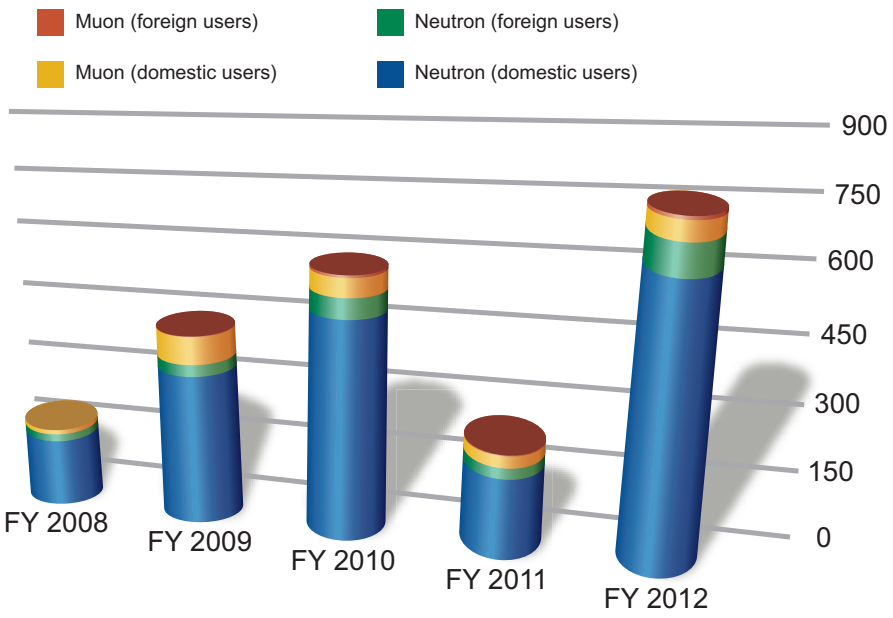

Figure. Number of domestic and foreign users in the fiscal year period.

Proposal Review System

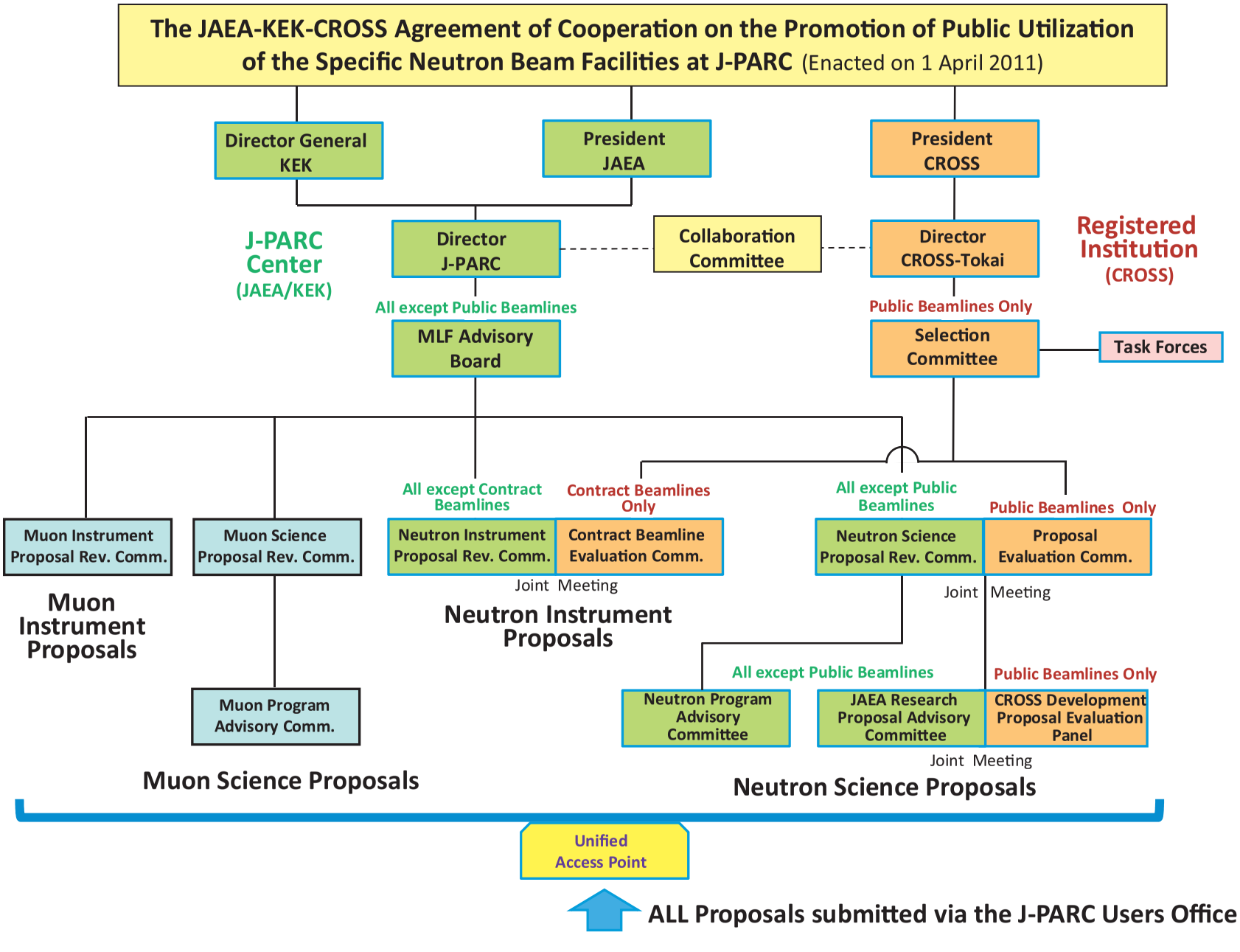

MLF Proposals Summary – FY2012

Table 1. Breakdown of Proposal Numbers for the 2012A & 2012B Rounds.

Beam-line	Instrument		2012A						2012B					
			Submitted			Approved			Submitted			Approved		
			GU	PU/S	IU	GU	PU/S	IU	GU	PU/S	IU	GU	PU/S	IU
BL01	4D-Space Access Neutron Spectrometer - ***4SEASONS***		9	2	2	9	2	2	15	2	2	8	2	2
BL02	Biomolecular Dynamics Spectrometer - ***DNA***		3	3	2	2	3	2	8(2#)	3	2	7(1#)	3	2
BL03	Ibaraki Biological Crystal Diffractometer - ***iBIX***	(100-β)‡	1	0	0	1	0	0	1	0	0	1	0	0
		(β)†	1	11	0	1	11	0	2	11	0	2	11	0
BL04	Accurate Neutron-Nucleus Reaction Measurement Instrument - ***ANNRI***		2	1	1	2	1	1	7	1	1	7	1	1
BL05	Neutron Optics and Physics - ***NOP***		2	1	0	2	1	0	1	1	0	1	1	0
BL08	Super High Resolution Powder Diffractometer -***S-HRPD***		9	1	0	6	1	0	16	1	0	10	1	0
BL10	Neutron Beamline for Observation and Research Use - ***NOBORU***		8	4	1	8	4	1	14	4	1	11	4	1
BL11	High-Pressure Neutron Diffractometer - ***PLANET***		0	0	1	0	0	1	0	0	1	0	0	1
BL12	High Resolution Chopper Spectrometer- ***HRC***		5	1	0	1	1	0	4	1	0	4	1	0
BL14	Cold-neutron Disk-chopper Spectrometer - ***AMATERAS***		16	2	1	11	2	1	16	2	1	11	2	1
BL15	Small and Wide Angle Neutron Scattering Instrument - ***TAIKAN***		16	6	1	16	6	1	35(5#, 2+)	6	1	19(5#, 2+)	6	1
BL16	High-Performance Neutron Reflectometer with a Horizontal Sample Geometry - ***SOFIA***		7	1	0	7	1	0	17	1	0	17	1	0
BL17	Polarized Neutron Reflectometer - ***SHARAKU***		8	3	2	5	3	2	18(3#)	3	2	9(3#)	3	2
BL18	Extreme Environment Single Crystal Neutron Diffractometer - ***SENJU***		4	2	3	4	2	3	11(1#)	2	3	5(1#)	2	3
BL19	Engineering Diffractometer - ***TAKUMI***		18	4	1	15	4	1	26	4	1	21	4	1
BL20	Ibaraki Materials Design Diffractometer - ***iMATERIA***	(100-β)‡	15	0	0	11	0	0	15	0	0	9	0	0
		(β)†	28	12	0	27	12	0	23	12	0	23	12	0
BL21	High Intensity Total Diffractometer - ***NOVA***		6	1	0	6	1	0	21	1	0	15	1	0
D1	Muon D1		7	1	1	5	1	1	16	1	1	13	1	1
D2	Muon D2		14	0	1	12	0	1	9	0	1	8	0	1
U	Muon U		0	1	0	0	1	0	0	1	0	0	1	0
Subtotal			179	57	17	151	57	17	275	57	17	161	57	17
Total			253			225			349			235		

GU : General Use **PU** : Project Use or Ibaraki Pref. Project Use **IU :** Instrument Group Use
S : S-type Proposals † : Ibaraki Pref. Exclusive Use Beamtime (β = 80% in FY2012)
‡ : J-PARC Center General Use Beamtime ((100-β = 20% in FY2011)
# : Proposal Numbers under Trial Use Access System in GU
+ : Proposal numbers under Element Strategy in GU

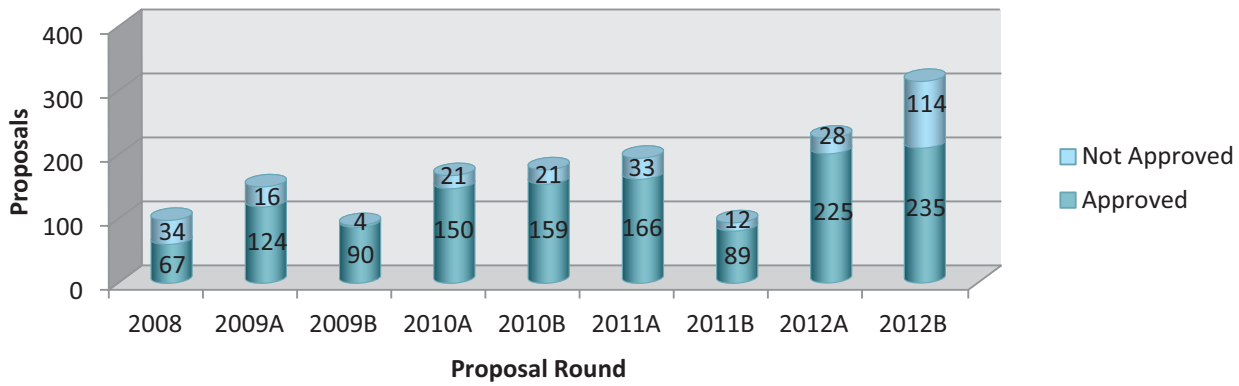

Figure 1. MLF Proposal Numbers over Time.

Table 2. Principal Investigator Affiliations in FY2012.

Universities (Japan)	JAEA	Companies (Japan)	KEK	Foreign Organizations	Research Institutes (Japan)
212	141	101	34	46	68

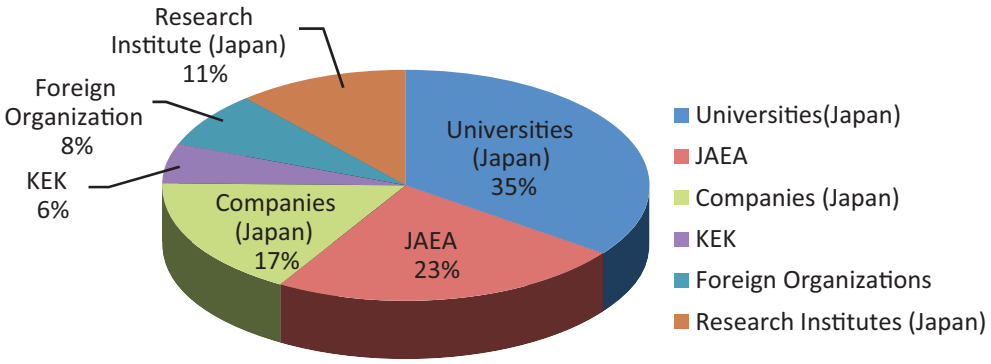

Figure 2. Origin of Proposals in FY2011.

Table 3. Proposals by Sub-committee/Expert Panel – FY2012.

Sub-committee Expert Panel	P1	P2	P3	P4	P5	P6	P7	P8	P9	P10	Q1	Q2
No. of Proposals	96	29	44	14	77	15	56	25	11	2	14	32

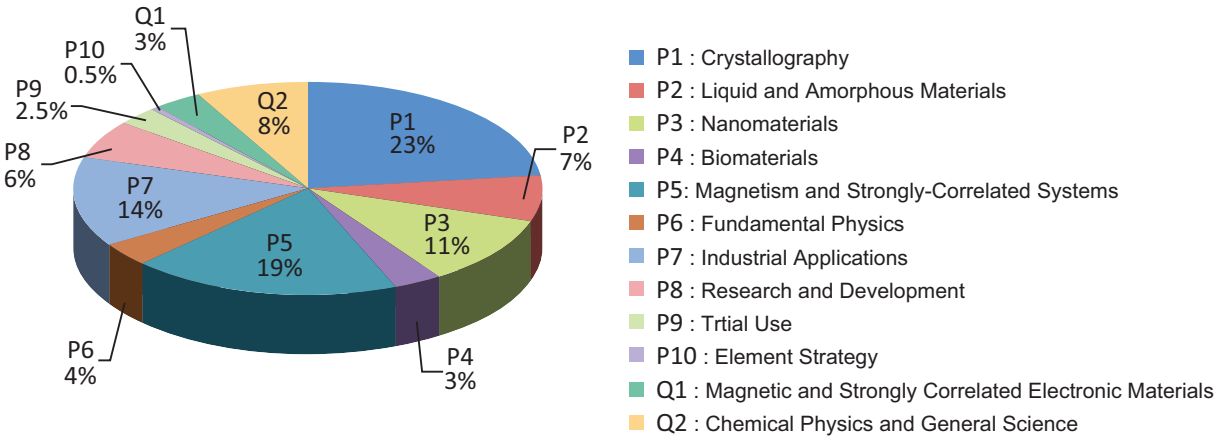

Figure 3. Submitted Proposals by Sub-committee/Expert Panel – FY2012.

MLF Division Staff 2012

Director	Masatoshi Arai (JAEA)
Vice Director	Hideki Seto (KEK)
	Masatoshi Futakawa (JAEA)

Neutron Source Section

	JAEA	
Leader	Hiroshi Takada	Toshiaki Uehara
Sub-Leader	Yoshimi Kasugai	Kiyomi Ikezaki
	Katsuhiro Haga	Kohei Hanano
	Shinichiro Meigo	Hideki Tatsumoto
	Kenji Sakai	Motoki Ooi
	Makoto Teshigawara	Yoshihiko Kawakami
	Tomokazu Aso	Hideki Ueno
	Hidetaka Kinoshita	Hisashi Sakurayama
	Kenichi Oikawa	Takashi Naoe
	Masahide Harada	Atsushi Akutsu
	Hiroyuki Kogawa	Toru Suzuki
	Takashi Wakui	Masato Ida
	Tetsuya Kai	Hideaki Ishii
	Masakazu Seki	Shoichi Hasegawa
	Akihiko Watanabe	Hiroki Matsui
	Akira Ogawa	Shizuka Yoshinari
	Kiichi Ohtsu	Chieko Higuchi

Neutron Science Section

	KEK	
Leader	Takashi Kamiyama	Naokatsu Kaneko
	Hideki Seto	Masao Yonemura
	Toshiya Otomo	Miki Nagao
	Tetsuya Yokoo	
	Norifumi Yamada	JAEA
	Shuki Torii	Sub-Leader Kazuya Aizawa
	Tomohiro Seya	Kentaro Suzuya
	Masataka Sakaguchi	Kenji Nakajima
	Zhang Junrong	Takayuki Oku
	Koichiro Sadakane	Mitsutaka Nakamura
	Kaoru Taketani	Stefanus Harjo
	Hidetoshi Ohshita	Takeshi Nakatani
	Shinichi Ito	Shinichi Takata
	Takashi Ino	Nobuaki Takahashi
	Setsuo Satoh	Takenao Shinohara
	Suguru Muto	Ryoji Kiyanagi

Yukinobu Kawakita
Seiko Kawamura
Yasuhiro Inamura
Tatsuya Kikuchi
Takuro Kawasaki
Jun Abe
Taiki Tominaga
Wu Gong
Yiwei Yang
Hiromichi Tanaka
Wataru Kambara
Yukihiro Ito
Takaaki Iwahashi
Tomonori Hosoya
Yasuhiro Yamauchi
Kentaro Moriyama
Masayasu Takeda
Toyotaka Osakabe
Kazuo Kurihara
Wataru Utsumi
Shuichi Wakimoto
Takanori Hattori
Itaru Tamura
Koji Kaneko
Satoru Fujiwara
Hiroshi Nakagawa
Asami Sano
Hideo Harada
Atsushi Kimura
Shoji Nakamura
Yosuke Toh
Mariko Segawa
Hiroshi Iikura
Hidehito Asaoka
Masato Kubota
Chiho Tobe
Naoko Shimizu
Junko Akutsu
Mayu Mizukoshi
Yukino Inoue

Neutron Instrumentation Section

JAEA

Leader
Kazuhiko Soyama
Kaoru Sakasai
Dai Yamazaki
Kentaro Toh
Tatsuya Nakamura
Ryuji Maruyama
Hirotoshi Hayashida
Katsunori Honda
Hiroyuki Suzuki
Takuro Sakai
Hideshi Yamagishi
Mana Hirayama

Muon Section

KEK

Leader
Yasuhiro Miyake
Ryosuke Kadono
Koichiro Shimomura
Kenji Kojima
Patrick Strasser
Naritoshi Kawamura
Akihiro Koda
Hiroshi Fujimori
Shunsuke Makimura
Yasuhisa Nemoto
Yasuo Kobayashi
Kusuo Nishiyama
Yutaka Ikedo
Tetsuya Masuda
Jumpei Nakamura
Masanori Miyazaki
Ichihiro Yamauchi
Takashi Nagatomo
Yohei Nakatsugawa
Yoshitomo Takahashi
Masatoshi Hiraishi
Yoshiro Irie
Yoshinori Ishiji

JAEA

Wataru Higemoto
Takashi Ito

CROSS-Tokai Staff 2012

Director Yasuhiko Fujii

Science Coordinators

Masatoshi Sato
Yoshiaki Fukushima

Neutron R&D Division

Head	Jun-ichi Suzuki	Koji Munakata
Head (Deputy)	Ryoichi Kajimoto	Koji Kiriyama
	Sungdae Ji	Takayoshi Ito
	Kazuhiko Ikeuchi	Yukihiko Kawamura
	Kaoru Shibata	Hiroshi Kira
	Kazuya Kamazawa	Motoyuki Ishikado
	Takeshi Yamada	Kazuhiro Akutsu
	Kazuki Ohishi	Makoto Kobayashi
	Hiroki Iwase	Akifumi Kishi
	Tazuko Mizusawa	Tadashi Futagami
	Yoshifumi Sakaguchi	Kaoru Sato
	Noboru Miyata	Jun-ichi Sato
	Takashi Ohhara	Satoshi Kasai
	Akiko Nakao	Sayaka Suzuki
	Takayasu Hanashima	

Health and Safety Division

Toshiyuki Yamashita

Utilization Promotion Division

Head	Tohru Matoba	Megumi Kawakami
Head (Deputy)	Garry John Foran	Aya Yamada
	Toshiki Asai	Katsumi Kunigihara
	Rei Ohuchi	Asami Inoue
	Junko Ohta	Emi Takaha
	Shin-ichi Yamaguchi	

Admin and Finance Division

Head	Yasuo Seishi	Tomoyuki Yabana
Head (Deputy)	Masaru Yokoyama	Mika Gunji
	Takahiro Koizumi	Mutsumi Shiraishi

Committee and Meetings

Materials and Life Science Facility Advisory Board

物質・生命科学実験施設利用委員会

Kazuya Aizawa	Japan Atomic Energy Agency, Japan
Masatoshi Arai	Japan Atomic Energy Agency, Japan
Yasuhiko Fujii	Comprehensive Research Organization for Science and Society, Japan
Toshiharu Fukunaga	Kyoto University, Japan
Masatoshi Futakawa	Japan Atomic Energy Agency, Japan
Makoto Hayashi	Ibaraki Prefecture, Japan
Mitsuhiro Hirai	Gunma University, Japan
Kazuaki Iwasa	Tohoku University, Japan
Masahiko Iwasaki	RIKEN, Japan
Ryosuke Kadono	High Energy Accelerator Research Organization, Japan
Shinichi Kamei	Mitsubishi Research Institute, Inc., Japan
Takashi Kamiyama	High Energy Accelerator Research Organization, Japan
Toshiji Kanaya (Chair)	Kyoto University, Japan
Takashi Kato	Japan Atomic Energy Agency, Japan
Youji Koike	Tohoku University, Japan
Yasuhiro Miyake	High Energy Accelerator Research Organization, Japan
Junichirou Mizuki	Japan Atomic Energy Agency, Japan
Toshiya Otomo	High Energy Accelerator Research Organization, Japan
Hideki Seto	High Energy Accelerator Research Organization, Japan
Mitsuhiro Shibayama	University of Tokyo, Japan
Jun Sugiyama	Toyota Central R&D Labs., Inc., Japan
Eiko Torikai	University of Yamanashi, Japan

Term of board appointments: 1 April 2011 - 31 March 2013

Neutron Instrument Proposal Review Committee

中性子実験装置部会

Masatoshi Arai	Japan Atomic Energy Agency, Japan
Koichiro Asahi	Tokyo Institute of Technology, Japan
Masatoshi Futakawa	Japan Atomic Energy Agency, Japan
Muneyuki Imafuku	Tokyo City University, Japan
Takashi Kamiyama	High Energy Accelerator Research Organization, Japan
Hideaki Kitazawa	National Institute for Material Science, Japan
Yoshiaki Kiyanagi (Chair)	Hokkaido University, Japan
Yukio Morii	Ibaraki Prefecture, Japan
Yukio Morimoto	Kyoto University, Japan
Kenji Nakajima	Japan Atomic Energy Agency, Japan
Toshiya Otomo	High Energy Accelerator Research Organization, Japan
Kenji Ohoyama	Tohoku University, Japan
Mamoru Sato	Yokohama City University, Japan
Hideki Seto	High Energy Accelerator Research Organization, Japan

Jun-ichi Suzuki	Comprehensive Research Organization for Science and Society, Japan
Naoya Torikai	Mie University, Japan
Hideki Yoshizawa	University of Tokyo, Japan

Term of committee appointments: 1 April 2011 - 31 March 2013

Neutron Science Proposal Review Committee

中性子課題審査部会

Yoshiaki Akiniwa	Yokohama National University, Japan
Masatoshi Arai	Japan Atomic Energy Agency, Japan
Takahisa Arima	University of Tokyo, Japan
Sung-Min Choi	Korea Advanced Institute of Science and Technology, Korea
Hideto En'yo	RIKEN, Japan
Toshiharu Fukunaga	Kyoto University, Japan
Yoshiaki Fukushima	Comprehensive Research Organization for Science and Society, Japan
Makoto Hayashi	Ibaraki Prefecture, Japan
Takashi Kamiyama	High Energy Accelerator Research Organization, Japan
Toshiji Kanaya	Kyoto University, Japan
Takashi Kato	Japan Atomic Energy Agency, Japan
Brendan Kennedy	University of Sydney, Australia
Yoshiaki Kiyanagi	Hokkaido University, Japan
Yasuhiro Miyake	High Energy Accelerator Research Organization, Japan
Yukio Morii	Ibaraki Prefecture, Japan
Yukio Noda	Tohoku University, Japan
Yuji Ohashi	Ibaraki Prefecture, Japan
Toshiya Otomo	High Energy Accelerator Research Organization, Japan
Je-Geun Park	Seoul National University, Korea
Mamoru Sato	Yokohama city University, Japan
Hideki Seto	High Energy Accelerator Research Organization, Japan
Mitsuhiro Shibayama (Chair)	University of Tokyo, Japan
Jun-ichi Suzuki	Comprehensive Research Organization for Science and Society, Japan
Peter Timmins	Institut Laue-Langevin, France
Yo Tomota	Ibaraki University, Japan
Xun-Li Wang	Oak Ridge National Laboratory, U.S.A
Hideki Yoshizawa	University of Tokyo, Japan

Term of committee appointments: 1 April 2011 - 31 March 2013

JAEA Research Proposal Advisory Committee

J-PARC物質・生命科学実験施設におけるJAEA研究課題諮問委員会

Masatoshi Arai	Japan Atomic Energy Agency, Japan
Toshiharu Fukunaga	Kyoto University, Japan
Mitsuhiro Hirai	Gunma University, Japan
Masayuki Imai	Ochanomizu University, Japan
Toshiji Kanaya	Kyoto University, Japan

Yuji Kawabata	Kyoto University, Japan
Yukinobu Kawakita	Japan Atomic Energy Agency, Japan
Hideaki Kitazawa	National Institute for Material Science, Japan
Yoshiaki Kiyanagi	Hokkaido University, Japan
Takashi Kato	Japan Atomic Energy Agency, Japan
Michiyasu Mori	Japan Atomic Energy Agency, Japan
Yoichi Murakami	High Energy Accelerator Research Organization, Japan
Kenji Nakajima	Japan Atomic Energy Agency, Japan
Hiroyuki Oigawa	Japan Atomic Energy Agency, Japan
Taku Sato	University of Tokyo, Japan
Hideki Seto	High Energy Accelerator Research Organization, Japan
Shinichi Shamoto	Japan Atomic Energy Agency, Japan
Hirohiko Shimizu	Nagoya University, Japan
Jun-ichi Suzuki	Comprehensive Research Organization for Science and Society, Japan
Keisuke Tanaka	Meijo University, Japan
Yo Tomota	Ibaraki University, Japan
Eiko Torikai	University of Yamanashi, Japan
Kazuyoshi Yamada	Tohoku University, Japan

Term of committee appointments: 1 April 2011 - 31 March 2014

Neutron Program Advisory Committee

中性子共同利用実験審査委員会

Koichiro Asahi	Tokyo Institute of Technology, Japan
Yasushi Idemoto	Tokyo University of Science, Japan
Shinichi Itoh	High Energy Accelerator Research Organization, Japan
Kazuaki Iwasa	Tohoku University, Japan
Ryosuke Kadono	High Energy Accelerator Research Organization, Japan
Hiroshi Kageyama	Kyoto University, Japan
Hiroyuki Kagi	University of Tokyo, Japan
Takashi Kamiyama	High Energy Accelerator Research Organization, Japan
Toshiji Kanaya	Kyoto University, Japan
Mikio Kataoka	Nara Institute of Science and Technology
Yoshiaki Kiyanagi	Hokkaido University, Japan
Yutaka Moritomo	University of Tsukuba, Japan
Youichi Murakami	High Energy Accelerator Research Organization, Japan
Toshiya Otomo	High Energy Accelerator Research Organization, Japan
Hideki Seto (Chair)	High Energy Accelerator Research Organization, Japan
Hirohiko Shimizu	High Energy Accelerator Research Organization, Japan
Masaaki Sugiyama	Kyoto University, Japan
Jun-ichi Suzuki	Comprehensive Research Organization for Science and Society, Japan
Soichi Wakatsuki	High Energy Accelerator Research Organization, Japan
Noboru Yamamoto	High Energy Accelerator Research Organization, Japan
Osamu Yamamuro	University of Tokyo, Japan

Term of committee appointments: 1 April 2011 - 31 March 2013

Muon Instrument Proposal Review Committee

ミュオン実験装置部会

Masatoshi Arai	Japan Atomic Energy Agency, Japan
Koichiro Asahi	Tokyo Institute of Technology, Japan
Wataru Higemoto	Japan Atomic Energy Agency, Japan
Masahiko Iwasaki	RIKEN, Japan
Ryosuke Kadono	High Energy Accelerator Research Organization, Japan
Takashi Kato	Japan Atomic Energy Agency, Japan
Kenji Kojima	High Energy Accelerator Research Organization, Japan
Kenya Kubo (Chair)	International Christian University, Japan
Yoshitaka Kuno	Osaka University, Japan
Yasuhiro Miyake	High Energy Accelerator Research Organization, Japan
Nobuhiko Nishida	Tokyo Institute of Technology, Japan
Hiroyuki Nojiri	Tohoku University, Japan
Toru Ogitsu	High Energy Accelerator Research Organization, Japan
Koichiro Shimomura	High Energy Accelerator Research Organization, Japan
Yasunori Yamazaki	RIKEN, Japan

Term of committee appointments: 1 April 2011 - 31 March 2013

Muon Science Proposal Review Committee

ミュオン課題審査部会

Masatoshi Arai	Japan Atomic Energy Agency, Japan
Koichiro Asahi	Tokyo Institute of Technology, Japan
Kim H. Chow	University of Alberta, Canada
Roberto De Renzi	University of Parma, Italy
Wataru Higemoto	Japan Atomic Energy Agency, Japan
Katsuhiko Ishida	RIKEN, Japan
Kenji Ishida	Kyoto University, Japan
Ryosuke Kadono	High Energy Accelerator Research Organization, Japan
Shinsaku Kambe	Japan Atomic Energy Agency, Japan
Takashi Kamiyama	High Energy Accelerator Research Organization, Japan
Hiroshi Kobori	Chiba University, Japan
Youji Koike (Chair)	Tohoku University, Japan
Kenya Kubo	International Christian University, Japan
Yasuhiro Miyake	High Energy Accelerator Research Organization, Japan
Yuichiro Nagame	Japan Atomic Energy Agency, Japan
Yasuo Nozue	Osaka University, Japan
Masao Ogata	University of Tokyo, Japan
Shinji Tsuneyuki	University of Tokyo, Japan
Soichi Wakatsuki	High Energy Accelerator Research Organization, Japan

Term of committee appointments: 1 April 2011 - 31 March 2013

Muon Program Advisory Committee

ミュオン共同利用実験審査委員会

Hiroshi Amitsuka	Hokkaido University, Japan
Masaharu Aoki	Osaka University, Japan
Wataru Higemoto	Japan Atomic Energy Agency, Japan
Katsuhiko Ishida	RIKEN, Japan
Kenji Ishida	Kyoto University, Japan
Kenji Itoh	High Energy Accelerator Research Organization, Japan
Ryosuke Kadono (Chair)	High Energy Accelerator Research Organization, Japan
Shinsaku Kambe	Japan Atomic Energy Agency, Japan
Yoh Kobori	Chiba University, Japan
Yoji Koike	Tohoku University, Japan
Kenji Kojima	High Energy Accelerator Research Organization, Japan
Tadashi Koseki	High Energy Accelerator Research Organization, Japan
Kenya Kubo	International Christian University, Japan
Yasuyuki Matsuda	University of Tokyo, Japan
Yasuhiro Miyake	High Energy Accelerator Research Organization, Japan
Yuichro Nagame	Japan Atomic Energy Agency, Japan
Hironori Nakao	High Energy Accelerator Research Organization, Japan
Yasuo Nozue	Osaka University, Japan
Masao Ogata	University of Tokyo, Japan
Toshiya Otomo	High Energy Accelerator Research Organization, Japan
Atsushi Shinohara	Osaka University, Japan
Shinji Tsuneyuki	University of Tokyo, Japan
Soichi Wakatsuki	High Energy Accelerator Research Organization, Japan

Term of committee appointments: 1 April 2011 - 31 March 2013

Selection Committee (CROSS)

選定委員会

Toshio Akai	Mitsubishi Rayon Co., Ltd., Japan
Hidetoshi Fukuyama (Chair)	Tokyo University of Science, Japan
Makoto Hayashi	Ibaraki Prefecture, Japan
Kazuaki Iwasa	Tohoku University, Japan
Shinichi Kamei	Mitsubishi Research Institute Inc., Japan
Toshiji Kanaya	Kyoto University, Japan
Mikio Kataoka	Nara Institute of Science and Technology, Japan
Naoki Kishimoto	National Institute of Material Science, Japan
Tomoko Nakanishi	University of Tokyo, Japan
Kazumi Nishijima	Mochida Pharmaceutical Co., Ltd., Japan
Mitsuhiro Shibayama	University of Tokyo, Japan
Masaki Takada	RIKEN, Japan
Kiyoyuki Terakura	Japan Advanced Institute of Science and Technology, Japan
Eiko Torikai	University of Yamanashi, Japan

Term of committee appointments: 15 June 2011 - 31 March 2013

Neutron Advisory Committee (NAC)

NAC-2013 convened 14-15 Feb 2013 at the IQBRC, Tokai

List of NAC-2013 Members

Kurt N. Clausen	Paul Scherrer Institute, Switzerland
Mahn Won Kim	Korea Advanced Institute of Science and Technology, Korea
Yoshiaki Kiyanagi	Hokkaido University, Japan
Dan A. Neumann	National Institute of Standards and Technology, USA
Robert Robinson	Australian Nuclear Science and Technology Organization, Australia
Uschi Steigenberger (Chair)	Science and Technology Facilities Council, UK
Werner Wagner	Paul Scherrer Institute, Switzerland

Group photo of NAC-2013

Muon Science Advisory Committee (MuSAC)

MuSAC-11 convened 22-23 Feb 2013 at the KEK Tokai Campus

List of MuSAC-11 Members

Hiroshi Amitsuka	Hokkaido University, Japan
Toshiyuki Azuma	RIKEN, Japan
Klaus P. Jungman	University of Groningen, Netherlands
Elvezio Morenzoni (Chair)	Paul Scherrer Institute, Switzerland
Yasuo Nozue	Osaka University, Japan
Francis Pratt	ISIS, UK
Jeff E. Sonier	Simon Fraser University, Canada
Jun Sugiyama	Toyota Central R&D Labs., Inc., Japan

Group photo of MuSAC-11

The Government Review of J-PARC

Hiroaki Aihara	University of Tokyo, Japan
Hidetoshi Fukuyama (Chair)	Tokyo University of Science, Japan
Takaaki Kajita	University of Tokyo, Japan
Toshiji Kanaya	Kyoto University, Japan
Michiyo Kaneko	Toyota Motor Corporation, Japan
Akio Komori	National Institutes of Natural Sciences, Japan
Noritaka Kumagai	Japan Synchrotron Radiation Research Institute, Japan
Kazumi Nishijima	Mochida Pharmaceutical Co., Ltd., Japan
Kiyotaka Okada	National Institutes of Natural Sciences, Japan
Nobuyuki Osakabe	Hitachi, Ltd., Japan
Hirokazu Tamura	Tohoku University, Japan
Eiko Torikai	University of Yamanashi, Japan
Yuriko Yamagata	Kumamoto University, Japan
Hiromi Yokoyama	University of Tokyo, Japan

Term of committee appointments: 24 February 2012 - 31 January 2013

The Government started their review of J-PARC on March, 2012. The accomplishment of early recovery from the Great East Japan Earthquake was highly appreciated. The major focus of this review was to establish the future five year plan. For Neutrons, the committee recommended that the extensive efforts should be made to improve the environments for sample preparations and data analyses. For Muons, the best effort for the coming five years for the Muon group should be to fill up two beamlines, called S and H. The construction of a research building and an isotope storage building were also discussed.

MLF Workshops in 2012

With the increasing level of scientific activity at the facility, the number and scope of research workshops held under the auspices of the MLF rapidly expanded in 2012.

Conferences and workshops held jointly by J-PARC MLF and CROSS-Tokai

4th MLF Symposium and Ibaraki Prefecture Beamlines User Meeting
10-11 Oct 2012, MIRAIKAN, Tokyo (230 participants, 38 oral and 81 poster presentations)

Joint Meeting of the 10th International Conference on Quasielastic Neutron Scattering (QENS) and the 5th International Workshop on Inelastic Neutron Spectrometers (WINS)
30 Sept – 4 Oct 2012, Nikko, Tochigi (99 participants, 104 presentations)

12th Korea-Japan Meeting on Neutron Science

3-6 Feb 2013, University of the Ryukyus, Okinawa (59 participants, 49 presentations)

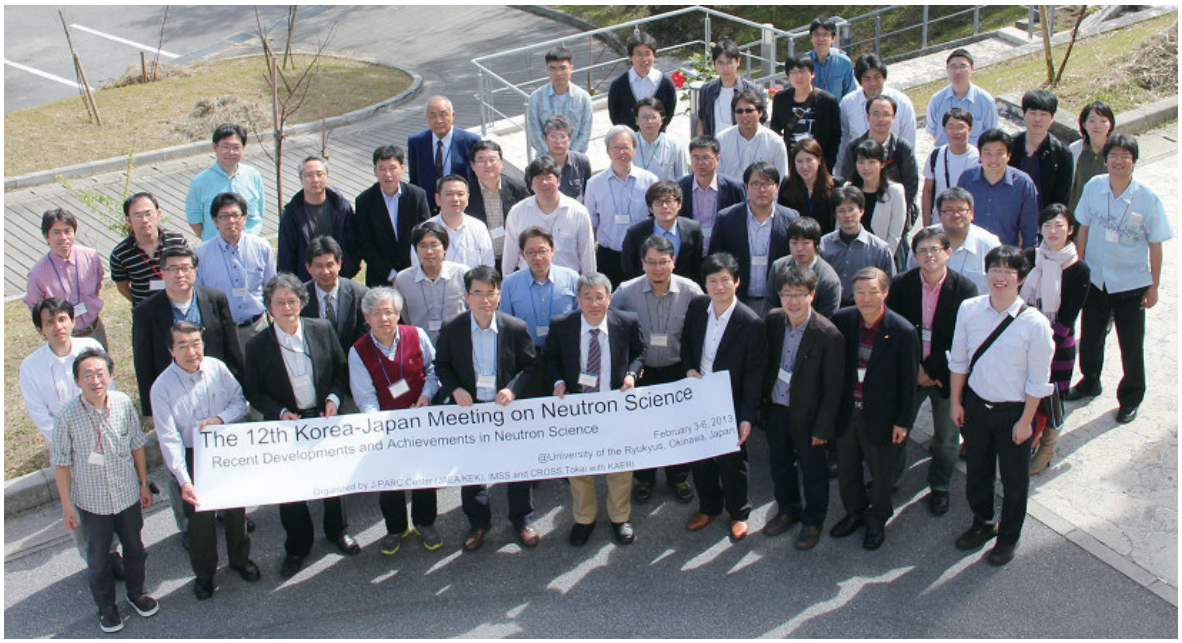

SNS - JSNS Collaboration on Source Development

27-29 Nov 2012, Oak Ridge National Laboratory, Tennessee, USA (held only by J-PARC MLF)

JSNS Annual Meeting 2012

10-11 Dec 2012, Kyoto University, Kyoto (Main sponsor: Japanese Society for Neutron Science)

Workshops co-sponsored by J-PARC Center, CROSS-Tokai and other organizations

The 17th Sagamore Conference, IUCr Commission on Charge, Spin, and Momentum Densities

15-20 Jul 2012, Daini Meisui Tei, Kitayuzawa, Hokkaido

Symposium on the Linkage Use of Synchrotron Radiation and Neutrons in Structural Biology – Realizing the construction of a high-resolution neutron spectrometer for biological polymers at J-PARC MLF

22 Jan 2013, Tokyo International Forum, Tokyo

Workshops in 2012

Workshops held by KEK

1st H-Line Workshop
18-19 May 2012, University of Tokyo, Komaba, Tokyo

3rd Progress Report Meeting of J-PARC·MUSE (Muon Science Establishment)
30 May 2012,　KEK Tokai, Tokai

Workshop on New Research Directions using Intense Quantum Beams – Analysis of Buried Interfaces in Thin Films and Multilayers
26-28 Jun 2012 ,　KEK Tsukuba, Tsukuba

Tsukuba Soft Matter Meeting 2012 in TOKAI
30-31 Aug 2012,　KEK Tokai, Tokai

BL16 Neutron Reflectometer Workshop 2012
3-4 Oct 2012, KEK Tokai, Tokai

High Resolution Chopper Spectrometer Workshop
6 Nov 2012, KEK Tokai, Tokai

POLANO Planning Workshop – A new polarized neutron scattering spectrometer for J-PARC
12 Nov 2012, KEK Tokai, Tokai

Neutron Spin-Echo Workshop
16 Nov 2012,　KEK Tsukuba, Tsukuba

Fundamental Physics with Neutrons
20-21 Nov 2012, Nagoya University, Nagoya

NOVA High-intensity Total Scattering Diffractometer Workshop
3-4 Dec 2012, KEK Tokai, Tokai

Super-HRPD & SPICA Workshop
14 Dec 2012, KEK Tokai, Tokai

5th Workshop on Muon Science and Accelerator Research
6-8 Jan 2013, KEK Tsukuba, Tsukuba

The 5th Japan-Taiwan Joint Meeting on Neutron and X-ray Scattering
25-26 Feb 2013, KEK Tokai, Tokai

IMSS Science Festa
14-15 Mar 2013, Tsukuba International Congress Center, Tsukuba

Workshops held by CROSS-Tokai

3rd CROSSroads Workshop
Structure and Function of Chiral Magnetic Materials
17 18 Dec 2012, Ibaraki Quantum Beam Center, Tokai

4th CROSSroads Workshop
Progress in Thin Film and Interface Science at J-PARC
10 Jan 2013, Kenkyusha, Tokyo

5th CROSSroads Workshop
Structure and Properties of Materials using the Single Crystal Diffractometers at J-PARC
25-26 Feb 2013, Ibaraki Quantum Beam Center, Tokai

6th CROSSroads Workshop
Leading Edge Research using Dynamics Spectrometers
14-15 Mar 2013, Tokyo Office of Kyoto University, Tokyo

Other Workshops co-sponsored by CROSS-Tokai

Industrial Applications of Neutrons Users Society Workshops

1st 2012 Workshop on Surfaces and Interfaces
3 Sept 2012, Kenkyusha, Tokyo

1st 2012 Workshop on Residual Stress and Strain
25 Sept 2012, Kenkyusha, Tokyo

1st 2012 Workshop on Metallographic Structure
27 Sept 2012, National Institute of Materials Science, Tsukuba

1st 2012 Workshop on Structural Biology
2 Oct 2012, Kenkyusha, Tokyo

1st 2012 Workshop on Non-destructive Visualization and Analysis Methods
9 Nov 2012, Kenkyusha, Tokyo

2nd 2012 Workshop on Metallographic Structure
3 Dec 2012, UDX Conference Center, Tokyo

6th Workshop on Soft Matter Neutron Scattering
21 Dec 2012, Kenkyusha, Tokyo

7th Workshop on Soft Matter Neutron Scattering
28 Feb 2013, Kenkyusha, Tokyo

2012 Workshop on Magnetic Materials
1 Mar 2013, Rengo Kaikan, Tokyo

2012 Workshop on Battery Materials
8 Mar 2013, Tokyo Office of Kyoto University, Tokyo

4th Workshop on Analytical Methods in Small Angle Scattering
13 Mar 2013, Tokyo Office of Kyoto University, Tokyo

Neutrons in Biology
13-14 Mar 2012, Tokyo Office of Kyoto University. Tokyo

2nd 2012 Workshop on Residual Stress and Strain
18 Mar 2013, Kenkyusha, Tokyo

2nd 2012 Workshop on Structural Biology
21 Mar 2013, Kenkyusha, Tokyo

Public Lectures

Applications of Synchrotron Radiation and Neutrons in Cultural Heritage
28 Sept 2012, Kenkyusha, Tokyo

Seminars and Courses in 2012

Seminars co-convened by CROSS-Tokai with other organizations

1st Seminar on Neutron Scattering at RIKEN
24 Apr 2012, RIKEN, Wako, Saitama

Industrial Applications of Neutron Scattering
27 Jul 2012, Mitsui Mining and Smelting Co., Saitama

Industrial Applications of Neutron Scattering in Osaka
8 Aug 2012, Osaka Science & Technology Center, Osaka

Industrial Applications of Neutron Scattering
9 Aug 2012, Sumitomo Chemical Co., Osaka

Industrial Applications of Neutron Scattering
19 Oct 2012, TOYOTA Central R&D Labs, Aichi

Industrial Applications of Neutron Scattering
28 Nov 2012, TORAY Research Center, Shiga

Industrial Application Seminar (at JSNS Annual Meeting 2012)
10 Dec 2012, Kyoto University, Kyoto

1st Synchrotron Radiation - Neutron Linkage Use Seminar
22 Mar 2013, LMJ Tokyo, Tokyo

Short Courses co-convened by J-PARC Center with other organizations

Z-Code Training Course
11-12 Mar 2013, LMJ Tokyo, Tokyo

Schools in 2012

The first MLF School was held in 2012.

MLF School 2012

18-21 Dec 2012, J-PARC MLF and IQBRC, Tokai


Lectures in class


24 Students


Hands-on experiments

Practical experiments at the MLF were newly included in the KEK Summer Challenge in 2012

KEK Summer Challenge

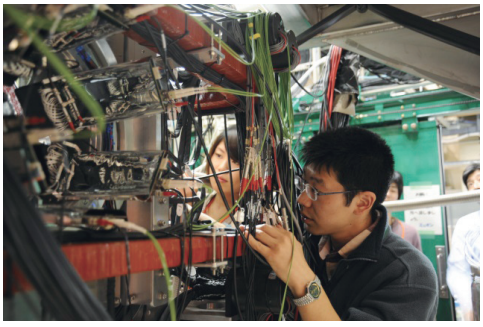

Lectures: 8 Aug 2012, KEK, Tsukuba
Experiments: 22-24 Nov 2012, J-PARC MLF, Tokai


9 Students

Award List

The JSNS Young Scientist Award

Novel Ordered Structures in the Mixture of Water / Organic Solvent / Salts Investigated by Neutron Scattering

The Japanese Society for Neutron Science
Koichiro Sadakane, December 2012

The JSNS Technology Award

Development of Automatic Sample Exchange and Transfer System in iMATERIA

The Japanese Society for Neutron Science
Akinori Hoshikawa, Toru Ishigaki and Masao Yonemura, December 2012

The JSNS President Choice

Neutron Spin Echo Spectrometer at the Pulsed Neutron Source

Hamon, Vol.21, No.4, pp.239—242, 2011
The Japanese Society for Neutron Science
Hideki Seto, Masahiro Hino, Norifumi L. Yamada, December 2012

平成 24 年度　科学技術分野の文部科学大臣表彰 科学技術賞 研究部門

(The Commendation for Science and Technology by the Minister of Education, Culture, Sports, Science and Technology: Prizes for Science and Technology: Research Category)

パルス中性子による高効率ナノダイナミクス計測技術の研究

新井正敏、中村充孝、梶本亮一
平成 24 年 4 月 17 日

日本油化学会　第 11 回オレオサイエンス賞

添加剤により誘起される巨大単層膜ベシクルの形成メカニズム

山田悟史、菱田真史
平成 24 年 10 月 3 日

第 33 回核物質管理学会日本支部年次大会優秀論文賞

NDA 用 ZnS シンチレーション中性子検出器開発計画

呉田昌俊、曽山和彦、瀬谷道夫、大図章、春山満夫、中村龍也、藤健太郎、坂佐井馨
平成 24 年 10 月

物構研サイエンスフェスタ学生奨励賞

$NaAlD_4$ における水素吸蔵放出反応の高強度中性子全散乱装置（NOVA）を用いた in-situ 測定

藤崎布美佳
平成 25 年 3 月 15 日

MLF Publication 2012

1 B. Adiperdana, I. A. Dharmawan, R. E. Siregar, I. Watanabe, K. Ohishi, Y. Ishii, T. Suzuki, T. Kawamata, Risdiana, R. Sheuermann, K. Sedlak, Y. Tomioka, T. Waki, Y. Tabata, and H. Nakamura
Muon Sites Estimation in La_2CuO_4 and A New Vanadium Cluster Compound, $V_4S_9Br_4$, using Electronic and Nuclear Dipole Field Calculations
Physics Procedia **30** 109 (2012)

2 M. Arai
Recovery from the Earthquake at MLF
MLF の震災からの復興（特集 震災からの復興）
Hamon / 波紋 **22** 216 (2012)

3 Y. Arimoto, H. Funahashi, N. Higashi, M. Hino, K. Hirota, S. Imajo, T. Ino, Y. Iwashita, R. Katayama, M. Kitaguchi, K. Mishima, S. Muto, H. Oide, H. Otono, Y. Seki, T. Shima, H. M. Shimizu, K. Taketani, T. Yamada, S. Yamashita, and T. Yoshioka
Present status of neutron fundamental physics at J-PARC
Progress of Theoretical and Experimental Physics **2012** 02B007 (2012)

4 Y. Arimoto, P. Gertenbort, S. Imajo, Y. Iwashita, M. Kitaguchi, Y. Seki, H. M. Shimizu, and T. Yoshioka
Demonstration of focusing by a neutron accelerator
Physical Review A **86** 023843 (2012)

5 Y. Arimoto, Y. Iwashita, T. Yoshioka, M. Kitaguchi, S. Imajo, H. M. Shimizu, K. Asahi, T. Ino, Y. Kamiya, K. Mishima, S. Muto, K. Sakai, T. Shima, K. Taketani, S. Yamashita, and A. Yoshimi
Development of Longitudinal-Gradient Magnet for Time Focusing of Ultra-Cold Neutron With Anisotropic Inter-Pole
IEEE Transactions on Applied Superconductivity **22** 4500704 (2012)

6 R. G. Burkovsky, A. V. Filimonov, A. I. Rudskoy, K. Hirota, M. Matsuura, and S. B. Vakhrushev
Diffuse scattering anisotropy and inhomogeneous lattice deformations in the lead magnoniobate relaxor PMN above the Burns temperature
Physical Review B **85** 094108 (2012)

7 K. H. Chow, M. Månsson, Y. Ikedo, J. Sugiyama, O. Ofer, E. J. Ansaldo, J. H. Brewer, M. Isobe, H. Gotou, T. Yagi, Y. Ueda, and C. Baines
μSR Investigation of the Hollandite Vanadate $K_2V_8O_{16}$
Physics Procedia **30** 117 (2012)

8 Neutron Source Section, Materials and Life Science Division
Technical design report of spallation neutron source facility in J-PARC
JAEA-Technology **2011-035** (2012)

9 T. Fujiwara, H. Takahashi, T. Yanagida, K. Kamada, K. Fukuda, Y. Fujimoto, N. Kawaguchi, N. L. Yamada, M. Furusaka, K. Watanabe, and M. Uesaka
Study on Ce: LiCAF scintillator for ^{3}He alternative detector
Neutron News **23** 31 (2012)

10 M. Futakawa
Seismic Damages at MLF Neutron Source
MLF 中性子源における震災（特集 震災からの復興）
Hamon / 波紋 **22** 228 (2012)

11 M. Futakawa
Present status of JSNS and R&D for high power operation in J-PARC
Proceedings of ICANS-XX 111 (2012)

12 M. Futakawa, T. Naoe, H. Kogawa, K. Haga, and K. Okita
Cavitation erosion induced by proton beam bombarding mercury target for high power spallation neutron source
Proceedings of the 8th International Symposium on Cavitation (CAV2012) 822 (2012)

13 K. Haga, H. Kogawa, T. Wakui, T. Naoe, and M. Futakawa
Development of the high power mercury target and the bubbler installation
Proceedings of ICANS-XX 307 (2012)

14 J. Han, J. Zhu, Y. Li, X. Yu, S. Wang, G. Wu, H. Xie, S. C. Vogel, F. Izumi, K. Momma, Y. Kawamura, Y. Huang, J. B. Goodenough, and Y. Zhao
Experimental visualization of lithium conduction pathways in garnet-type $Li_7La_3Zr_2O_{12}$
Chemical communications **48** (79) 9840 (2012)

15 M. Hase, A. Dönni, K. Ozawa, H. Kitazawa, O. Sakai, V. Y. Pomjakushin, L. Keller, K. Kaneko, N. Metoki, K. Kakurai, M. Matsuda, T. Yang, R. Cong, and J. Lin
Neutron scattering studies of the spin-5/2 antiferromagnetic linear trimer substance $SrMn_3P_4O_{14}$
Journal of Physics: Conference Series **340** 012066 (2012)

16 K. Hemmi, R. Fukuta, E. Uykur, S. Miyasaka, S. Tajima, A. Nakao, H. Nakao, R. Kumai, and Y. Murakami
Cr- and Mo-Doping Effects on Structural and Orbital Order Phase Transition in Spinel-Type MnV_2O_4
Journal of the Physical Society of Japan **81** SB030 (2012)

17 W. Higemoto, T. U. Ito, K. Ninomiya, R. H. Heffner, K. Shimomura, K. Nishiyama, and Y. Miyake
Muon Beam Slicer at J-PARC MUSE
Physics Procedia **30** 30 (2012)

18 W. Higemoto, T. U. Ito, K. Ninomiya, T. Onimaru, K. T. Matsumoto, and T. Takabatake
Multipole and superconducting state in $PrIr_2Zn_{20}$ probed by muon spin relaxation
Physical Review B **85** 235152 (2012)

19 W. Higemoto, T. U. Ito, K. Ninomiya, T. Onimaru, K. T. Matsumoto, and T. Takabatake
μSR Studies on Caged Compound $PrIr_2Zn_{20}$
Physics Procedia **30** 125 (2012)

20 K. Hikawa, Y. Shirai, T. Takegami, M. Shiotsu, H. Tatsumoto, K. Hata, H. Kobayashi, Y. Naruo, Y. Inatani, and N. Narita
Over-Current Characteristics of MgB_2 Wire Cooled by Liquid Hydrogen
Proceeding of ICEC24-ICMC2012 203 (2012)

21 Y. Hirata, K. M. Kojima, M. Ishikado, S. Uchida, A. Iyo, H. Eisaki, and S. Tajima
Correlation between the interlayer Josephson coupling strength and an enhanced superconducting transition temperature of multilayer cuprate superconductors
Physical Review B **85** 054501 (2012)

22 T. Hirayama, K. Matsubayashi, T. Yamashita, S. Ohara, K.

Munakata, and Y. Uwatoko
Pressure-induced Suppression of the Antiferromagnetic Transition in $YbNi_3Al_9$ Single Crystal
Journal of Physics: Conference Series **391** 012020 (2012)

23 N. Hoshino, F. Iijima, N. N. Graham, N. Yoshida, T. Shiga, H. Nojiri, A. Nakao, R. Kumai, Y. Murakami, and H. Oshio
Three-way switching in a cyanide-bridged [CoFe] chain
Nature Chemistry **4** 921 (2012)

24 Y. Idemoto, T. Kashima, and N. Kitamura
Investigation on Crystal and Electronic Structures of $0.5Li_2MnO_3$-$0.5LiMn_xNi_xCo_{(1-2x)}O_2$ (x = 1/3, 5/12) Samples Heat-Treated under Vacuum Reducing Conditions
Electrochemistry **80** 791 (2012)

25 Y. Idemoto, M. Tashiro, and N. Kitamura
Dependencies of Piezoelectric and Ferroelectric Properties and Crystal Structure on Synthesis and Sintering Processes in $BaTiO_3$ Prepared by Hydrothermal and Solid-state Methods
Journal of the Japan Society of Powder and Powder Metallurgy **59** 101 (2012)

26 K. Iida, J. Lee, M. B. Stone, M. Kofu, Y. Yoshida, and S.-H. Lee
Two-dimensional incommensurate magnetic fluctuations in $Sr_2(Ru_{0.99}Ti_{0.01})O_4$
Journal of the Physical Society of Japan **81** 124710 (2012)

27 K. Iida, S.-H. Lee, and S.-W. Cheong
Coexisting Order and Disorder Hidden in a Quasi-Two-Dimensional Frustrated Magnet
Physical Review Letters **108** 217207 (2012)

28 K. Iida, S.-H. Lee, T. Onimaru, K. Matsubayashi, and T. J. Sato
Determination of spin Hamiltonian in the Ni_4 magnetic molecule
Physical Review B **86** 064422 (2012)

29 T. Iiyama, F. Fujisaki, R. Futamura, A. Hamasaki, S. Ozeki, A. Hoshikawa, and T. Ishigaki
Structure Determination of Hydrogen-bonding Network of Water in Hydrophobic Nanospace by Neutron and X-ray Diffractions
Chemistry Letters **41** 1267 (2012)

30 K. Ikeda, T. Oku, J. Suzuki, M. Takeda, A. Hoshikawa, and Y. Miyake
The Materials and Life Science Experimental Facility of J-PARC
J-PARC の物質・生命科学実験施設
Engineering Materials / 工業材料 **60** 28 (2012)

31 K. Ikeda, T. Otomo, K. Suzuya, M. Misawa, H. Ohshita, M. Tsubota, N. Kaneko, T. Seya, T. Fukunaga, K. Itoh, Y. Kameda, T. Yamaguchi, K. Yoshida, K. Maruyama, S. Shamoto, K. Kodama, Y. Kawakita, and F. Fujisaki
Structural Analysis of Hydrogen Storage Materials by High Intensity Neutron Total Diffractometer NOVA
高強度中性子全散乱装置 NOVA による水素貯蔵材料の構造解析
Journal of the Hydrogen Energy Systems Society of Japan / 水素エネルギーシステム **37** 328 (2012)

32 Y. Ikedo, Y. Miyake, K. Shimomura, P. Strasser, K. Nishiyama, N. Kawamura, H. Fujimori, S. Makimura, A. Koda, T. Ogitsu, Y. Makida, T. Adachi, K. Nakahara, M. Yoshida, A. Yamamoto, T. Nakamoto, K. Sasaki, K. Tanaka, N. Kimura, W. Higemoto, Y. Ajima, K. Ishida, Y. Matsuda, and A. Sato
Status of the Superomega Muon Beam Line at J-PARC
Physics Procedia **30** 34 (2012)

33 T. Ino, Y. Arimoto, H. M. Shimizu, Y. Sakaguchi, K. Sakai, H. Kira, T. Shinohara, T. Oku, J. Suzuki, K. Kakurai, and L. Chang
A compact SEOP ^{3}He neutron spin filter with AFP NMR
Journal of Physics: Conference Series **340** 012006 (2012)

34 K. Ishii, K. Tsutsui, K. Ikeuchi, I. Jarrige, J. Mizuki, H. Hiraka, K. Yamada, T. Tohyama, S. Maekawa, Y. Endoh, H. Ishii, and Y. Q. Cai
Electronic excitations around the substituted atom in $La_2Cu_{1-y}Ni_yO_4$ as seen via resonant inelastic x-ray scattering
Physical Review B **85** 104509 (2012)

35 T. Isono, H. Kamo, A. Ueda, K. Takahashi, A. Nakao, R. Kumai, H. Nakao, K. Kobayashi, Y. Murakami, and H. Mori
Hydrogen bond-promoted metallic state in a purely organic single-component conductor under pressure
Nature Communications **4** 1344 (2012)

36 T. U. Ito, W. Higemoto, K. Ninomiya, A. Sakai, and S. Nakatsuji
Microscopic Evidence for Long-Range Magnetic Ordering in the Γ_8 Ground Quartet Systems $SmTr_2Al_{20}$ (Tr: Ti, V, Cr)
Journal of the Physical Society of Japan Supplement **81** SB050 (2012)

37 S. Itoh and M. A. Adams
Anomalous Spin Diffusion on Two-Dimensional Percolating Network in Dilute Antiferromagnet $Rb_2Mn_{0.6}Mg_{0.4}F_4$
Journal of the Physical Society of Japan **81** 074704 (2012)

38 S. Itoh, T. Nakayama, and M. A. Adams
Two-Dimensional Antiferromagnetic Fractons in $Rb_2Mn_{0.598}Mg_{0.402}F_4$
Journal of Physics: Conference Series **400** 032030 (2012)

39 S. Itoh, K. Ueno, R. Ohkubo, H. Sagehashi, Y. Funahashi, and T. Yokoo
T0 chopper developed at KEK
Nuclear Instruments and Methods in Physics Research A **661** 86 (2012)

40 S. Itoh, K. Ueno, and T. Yokoo
Fermi chopper developed at KEK
Nuclear Instruments and Methods in Physics Research A **661** 58 (2012)

41 S. Itoh, T. Yokoo, K. Ueno, J. Suzuki, T. Teraoku, and M. Tsuchiya
Large area window on vacuum chamber surface for neutron scattering instruments
Nuclear Instruments and Methods in Physics Research A **670** 1 (2012)

42 S. Itoh, T. Yokoo, S. Yano, D. Kawana, H. Tanaka, and Y. Endoh
Quantum Renormalization Effect in One-Dimensional Heisenberg Antiferromagnets
Journal of the Physical Society of Japan **81** 084706 (2012)

43 K. Iwasa, T. Orihara, K. Saito, K. Tomiyasu, Y. Murakami, H. Sugawara, K. Kuwahara, H. Kimura, R. Kiyanagi, Y. Ishikawa, Y. Noda, Y. Aoki, H. Sato, and M. Kohgi
Neutron scattering study on magnetic ordering in a partially rare-earth filled skutterudite $Pr_xFe_4Sb_{12}$
Journal of Physics: Conference Series **391** 012025 (2012)

44 H. Iwase, M. Katagiri, and M. Shibayama
Optimization of the thickness of a ZnS/^{6}LiF scintillator for a high-resolution detector installed on a focusing small-angle neutron scattering spectrometer (SANS-U)
Journal of Applied Crystallography **45** 507 (2012)

45 K. Iwase, H. Sato, S. Harjo, T. Kamiyama, T. Ito, S. Takata, K. Aizawa, and Y. Kiyanagi
In situ lattice strain mapping during tensile loading using the neutron transmission and diffraction methods
Journal of Applied Crystallography **45** 113 (2012)

46 H. Iwase, S. Sawada, T. Yamaki, S. Koizumi, M. Ohnuma, and Y.

Maekawa
Hierarchical Structure Analysis of Graft-Type Polymer Electrolyte Membranes Consisting of Cross-Linked Polytetrafluoroethylene by Small-Angle Scattering in a Wide - Q Range
Macromolecules **45** 9121 (2012)

47 A. Izumi, T. Nakao, H. Iwase, and M. Shibayama
Structural analysis of cured phenolic resins using complementary small-angle neutron and X-ray scattering and scanning electron microscopy
Soft Matter **8** 8438 (2012)

48 I. Jarrige, T. Nomura, K. Ishii, H. Gretarsson, Y.-J. Kim, J. Kim, M. Upton, D. Casa, T. Gog, M. Ishikado, T. Fukuda, M. Yoshida, J. P. Hill, X. Liu, N. Hiraoka, K. D. Tsuei, and S. Shamoto
Resonant inelastic x-ray scattering study of charge excitations in superconducting and nonsuperconducting $PrFeAsO_{1-y}$
Physical Review B **86** 115104 (2012)

49 J. Jeong, E. A. Goremychkin, T. Guidi, K. Nakajima, G. S. Jeon, S.-A. Kim, S. Furukawa, Y. B. Kim, S. Lee, V. Kiryukhin, S.-W. Cheong, and J.-G. Park
Spin Wave Measurements over the Full Brillouin Zone of Multiferroic $BiFeO_3$
Physical Review Letters **108** 077202 (2012)

50 X. Jin, T. Nakamoto, S. Harjo, T. Ito, T. Ogitsu, K. Tsuchiya, A. Yamamoto, A. Kikuchi, T. Takeuchi, and T. Hemmi
Observation of A15 phase transformation in RHQ-Nb_3Al wire by neutron diffraction at high-temperature
Journal of Alloys and Compounds **535** 124 (2012)

51 X. Jin, T. Nakamoto, T. Ito, S. Harjo, A. Kikuchi, T. Takeuchi, K. Tsuchiya, T. Hemmi, T. Ogitsu, and A. Yamamoto
Residual strain dependence on the matrix structure in RHQ-Nb_3Al wires by neutron diffraction measurement
Superconductor Science and Technology **25** 065021 (2012)

52 X. Jin, H. Oguro, T. Nakamoto, S. Awaji, A. Yamamoto, K. Tsuchiya, T. Ogitsu, A. Kikuchi, T. Takeuchi, S. Harjo, and T. Ito
Tensile strain dependence of critical current of RHQ-Nb_3Al wires
Cryogenics **52** 805 (2012)

53 R. Kadono, A. Koda, W. Higemoto, K. Ohishi, H. Ueda, C. Urano, S. Kondo, M. Nohara, and H. Takagi
Quasi-One-Dimensional Spin Dynamics in LiV_2O_4: One-to-Three-Dimensional Crossover as a Possible Origin of Heavy Fermion State
Journal of the Physical Society of Japan **81** 014709 (2012)

54 R. Kadono and Y. Miyake
MUSE, the goddess of muons, and her future
Reports on Progress in Physics **75** 026302 (2012)

55 R. Kajimoto, K. Nakajima, S. Ohira-Kawamura, Y. Inamura, K. Kakurai, M. Arai, T. Hokazono, S. Oozono, and T. Okuda
Neutron scattering study of Ag, Mg and Al substitution effects on the magnetic excitations in $CuCrO_2$
Journal of Physics: Conference Series **400** 032034 (2012)

56 R. Kajimoto, M. Nakamura, Y. Inamura, T. Nakatani, W. Kambara, T. Yokoo, and F. Mizuno
Development of a High-efficient Inelastic Neutron Scattering Method with Multiple Incident Energies on a Chopper Spectrometer
チョッパー分光器における複数入射エネルギー同時測定法による高効率非弾性中性子散乱測定法の開発
Hamon / 波紋 **22** 145 (2012)

57 S. Kambe, H. Sakai, Y. Tokunaga, and K. Kaneko
Correlation between the superconducting pairing symmetry and magnetic anisotropy in f -electron unconventional superconductors
Journal of Physics: Conference Series **344** 012003 (2012)

58 Y. Kameda
Neutron diffractometer in J-PARC
J-PARC の中性子散乱測定装置
The Japan Association of Solution Chemistry News Letter / 溶液化学研究会ニュース **65** 1 (2012)

59 K. Kaneko, O. Stockert, M. Skoulatos, A. Schneidewind, T. Takeuchi, T. D. Matsuda, Y. Haga, R. Settai, Y. Ōnuki, and N. Metoki
Neutron Scattering Study on High-Quality Single Crystals of Non-Centrosymmetric Heavy-Fermion Superconductor $CePt_3Si$
Journal of the Physical Society of Japan **81** SB006 (2012)

60 K. Kaneko, S. Yoshiuchi, T. Takeuchi, F. Honda, R. Settai, and Y. Ōnuki
Effect of magnetic field in heavy-fermion compound $YbCo_2Zn_{20}$
Journal of Physics: Conference Series **391** 012026 (2012)

61 Y. Kasugai, N. Matsuda, Y. Sakamoto, H. Nakashima, H. Yashima, H. Iwase, H. Hirayama, N. Mokov, A. Leveling, D. Boehnlein, K. Vaziri, G. Lauten, K. Oishi, and T. Nakamura
Fitting Method for Spectrum Deduction in High-Energy Neutron Field Induced by GeV-Protons Using Experimental Reaction-Rate Data
Journal of ASTM International **9** 675 (2012)

62 M. Kawai, H. Kurishita, H. Kokawa, S. Watanabe, N. Sakaguchi, K. Kikuchi, S. Saito, T. Yoshiie, H. Iwase, T. Ito, S. Hashimoto, Y. Kaneko, M. Futakawa, S. Ishino, and J. G. Team
Development of advanced materials for spallation neutron sources and radiation damage simulation based on multi-scale models
Journal of Nuclear Materials **431** 16 (2012)

63 T. Kawamoto, T. Mori, A. Nakao, Y. Murakami, and J. A. Schlueter
T_c of 11 K Identified for the Third Polymorph of the (BEDT-TTF)$_2$Ag(CF$_3$)$_4$(TCE) Organic Superconductor
Journal of the Physical Society of Japan **81** 023705 (2012)

64 T. Kawasaki, M. Takahashi, T. Ohhara, I. Tanaka, K. Kusaka, T. Hosoya, T. Yamada, and K. Kurihara
Structure of Morpholinium Tribromoplumbate $C_4H_8ONH_2PbBr_3$ Studied Using Single-Crystal Neutron Diffraction
Journal of the Physical Society of Japan **81** 094602 (2012)

65 Y. Kawasaki, T. Minami, M. Izumi, Y. Kishimoto, T. Ohno, K. H. Satoh, A. Koda, R. Kadono, J. L. Gavilano, H. Luetkens, T. Nakajima, and Y. Ueda
μSR investigation of magnetically ordered states in the A-site ordered perovskite manganites $RBaMn_2O_6$ (R=Y and La)
Physical Review B **86** 125141 (2012)

66 A. Kimura, T. Fujii, S. Fukutani, K. Furutaka, S. Goko, K. Y. Hara, H. Harada, K. Hirose, J. Hori, M. Igashira, T. Kamiyama, T. Katabuchi, T. Kin, K. Kino, F. Kitatani, Y. Kiyanagi, M. Koizumi, M. Mizumoto, S. Nakamura, M. Ohta, M. Oshima, K. Takamiya, and Y. Toh
Neutron-capture cross-sections of Cm-244 and Cm-246 measured with an array of large germanium detectors in the ANNRI at J-PARC/MLF
Journal of Nuclear Science and Technology **49** 708 (2012)

67 H. Kinoshita, K. Haga, M. Seki, T. Suzuki, M. Ito, Y. Kasugai, T. Wakui, H. Kogawa, T. Naoe, K. Hanano, M. Teshigawara, F. Maekawa, S. Sakamoto, and M. Futakawa
Development of cut out machine for PIE test pieces from mercury target vessel in J-PARC
Proceedings of ICANS-XX 334 (2012)

68 N. Kitamura, K. Uchino, and Y. Idemoto
Particle morphology, electrical conductivity, crystal and electronic structures of hydrothermally synthesized (Ce,Sr)PO_4
Journal of Materials Science **47** 6220 (2012)

69 R. Kiyanagi, T. Yamazaki, Y. Sakamoto, H. Kimura, Y. Noda, K. Ohyama, S. Torii, M. Yonemura, J. Zhang, and T. Kamiyama
Structural and Magnetic Phase Determination of (1-x) $BiFeO_3$--$xBaTiO_3$ Solid Solution
Journal of the Physical Society of Japan **81** 024603 (2012)

70 Y. Kiyanagi, H. Sato, T. Kamiyama, and T. Shinohara
A new imaging method using pulsed neutron sources for visualizing structural and dynamical information
Journal of Physics: Conference Series **340** 012010 (2012)

71 Y. Kobayashi, T. Iida, K. Suzuki, E. Satomi, T. Kawamata, M. Itoh, and M. Sato
NMR Studies on Iron Pnictide Superconductors of $LaFeAsO_{0.89}F_{0.11}$ and Ca-Fe-Pt-As
Journal of Physics: Conference Series **400** 022056 (2012)

72 T. Kusano, H. Iwase, T. Yoshimura, and M. Shibayama
Structural and Rheological Studies on Growth of Salt-Free Wormlike Micelles Formed by Star-Type Trimeric Surfactants
Langmuir **28** 16798 (2012)

73 S. C. Lee, A. Ueda, H. Kamo, K. Takahashi, M. Uruichi, K. Yamamoto, K. Yakushi, A. Nakao, R. Kumai, K. Kobayashi, H. Nakao, Y. Murakami, and H. Mori
Charge-order driven proton arrangement in a hydrogen-bonded charge-transfer complex based on a pyridyl-substituted TTF derivative
Chemical Communications **48** 8673 (2012)

74 A. Machida, M. Honda, T. Hattori, A. Sano-Furukawa, T. Watanuki, Y. Katayama, K. Aoki, K. Komatsu, H. Arima, H. Ohshita, K. Ikeda, K. Suzuya, T. Otomo, M. Tsubota, K. Doi, T. Ichikawa, Y. Kojima, and D.Y. Kim
Formation of NaCl-type monodeuteride LaD by the disproportionation reaction of LaD_2
Physical Review Letters **108** 205501 (2012)

75 S. Makimura, Y. Kobayashi, Y. Miyake, N. Kawamura, P. Strasser, A. Koda, K. Shimomura, H. Fujimori, K. Nishiyama, M. Kato, K. Kojima, W. Higemoto, T. Ito, R. Shimizu, and R. Kadono
Development of a Muon Rotating Target for J-PARC/MUSE
Physics Procedia **32** 795 (2012)

76 K. Matsubayashi, R. Yamanaka, H. S. Suzuki, K. Munakata, and Y. Uwatoko
Low temperature properties of a low carrier heavy fermion YbPtSb
Journal of Physics: Conference Series **391** 012040 (2012)

77 H. Matsumura, S. Sekimoto, H. Yashima, A. Toyoda, Y. Kasugai, N. Matsuda, K. Oishi, K. Bessho, Y. Sakamoto, H. Nakashima, D. Boehnlein, G. Lauten, A. Leveling, N. Mokhov, and K. Vaziri
Colloid Formation Rates of Radionuclides Produced from Cu Foils in Waterbombarded with 120-GeV Protons
Progress in Nuclear Science and Technology **3** 127 (2012)

78 Y. Matsuo, J. Hatori, K. Kamazawa, J. Sugiyama, Y. Yoshida, and S. Ikehata
Scaling of superionic transition temperature in $M_3D(XO_4)_2$
Solid State Ionics **225** 40 (2012)

79 M. Matsuura, M. Fujita, H. Hiraka, M. Kofu, H. Kimura, S. Wakimoto, T. G. Perring, C. D. Frost, and K. Yamada
Ni-substitution effects on the spin dynamics and superconductivity in $La_{1.85}Sr_{0.15}CuO_4$
Physical Review B **86** 134529 (2012)

80 S. Meigo, H. Fujimori, S. Sakamoto, and M. Futakawa
Development of Beam Flattening System Using Non-Linear Beam Optics at J-PARC
Proceedings of ICANS-XX 207 (2012)

81 S. Meigo, M. Ooi, A. Akutsu, K. Ikezaki, T. Kai, H. Fujimori, S. Sakamoto, and M. Futakawa
Beam Commissioning at J-PARC/JSNS and MUSE
Proceedings of ICANS-XX 314 (2012)

82 S. Meigo, M. Ooi, K. Ikezaki, A. Akutsu, S. Sakamoto, and M. Futakawa
Development of profile monitor system for high intense spallation neutron source
Proceedings of IBIC2012,Tsukuba, Japan 227 (2012)

83 S. Meigo, H. Fujimori, S. Sakamoto, and M. Futakawa
Development of Beam Flattening System Using Non-Linear Beam Optics at J-PARC/JSNS
Proc of 9th Meeting of Particle Accelerator Society of Japan 75 (2012)

84 T. Mito, T. Koyama, K. Nakagawara, T. Ishida, K. Ueda, T. Kohara, K. Matsubayashi, Y. Saiga, K. Munakata, Y. Uwatoko, M. Mizumaki, N. Kawamura, B. Idzikowski, and M. Reiffers
Mechanism of Field Induced Fermi Liquid State in Yb-Based Heavy-Fermion Compound: X-ray Absorption Spectroscopy and Nuclear Magnetic Resonance Studies of $YbCo_2Zn_{20}$
Journal of the Physical Society of Japan **81** 033706 (2012)

85 Y. Miyake, K. Shimomura, N. Kawamura, P. Strasser, A. Koda, S. Makimura, H. Fujimori, Y. Ikedo, K. Nakahara, S. Takeshita, M. Kato, K. Kojima, Y. Kobayashi, K. Nishiyama, R. Kadono, W. Higemoto, T. U. Ito, K. Ninomiya, K. Kubo, and K. Nagamine
J-PARC Muon Facility, MUSE
Physics Procedia **30** 46 (2012)

86 M. Mizuguchi, Y. Yokoyama, Y. Nabeshima, K. Kawano, I. Tanaka, and N. Niimura
Quaternary structure, aggregation and cytotoxicity of transthyretin
Amyloid **19** 5 (2012)

87 S. Morooka, H. Kawata, S. Harjo, and O. Umezawa
In-Situ Neutron Diffraction Study on Tensile Deformaiton Behavior of Steels
New Methods of Damage and Failure Analysis of Structural Parts, ed. by Zdeněk Bůžek, Bohumír Strnadel 369 (2012)

88 S. Morooka, O. Umezawa, S. Harjo, K. Hasegawa, and Y. Toji
Quantitative Analysis of Tensile Deformation Behavior by In-Situ Neutron Diffraction for Ferrite-Martensite Type Dual-Phase Steels
その場中性子回折法によるフェライト - マルテンサイト型複合組織鋼における引張変形挙動の定量的解析
Tetsu-to-Hagane / 鉄と鋼 **98** 311 (2012)

89 N. Murai, T. Masui, M. Ishikado, S. Ishida, H. Eisaki, S. Uchida, and S. Tajima
Effect of out-of-plane disorder on superconducting gap anisotropy in $Bi_{2+x}Sr_{2-x}CaCu_2O_{8+\delta}$ as seen via Raman spectroscopy
Physical Review B **85** 020507 (2012)

90 K. Murakami, Y. Shirai, T. Takegami, K. Hikawa, M. Shiotsu, H. Tatsumoto, K. Hata, H. Kobayashi, Y. Naruo, Y. Inatani, and N. Narita
Preliminary Test of Hot-Wire Type Flow-Meter for Liquid Hydrogen
Proceeding of ICEC24-ICMC2012 51 (2012)

91 M. Nagano, F. Yamaga, D. Yamazaki, R. Maruyama, H. Hayashida, K. Soyama, and K. Yamamura

High-precision figured thin supermirror substrates for multiple neutron focusing device
Journal of Physics: Conference Series **340** 012016 (2012)

92 M. Nagano, F. Yamaga, D. Yamazaki, R. Maruyama, H. Hayashida, K. Soyama, and K. Yamamura
One-dimensional neutron focusing with large beam divergence by 400mm-long elliptical supermirror
Journal of Physics: Conference Series **340** 012034 (2012)

93 S. Nakajima, T. Suzuki, Y. Ishii, K. Ohishi, I. Watanabe, T. Goto, A. Oosawa, N. Yoneyama, N. Kobayashi, F. L. Pratt, and T. Sasaki
Microscopic Phase Separation in Triangular-Lattice Quantum Spin Magnet κ-(BEDT-TTF)$_2$Cu$_2$(CN)$_3$ Probed by Muon Spin Relaxation
Journal of the Physical Society of Japan **81** 063706 (2012)

94 T. Nakamura
Scintillation Neutron Detectors with a High Spatial Resolution -Position-Sensitive Detectors for Single-Crystal Diffractometer in J-PARC-
中性子を光に変えて高位置分解能で検出する
—J-PARC の結晶構造解析装置用 2 次元シンチレータ中性子検出器を開発—
JAEA R&D Review 2012 / 未来を拓く原子力 原子力機構の研究開発成果 2012 114 (2012)

95 T. Nakamura, M. Katagiri, T. Hosoya, K. Toh, M. Kitaguchi, M. Hino, T. Ebisawa, K. Sakasai, and K. Soyama
Development of Two-Dimensional Scintillation Detectors for Neutron Spin Echo Spectrometers in J-PARC/MLF
2012 IEEE Nuclear Science Symposium and Medical Imaging Conference Record 222 (2012)

96 T. Nakamura, T. Kawasaki, T. Hosoya, K. Toh, M. Ebine, A. Birumachi, K. Sakasai, K. Soyama, and M. Katagiri
A wavelength-shifting-fibre-based scintillator neutron detector implemented with the median point calculation method
Journal of Instrumentation **7** C02003 (2012)

97 T. Nakamura, T. Kawasaki, T. Hosoya, K. Toh, K. Oikawa, K. Sakasai, M. Ebine, A. Birumachi, K. Soyama, and M. Katagiri
A large-area two-dimensional scintillator detector with a wavelength-shifting fibre readout for a time-of-flight single-crystal neutron diffractometer
Nuclear Instruments and Methods in Physics Research A **686** 64 (2012)

98 T. Nakano, M. Matsuura, A. Hanazawa, K. Hirota, and Y. Nozue
Direct Observation by Neutron Diffraction of Antiferromagnetic Ordering in s Electrons Confined in Regular Nanospace of Sodalite
Physical Review Letters **109** 167208 (2012)

99 A. Nakao, Y. Yamaki, H. Nakao, Y. Murakami, K. Hasegawa, M. Isobe, and Y. Ueda
Observation of Structural Change in the Novel Ferromagnetic Metal--Insulator Transition of $K_2Cr_8O_{16}$
Journal of the Physical Society of Japan **81** 054710 (2012)

100 Y. Nambu, K. Ohgushi, S. Suzuki, F. Du, M. Avdeev, Y. Uwatoko, K. Munakata, H. Fukazawa, S. Chi, Y. Ueda, and T. J. Sato
Block magnetism coupled with local distortion in the iron-based spin-ladder compound $BaFe_2Se_3$
Physical Review B **85** 064413 (2012)

101 T. Naoe, Y. Yamaguchi, and M. Futakawa
Quantification of fatigue crack propagation of an austenitic stainless steel in mercury embrittlement
Journal of Nuclear Materials **431** 133 (2012)

102 K. Ninomiya, T. Nagatomo, K. Kubo, T. U. Ito, W. Higemoto, M. Kita, A. Shinohara, P. Strasser, N. Kawamura, K. Shimomura, Y. Miyake, and T. Saito
Development of Nondestructive and Quantitative Elemental Analysis Method Using Calibration Curve between Muonic X-ray Intensity and Elemental Composition in Bronze
Bulletin of the Chemical Society of Japan **85** 228 (2012)

103 K. Nyuta, T. Yoshimura, K. Tsuchiya, H. Sakai, M. Abe, and H. Iwase
Zwitterionic heterogemini surfactants containing ammonium and carboxylate headgroups 2: Aggregation behavior studied by SANS, DLS, and cryo-TEM
Journal of Colloid and Interface Science **370** 80 (2012)

104 Y. Oba, S. Koppoju, M. Ohnuma, Y. Kinjo, S. Morooka, Y. Tomota, J. Suzuki, D. Yamaguchi, S. Koizumi, M. Sato, and T. Shiraga
Quantitative Analysis of Inclusions in Low Carbon Free Cutting Steel Using Small-angle X-ray and Neutron Scattering
ISIJ International **52** 457 (2012)

105 K. Ohishi, Y. Ishii, I. Watanabe, H. Fukazawa, T. Saito, Y. Kohori, K. Kihou, C.-H. Lee, H. Kito, A. Iyo, and H. Eisaki
Flux-line lattice state in FeAs-based superconducrot KFe_2As_2
Journal of Physics: Conference Series **400** 022087 (2012)

106 K. Ohishi, Y. Ishii, I. Watanabe, H. Fukazawa, T. Saito, Y. Kohori, K. Kihou, C.-H. Lee, H. Kito, A. Iyo, and H. Eisaki
Magnetic penetration depth in the FeAs-based superconductor KFe_2As_2
Journal of the Physical Society of Japan : Supplements **81** SB046 (2012)

107 K. Ohoyama, K. Tsutsumi, T. Ino, H. Hiraka, Y. Yamaguchi, H. Kira, T. Oku, Y. Sakaguchi, Y. Arimoto, W. Zhang, H. Kimura, K. Iwasa, M. Takeda, J. Suzuki, K. Yamada, and K. Kakurai
Development of a non-adiabatic two-coil spin flipper for a polarised thermal neutron diffractometer with a ^{3}He spin filter
Nuclear Instruments and Methods in Physics Research A **680** 75 (2012)

108 Y. Ohshima, Y. Noguchi, T. Oguchi, Y. Kitanaka, M. Miyayama, S. Torii, and T. Kamiyama
High-Temperature-Operating Dielectrics of Perovskite Oxides
ECS Transactions **45** 195 (2012)

109 H. Ohshita, T. Otomo, S. Uno, K. Ikeda, T. Uchida, N. Kaneko, T. Koike, M. Shoji, K. Suzuya, T. Seya,, and M. Tsubota
Stability of neutron beam monitor for High Intensity Total Diffractometer at J-PARC
Nuclear Instruments and Methods in Physics Research A **672** 75 (2012)

110 R. Oishi-Tomiyasu, M. Yonemura, T. Morishima, A. Hoshikawa, S. Torii, T. Ishigaki, and T. Kamiyama
Application of matrix decomposition algorithms for singular matrices to the Pawley method in Z-Rietveld
Journal of Applied Crystallography **45** 299 (2012)

111 T. Okuchi, S. Sasaki, Y. Ohno, J. Abe, H. Arima, T. Osakabe, T. Hattori, A. Sano-Furukawa, K. Komatsu, H. Kagi, W. Utsumi, S. Harjo, T. Ito, and K. Aizawa
Neutron powder diffraction of small-volume samples at high pressure using compact opposed-anvil cells and focused beam
Journal of Physics: Conference Series **377** 012013 (2012)

112 T. Okuda, S. Oozono, T. Hokazono, K. Uto, Y. Fujii, Y. Beppu, S. Seki, Y. Onose, Y. Tokura, R. Kajimoto, and M. Matsuda
Substitution Effect on the Magnetic State of Delafossite $CuCrO_2$ Having a Spin-3/2 Antiferromagnetic Triangular Sublattice
Journal of Physics: Conference Series **400** 032072 (2012)

113 N. Onishi, K. Oka, M. Azuma, Y. Shimakawa, Y. Motome, T. Taniguchi, M. Hiraishi, M. Miyazaki, T. Masuda, A. Koda, K. M. Kojima, and R. Kadono
Magnetic ground state of the frustrated honeycomb lattice antiferromagnet $Bi_3Mn_4O_{12}(NO_3)$
Physical Review B **85** 184412 (2012)

114 Y. Onodera, K. Mori, T. Otomo, A. C. Hannon, M. Sugiyama, and T. Fukunaga
Reverse Monte Carlo modeling of Li_2S-P_2S_5 superionic conductors
Journal of Physics: Conference Series **340** 012058 (2012)

115 Y. Onodera, K. Mori, T. Otomo, M. Sugiyama, and T. Fukunaga
Structural Evidence for High Ionic Conductivity of $Li_7P_3S_{11}$ Metastable Crystal
Journal of the Physical Society of Japan **81** 044802 (2012)

116 M. Ooi, M. Teshigawara, M. Segawa, E. Hashimoto, F. Maekawa, M. Harada, and M. Kureta
Elemental distribution measurement of the Au-In-Cd alloy by neutron resonance imaging
Proceedings of ICANS-XX 439 (2012)

117 M. Ooi, M. Teshigawara, T. Wakui, T. Nishi, M. Harada, F. Maekawa, and M. Futakawa
Development status of low activation ternary Au–In–Cd alloy decoupler for a MW class spallation neutron source: 1st Production of Au–In–Cd alloy
Journal of Nuclear Materials **431** 218 (2012)

118 S. Raymond, K. Kaneko, A. Hiess, P. Steffens, and G. Lapertot
Evidence for Three Fluctuation Channels in the Spin Resonance of the Unconventional Superconductor $CeCoIn_5$
Physical Review Letters **109** 237210 (2012)

119 B. W. Riemer, A. Abdou, D. K. Felde, R. L. Sangrey, T. J. Shea, M. W. Wendel, D. L. West, A. L. Kaminsky, M. Futakawa, S. Hasegawa, H. Kogawa, T. Naoe, and C. H. Farny
Demonstration of Small Gas Bubbles for Mitigation of Cavitation Damage and Pressure Waves in Short-pulse Mercury Spallation Targets
Proceedings of ICANS-XX 320 (2012)

120 P. K. Saha, H. Hocchi, H. Harada, N. Tani, M. Yoshimoto, and S. Meigo
Effect of the 2011 Great East Japan Earthquake in the injection and extraction of the J-PARC 3-GeV RCS
Proceedings of 3rd International Particle Accelerator Conference (IPAC '12) (Internet) 490 (2012)

121 Y. Saito, F. Naito, C. Kubota, S. Meigo, H. Fujimori, N. Ogiwara, J. Kamiya, M. Kinsho, Z. Kabeya, and T. Kubo
Material and surface processing in J-PARC vacuum system
Vacuum **86** 817 (2012)

122 K. Sakai, M. Futakawa, H. Takada, S. Sakamoto, F. Maekawa, H. Kinoshita, M. Seki, K. Haga, H. Kogawa, T. Wakui, T. Naoe, Y. Kasugai, H. Tatsumoto, T. Aso, S. Hasegawa, K. Oikawa, M. Ooi, A. Watanabe, M. Teshigawara, S. Meigo, K. Ikezaki, A. Akutsu, and M. Harada
Influence of Great East Japan Earthquake on Neutron Target Station in J-PARC
Proceedings of ICANS-XX 113 (2012)

123 K. Sakai, T. Oku, T. Shinohara, H. Kira, M. Ooi, F. Maekawa, K. Kakurai, T. Ino, Y. Arimoto, H. M. Shimizu, Y. Sakaguchi, J. Suzuki, K. Ohoyama, and L. J. Chang
Development of polarized Xe gas target for neutron experiment at J-PARC
Journal of Physics: Conference Series **340** 012037 (2012)

124 K. Sakai, S. Sakamoto, H. Kinoshita, M. Seki, K. Haga, H. Kogawa, T. Wakui, T. Naoe, Y. Kasugai, H. Tatsumoto, T. Aso, S. Hasegawa, F. Maekawa, K. Oikawa, M. Oi, A. Watanabe, M. Teshigawara, S. Meigo, K. Ikezaki, A. Akutsu, M. Harada, H. Takada, and M. Futakawa
Influence of Great East Japan Earthquake on neutron source station in J-PARC
東日本大地震の J-PARC 中性子源ステーションに対する影響
JAEA-Technology **2011-039** (2012)

125 K. Sakasai, K. Toh, T. Nakamura, K. Takakura, C. Konno, and Y. Iwamoto
Storage Characteristics of Mixtures of $KCl:Eu^{2+}$ Phosphors and Polyethylene Powder by Irradiation of Fast Neutrons
2012 IEEE Nuclear Science Symposium and Medical Imaging Conference Record 318 (2012)

126 H. Sato
Quantitative Imaging of Crystalline Structural Information by Pulsed Neutron Transmission
パルス中性子透過法による結晶組織構造情報の定量的イメージング
Hamon / 波紋 **22** 156 (2012)

127 M. Sato, T. Kawamata, Y. Kobayashi, Y. Yasui, T. Iida, K. Suzuki, M. Itoh, T. Moyoshi, K. Motoya, R. Kajimoto, M. Nakamura, Y. Inamura, and M. Arai
Study of magnetic excitation spectra of several Fe-pnictide systems
Journal of Physics: Conference Series **400** 022105 (2012)

128 M. Sato and Y. Kobayashi
On the superconducting pairing mechanism of Fe-based systems—Is it new or well-known ?
Solid State Communications **152** 688 (2012)

129 M. Sato, Y. Kobayashi, S. Satomi, T. Kawamata, and M. Itoh
Impurity effects on the superconducting transition temperatures of Fe pnictides and superconducting symmetry of the order parameter
Journal of Physics: Conference Series **400** 022014 (2012)

130 S. Shamoto, M. Ishikado, S. Wakimoto, K. Kodama, R. Kajimoto, and M. Arai
Dynamical Spin Susceptibility Studied by Inelastic Neutron Scattering on $LaFeAsO_{1-x}F_x$
Journal of Physics: Conference Series **340** 012075 (2012)

131 T. Shikama, T. Shimokawa, S. C. Lee, T. Isono, A. Ueda, K. Takahashi, A. Nakao, R. Kumai, H. Nakao, K. Kobayashi, Y. Murakami, M. Kimata, H. Tajima, K. Matsubayashi, Y. Uwatoko, Y. Nishio, K. Kajita, and H. Mori
Magnetism and Pressure-Induced Superconductivity of Checkerboard-Type Charge-Ordered Molecular Conductor β-(meso-DMBEDT-TTF)$_2X$ ($X = PF_6$ and AsF_6)
Crystals **2** 1502 (2012)

132 H. Shimakura, Y. Kawakita, Y. Inamura, T. Kikuchi, H. Ueno, M. Nakamura, K. Nakajima, S. Ohira-Kawamura, K. Shibata, M. Arai, and S. Takeda
Quasi-elastic neutron scattering of dense molecular liquid selenium bromide
Journal of Physics: Conference Series **340** 012080 (2012)

133 K. Shimomura, P. Bakule, F. L. Pratt, K. Ishida, K. Ohishi, I. Watanabe, Y. Matsuda, K. Nagamine, E. Torikai, and K. Nishiyama
Photo Detachment of Negatively Charged Muonium in GaAs by Laser Irradiation
Physics Procedia **30** 224 (2012)

134 M. Shiotsu, H. Kobayashi, T. Takegami, Y. Shirai, H. Tatsumoto, K. Hata, H. Kobayashi, Y. Naruo, and Y. Inatani

Transient heat transfer from a horizontal flat plate in a pool of liquid hydrogen
Advances in Cryogenic Engineering, AIP Conf. Proc. **1434** 1059 (2012)

135 M. Shiotsu, T. Takegami, K. Hikawa, Y. Shirai, H. Tatsumoto, K. Hata, H. Kobayashi, Y. Naruo, and Y. Inatani
Heat Transfer Characteristic Test of Forced Flow Supercritical Hydrogen for Superconductor Cooling
Proceeding of ICEC24-ICMC2012 165 (2012)

136 Y. Shirai, M. Shiotsu, H. Kobayashi, T. Takegami, H. Tatsumoto, K. Hata, H. Kobayashi, Y. Naruo, Y. Inatani, and K. Kinoshita
DNB heat flux in forced flow of subcooled liquid hydrogen under pressures
Advances in Cryogenic Engineering, AIP Conf. Proc. **1434** 1067 (2012)

137 P. Strasser, H. Fujimori, K. Koseki, Y. Hori, H. Matsumoto, K. Shimomura, A. Koda, N. Kawamura, S. Makimura, M. Kato, Y. Kobayashi, W. Higemoto, T. U. Ito, K. Ninomiya, K. Kojima, R. Kadono, K. Nishiyama, and Y. Miyake
New Muon Kicker System for the Decay Muon Beamline at J-PARC
Physics Procedia **30** 65 (2012)

138 C. Su, C. Chen, M. Lin, H. Chen, H. Iwase, S. Koizumi, and T. Hashimoto
Nucleosome-like Structure from Dendrimer-Induced DNA Compaction
Macromolecules **45** 5208 (2012)

139 Y. H. Su, Y. Tomota, S. Harjo, and Y. Adachi
Deformation-induced grain coalescence in an electrodeposited pure iron sheet studied by in situ neutron diffraction and electron backscatter diffraction
Acta Materialia **60** 3393 (2012)

140 J. Sugiyama, M. Månsson, K. Kamazawa, M. Harada, O. Ofer, D. Andreica, A. Amato, J. H. Brewer, E. J. Ansaldo, H. Ohta, C. Michioka, and K. Yoshimura
Successive Magnetic Transitions in RECoAsO
Physics Procedia **30** 262 (2012)

141 J. Sugiyama, K. Mukai, H. Nozaki, M. Harada, K. Kamazawa, Y. Ikedo, M. Månsson, O. Ofer, E. J. Ansaldo, J. H. Brewer, K. H. Chow, I. Watanabe, Y. Miyake, and T. Ohzuku
Lithium Diffusion in Lithium-Transition-Metal Oxides Detected by μ^+SR
Physics Procedia **30** 105 (2012)

142 J. Sugiyama, H. Nozaki, M. Harada, K. Kamazawa, Y. Ikedo, Y. Miyake, O. Oren, M. Månsson, E. J. Ansaldo, K. H. Chow, G. Kobayashi, and R. Kanno
Diffusive behavior in $LiMPO_4$ with M=Fe, Co, Ni probed by muon-spin relaxation
Physical Review B **85** 054111 (2012)

143 J. Sugiyama, H. Nozaki, K. Kamazawa, O. Ofer, M. Månsson, E. J. Ansaldo, J. H. Brewer, K. H. Chow, I. Watanabe, Y. Ikedo, Y. Miyake, G. Kobayashi, and R. Kanno
Magnetic and Diffusive Nature of $LiFePO_4$
Physics Procedia **30** 190 (2012)

144 K. Takahashi, H. Oguro, S. Awaji, K. Watanabe, S. Harjo, and K. Aizawa
Strain measurements by neutron diffraction on Nb_3Sn cable with stainless steel reinforcement strands
Superconductor Science and Technology **25** 054001 (2012)

145 K. Takahashi, H. Oguro, S. Awaji, K. Watanabe, S. Harjo, K. Aizawa, S. Machiya, H. Suzuki, and K. Osamura
Prebending effect on three-dimensional strain in CuNb/(Nb, Ti)$_3$Sn wires under a tensile load
IEEE Transactions on Applied Superconductivity **22** 6000204 (2012)

146 K. Takahashi, H. Oguro, G. Nishijima, S. Awaji, K. Watanabe, S. Harjo, and K. Aizawa
Axial and lateral lattice strain states under a tensile load in as-reacted and prebent CuNb/Nb_3Sn wires using neutron diffraction
Journal of Applied Physics **111** 043908 (2012)

147 M. Takeda
Structural analysis of interfaces in thin films using neutron reflectometry
Journal of the Japan Institute of Electronics Packaging **15** 492 (2012)

148 M. Takeda, J. Suzuki, T. Akiya, and H. Kato
Small-Angle Neutron Scattering Measurements of the Averaged Internal Structures in Neodymium-Iron-Boron (Nd-Fe-B) Sintered Magnets
Journal of the Japan Institute of Metals **76** 165 (2012)

149 M. Takeda and D. Yamazaki
Polarized neutron reflectometer SHARAKU (BL17) at J-PARC
SHIKI **16** 4 (2012)

150 M. Takeda, D. Yamazaki, K. Soyama, R. Maruyama, H. Hayashida, H. Asaoka, T. Yamazaki, M. Kubota, K. Aizawa, M. Arai, Y. Inamura, T. Itoh, K. Kaneko, T. Nakamura, K. Oikawa, T. Ohhara, Y. Sakaguchi, K. Sakasai, T. Shinohara, J. Suzuki, K. Suzuya, I. Tamura, K. Toh, H. Yamagishi, N. Yoshida, and T. Hirano
Current Status of a New Polarized Neutron Reflectometer at the Intense Pulsed Neutron Source of the Materials and Life Science Experimental Facility (MLF) of J-PARC
Chinese Journal of Physics **50** 161 (2012)

151 A. Takemori, S. Saijo, S. Suzuki, S. Miyasaka, S. Tajima, A. Nakao, H. Nakao, R. Kumai, and Y. Murakami
Correlation between Tc and Transport Properties in $PrFeP_{1-x}As_xO_{0.9}F_{0.1}$
Journal of the Physical Society of Japan **81** SB043 (2012)

152 I. Tamura, K. Oikawa, T. Kawasaki, T. Ohhara, K. Kaneko, R. Kiyanagi, H. Kimura, M. Takahashi, T. Kiyotani, M. Arai, Y. Noda, and K. Ohshima
Current status of a time-of-flight single crystal neutron diffractometer SENJU at J-PARC
Journal of Physics: Conference Series **340** 012040 (2012)

153 H. Tatsumoto, T. Aso, K. Ohtsu, H. Sakurayama, Y. Kawakami, and M. Futakawa
Dynamic behavior of the cryogenic hydrogen system using only a heater control
Advances in Cryogenic Engineering, AIP Conf. Proc. **1434** 391 (2012)

154 H. Tatsumoto, T. Aso, K. Ohtsu, T. Uehara, H. Sakurayama, Y. Kawakami, T. Kato, and M. Futakawa
Design of a compact type cryogenic accumulator to mitigate a pressure fluctuation caused by a sudden KW-order heat load
Advances in Cryogenic Engineering, AIP Conf. Proc. **1434** 368 (2012)

155 H. Tatsumoto, Y. Shirai, M. Shiotsu, K. Hata, Y. Naruo, H. Kobayashi, Y. Inatani, and K. Kinoshita
Forced convection heat transfer of subcooled liquid hydrogen in horizontal tubes
Advances in Cryogenic Engineering, AIP Conf. Proc. **1434** 747 (2012)

156 H. Tatsumoto, Y. Shirai, M. Shiotsu, K. Hata, Y. Naruo, H. Kobayashi, Y. Inatani, and N. Narita

Effect of a Heated Pipe Length on DNB Heat Flux in Forced Flow of Liquid Hydrogen
Proceeding of ICEC24-ICMC2012 157 (2012)

157 M. Teshigawara, M. Harada, M. Ooi, T. Kai, F. Maekawa, and M. Futakawa
Development of invar joint for hydrogen transfer line in JSNS
Journal of Nuclear Materials **431** 212 (2012)

158 M. Teshigawara, M. Harada, M. Ooi, T. kai, F. Maekawa, and M. Futakawa
R&D on 2nd moderator fabrication for JSNS
Proceedings of ICANS-XX 326 (2012)

159 M. Teshigawara, H. Kinoshita, T. Wakui, S. Meigo, M. Seki, M. Harada, M. Ito, T. Suzuki, K. Ikezaki, F. Maekawa, M. Futakawa, K. Sato, T. Tajima, and T. Nakazawa
Maintenance of Used Components in Spallation Neutron Source -Moderator・Reflector and Proton Beam Window-
核破砕中性子源使用済み機器の保守
―モデレータ・反射体、陽子ビーム窓―
JAEA-Technology **2012-024** (2012)

160 K. Toh, T. Nakamura, K, Sakasai, K. Soyama, H. Yamagishi
Development of Gas-Based 2-Dimensional Neutron Detector with Individual Line Readout and Optical Signal Transmission System
2012 IEEE Nuclear Science Symposium and Medical Imaging Conference Record 153 (2012)

161 K. Toh, T. Nakamura, K. Sakasai, K. Soyama, and H. Yamagishi
Improved micro-pixel detector element for neutron measurement under high pressure
Journal of Instrumentation **7** C01025 (2012)

162 M. Tomita, M. Muralidhar, K. Suzuki, A. Ishihara, Y. Fukumoto, K. Osamura, S. Machiya, and S. Harjo
Non-destructive magneto-strain analysis of $YB_2Cu_3O_y$ superconducting magnets using neutron diffraction in the time-of-flight mode
Journal of Applied Physics **112** 063923 (2012)

163 K. Tomiyasu, M. Matsuura, H. Kimura, K. Iwasa, K. Ohoyama, T. Yokoo, S. Itoh, E. Kudoh, T. Sato, and M. Fujita
Modified cross-correlation for efficient white-beam inelastic neutron scattering spectroscopy
Nuclear Instruments and Methods in Physics Research A **677** 89 (2012)

164 Y. Ueda, A. Nakao, H. Nakao, and Y. Ohta
Ferromagnetic Metal-Insulator Transition : Peierls Mechanism for Spinless Fermions (Current Topics)
強磁性金属絶縁体転移：完全スピン分極した電子系のパイエルス転移（最近の研究から）
BUTSURI / 日本物理学会誌 **67** 571 (2012)

165 T. Wakui, T. Naoe, M. Teshigawara, H. Kogawa, K. Haga, and M. Futakawa
First trial for post irradiation examination on the JSNS target
Proceedings of ICANS-XX 353 (2012)

166 J. M. Wikberg, M. Månsson, M. Dahbi, K. Kamazawa, and J. Sugiyama
Magnetic Order and Frustrated Dynamics in Li $(Ni_{0.8}Co_{0.1}Mn_{0.1})O_2$: A Study by μ^+SR and SQUID Magnetometry
Physics Procedia **30** 202 (2012)

167 H. Yamagishi, T. Toh, T. Nakamura, K. Sakai, and K. Soyama
A Low Noise ASIC for Two Dimensional Neutron Gas Detector with Performance of High Spatial Resolution (Contract Research)
高分解能二次元ガス型中性子検出器用低雑音 ASIC の設計と性能評価（委託研究）
JAEA-Research **2011-051** (2012)

168 T. Yamazaki, H. Asaoka, T. Taguchi, S. Yamamoto, D. Yamazaki, R. Maruyama, M. Takeda, and S. Shamoto
Analysis of buried heterointerfacial hydrogen in highly lattice-mismatched epitaxy on silicon
Thin Solid Films **520** 3300 (2012)

169 S. Yano, J. Akimitsu, S. Itoh, T. Yokoo, S. Satoh, D. Kawana, and Y. Endoh
Magnetic excitations in MnP
Journal of Physics: Conference Series **391** 012113 (2012)

170 H. Yashima, Y. Kasugai, N. Matsuda, H. Matsumura, S. Sekimoto, A. Toyoda, H. Iwase, N. Mokhov, A. Leveling, D. Boehnlein, K. Vaziri, K. Oishi, H. Nakashima, and Y. Sakamoto
Spatial Distribution Measurement of Neutrons Produced by 120-GeV Proton Beam in Concrete Shield
Progress in Nuclear Science and Technology **3** 40 (2012)

171 M. Yashima, H. Yamada, S. Nuansaeng, and T. Ishihara
Role of Ga^{3+} and Cu^{2+} in the High Interstitial Oxide-Ion Diffusivity of Pr_2NiO_4-based Oxides: Design Concept of Interstitial Ion Conductors through the Higher-Valence d^{10} Dopant and Jahn-Teller Effect
Chemistry of Materials **24** 4100 (2012)

172 T. Yokoo, S. Itoh, F. Trouw, A. Llobet-Megias, and J. Akimitsu
Magnetic excitations in possible spin-Peierls system TiOBr
Journal of Physics: Conference Series **400** 032123 (2012)

173 K. Yokoyama, K. Nagamine, K. Shimomura, H.W.K. Tom, R. Kawakami, P. Bakule, Y. Matsuda, K. Ishida, K. Ohishi, F.L. Pratt, I. Shiraki, and E. Torikai
Detection of Conduction Electron Spin Polarization in n-GaAs by Negative Muonium
Physics Procedia **30** 231 (2012)

174 T. Yokoyama, M. Mizuguchi, Y. Nabeshima, K. Kusaka, T. Yamada, T. Hosoya, T. Ohhara, K. Kurihara, K. Tomoyori, I. Tanaka, and N. Niimura
Hydrogen-bond network and pH sensitivity in transthyretin: Neutron crystal structure of human transthyretin
Journal of Structural Biology **177** 283 (2012)

175 M. Yoshimoto, K. Yamamoto, P. K. Saha, S. Meigo, H. Hotchi, N. Hayashi, K. Okabe, and M. Kinsho
Development of the beam halo monitor in the J-PARC 3-GeV RCS
Proceedings of IPAC2012 2122 (2012)

176 T. Yoshimura, T. Kusano, H. Iwase, M. Shibayama, T. Ogawa, and H. Kurata
Star-Shaped Trimeric Quaternary Ammonium Bromide Surfactants: Adsorption and Aggregation Properties
Langmuir **28** 9322 (2012)

177 I. M. Vishik, M. Hashimoto, R.-H He, W. S. Lee, F. Schmitt, D. H. Lu, R. G. Moore, C. Zhang, W. Meevasana, T. Sasagawa, S. Uchida, K. Fujita, S. Ishida, M. Ishikado, Y. Yoshida, H. Eisaki, Z. Hussain, T. P. Devereaux, and Z. -X. Shen
Phase competition in trisected superconducting dome
Proceedings of the National Academy of Science **109** 18332 (2012)

Editorial Board - MLF Annual Report 2012

Chief Editor
Kaoru Sakasai
Neutron Instrumentation Section

Shin-ichiro Meigo
Neutron Source Section

Hideki Tatsumoto
Neutron Source Section

Mitsutaka Nakamura
Neutron Science Section

Kaoru Shibata
Neutron Science Section

Takashi Ino
Neutron Science Section

Kenji M. Kojima
Muon Science Section

Toshiki Asai
CROSS-Tokai

Garry Foran
CROSS-Tokai

Taketo Moyoshi
CROSS-Tokai

Yoshifumi Sakaguchi
CROSS-Tokai

J-PARC 13-03
KEK Progress Report 2013-4

J-PARC/MLF
Materials and Life Science Division
J-PARC Center
Tokai, Naka-gun, Ibaraki 319-1195, Japan
http://j-parc.jp/MatLife/en/index.html

CROSS
Comprehensive Research Organization for Science and Society
http://www.cross-tokai.jp/